# Microstructural Controls on the Crystallization and Exhumation of Metamorphic Rocks

Alexandra Bobiak Nagurney

Dissertation submitted to the faculty of the Virginia Polytechnic Institute and State University in partial fulfillment of the requirements for the degree of

Doctor of Philosophy
In
Geosciences

Mark J. Caddick, Chair
F. Marc Michel, Co-Chair
Besim Dragovic
Richard D. Law
Nancy L. Ross
Christopher R. Winkler

April 26, 2021
Blacksburg, VA

Keywords: metamorphism, metamorphic microstructure, garnet, epitaxial nucleation, grain boundaries

# Microstructural Controls on the Crystallization and Exhumation of Metamorphic Rocks

## Abstract

Alexandra Bobiak Nagurney

Microstructural data on the orientation and distribution of minerals can be utilized to better understand the processes controlling mineral crystallization during metamorphism and the extent to which equilibrium versus kinetic factors control the evolution of metamorphic rocks. Four studies in this dissertation address this, finding that: i) garnet crystals crystallize via epitaxial nucleation in which garnet crystallizes by templating on the crystal structure of muscovite; ii) the distribution of grain boundary void space at quartz-quartz and garnet-quartz grain boundaries is a function of the orientation of quartz crystals on either side of the grain boundary. There are more voids, and in some cases larger voids, at grain boundaries in which the *a*-axis of a neighboring quartz grain is perpendicular to the grain boundary than any other orientation; iii) the chemical potentials of garnet-forming components evolve differently in samples in which garnet growth either significantly or minimally overstepped equilibrium garnet-forming reactions; iv) the southwestern Meguma Terrane, Nova Scotia, experienced peak metamorphic conditions of ~630ºC & 4.0 kbar, likely resulting from regional metamorphism during the Neoacadian orogeny. A case study on the mechanisms controlling garnet crystallization in one Nova Scotian sample reveals that the rate limiting step of garnet crystallization was probably the diffusional transport of Al through the intergranular matrix. Taken together, this work has implications for understanding: i) the properties of grain boundaries in metamorphic rocks and ii) the extent to which equilibrium versus kinetic factors impact metamorphic petrogenesis.

Microstructural Controls on the Crystallization and Exhumation of Metamorphic Rocks

## General Audience Abstract

Alexandra Bobiak Nagurney

A fundamental question in the development of metamorphic rocks, or rocks that form due to changes in pressure and temperature conditions deep in the Earth's mountain belts, is: what controls the crystallization of new minerals? While pressure, temperature, and bulk composition likely play a major role in this, it is also possible that the distribution of reactant minerals and the transport of elements through the rock may also play a role in mineral crystallization. This dissertation explores several projects related to this broad topic. In one example, garnet, an important metamorphic mineral, was found to crystallize by utilizing the atomic structure of another mineral in the rock. This creates a favorable pathway for the crystallization of garnet, which preferentially grows on this 'parent' mineral. Further, the distribution of porosity, or void space, at the interfaces between mineral grains in metamorphic rocks is found to be controlled by the orientation of those minerals. This porosity likely formed when the rocks were exhumed from deep in the Earth towards its surface. Metamorphic rocks can also tell the story of continental plates colliding millions of years ago. In an example from the formation of the Appalachian Mountains ~400 million years ago, a combination of collisional tectonic forces and the heat from magmas in the shallow crust resulted in metamorphic rock, which make up much of southern Nova Scotia today. This work has important implications for understanding: i) porosity in metamorphic rocks and ii) how minerals crystallize during metamorphism.

“*Figuring out the Appalachians was Problem 1 in American geology, and a difficult place to begin, for it was scarcely a matter of layer-cake legibility, like the time scale in the walls of the Grand Canyon. It was a compressed, chaotic, ropy enigma four thousand kilometers from end to apparent end, full of overturned strata and recycled rock, of steep faults and horizontal thrust sheets, of folds so tight that what had once stretched twenty miles might now fit into five.”*

John McPhee, In Suspect Terrain

# Acknowledgements

Well we've made it this far, so here this goes. There are a lot of people I need to thank that helped me along with this PhD journey. To my advisor, Mark Caddick, thank you for the research mentorship and the sense of community that you, Kristie and James provided me in Blacksburg. To Marc Michel, my co advisor, thank you for your research help over the last few years. Thanks to both Mark and Marc for letting me drive the direction of my research (after a careful lit search, clear justification, and development of testable hypotheses).

I would like to thank Besim Dragovic for many helpful conversations about life, millennial culture, and garnet crystallization kinetics over the last few years. Rick Law is thanked for providing me with an appreciation for quartz microstructures that I did not expect to develop during my PhD and helpful conversations about life during my PhD. I would like to thank Nancy Ross for her help with understanding crystallography and the elastic properties of minerals. I would like to thank Chris Winkler for teaching me how to use the TEM. I would also like to thank Ken Eriksson for fun and helpful conversations at Bollos, the taco truck, and Gillies during my PhD. I would like to thank Dr. M and Dr. Carley at Lafayette College for providing me with the research foundations I needed to take on this PhD. Finally, I would like to thank Bob Tracy for conversations about microprobes, politics, wine, and Appalachian geology, and for the comfiest office chair ever.

I would like to thank my friends in the Petrology and Nanoscience groups at Virginia Tech who provided research feedback, friendship, and laughs over the last few years. They include: Victor Guevara, Emma Tulsky, Jen Gorce, Calvin Mako, Kirk Broadwell, Lisa Whalen, Jonny Prouty, Dalton Anderson, Alix Ehlers, Priya Bose, Rose McGoarty, Rui Serra-Maia, McNeil Bauer, Aly Hoeher, Ali Namayandeh, and Faisal Adams. I would also like to thank other

friends within the department that helped make Derring Hall a more bearable place to spend my days: Mike Vadman, Jess DePaolis, Sarah Ulrich, Brady Ziegler, Drew Parent, Kristin Chilton, Natalia Varela, Stacey Law, Rick Jayne, Sebastian Merglesberg, and Lowell Moore. Finally, to my other friends both in Blacksburg: Natalie Sievers, Meg Beatty, Marie Stettler Kleine, Claudia Rodriguez, Kaylyn Messenger, Angela Bladen, Cameron Varano, and out of Blacksburg: Anna Golub, Gabby Rudolph, Carrie McIntosh, Christine Pigott, and the cast of 'We were at Lafayette and now it's real' thank you for providing perspective and a break from PhD-ing over the last few years.

I would also like to thank the Virginia Tech ICTAS Doctoral Scholars Program for funding the first four years of my PhD, and the Virginia Tech Department of Geosciences, Geological Society of America, Virginia Tech Graduate School, and the American Association of Petroleum Geologists for funding various aspects of my projects. This research was also made possible by a lot of great people being willing to help with it. Those people include: Ya Peng Yu, Steve McCartney, and Sayako Inoue at the NCFL, Seth Kruckenberg at Boston College, David Pattison at the University of Calgary, Chris White at the Nova Scotia Department of Mines and Energy, and Lowell Moore in the Department of Geosciences.

Finally, I would like to thank my parents for all over their support over the last 27 years and for encouraging me to become the third Dr. Nagurney in our family, my Uncle Andrew, and my dog Maggie.

# Attribution

**Chapter 2** is a manuscript that has been published as: "Nagurney, A.B., Caddick, M.J., Pattison, D.R.M., & Michel, F.M., 2021, Preferred orientation of garnet porphyroblasts reveal previously cryptic templating during nucleation, *Scientific Reports,* https://doi.org/10.1038/s41598-021-85525-7*"*. Nagurney conceptualized the study, developed the methodology, performed the TEM, EBSD, and software analyses, wrote the original draft, and made the figures and tables. Caddick helped conceptualize the study, develop the methodology, interpret the results, and reviewed and edited the manuscript. Pattison collected the sample, helped interpret the results, and reviewed and edited the manuscript. Michel helped conceptualize the study, develop the methodology, interpret the results, and reviewed and edited the manuscript. See the acknowledgements section of this chapter for more information.

**Chapter 3** is a manuscript that has been published as: "Nagurney, A.B., Caddick, M.J., Law, R.D., Ross, N.L., Kruckenberg, S.C., 2021, Crystallographically controlled void space at grain boundaries in the Harkless quartzite, *Journal of Structural Geology,* https://doi.org/10.1016/j.jsg.2020.104235". Nagurney conceptualized the study, performed the EBSD, SEM, and statistical analyses, drafted the figures and tables, helped make interpretations, and wrote the original draft of the manuscript. Caddick helped conceptualize the study, helped with interpretations, drafted Figure 6, and edited the manuscript. Law collected the sample, provided information about the geologic context of the sample, and helped interpret the results. Ross helped conceptualize the study, provided resources on the elastic properties of quartz, and edited the manuscript. Kruckenberg helped perform the EBSD analytical work and edited the manuscript. Additional information is available in the Acknowledgements section of this chapter.

**Chapter 4** is a manuscript that is In Press as: "Nagurney, A.B., Caddick, M.J., Dragovic, B., Busse, K.M., 2021, The (chemical) potential for understanding overstepped garnet nucleation and growth. *American Mineralogist.* https://doi.org/10.2138/am-2020-7354" Nagurney wrote the manuscript, ran the thermodynamic model calculations, helped interpret the results, and wrote the first draft of the manuscript. Caddick helped design the study, interpret the results, edit the manuscript, and drafted Figures 8 & 9. Dragovic helped interpret the results and edited the manuscript. Busse performed earlier calculations that this study was built on, helped interpret the results, and edited the manuscript. Additional information can be found the Acknowledgements section of that chapter.

**Chapter 5** is a manuscript that will be submitted to the Journal of Metamorphic Geology. Nagurney wrote the manuscript, performed the analysis and interpretation, and drafted the figures. Caddick helped conceptualize the study, interpret the results, and edited the manuscript.

# Table of Contents

# Chapter 1: Introduction

Rocks can be metamorphosed upon experiencing changes in pressure (*P*) or temperature (*T*), or upon interaction with fluids. Studies of metamorphic rocks can help us understand the tectonic evolution of the regions that they form in, such as during mountain building, because they chemically and texturally record processes of burial, deformation, fluid movement, and heat transfer (e.g. Tracy et al. 1976; Spear et al. 1984; Austrheim 1987; Brown 1993; Lasaga and Rye 1993; Ferry and Gerdes 1998; Rubatto and Hermann 2001; Blatt et al. 2006; Putnis and Austrheim 2010).

Metamorphic petrologists generally study crustal rocks through the lens of an equilibrium paradigm. Here, with changing *P*-*T* conditions, minerals continually react so that the mineral assemblage, and the compositions of those minerals (and accompanying melts), achieve the lowest possible Gibbs free energy of the system. This has led to many advancements in understanding crustal processes in the Earth, and has been the standard for understanding how rocks respond to heat and pressure in our planet (e.g. Thompson 1957; Essene 1982; Spear and Selverstone 1983; Powell et al. 1998; Kerrick and Connolly 2001; Waters and Lovegrove 2002; White and Powell 2002; Hacker et al. 2003; Pattison and Tinkham 2009). The concept of metamorphic facies, which states that two chemically similar metamorphic rocks that formed under the same *P*-*T* conditions should contain similar minerals, and the repetition of metamorphic facies series worldwide, continues to suggest that pressure, temperature, and bulk composition play an important role in controlling metamorphic mineral assemblages.

However, based on interpretations of rock textures, quantitative thermo-barometry, and comparisons of observed mineral assemblages and compositions in natural rocks to those calculated via equilibrium thermodynamic models, it appears that many metamorphic rocks may have deviated substantially from their equilibrium states (e.g. Ridley and Thompson 1986; Waters and Lovegrove 2002; Zeh and Holness 2003; Pattison and Tinkham 2009; Dragovic et al. 2012; Spear et al. 2014; Castro and Spear 2016; Wolfe and Spear 2017). In these examples, kinetic processes including reactant breakdown, intergranular diffusion, nucleation, and crystal growth likely play an important role in the development of metamorphic mineral assemblages (Kretz 1973; Ridley and Thompson 1986; Carlson 2011).

Therefore, it is important to discern the extent to which equilibrium versus kinetic factors control the evolution of metamorphic rocks. It is likely that in some cases the equilibrium model provides an appropriate model for metamorphism (Gaidies et al. 2008; Gatewood et al. 2015; George and Gaidies 2017; Catlos et al. 2018), while in other cases it appears that rocks deviate far from equilibrium during their evolution (Pattison and Tinkham 2009; Pattison et al. 2011; Dragovic et al. 2012; Spear et al. 2014; Carlson et al. 2015; Castro and Spear 2016). Specifically, garnet is an important mineral to study equilibrium versus kinetic controls on metamorphism because it is such a useful mineral for deciphering *P*-*T* paths and rates of tectonic processes (e.g. Tracy et al. 1976; Ferry and Spear 1978; Spear and Selverstone 1983; Spear et al. 1984; St-Onge 1987; Florence and Spear 1991; Konrad-Schmolke et al. 2006; Pollington and Baxter 2010; Baxter and Scherer 2013; Caddick and Kohn 2013; Moynihan and Pattison 2013; Gaidies et al. 2014; Dragovic et al. 2015; Baxter et al. 2017). Further, certain aspects of garnet, such as its cubic crystal structure, its propensity to incorporate a wide range of elements into its structure, and the common knowledge that garnet often grows radially out from its crystal center, make it possible to study crystallization processes in detail.

This dissertation takes multiple approaches to investigating the relative importance of equilibrium versus kinetics in controlling metamorphic petrogenesis. These approaches include:

investigating microstructural relationships between mineral phases, interrogating equilibrium-based thermodynamic models, and studying the properties of grain boundaries. I will briefly outline the chapters below.

**Chapter 2** discusses how garnet may crystallize via epitaxial nucleation on muscovite during the metamorphism of foliated, pelitic amphibolite facies rocks. This study looks at three samples from two terranes: the Nelson Aureole, British Columbia and the Mosher's Island Formation, Nova Scotia. The orientations of twenty-two garnet crystals were analyzed via electron backscatter diffraction (EBSD) and one sample via transmission electron microscopy (TEM) to investigate the crystallographic relationships between garnet and both muscovite and chlorite (which define the foliation in these rocks). All twenty-two garnet crystals have one of three crystal directions parallel to the foliation of the rock. Comparison of atomic-scale crystal structure models of garnet, muscovite, and chlorite in those orientations reveal that the crystal structure of garnet and muscovite (specially the spacing and orientation of Al and Si) is similar enough that garnet could crystallize by templating on the crystal structure of muscovite. This chapter highlights the fact that epitaxial nucleation may be a common, but overlooked, process in controlling the crystallization of garnet.

**Chapter 3** also looks at how microstructure can control metamorphic processes, but here we study how the crystal orientation of quartz controls the distribution of porosity in exhumed quartzites from the Harkless quartzite, eastern California. During exhumation (cooling and exhumation), the molar volume of quartz decreases anisotropically, meaning that the length of the *a*-axis of quartz decreases by more than that of the *c*-axis. Here, we compare the distribution of grain boundary void space (porosity) to the crystal orientation of quartz and find that there is a statistically significant relationship in which there are more void spaces at grain boundaries normal to the *a*-axis of quartz than any other orientation. These results are interpreted as grain boundaries preferentially opening at locations at which the length of the adjacent grain decreases substantially during exhumation.

**Chapter 4** takes a different approach to studying the crystallization of garnet, and utilizes equilibrium thermodynamic modeling to investigate the energetic consequences of overstepped garnet nucleation and growth. Twelve examples from the literature that show varying degrees of overstepping from effectively none to >50ºC and 1 kbar are utilized. For each example, two phase equilibria diagrams were calculated: one in which all the phases equilibrated and a second one in which the stability of garnet was prohibited. This allowed us to investigate the energetic differences between a garnet-bearing and a garnet-absent calculation. The examples in which garnet was previously shown to not be overstepped showed a difference in the chemical potential ($\mu$) of all garnet-forming components between the two calculations right at garnet-in. In the examples in which garnet was previously shown to be overstepped, there was an immediate difference at garnet-in for some components (i.e. MnO) but not for other components (i.e. $Al_2O_3$). In all examples, $\Delta\mu_{Al2O3}$ was the final component to deviate from zero, near the previously determined *P*-*T* of garnet-in.

**Chapter 5** includes both a regional metamorphic study of the Appalachian orogen with a deeper discussion of the kinetics of garnet crystallization in one sample. Here, quantitative *P*-*T* constraints were placed on a suite of samples from the southwestern Meguma Terrane, Nova Scotia, the most outboard terrane of the Appalachian orogen. These results show that peak metamorphism conditions in the Meguma Terrane ~400-370 Ma were ~630ºC and 4.0 kbar. The metamorphism of the southwestern Meguma Terrane was likely a function of both regional metamorphism during the Neoacadian Orogeny (405-390 Ma) with heat from granitic plutons

373 Ma likely enhancing metamorphic recrystallization. Interpretation of X-Ray Computed Tomography (X-Ray CT) data on the 3D size, location, and shape of garnet crystals in one sample reveals that the average garnet radius in 126 μm and the crystal size distribution (CSD) is skewed to the right. 3D special statistical analysis of the garnet crystals reveal that they are ordered relative to a random distribution. This is interpreted such that the rate limiting step for garnet crystallization was likely the intergranular diffusion of Al through the matrix. This chapter serves to both provide new *P-T* constrains and tectonic interpretations of the Meguma Terrane, Nova Scotia and utilize one sample as a case study for understanding garnet crystallization kinetics.

**Appendix A** presents data on the nanoscale properties of garnet-quartz grain boundaries from two samples from the Nelson Aureole, British Columbia. Two samples were investigated via TEM. In the low *T* sample (530ºC, 3.5 kbar), the garnet-quartz grain boundary is a planar structure with no void space and there does not appear to be any compositional changes in either phase next to the grain boundary. In the higher *T* sample (650ºC, 3.5 kbar), there is a void space at the grain boundary and the quartz crystal shows evidence of undergoing dynamic recrystallization (subgrain boundaries, evidence of dislocation climb). Once again, there is no evidence of any compositional changes in either phase at the grain boundary. Further characterization of the garnet-quartz grain boundaries via SEM in this sample reveals a wide range in the size of void spaces (0-963 nm) between garnet and quartz crystals. However, the size of void spaces correlates well with the orientation of quartz crystals, which is likely once again due to the anisotropic volume change of quartz during exhumation, in which larger void spaces correlate with the *a*-axis of quartz being normal to the grain boundary. This work highlights the fact that the elastic properties of minerals may control the properties of grain boundaries in exhumed metamorphic rocks and may be written up for publication at a later date.

In summary, work from this dissertation falls into two overlapping themes: i) elucidating how microstructural relationships can be utilized to better understand metamorphic processes (Chapters 2,3,5, Appendix A) and ii) clarifying the processes that control garnet crystallization during metamorphism (Chapters 2,45). I discuss how epitaxial nucleation of garnet on muscovite may be an important mechanism by which garnet crystallizes during metamorphism. I also show how equilibrium thermodynamic modeling can be utilized to understand overstepped metamorphic reactions. Data from quartz-quartz and garnet-quartz grain boundaries both reveal that the elastic properties of minerals may control the properties of grain boundaries in exhumed metamorphic rocks. Finally, I present new data on the metamorphism of the Meguma Terrane. In summary, this dissertation provides several examples of how studying the microstructural aspects of metamorphic rocks may improve understanding of metamorphic processes during mineral crystallization and exhumation.

## 1.2 REFERENCES

Austrheim, H. (1987) Eclogitization of lower crustal granulites by fluid migration through shear zones. Earth and Planetary Science Letters, 81, 221–232.

Baxter, E.F., and Scherer, E.E. (2013) Garnet geochronology: Timekeeper of tectonometamorphic processes. Elements, 9, 433–438.

Baxter, E.F., Caddick, M.J., and Dragovic, B. (2017) Garnet: A Rock-Forming Mineral Petrochronometer. Reviews in Mineralogy & Geochemistry, 83, 469–533.

Berman, R.G. (1988) Internally consistent thermodynamic data for minerals in the system Na2O-K2O-CaO-MgO-FeO-Fe2O-SiO2-TiO2-H2O-CO2. Journal of Petrology, 29, 445–552.

Blatt, H., Tracy, R.J., and Owens, B.E. (2006) Petrology: Igneous, Sedimentary, and Metamorphic, Fourth. W. H. Freeman and Company, New York.

Brown, M. (1993) P - T - t evolution of orogenic belts and the causes of regional metamorphism. Journal of the Geological Society, 150, 227–241.

Caddick, M.J., and Kohn, M.J. (2013) Garnet: Witness to the evolution of destructive plate boundaries. Elements, 9, 427–432.

Carlson, W.D. (1989) The significance of intergranuar diffusion to the mechanisms and kinetics of porphyroblast crystallization. Contribution to Mineralogy and Petrology, 103, 1–24.

——— (2010) Dependence of reaction kinetics on H2O activity as inferred from rates of intergranular diffusion of aluminium. Journal of Metamorphic Geology, 28, 735–752.

——— (2011) Porphyroblast crystallization: linking processes, kinetics, and microstructures. International Geology Review, 53, 406–445.

Carlson, W.D., Pattison, D.R.M., and Caddick, M.J. (2015) Beyond the equilibrium paradigm: How consideration of kinetics enhances metamorphic interpretation. American Mineralogist, 100, 1659–1667.

Castro, A.E., and Spear, F.S. (2016) Reaction overstepping and re-evaluation of peak P–T conditions of the blueschist unit Sifnos, Greece: implications for the Cyclades subduction zone. International Geology Review, 59, 1–15.

Catlos, E.J., Lovera, O.M., Kelly, E.D., Ashley, K.T., Harrison, T.M., and Etzel, T. (2018) Modeling High-Resolution Pressure-Temperature Paths Across the Himalayan Main Central Thrust (Central Nepal): Implications for the Dynamics of Collision. Tectonics, 37, 2363–2388.

Connolly, J.A.D. (2005) Computation of phase equilibria by linear programming: A tool for geodynamic modeling and its application to subduction zone decarbonation. Earth and Planetary Science Letters, 236, 524–541.

de Capitani, C., and Petrakakis, K. (2010) The computation of equilibrium assemblage diagrams with Theriak/Domino software. American Mineralogist, 95, 1006–1016.

Denison, C., Carlson, W.D., and Ketcham, R.A. (1997) Three-dimensional quantitative textural analysis of metamorphic rocks using high-resolution computed X-ray tomography: Part I. Methods and techniques. Journal of Metamorphic Geology, 15, 29–44.

Dohmen, R., and Milke, R. (2010) Diffusion in polycrystalline materials: grain boundaries, mathematical models, and experimental data. Reviews in Mineralogy & Geochemistry, 72, 921–970.

Dragovic, B., Samanta, L.M., Baxter, E.F., and Selverstone, J. (2012) Using garnet to constrain the duration and rate of water-releasing metamorphic reactions during subduction: An example from Sifnos, Greece. Chemical Geology, 314–317, 9–22.

Dragovic, B., Baxter, E.F., and Caddick, M.J. (2015) Pulsed dehydration and garnet growth during subduction revealed by zoned garnet geochronology and thermodynamic modeling, Sifnos, Greece. Earth and Planetary Science Letters, 413, 111–122.

Essene, E.J. (1982) Geologic thermometry and barometry. In Characterization of Metamorphism through Mineral Equilbria: Mineralogical Society of America pp. 153–206.

Ferry, J.M., and Gerdes, M.L. (1998) Chemically Reactive Fluid Flow During Metamorphism. Annual Review of Earth and Planetary Sciences, 26, 255–287.

Ferry, J.M., and Spear, F.S. (1978) Experimental calibration of the partitioning of Fe and Mg between biotite and garnet. Contributions to Mineralogy and Petrology, 66, 113–117.

Florence, F.P., and Spear, F.S. (1991) Effects of diffusional modification of garnet growth zoning on P-T path calculations. Contributions to Mineralogy and Petrology, 107, 487–500.

Frondel, C. (1940) Orientated inclusions of staurolite, zircon, and garnet in muscovite. Skating crystals and their significance. American Mineralogist, 25, 69–87.

Gaidies, F., Krenn, E., De Capitani, C., and Abart, R. (2008) Coupling forward modelling of garnet growth with monazite geochronology: An application to the Rappold Complex (Austroalpine crystalline basement). Journal of Metamorphic Geology, 26, 775–793.

Gaidies, F., Petley-Ragan, A., Chakraborty, S., Dasgupta, S., and Jones, P. (2015) Constraining the conditions of Barrovian metamorphism in Sikkim, India: P-T-t paths of garnet crystallization in the Lesser Himalayan Belt. Journal of Metamorphic Geology, 33, 23–44.

Gatewood, M.P., Dragovic, B., Stowell, H.H., Baxter, E.F., Hirsch, D.M., and Bloom, R. (2015) Evaluating chemical equilibrium in metamorphic rocks using major element and Sm-Nd isotopic age zoning in garnet, Townshend Dam, Vermont, USA. Chemical Geology, 401, 151–168.

George, F.R., and Gaidies, F. (2017) Characterisation of a garnet population from the Sikkim Himalaya: insights into the rates and mechanisms of porphyroblast crystallisation. Contributions to Mineralogy and Petrology, 172, 1–22.

Guevara, V.E., and Caddick, M.J. (2016) Shooting at a moving target: Phase equilibria modelling of high-temperature metamorphism. Journal of Metamorphic Geology, 34, 209–235.

Hacker, B.R., Abers, G.A., and Peackcock, S.M. (2003) Subduction factory 1. Theoretical mineralogy, densities, seismic wave speeds, and H2O contents. Journal of Geophysical Research, 108, 1–26.

Hirsch, D.M., Ketcham, R.A., and Carlson, W.D. (2000) An evaluation of spatial correlation functions in textural analysis of metamorphic rocks. Geologic Materials Research, 2, 1–42.

Holland, T.J.B., and Powell, R. (1998) An internally consistent thermodynamic data set for phases of petrological interest. Journal of Metamorphic Geology, 16, 309–343.

Joesten, R. (1991) Grain-boundary diffusion kinetics in silicate and oxide minerals. In J. Ganguly, Ed., Diffusion, Atomic Ordering, and Mass Transport. Advances in Physical Geochemistry. Springer, New York, NY.

Kelly, E.D., Carlson, W.D., and Ketcham, R.A. (2013) Crystallization kinetics during regional metamorphism of porphyroblastic rocks. Journal of Metamorphic Geology, 31, 963–979.

Kerrick, D.M., and Connolly, J.A.D. (2001) Metamorphic devolatilization of subducted oceanic metabasalts: Implications for seismicity, arc magmatism and volatile recycling. Earth and Planetary Science Letters, 189, 19–29.

Ketcham, R.A., and Carlson, W.D. (2012) Numerical simulation of diffusion-controlled nucleation and growth of porphyroblasts. Journal of Metamorphic Geology, 30, 489–512.

Konrad-Schmolke, M., Babist, J., Handy, M.R., and O’Brien, P.J. (2006) The physico-chemical properties of a subducted slab from garnet zonation patterns (Sesia Zone, western Alps). Journal of Petrology, 47, 2123–2148.

Konrad-Schmolke, M., O’Brien, P.J., and Heidelbach, F. (2007) Compositional re-equilibration of garnet: the importance of sub-grain boundaries. European Journal of Mineralogy, 19, 431–438.

Kostenko, O., Jamtveit, B., Austrheim, H., Pollok, K., and Putnis, C. (2002) The mechanism of fluid infiltration in peridotites at Almklovdalen, western Norway. Geofluids, 2, 203–215.

Kretz, R. (1973) Kinetics of the crystallization of garnet at two localities near Yellowknife. Canadian Mineralogist, 12, 1–20.

Lasaga, A.C., and Rye, D.M. (1993) Fluid flow and chemical kinetics in metamorphic systems. American Journal of Science, 293, 361–404.

Moore, S.J., Cesare, B., and Carlson, W.D. (2015) Epitaxial nucleation of garnet on biotite in the polymetamorphic metapelites surrounding the Vedrette di Ries intrusion (Italian Eastern Alps). European Journal of Mineralogy, 27, 5–18.

Moynihan, D.P., and Pattison, D.R.M. (2013) An automated method for the calculation of P-T paths from garnet zoning, with application to metapelitic schist from the Kootenay Arc, British Columbia, Canada. Journal of Metamorphic Geology, 31, 525–548.

Pattison, D.R.M., and Tinkham, D.K. (2009) Interplay between equilibrium and kinetics in prograde metamorphism of pelites: an example from the Nelson aureole, British Columbia. Journal of Metamorphic Geology, 27, 249–279.

Pattison, D.R.M., de Capitani, C., and Gaidies, F. (2011) Petrological consequences of variations in metamorphic reaction affinity. Journal of Metamorphic Geology, 29, 953–977.

Pollington, A.D., and Baxter, E.F. (2010) High resolution Sm-Nd garnet geochronology reveals the uneven pace of tectonometamorphic processes. Earth and Planetary Science Letters, 293, 63–71.

Powell, R., Holland, T.J.B., and Worley, B. (1998) Calculating phase diagrams involving solid solutions via non-linear equations, with examples using THERMOCALC. Journal of Metamorphic Geology, 16, 577–588.

Putnis, A., and Austrheim, H. (2010) Fluid-induced processes: metasomatism and metamorphism. Geofluids, 10, 254–269.

Ridley, J., and Thompson, A.B. (1986) The role of mineral kinetics in the development of metamorphic microtextures. Advances in Physical Geochemistry, 5, 154–193.

Rubatto, D., and Hermann, J. (2001) Exhumation as fast as subduction? Geology, 29, 3–6.

Shannon, R.D., and Rossi, R.C. (1964) The definition of topotaxy. Nature, 202, 1000–1001.

Spear, F.S., and Selverstone, J. (1983) Quantitative P-T paths from zoned minerals: Theory and tectonic applications. Contributions to Mineralogy and Petrology, 83, 348–357.

Spear, F.S., Selverstone, J., Hickmott, D., Crowley, P., and Hodges, K.V. (1984) P-T paths from garnet zoning: A new technique for deciphiering tectonic process in crystalline terranes. Geology, 12, 87–90.

Spear, F.S., Thomas, J.B., and Hallett, B.W. (2014) Overstepping the garnet isograd: A comparison of QuiG barometry and thermodynamic modeling. Contributions to Mineralogy and Petrology, 168.

Spiess, R., Groppo, C., and Compagnoni, R. (2007) When epitaxy controls garnet growth. Journal of Metamorphic Geology, 25, 439–450.

St-Onge, M.R. (1987) Zoned poikiloblastic garnets: P-T paths and syn-metamorphic uplift through 30 km of structural depth, Wopmay Orogen, Canada. Journal of Petrology, 28, 1–21.

Thomas, J.B., and Watson, E.B. (2014) Diffusion and partitioning of magnesium in quartz grain boundaries. Contributions to Mineralogy and Petrology, 168, 1–12.

Thompson, J.B. (1957) The graphical analysis of mineral assemblages in pelitic schists. American Mineralogist, 42, 842–858.

Tracy, R.J., Robinson, P., and Thompson, A.B. (1976) Garnet composition and zoning in the determination of temperatuer and pressure of metamorphism, central Massachusetts. American Mineralogist, 61, 762–775.

Vorhies, S.H., and Ague, J.J. (2011) Pressure – temperature evolution and thermal regimes in the

Barrovian zones, Scotland. Journal of the Geological Society, 168, 1147–1166.

Waters, D.J., and Lovegrove, D.P. (2002) Assessing the extent of disequilibrium and overstepping of prograde metamorphic reactions in metapelites from the Bushveld Complex aureole, South Africa. Journal of Metamorphic Geology, 20, 135–149.

White, R.W., and Powell, R. (2002) Melt loss and the preservation of granulite facies mineral assemblages. Journal of Metamorphic Geology, 20, 621–632.

White, R.W., Powell, R., Holland, T.J.B., Johnson, T.E., and Green, E.C.R. (2014) New mineral activity-composition relations for thermodynamic calculations in metapelitic systems. Journal of Metamorphic Geology, 32, 261–286.

Whitney, D.L., Goergen, E.T., Ketcham, R.A., and Kunze, K. (2008) Formation of garnet polycrystals during metamorphic crystallization. Journal of Metamorphic Geology, 26, 365–383.

Wolfe, O.M., and Spear, F.S. (2018) Determining the amount of overstepping required to nucleate garnet during Barrovian regional metamorphism, Connecticut Valley Synclinorium. Journal of Metamorphic Geology, 36, 79–94.

Zeh, A., and Holness, M.B. (2003) The effect of reaction overstep on garnet microtextures in metapelitic rocks of the Ilesha Schist Belt, SW Nigeria. Journal of Petrology, 44, 967–991.

# Chapter 2: Preferred Orientations of Garnet Porphyroblasts Reveal Previously Cryptic Templating During Nucleation

Alexandra B. Nagurney[1*], Mark J. Caddick[1], David R.M. Pattison[2], and F. Marc Michel[1]

[1]*Deparment of Geosciences, Virginia Tech, 926 West Campus Drive Blacksburg, VA 24060 USA*

[2]*Department of Geoscience, University of Calgary, Calgary, 2500 University Drive NW, Alberta, T2N 1N4 Canada*

This chapter has been published (2021) in *Scientific Reports.*

https://doi.org/10.1038/s41598-021-85525-7.

## 2.1 ABSTRACT

Electron back scattered diffraction data of garnet crystals from the Nelson Aureole, British Columbia, and the Mosher's Island formation, Nova Scotia, reveals that 22 garnet crystals are all oriented with one of three crystal directions parallel to the trace of the foliation plane in thin section. Structural models suggest that these relationships are due to preferential garnet nucleation onto muscovite, with the alignment of repeating rows of Al octahedra and Si tetrahedra in each leading to inheritance of garnet orientation from the muscovite. These results highlight that epitaxial nucleation may be a prevalent process by which porphyroblast minerals nucleate during metamorphism and carry implications for the role that non-classic nucleation pathways play in the crystallization of metamorphic minerals, the distribution of porphyroblasts in metamorphic rocks, and, in cases in which nucleation is the rate limiting step for crystallization, the energetics of metamorphic reactions.

## 2.2 INTRODUCTION

Deciphering the mechanisms of mineral crystallization has important implications for understanding many geologic processes. Classical theory states that nucleation and growth are each a single step process based on monomer-by-monomer addition of simple chemical species[1]. However, this model may not be appropriate for many geologic systems, and minerals may crystallize via multi-step non-classical pathways, such as the formation of intermediate nanocrystals, amorphous nanoparticles, or via nucleation on a substrate[2]. Two common examples of non-classical nucleation pathways are epitaxy, which is when a phase overgrows a substrate, and topotaxy, in which a reactant phase is converted into a new product phase that utilizes part of the precursor structure[3].

Epitaxy and topotaxy have been previously identified in a range of geologic settings. In igneous systems, epitaxial nucleation may influence alignment and fabrics of ferromagnetic minerals and influence magma composition evolution[4]. In both calcareous deep sea sediments and high pressure eclogite facies rocks, seismic anisotropy may be enhanced by the oriented crystallization of minerals[5,6]. During continental collision, the products of dehydration melting reactions may preferentially crystallize on certain phases[7]. Some readily identified forms of epitaxy during prograde metamorphism include sillimanite nucleation on biotite, staurolite on kyanite, sillimanite on andalusite, and K-feldspar on albite[8–11]. It is currently unclear whether epitaxial nucleation is a more widespread process that also controls the development of rocks without clearly preserved evidence of such templating.

Garnet is an important and widespread metamorphic mineral, with a composition that is sensitive to changing pressure-temperature (*P-T*) conditions, hence its common use in quantitative thermobarometry[12] It can be dated using multiple isotopic systems, which can be coupled with thermodynamic models to understand the rates of tectonic processes[13] and with stable isotope studies to reveal records of fluid-rock interaction in the crust[14]. Despite its clear petrologic utility, details of the atomic-scale processes by which garnet crystallizes (nucleates and grows), and their controls on suitable nucleation sites, growth rates, and the apparent overstepping of reactions in which garnet is a product phase, are poorly constrained. Here, we utilize garnet crystal orientation data and models for the atomic structure of garnet, chlorite, and muscovite to explore whether initial garnet crystallization inherits aspects of pre-existing mineral phases, thus biasing crystal growth to specific textural locations within metamorphic rocks.

Despite its cubic crystal structure and common form as a porphyroblast, garnet has been previously identified to crystallize via epitaxial and topotaxial relationships with muscovite, biotite, and pyroxene. This manifests as the parallelism of high symmetry crystal planes in one phase to those in another phase[15,16] with the most commonly reported relationship being $\{1\ 1\ 0\}_{\text{garnet}}$ // $(0\ 0\ 1)_{\text{mica}}$ (where '//' = 'parallel' and (hkl) are crystal planes)[16–19], though others have also been identified[20–22]. However, these examples all either represent unusual microstructures, such as atoll or snowball garnets[21,22], or formed at extreme environments such as ultra-high pressure metamorphism[17]. There is currently little understanding of whether epitaxial and/or topotaxial nucleation processes occur more broadly during regional and contact metamorphism of less exotic, foliated, pelitic rocks. More generally, it is unclear whether these processes are important for, or potentially control, porphyroblast crystallization. Deciphering whether epitaxial and/or topotaxial nucleation may play a role in more typical metamorphic rocks, where 'unusual' growth habits are absent is important to elucidate which kinetic factors may be the rate-limiting step for mineral crystallization.

## 2.3 RESULTS

### 2.3.1 Sample Description

We investigated whether epitaxial and/or topotaxial nucleation played a role in garnet crystallization in three samples from two localities: the garnet zone of the Nelson contact aureole, British Columbia (samples 08-CW-7.5 and 08-CW-7A)[23,24], and the staurolite grade Mosher's Island formation, Nova Scotia (sample 2018PPGrt_01)[25,26] (Supplemental Fig. S1-3). All three samples contain biotite, chlorite, garnet, muscovite, plagioclase, and quartz. In each case, garnet overgrows a foliation which is defined by the shape preferred orientation of prograde chlorite and muscovite. This persistence of primary chlorite and muscovite is consistent with calculated phase assemblages for the Nelson aureole samples at apparent peak temperatures of ~530˚C and 3.5 kbar[24] and for the Mosher's Island formation sample at 550ºC and 4.1 kbar[27].

Sample 2018PPGrt_01 also contains staurolite and late-stage chlorite overgrowths that are texturally distinct from the primary chlorite (Supplemental Fig. S3). Thin sections of the samples were cut perpendicular to the rock foliation and lineation.

### 2.3.2 Electron Back Scattered Diffraction Analysis

We analyzed the crystallographic orientation of seven garnet crystals from the Nelson Aureole (NA) and fifteen crystals from the Mosher's Island Formation (MI) with Electron Back Scattered Diffraction (EBSD). The plotting schematic for all EBSD images is shown in Fig. 1A, with EBSD data for a representative garnet crystal shown in Fig. 1B. Data for the remaining crystals are shown in the Supplemental Fig. S4-5, and Supplemental Table 1, with the trace of the primary foliation (which is defined by the shape preferred orientation muscovite and chlorite in all samples) parallel to the horizontal direction of the thin section plane in each case. Garnet is color coded for the crystal direction that is parallel to the trace of the $S_1$ foliation of the rock in the thin section plane shown in the IPF color scheme in the inset. For the representative sample shown in Fig. 1B, (NA Garnet 7A), $[\bar{1}\ 4\ 5]_{gt}$ and $[\bar{7}\ 7\ 10]_{gt}$ are parallel and perpendicular to the foliation, respectively.

### 2.3.3 Transmission Electron Microscopy

A garnet-chlorite and garnet-muscovite interface from NA Garnet 7A was investigated at higher resolution by Transmission Electron Microscopy (TEM) so that the nanoscale structure of the grain boundary could be compared to the larger area EBSD orientation results. The location of the TEM foil is shown in Fig. 1B and Supplemental Fig. S6. In Fig. 2A, the smaller 'wedge' shaped muscovite crystal (compared to the larger chlorite) is a function of the TEM foil preparation. The muscovite grain extends beyond the prepared foil, but was truncated due to the small (10 μm x 10 μm) foil size. In this orientation, $(0\ 0\ 1)_{chl}\ //\ (0\ 0\ 1)_{ms}$ (Supplemental Fig. S7).

Fig. 2A shows that the interface is a planar surface without void spaces. The sharpness of the diffraction patterns indicates that both phases are crystalline, with diffraction patterns of the garnet-chlorite and garnet-muscovite interfaces (located with black circles in Fig. 2A) revealing a doubling of the $(0\ 0\ 1)_{chl,ms}$ and $(\bar{1}\ 1\ 1)_{gt}$ planes (red circles). This indicates that the $(0\ 0\ 1)_{chl,ms}$ and $(\bar{1}\ 1\ 1)_{gt}$ planes are parallel to each other, which can be interpreted as an epitaxial and topotaxial relationship in which $[0\ 0\ 1]_{chl,ms}$ is parallel to $[\bar{1}\ 1\ 1]_{gt}$. Compositional analyses reveal that, in addition to muscovite at the grain boundary, there is also a nano-sized quartz grain at this interface (Fig. 2B).

Comparison of this relationship apparent at the nanoscale (Fig. 2) with EBSD results for the same garnet crystal (Fig. 1) reveals consistency between the interpretation of the two datasets. The EBSD and TEM results show that $[\bar{7}\ 7\ 10]_{gt}$ and $[\bar{1}\ 1\ 1]_{gt}$ are perpendicular to the foliation, respectively. Plotting these directions and their corresponding planes on the crystal structure of garnet[28] (lines and rectangular planes, respectively, in Fig. 2C), reveals that these orientations are within 10° of each other. Therefore, the macroscale orientations observed via EBSD for a relatively large population of garnet crystals are consistent with nanoscale TEM observations of the mineral interface.

### 2.3.4 Synthesis of Results for Twenty-Two Garnet Crystals

The orientations of all twenty-two analyzed garnet crystals were plotted on crystal structure models of garnet[28]. Fig. 3A shows the $[\bar{1}45]_{gt}$ crystal direction (teal arrow), which is oriented parallel to the trace of the foliation in thin section in Fig. 1, and the corresponding $(\bar{1}45)_{gt}$ crystal plane (teal plane) plotted on the crystal structure model. This demonstrates that it is more illustrative to utilize crystal planes (instead of vector directions) to study relationships within the atomic structure of garnet. Accordingly, although our EBSD results are initially recorded as crystal directions parallel to the trace of the foliation, we show the corresponding planes (the poles to these directions) for all twenty-two garnet crystals on the garnet structure model in Fig. 3B.

The orientations of all twenty-two analyzed garnets fall into just three clusters: nine are oriented within 13° of the $(\bar{1}\ 1\ 6)$ plane (pink in Fig. 3B), eight are within 14° of the $(0\ 7\ 9)$ plane (green), and five are within 12° of the $(\bar{7}\ 7\ 9)$ (purple) plane (Fig. 3B). As an example, Fig. 3A shows both the $[\bar{1}\ 4\ 5]_{gt}$ and $[0\ 7\ 9]_{gt}$ crystal directions (teal and lime green arrows), and the corresponding $(\bar{1}\ 4\ 5)_{gt}$ and $(0\ 7\ 9)_{gt}$ crystal planes (teal and lime green surfaces), highlighting that $(\bar{1}\ 4\ 5)_{gt}$ is only 9° from the $(0\ 7\ 9)_{gt}$, which is the average crystal orientation for that cluster of planes.

The results are summarized as nine garnet crystals oriented with $[\bar{1}\ 1\ 6]_{gt}$ approximately parallel to the trace of the foliation in thin section, eight in which $[0\ 7\ 9]_{gt}$ is parallel to the foliation, and five in which $[\bar{7}\ 7\ 9]_{gt}$ is parallel to the foliation. Both $(0\ 7\ 9)_{gt}$ and $(\bar{7}\ 7\ 9)_{gt}$ are close to low index planes of garnet, with $(0\ 7\ 9)_{gt}$ having a 7° angular misorientation from $(0\ 1\ 1)_{gt}$ and $(\bar{7}\ 7\ 9)_{gt}$ having a 7° angular misorientation from $(\bar{1}\ 1\ 1)_{gt}$. $(\bar{1}\ 1\ 6)_{gt}$ is not close to low index planes of garnet. Further, there are only four crystal directions: $[\bar{3}\ 4\ 6]_{gt}$, $[\bar{2}\ 11\ 11]_{gt}$, $[0\ 1\ 2]_{gt}$, and $[\bar{7}\ 7\ 10]_{gt}$, that are perpendicular to the foliation of the samples (Supplemental Table S1). As such, there is also a clustering in which $\{\bar{3}\ 4\ 6\}_{gt,}$ $\{\bar{2}\ 11\ 11\}_{gt,}$ $\{0\ 1\ 2\}_{gt}$, or $\{\bar{7}\ 7\ 10\}_{gt}$ are preferentially parallel to $(0\ 0\ 1)_{ms,chl}$.

## 2.4 DISCUSSION

The relationship between garnet crystal orientation and rock foliation shown in Fig. 3B requires an assessment of its potential crystallographic controls. Muscovite and chlorite define the rock foliation so it is possible that garnet will template on the crystal structure of one or both of these minerals. Al octahedra and Si tetrahedra are the building blocks of the garnet structure, so templating on these structures seems most likely. Here, we investigate the crystal structures of both chlorite and muscovite to determine which mineral's crystal structure contains elements that may be advantageous for garnet to template on.

Despite both being sheet silicate minerals, the types of bonds, geometries, and interatomic distances between Al and Si are different in chlorite and muscovite. In chlorite, the sheet layers are bonded together via hydrogen bonds and van der Waals forces, while in muscovite the sheets are connected via bridging oxygens (Fig. 4A-B)[29,30]. In chlorite, Al occurs either in the interlayer octahedral sheet or substitutes for Si in the tetrahedral layer (Fig. 4A)[29,31]. In muscovite, Al is in the octahedral layer and connected to the Si tetrahedral layer via bridging oxygens (Fig. 4B)[30]. Further, the geometric arrangements of Al and Si are different in chlorite and muscovite (Fig. 4C). Finally, the distance between Al and Si in chlorite is 4.75 Å, while in muscovite the distance between the cations is 3.23 Å (Fig. 4C)[29,30].

The geometry and distance between Al and Si in muscovite are similar to that in garnet, with 3.23 Å between Al and Si atoms in muscovite and 3.22 Å in garnet (Fig. 4C)[28,30]. Any section of muscovite oriented as shown in Fig. 4B will expose Al-Si frameworks that could theoretically be adopted by the garnet crystal structure, providing potentially preferable nucleation sites. As such, due to the similarities between: i) interatomic distances and ii) Al-Si geometries in muscovite and garnet (that are lacking between garnet and chlorite), we interpret that it is more likely for garnet to template on the crystal structure of muscovite than chlorite. As such, we focus here on how elements of the garnet structure in the $(0\ 7\ 9)_{gt}$ and $(\bar{7}\ 7\ 9)_{gt}$, and $(\bar{1}\ 1\ 6)_{gt}$ planes may align with that of muscovite.

Fig. 4D-I shows how the three garnet orientations found to be parallel to the trace of the foliation in our dataset may template on to the muscovite crystal structure, with Supplemental Videos S1-3 showing these relationships in the third dimension. In these three orientations, multiple horizontal 'rows' of Al atoms in garnet are separated by distances that are very similar to the stacking distances of corresponding Al sheet-like layers in muscovite (these rows are annotated by dashed lines between Fig. 4 D-F and G-I). Furthermore, the distances between Si sheet-like layers in muscovite corresponds well with equivalent 'rows' of Si tetrahedra in garnet in those orientations (Table 1), as does the distance between Al and Si atoms within each row. These relationships are clearer for $(0\ 7\ 9)_{gt}$ and $(\bar{7}\ 7\ 9)_{gt}$, than $(\bar{1}\ 1\ 6)_{gt}$ (Fig. 4).

For comparison $(1\ 0\ 0)_{gt}$ is shown in Fig. 4I. Rows of Al octahedra in muscovite and garnet can be matched. However, there are no corresponding 'rows' of Si tetrahedra in garnet with similar distances to those in muscovite. Since $(1\ 0\ 0)_{gt}$ lacks this similarity with $(1\ 0\ 0)_{ms}$, we infer that garnet is less likely to template onto muscovite in this orientation. This highlights that certain crystal planes of garnet share more similarities with aspects of $(1\ 0\ 0)_{ms}$, implying a control for the relationships determined by EBSD. The clear similarities in bond geometry and interatomic spacings between muscovite and the observed garnet orientations suggest that it is likely that muscovite provides an ideal structure for garnet to template onto. This nucleation likely occurs across the terminations of the muscovite crystals with garnet oriented in one of the three orientations discussed above. Further, the prevalence of muscovite in these rocks suggests that muscovite provides plentiful nucleation sites for which garnet to nucleate on during prograde metamorphism. As such, the crystallographic relationship between garnet and chlorite shown in Fig. 2A may be coincidental rather than genetic: muscovite and chlorite are generally sub-parallel in these samples (Supplemental Figs. S3-7), so inheritance of garnet orientation from muscovite resulted in parallelism with chlorite.

These interpretations agree well with previous studies that interpret that garnet can nucleate on the crystal structure of muscovite and/or biotite[16–18,21], with these previous studies showing $(1\ 1\ 0)_{gt}$ or $(\bar{1}\ 1\ 1)_{gt}$ being within 20° of parallel to $(0\ 0\ 1)_{ms,bt}$. Our results show a clustering in which one of $(\bar{3}\ 4\ 6)_{gt,}$ $(\bar{2}\ 11\ 11)_{gt,}$ $(0\ 1\ 2)_{gt}$, or $(\bar{7}\ 7\ 10)_{gt}$ are preferentially parallel to $(0\ 0\ 1)_{ms}$. These crystal planes are plotted on the crystal structure of garnet in Fig. 5, illustrating that $(\bar{3}\ 4\ 6)_{gt}$ and $(\bar{7}\ 7\ 10)_{gt}$ are within 16° of $(\bar{1}\ 1\ 1)_{gt}$ and that $(\bar{2}\ 11\ 11)_{gt}$ and $(0\ 1\ 2)_{gt}$ are 7° and 18° from $(0\ 1\ 1)_{gt}$, respectively. This generally agrees with previous results[16–18,21], suggesting that garnet nucleates epitaxially on the crystal structure of muscovite and/or biotite in the more exotic microstructures presented in those studies. Our results and interpretations further show that epitaxial nucleation is not restricted to unusual microstructures, but instead may be important during crystallization of many or most regional and contact metamorphic rocks.

An alternative atomic scale model for epitaxial nucleation of garnet on biotite involves garnet nucleation on distorted pseudo-hexagonal oxygen ring structures on $(0\ 0\ 1)_{bt}$ surfaces[17]. This requires the addition of Al and extra O atoms to the biotite ring structure, driving distortion of the pseudo-hexagonal rings, and providing the surface for which garnet can template onto. In comparison, our mechanism of garnet templating does not require any addition or movement of atoms to the muscovite crystal lattice, potentially implying a more favorable mechanism for garnet to nucleate, though both mechanisms of templating are likely possible. More work modelling the atomic scale energetic interactions between these minerals is necessary to resolve these different interpretations.

From a different perspective, energetically favorable nucleation sites for garnet in a natural rock include crystal dislocations[32] and locations of elevated HREE + Y concentrations[33]. Even in these situations, the garnet that grows may template onto nearby muscovite grains. Our study also supports the model in which garnet nucleation is controlled by a preexisting fabric and garnet first nucleates at grain boundaries in mica-rich layers[34,35]. Garnet thus likely preferentially nucleates at the edge of muscovite crystals, adopting a specific crystal orientation, with grain boundaries providing efficient transport of nutrient elements to the growing nucleus.

The interpretations of epitaxial nucleation presented here and in previous studies[10,16,17], are examples of nucleation via non-classical pathways in geologic materials[2]. Case studies that model nucleation and growth energetics during metamorphism should consider these nucleation pathways and the importance of inherited texture. This may require re-evaluation of the petrographic and 3D textures of minerals in an ostensibly homogeneous matrix, taking account of the possibility that porphyroblast distribution may be controlled to the first order by the availability of specific, energetically favorable, non-randomly distributed nucleation sites including sites of epitaxial nucleation.

Previous models provide important context of how the growth of garnet would be controlled by the distribution and transport of aluminum[36–38]. The seeming importance of epitaxial nucleation in the samples studied here suggests that nucleation is strongly favoured on precursor phases such as muscovite and may be controlled by the distribution of nucleation sites. For garnet growth reactions in which muscovite or any other potential templating phase is also a major reactant, both favourable nucleation sites and a source of Al may be provided, leading to efficient topotaxial overgrowth. It appears here, however, that muscovite provided the nucleation sites but was not a reactant phase, with chlorite likely providing the primary flux of nutrients.

Thus the natural rock archive is likely to record a complex interplay between the location of preferable nucleation sites, the location of reactant phases, and the transport properties of nutrient components[37,39]. For the simple case of samples such as ours, the relative abundance and distributions of precursor chlorite and muscovite may serve as an important control on whether garnet growth is predominantly controlled by nucleation site distribution or the transport of nutrients.

It may also be necessary to consider how epitaxial nucleation may reduce the energetic barrier to garnet crystallization in cases where nucleation is the rate limiting step for garnet crystallization[24,40,41]. This follows from interpretations that garnet crystallization may often be overstepped (i.e. crystallize at $P$-$T$ conditions greater than its initial equilibrium stability)[42]. The relative importance of epitaxy and other microtextural relationships as potential controls on macroscale energetics during metamorphism is relatively poorly understood and warrants additional research. Questions remain regarding the absolute energetic contribution that epitaxy might play in modifying the pressure and temperature conditions at which garnet may first grow during prograde metamorphism. It may be necessary to reinterpret metamorphic recrystallization in light of non-classical, specifically epitaxial, nucleation, which may represent a common but generally overlooked process controlling mineral crystallization.

## 2.5 METHODS

### 2.5.1 Electron Back Scattered Diffraction (EBSD)

EBSD data were collected on a Tescan MIRA3 LMU Field Emission Gun Scanning Electron Microscope (FEG-SEM) equipped with an Oxford Instruments Symmetry EBSD detector at the Department of Earth and Environmental Sciences at Boston College. Analyses used a 25 kV accelerating voltage and 50-75 nA beam currents, which equates to an angular resolution of 0.7-1.0°[43]. Large area maps of crystallographic texture were produced using Oxford Instruments AZtecHKL acquisition and analysis software (version 4.3). The resulting orientation maps contained 1-4 garnet crystals, which allowed for the complete characterization of garnet crystals and the surrounding minerals. A 1 μm step size was used to achieve a high density of crystallographic solutions within individual grains. This step size is smaller than all individual grains, ensuring >1 point/grain. Indexing rates for garnet crystals were high (>95%), commonly resulting in more than 50,000 garnet solutions per map. Indexing rates for muscovite and chlorite were lower, resulting in <500 solutions per map. Only samples that contained >100 data points were used for pole figure construction.

EBSD data were analyzed using the MATLAB-based MTEX Toolbox (Version 5.2)[44] MTEX codes used for this study are available from the author upon request. All data were rotated to a frame of reference with the trace of the rock foliation being horizontal. Individual crystal orientations with median absolute values (M.A.D) >0.9 were excluded from the dataset, as they equate to a low confidence in the EBSD solution. Inverse pole figures for garnet were calculated and then contoured for multiples of uniform density (M.U.D.). Pole figures for garnet, chlorite, and muscovite were calculated using the orientation distribution function[45,46] such that the mean orientation of each phase was plotted on a lower hemisphere, equal angle pole figure.

### 2.5.2 Transmission Electron Microscopy (TEM)

TEM foil location was determined via optical petrography and Scanning Electron Microscopy (SEM). Foil preparation used a Focused Ion Beam (FIB) liftout on a FEI Helios 600 NanoLab SEM following methodology similar to Wirth (2009), using an oil free high vacuum at Virginia Tech's Nanoscale Characterization and Fabrication Laboratory (NCFL). The location of the TEM foil was marked by depositing Pt on to the sample to protect the sample from the Ga-ion beam. TEM foils (approximately 2.5μm x 3.5μm x 150nm) were prepared using a Ga-ion beam, with the foil oriented normal to the garnet-chlorite grain boundary. The foil was prepared thicker than common TEM samples to mitigate sample damage in the TEM and ensure a strong diffraction contrast.

TEM analysis used a JEOL2100 TEM operated at 200 kV, with images obtained using a Gatan Ultrascan 1000XP camera. Selected Area Diffraction Patterns (SAED) were taken on ~150 nm radius circles. Diffraction patterns were obtained using a Gatan Orius SC200D camera and analyzed using Gatan Digital Micrograph. Electron Dispersive Spectrometry (EDS) scans of the sample utilized the Scanning Transmission Electron Microscopy mode and JEOL EDS Detector. All crystal structure models were made using VESTA[47].

## 2.6 REFERENCES

1. Karthika, S., Radhakrishnan, T. K. & Kalaichelvi, P. A Review of Classical and Nonclassical Nucleation Theories. *Cryst. Growth Des.* **16**, 6663–6681 (2016).
2. De Yoreo, J. J. *et al.* Crystallization by particle attachment in synthetic, biogenic, and geologic environments. *Science (80-. ).* **349**, 499–507 (2015).
3. Shannon, R. D. & Rossi, R. C. The definition of topotaxy. *Nature* **202**, 1000–1001 (1964).
4. Hammer, J. E., Sharp, T. G. & Wessel, P. Heterogeneous nucleation and epitaxial crystal growth of magmatic minerals. *Geology* **38**, 367–370 (2010).
5. Carlson, R. L. & Christensen, N. I. Velocity anisotropy in semi-indurated calcareous deep sea sediments. *J. Geophys. Res.* **84**, 205–211 (1979).
6. McNamara, D. D., Wheeler, J., Pearce, M. & Prior, D. J. Fabrics produced mimetically during static metamorphism in retrogressed eclogites from the Zermatt-Saas zone, Western Italian Alps. *J. Struct. Geol.* **44**, 167–178 (2012).

7. Dyck, B., Waters, D. J., St-Onge, M. R. & Searle, M. P. Muscovite dehydration melting; reaction mechanisms, microstructures, and implications for anatexis. *J. Metamorph. Geol.* **38**, 1–24 (2020).

8. Carmichael, D. M. On the mechanism of prograde metamorphic reactions in quartz-bearing pelitic rocks. *Contrib. to Mineral. Petrol.* **20**, 244–267 (1969).

9. Niedermeier, D. R. D., Putnis, A., Geisler, T., Golla-Schindler, U. & Putnis, C. V. The mechanism of cation and oxygen isotope exchange in alkali feldspars under hydrothermal conditions. *Contrib. to Mineral. Petrol.* **157**, 65–76 (2009).

10. Cesare, B. & Grobety, B. Epitaxial replacement of kyanite by staurolite: a TEM study of the microstructures. *Am. Mineral.* **80**, 78–86 (1995).

11. Putnis, A. & Putnis, C. V. The mechanism of reequilibration of solids in the presence of a fluid phase. *J. Solid State Chem.* **180**, 1783–1786 (2007).

12. Caddick, M. J. & Kohn, M. J. Garnet: Witness to the evolution of destructive plate boundaries. *Elements* **9**, 427–432 (2013).

13. Baxter, E. F., Caddick, M. J. & Dragovic, B. Garnet: A rock-forming mineral petrochronometer. *Rev. Mineral. Geochemistry* **83**, 469–533 (2017).

14. Valley, J. W. Stable isotope geochemistry of metamorphic rocks. *Rev. Mineral. Geochemistry* **16**, 445–489 (1986).

15. Frondel, C. Orientated inclusions of staurolite, zircon, and garnet in muscovite. Skating crystals and their significance. *Am. Mineral.* **25**, 69–87 (1940).

16. Moore, S. J., Cesare, B. & Carlson, W. D. Epitaxial nucleation of garnet on biotite in the polymetamorphic metapelites surrounding the Vedrette di Ries intrusion (Italian Eastern Alps). *Eur. J. Mineral.* **27**, 5–18 (2015).

17. Spiess, R., Groppo, C. & Compagnoni, R. When epitaxy controls garnet growth. *J. Metamorph. Geol.* **25**, 439–450 (2007).

18. George, F. R. & Gaidies, F. Simultaneous operation of opposing reaction mechanisms: The influence of matrix heterogeneity on post-kinematic garnet crystallisation in an inverted metamorphic sequence. *J. Metamorph. Geol.* **38**, 743–769 (2020).

19. Putnis, A. *An Introduction to Mineral Science*. (Cambridge University Press, 1992).

20. Padrón-Navarta, J. A. *et al.* Oriented growth of garnet by topotactic reactions and epitaxy in high-pressure, mafic garnet granulite formed by dehydration melting of metastable hornblende-gabbronorite (Jijal Complex, Kohistan Complex, north Pakistan). *J. Metamorph. Geol.* **26**, 855–870 (2008).

21. Ruiz Cruz, M. D. Origin of atoll garnet in schists from the Alpujárride complex (central zone of the Betic Cordillera, Spain): Implications on the P-T evolution. *Mineral. Petrol.* **101**, 245–261 (2011).

22. Robyr, M., Carlson, W. D., Passchier, C. & Vonlanthen, P. Microstructural, chemical and textural records during growth of snowball garnet. *J. Metamorph. Geol.* **27**, 423–437 (2009).

23. Pattison, D. R. M. & Vogl, J. J. Contrasting sequences of metapelitic mineral-assemblages in the aureole of the tilted Nelson Batholith, British Columbia: Implications for phase equilibria and pressure determination in andalusite-sillimanite-type settings. *Can. Mineral.* **43**, 51–88 (2005).

24. Pattison, D. R. M. & Tinkham, D. K. Interplay between equilibrium and kinetics in prograde metamorphism of pelites: an example from the Nelson aureole, British Columbia. *J. Metamorph. Geol.* **27**, 249–279 (2009).

25. White, C. E. & Barr, S. M. Lithochemistry of the Lower Paleozoic Goldenville and Halifax groups, southwestern Nova Scotia, Canada: Implications for stratigraphy, provenance, and tectonic setting of the Meguma terrane. *Geol. Soc. Am. Mem.* **206**, 347–366 (2010).

26. Taylor, F. & Schiller, E. Metamorphism of the Meguma group of Nova Scotia. *Can. J. Earth Sci.* **3**, 959–974 (1966).

27. Nagurney, A. & Caddick, M. J. Microstructural and geochemical controls on the crystallization of garnet and staurolite: An example from the Meguma terrane, Nova Scotia. in *Geological Society of America Program with Abstracts* (2020).

28. Novak, G. A. & Gibbs, G. V. The crystal chemistry of the silicate garnets. *Am. Mineral.* **56**, 791 (1971).

29. Bailey, S. W. X-ray diffraction identification of the polytypes of mica, serpentine, and chlorite. *Clays Clay Miner.* **36**, 193–213 (1988).

30. Richardson, S. M. & Richardson, J. W. Crystal structure of a pink muscovite from Archer's Post, Kenya: Implications for reverse pleochroism in dioctahedral micas. *Am. Mineral.* **67**, 69–75 (1982).

31. Inoué, S. & Kogure, T. High-angle annular dark field scanning transmission electron microscopic (HAADF-STEM) study of Fe-rich 7 Å–14 Å interstratified minerals from a hydrothermal deposit. *Clay Miner.* **51**, 603–613 (2016).

32. Gaidies, F. Nucleation in geological materials. *EMU Notes Mineral.* **16**, 347–371 (2017).

33. George, F. R., Gaidies, F. & Boucher, B. Population-wide garnet growth zoning revealed by LA-ICP-MS mapping: Implications for trace element equilibration and syn-kinematic deformation during crystallisation. *Contrib. to Mineral. Petrol.* **173**, 1–24 (2018).

34. Daniel, C. G. & Spear, F. S. The clustered nucleation and growth processes of garnet in regional metamorphic rocks from north-west Connecticut, USA. *J. Metamorph. Geol.* **17**, 503–520 (1999).

35. Daniel, C. G. & Spear, F. S. Three-dimensional patterns of garnet nucleation and growth. *Geology* **26**, 505–506 (1998).

36. Carlson, W. D. The significance of intergranuar diffusion to the mechanisms and kinetics of porphyroblast crystallization. *Contrib. to Mineral. Petrol.* **103**, 1–24 (1989).

37. Carlson, W. D. Porphyroblast crystallization: linking processes, kinetics, and microstructures. *Int. Geol. Rev.* **53**, 406–445 (2011).

38. Ketcham, R. A. & Carlson, W. D. Numerical simulation of diffusion-controlled nucleation and growth of porphyroblasts. *J. Metamorph. Geol.* **30**, 489–512 (2012).

39. Gaidies, F., Pattison, D. R. M. & de Capitani, C. Toward a quantitative model of metamorphic nucleation and growth. *Contrib. to Mineral. Petrol.* **162**, 975–993 (2011).

40. Waters, D. J. & Lovegrove, D. P. Assessing the extent of disequilibrium and overstepping of prograde metamorphic reactions in metapelites from the Bushveld Complex aureole, South Africa. *J. Metamorph. Geol.* **20**, 135–149 (2002).

41. Nagurney, A., Caddick, M. J., Dragovic, B. & Busse, K. The (chemical) potential for understanding overstepped garnet nucleation and growth. *Am. Mineral.* **In press**, (2021).

42. Carlson, W. D., Pattison, D. R. M. & Caddick, M. J. Beyond the equilibrium paradigm: How consideration of kinetics enhances metamorphic interpretation. *Am. Mineral.* **100**, 1659–1667 (2015).

43. Humphreys, F. J. Grain and subgrain characterisation by electron backscatter diffraction. *J. Mater. Sci.* **36**, 3833–3854 (2001).

44. Bachmann, F., Hielscher, R. & Schaeben, H. Texture analysis with MTEX- Free and open source software toolbox. *Solid State Phenom.* **160**, 63–68 (2010).

45. Wenk, H. & Wilde, W. Orientation distribution fabrics for 3 Yule marble fabrics. in *Flow and Fracture of Rocks: American Geophysical Union Geophysical Monograph* (eds. Heard, H. C., Borg, I. Y., Carter, N. L. & Raleigh, C. B.) **16**, 83–94 (1972).

46. Ismaïl, W. Ben & Mainprice, D. An olivine fabric database: An overview of upper mantle fabrics and seismic anisotropy. *Tectonophysics* **296**, 145–157 (1998).

47. Koichi, M. & Fujio, I. VESTA: a three-dimensional visualization system for electronic and structural analysis. *J. Appl. Crystallogr.* **41**, 653–658 (2008).

48. Zanazzi, P. F., Montagnoli, M., Nazzareni, S. & Comodi, P. Structural effects of pressure on triclinic chlorite: A single-crystal study. *Am. Mineral.* **91**, 1871–1878 (2006).

## 2.7 ACKNOWLEDGMENTS

This work was funded by two GSA Graduate Student Research Grants, an AAPG Grant in Aid, and a research scholarship from the Virginia Tech Department of Geosciences to Nagurney. Nagurney also acknowledges support from the Virginia Tech ICTAS Doctoral Scholars Program. Seth Kruckenberg (Boston College) is acknowledged for help with EBSD analytical work. Nancy Ross and members of the Metamorphic Processes Group at Virginia Tech are thanked for helpful conversations on various aspects of this project. The authors acknowledge use of the facilities and assistance of Chris Winkler and Ya Peng Yu at the Nanoscale Characterization and Fabrication Laboratory at Virginia Tech.

## 2.8 FIGURES

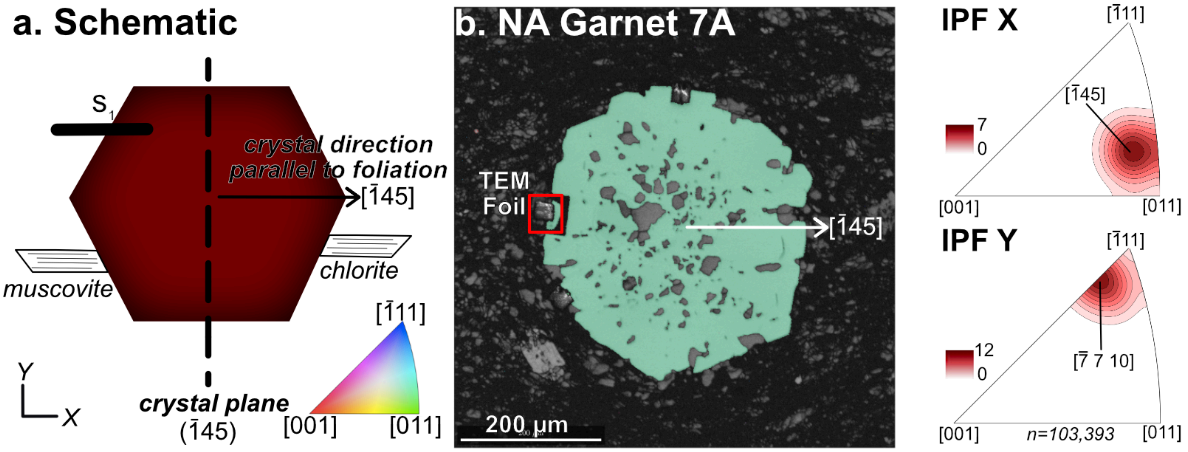

Figure 2.1. **EBSD Results.** (**a**) Plotting schematic of garnet in B, showing garnet crystal direction and corresponding crystal plane. The trace of the $S_1$ foliation in the thin section is parallel to the horizontal (X) direction. XY coordinates are defined here as X: parallel to the horizontal direction of the thin section plane (parallel to foliation), Y: parallel to the vertical direction of the thin section plane (perpendicular to foliation). (**b**) Electron back scattered diffraction (EBSD) analyzed garnet crystal, color-coded for crystal direction parallel to the X direction and the $S_1$ foliation (color coding following inset in 1A). Location of TEM foil (Fig. 2) is shown. TEM foil was cut perpendicular (into) to the thin section plane. Orientation data are plotted on the EBSD band contrast image. Inverse pole figures (IPF) X and Y show the crystal directions of garnet that are parallel (X) and perpendicular (Y) to the foliation. IPFs are contoured for multiples of uniform distribution.

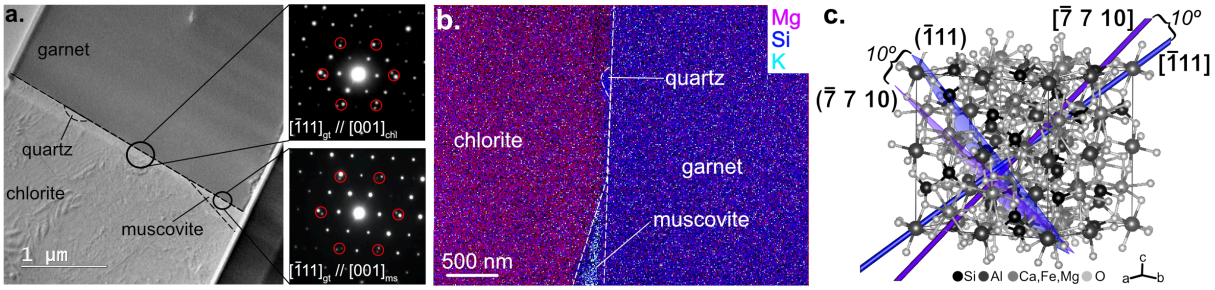

Figure 2.2. **TEM Results.** (**a**) Transmission Electron Microscopy (TEM) image of mineral interface. Diffraction patterns of the garnet-chlorite interface (top) and garnet-muscovite interface (bottom) oriented such that $[\bar{1}\ 1\ 1]_{gt}$ is parallel to $[0\ 0\ 1]_{chl,ms}$. The doubling of planes (highlighted by red circles) suggests an epitaxial relationship between garnet and chlorite and between garnet and muscovite. (**b**) Stacked electron dispersive spectrometry maps of Mg (magenta), Si (blue), and K (light blue) abundances showing the 4 phases in the TEM foil. Sample is rotated relative to A. (**c**) Garnet crystal structure (from Novak and Gibbs, 1971) highlighting the $[\bar{1}\ 1\ 1]_{gt}$ and $[\bar{7}\ 7\ 10]_{gt}$ crystal directions (blue and purple lines, respectively) and $(\bar{1}\ 1\ 1)_{gt}$ and $(\bar{7}\ 7\ 10)_{gt}$ planes (blue purple sheets).

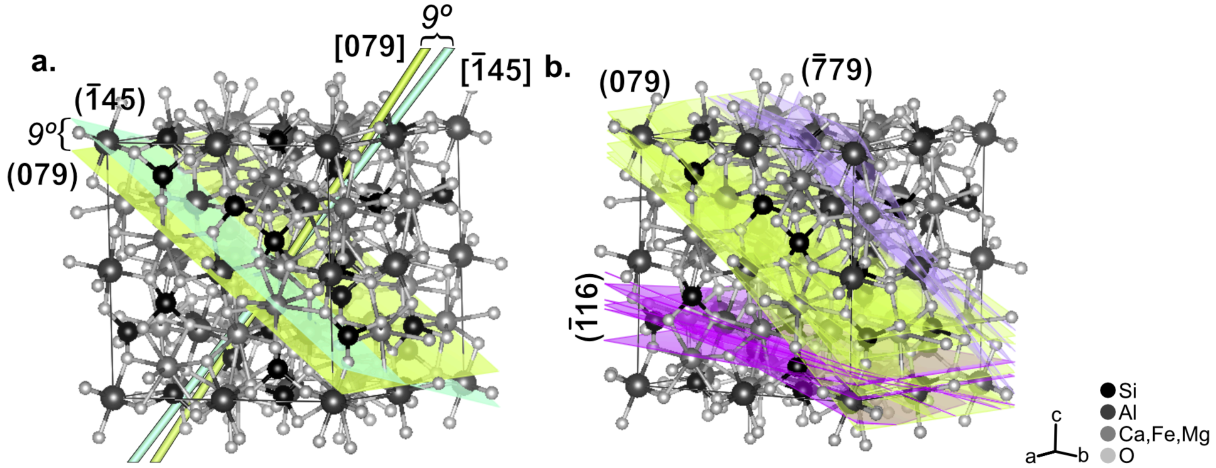

Figure 2.3. **Summary of EBSD Results.** (**a**) Garnet crystal structure showing the [$\bar{1}$ 4 5]$_{gt}$ crystal direction (teal line) and ($\bar{1}$ 4 5)$_{gt}$ crystal plane (teal line and sheet), and the [0 7 9] direction and plane (lime green line and sheet). ($\bar{1}$ 4 5)$_{gt}$ and (0 7 9)$_{gt}$ have 9º angular misorientation. See text for explanation. (**b**) Garnet crystal structure showing the planes corresponding to the 22 crystal directions of garnet that were found to be parallel to the trace of the foliation in thin section. Planes cluster into three groups centered around ($\bar{1}$ 1 6) (pink), (0 7 9) (green), and ($\bar{7}$ 7 9) (purple).

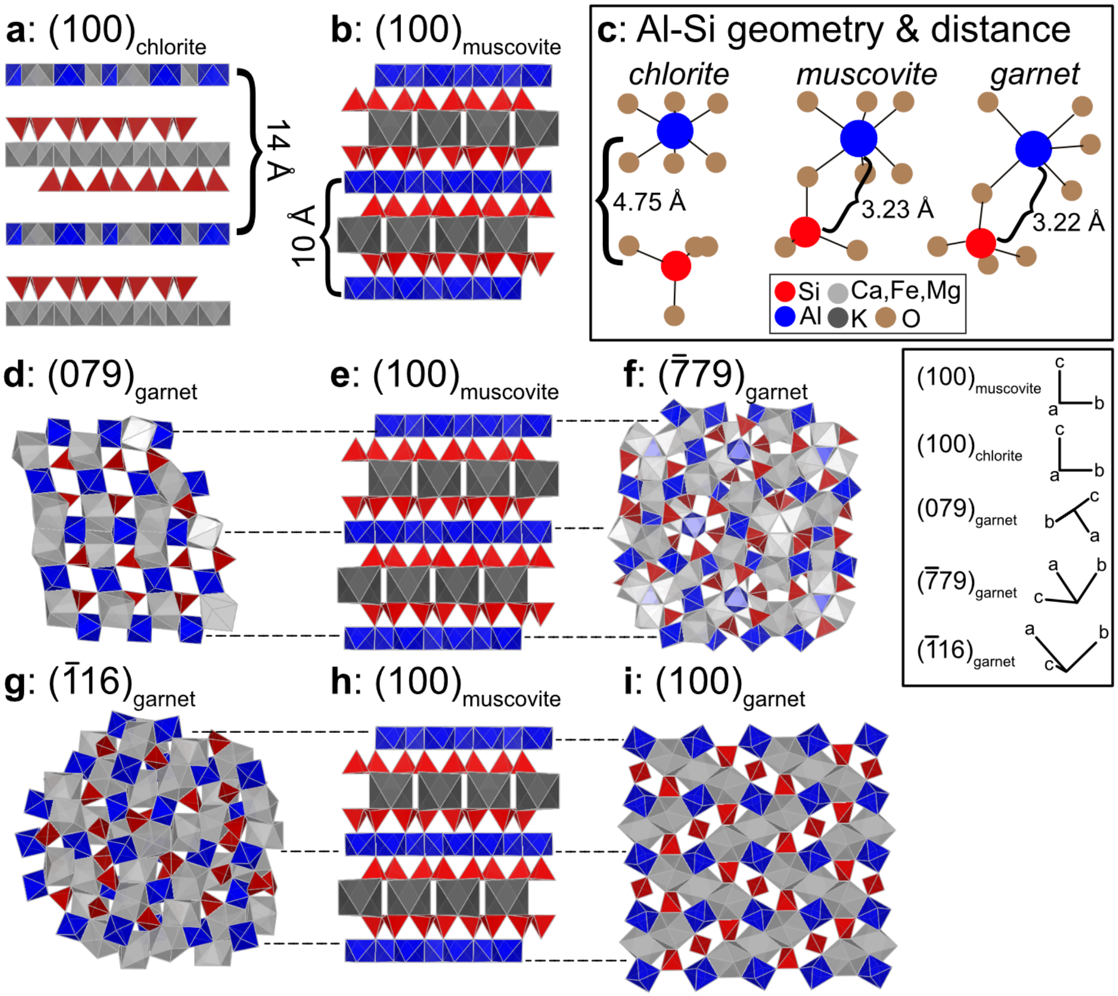

Figure 2.4. **Crystal structure models** of (**a**) chlorite[48] and (**b**) muscovite[30]. (**c**) Al octahedra – Si tetrahedra geometries and distances in chlorite, muscovite, and garnet. (**d-i**) Crystal structure models of $(0\ 7\ 9)_{gt}$, $(100)_{ms}$, $(\bar{7}\ 7\ 9)_{gt}$, $(\bar{1}\ 1\ 6)_{gt}$, $(1\ 0\ 0)_{ms}$, and $(1\ 0\ 0)_{gt}$, with dashed lines highlighting relationships between Al in each. The inset shows the 3D orientation of all of the crystal planes.

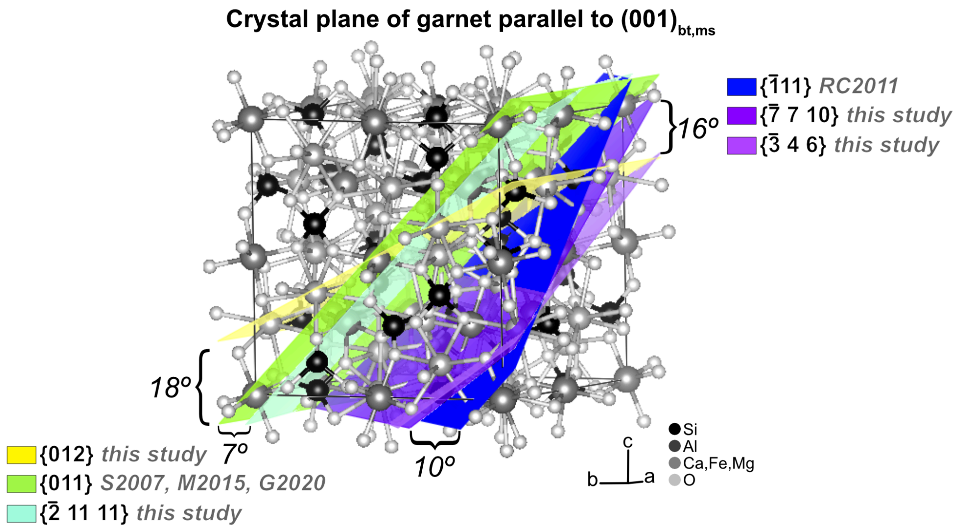

Figure 2.5. **Comparison of crystal planes** discussed in this study with others previously described as being preferentially parallel to $(0\ 0\ 1)_{bt,ms}$ [RC2011 = Ruiz Cruz, (2011), S2007 = Spiess et al., (2007), M2015 = Moore et al., (2015), and G2020 = George and Gaidies, (2020)].

## 2.9 TABLES

Table 2.1. Distances between and along Al and Si rows in chlorite, garnet, and muscovite. All measurements were made using VESTA[47].

| **Distance Between Al 'Rows'** | | **Distance Between Si 'Rows'** | | **Al-Al Distances Along the Row** | | **Si-Si Distances Along the Row** | | | **Si-O-Al Distance** | |
|---|---|---|---|---|---|---|---|---|---|---|
| $(1\ 0\ 0)_{chl}$ | 14.38 Å | $(1\ 0\ 0)_{chl}$ | 8.97 Å | $(1\ 0\ 0)_{chl}$ | 9.23 Å | $(1\ 0\ 0)_{chl}$ | 3.07 Å | 6.16 Å | $(1\ 0\ 0)_{chl}$ | 4.75 Å |
| $(1\ 0\ 0)_{ms}$ | 10.12 Å | $(1\ 0\ 0)_{ms}$ | 5.64 Å | $(1\ 0\ 0)_{ms}$ | 6.03 Å | $(1\ 0\ 0)_{ms}$ | 2.97 Å | 6.06 Å | $(1\ 0\ 0)_{ms}$ | 3.23 Å |
| $(0\ 7\ 9)_{gt}$ | 9.56 Å | $(0\ 7\ 9)_{gt}$ | 5.39 Å | $(0\ 7\ 9)_{gt}$ | 4.99 Å | $(0\ 7\ 9)_{gt}$ | | 5.39 Å | $(0\ 7\ 9)_{gt}$ | 3.22 Å |
| $(\bar{7}\ 7\ 9)_{gt}$ | 9.99 Å | $(\bar{7}\ 7\ 9)_{gt}$ | 5.39 Å | $(\bar{7}\ 7\ 9)_{gt}$ | 4.99 Å | $(\bar{7}\ 7\ 9)_{gt}$ | 3.53 Å | | $(\bar{7}\ 7\ 9)_{gt}$ | 3.22 Å |
| $(\bar{1}\ 1\ 6)_{gt}$ | 8.15 Å | $(\bar{1}\ 1\ 6)_{gt}$ | 5.39 Å | $(\bar{1}\ 1\ 6)_{gt}$ | 4.99 Å | $(\bar{1}\ 1\ 6)_{gt}$ | | 5.39 Å | $(\bar{1}\ 1\ 6)_{gt}$ | 3.22 Å |
| $(1\ 0\ 0)_{gt}$ | 11.53 Å | $(1\ 0\ 0)_{gt}$ | X | $(1\ 0\ 0)_{gt}$ | 5.77 Å | $(1\ 0\ 0)_{gt}$ | X | X | $(1\ 0\ 0)_{gt}$ | 3.22 Å |

# Chapter 3: Crystallographically controlled void space at grain boundaries in the Harkless quartzite

Alexandra B. Nagurney[1]*, Mark J. Caddick[1], Richard D. Law[1], Nancy L. Ross[1], Seth C. Kruckenberg[2]

*[1] Department of Geosciences, Virginia Tech, 926 West Campus Drive, Blacksburg, VA, 24060 USA [2] Department of Earth and Environmental Science Boston College, 140 Commonwealth Ave, Chestnut Hill, MA, 02467, USA*

This chapter has been published (2021) in the Journal of Structural Geology.

https://doi.org/10.1016/j.jsg.2020.104235

## 3.1 ABSTRACT

Electron backscatter diffraction analysis of quartz grains and imaging of void spaces at grain boundaries in two orthogonal sections of a sample from the plastically deformed and dynamically recrystallized Harkless quartzite reveals the presence of void spaces at quartz-quartz grain boundaries. The distribution of these voids correlates with the crystallographic orientation of neighboring quartz grains relative to the grain boundary. Void spaces are more prevalent along grain boundaries where the *a*-axis of quartz is normal to the grain boundary. These void spaces likely formed during the exhumation (decrease in temperature and pressure) of the Harkless quartzite as a consequence of the volume change associated with an anisotropic elastic change in quartz crystal lattice dimensions, in which the length of the *a*-axis decreases by more than that of the *c*-axis. This volume change results in void space preferentially forming at grain boundaries neighbored by quartz with the *a*-axis normal to the grain boundary. The preferred orientation of the void spaces thus matches the preferred crystal orientation of quartz in the samples, suggesting that the preexisting rock microstructure and crystal fabric plays an important role in controlling the development and distribution of porosity during exhumation, which more generally may have important implications for fluid migration and the strength of exhumed rocks.

## 3.1 INTRODUCTION

Grain boundaries, which can be defined as the region between two crystals whose misorientation differs by >10º (White & White, 1981), play a fundamental role in the recrystallization of minerals under metamorphic conditions and influence the rheological and petrophysical properties of rocks. Grain boundaries are: (i) pathways for the transport of elements, elemental complexes, fluids, and melt (Austrheim, 1987; Joesten, 1991; Farver and

Yund, 1999; Kostenko et al., 2002; Rosenberg and Handy, 2005; Dohmen and Milke, 2010; Putnis and Austrheim, 2010; Carlson, 2011; Sawyer et al., 2011; Thomas and Watson, 2014; Moore et al., 2019), (ii) hosts for incompatible elements and noble gases (Hiraga et al., 2004; Baxter et al., 2007), and (iii) sites for the nucleation of new mineral phases (Carmichael, 1969; Urai et al., 1986; Drury and Urai, 1990). Given that each of these processes are crucial for the equilibration and evolution of metamorphic systems, grain boundaries thereby exert a fundamental control on equilibration and crystallization processes in metamorphic rocks (Konrad-Schmolke et al., 2007; Carlson, 2010).

The specific roles that grain boundaries play in recrystallization, and how grain boundaries effect the rheological properties of rocks, is relatively well understood in monomineralic rocks, such as quartzite. In response to increasing temperatures and decreasing strain rates, quartz will recrystallize at grain boundaries via several mechanisms: grain boundary bulging, subgrain rotation, and grain boundary migration (Hirth and Tullis, 1992; Stipp et al., 2002; Law, 2014). The microstructure, crystallographic texture, and misorientation between grains (which is dependent on grain boundary processes) can influence the petrophysical properties of quartzite (Mainprice et al., 1993; Lloyd and Kendall, 2005). Grinding at quartz grain boundaries can form an amorphous nanopowder, which contributes to slip-weakening during earthquake propagation in the upper crust (Rowe et al., 2019). Stress concentrations that develop at grain boundaries can evolve into microfractures and fault rocks (Lloyd, 2000).

Thus, the presence of void space, porosity, and/or microcracks at grain boundaries may also influence the macroscale properties of rocks. The presence of water, either dissolved within the crystal structure, distributed throughout grains as fluid inclusions, or within grain boundaries, fundamentally controls the strength of quartzite (Griggs, 1967; Jaoul et al., 1984; Kronenberg and Tullis, 1984; Mainprice and Paterson, 1984; Kronenberg et al., 1990). The presence of pores at grain boundaries in fault rocks will reduce rock strength, and may act as a weakening mechanism in shear zones (Billia et al., 2013). In deep shear zones, pores may form during ultramylonite formation and potentially develop sites of mechanical instability (Gilgannon et al., 2020). Finally, in ductile shear zones, a combination of viscous grain boundary sliding, creep cavitation (or the formation of porosity) and dissolution-reprecipitation processes creates dynamic porosity, which in turn may control fluid flow and strain localization (Fusseis et al., 2009).

Documenting the development of void space, or porosity, at grain boundaries is crucial to understanding each of these processes. In exhumed rocks, void spaces may be healed microcracks either occupied with a fluid or likely previously fluid-bearing (Kronenberg et al., 1990; Hiraga et al., 1999, 2001). Quantitative measurements of void space in quartzites have previously revealed: <100 nm lens shaped voids (Hiraga et al., 1999), a ‘necklace microstructure’ of alternating open and closed grain boundary segments (Hiraga et al., 2001), 40-500 nm voids along the grain boundaries, cavities along the grain boundaries, and cone shaped depressions where dislocation lines meet open grain boundaries (Kruhl et al., 2013), and pore spaces that vary from the nanometer to centimeter scale (Anovitz et al., 2013). These void spaces may form: (i) via crystal growth or deformation induced structural incompatibilities across grain boundaries (White and White, 1981); (ii) through the migration of fluids to grain boundaries during pressure release or annealing (White, 1973); (iii) by anisotropic volume decrease in quartz during exhumation (Kruhl et al., 2013); or (iv) at locations where the deviatoric stress is above a critical threshold for a given confining pressure (Behrmann, 1985). Combined, these studies show that void space forms via different processes and exist over a range of length scales in quartzite.

Change in the molar volume of quartz as a result of evolving temperature (*T)* and pressure (*P)* conditions may control the distribution of void space in exhumed quartzite. How the molar volume of a mineral responds to changing *P-T* conditions is a function of the elastic properties (i.e. thermal expansion and bulk modulus) of that mineral. During metamorphism at most upper crustal conditions, the molar volume of quartz is greater than it is at 25˚C and 1 bar (Ackermann and Sorrell, 1974; Angel et al., 1997, 2017; Raz et al., 2002; Scheidl et al., 2016). As a result, during exhumation from upper crustal conditions the molar volume of quartz will decrease, which may result in void spaces opening up at grain boundaries (Bruner, 1984; Kruhl et al., 2013; Raghami et al., 2020).

Many of the studies on grain boundaries in quartzites have focused on transmission electron microscopy (TEM) analyses of relatively small number of quartz grain boundaries (White, 1973; White and White, 1981; Behrmann, 1985; Kronenberg et al., 1990; Hiraga et al., 1999, 2001). In case studies where larger datasets were used [n= 25 grain boundaries, Kruhl et al. (2013); 2 x 3 cm thin sections (Anovitz et al., 2013)], no clear relationship could be established between the observed void spaces at grain boundaries and the microstructure of the rock.

In this study, we investigate how the orientation of quartz, and the resultant microstructure of the rock, may play a role in the development of void space at grain boundaries in two orthogonal sections of a sample of Harkless quartzite. We use a combination of electron backscatter diffraction (EBSD) and scanning electron microscopy (SEM) imaging techniques to determine the microstructure and crystallographic orientations of quartz grains and the distribution of grain boundary voids. These methods allow for the characterization of large area (25 $mm^2$) maps of crystallographic orientation and systematic measurement of grain boundaries, allowing us to demonstrate how volume changes associated with an anisotropic elastic change in quartz crystal lattice dimensions may preferentially open up void spaces along grain boundaries with specific crystallographic orientations during exhumation.

## 3.2 GEOLOGIC BACKGROUND AND SAMPLE DESCRIPTION

### 3.2.1 Geologic background: The White-Inyo Mountain Range, Papoose Flat Pluton, and Harkless quartzite

The studied sample (PF77) was collected from the Harkless quartzite in the contact aureole of the Papoose Flat Pluton, located in the White-Inyo Mountain Range of eastern California (Fig. 1a). The White-Inyo Range is a NW-trending horst block that parallels the Sierra Nevada Batholith and is composed of Pre-Cambrian to Cambrian pelitic and psammitic sedimentary rocks that were intruded by Mesozoic granitic plutons (Nelson, 1962; Nelson et al., 1978). The sedimentary rocks were folded around the S-plunging Inyo anticline and regionally metamorphosed at up to chlorite grade (lower greenschist facies) conditions (Nelson, 1962; Sylvester et al., 1978; Ernst et al., 1993; Ernst, 1996). Surrounding the granitic plutons, the sedimentary rocks have been deformed, deflected and locally contact metamorphosed to higher grades (Figure 1b) (Nelson, 1962; Nelson et al., 1978; Sylvester et al., 1978; Ernst et al., 1993; Nyman et al., 1995). The Papoose Flat Pluton is a Cretaceous (82.91 ± 0.96 Ma) quartz monzonite pluton that was emplaced into the SW limb of the Inyo Anticline at a depth of 12-15 km (Morgan et al., 1998; de Saint-Blanquat et al., 2001). Based on andalusite porphyroblast-matrix relationships in the surrounding contact aureole, the Papoose Flat Pluton was emplaced in two stages: initially as an inclined sill and then inflated into a laccolith (Morgan et al., 1998; Chen and Nabelek, 2017).

Along the western edge of the pluton, there is a clearly defined contact metamorphic aureole containing Cambrian metasedimentary units that include the Harkless Formation quartzite (from which sample PF77 was collected) and the Poleta Formation marbles and pelites (Fig. 1b). Forcible intrusion of the Papoose Flat Pluton plastically deformed the aureole metasedimentary rocks and thinned them to 10% of their original stratigraphic thickness while retaining their stratigraphic coherency (Fig. 1b) (Nelson et al., 1978; Sylvester et al., 1978; Morgan et al., 1998). Foliation in the aureole rocks is concordant with the outer edge of the pluton, and the recrystallized aureole rocks have a NW-SE trending, shallowly plunging stretching lineation (Law et al., 1992) that is parallel to lineation within the pluton (Nelson et al., 1978; Sylvester et al., 1978; de Saint-Blanquat et al., 2001). Textural analysis of the Harkless quartzite on the northwestern margin of the pluton indicates a dominantly plane strain non-coaxial deformation with a km-scale domanial distribution of top-to-the-SE and top-to-the-NW sense of shear associated with pluton emplacement (Law et al., 1992).

The pelitic aureole rocks contain biotite and andalusite (Poleta Formation) closer to the pluton/wall rock contact and biotite and muscovite (Harkless Formation) further away from the pluton, indicating a thermal gradient of contact metamorphism (Sylvester, 1969; Nyman et al., 1995). Calcite-dolomite thermometry profiles across the aureole indicate an initially shallow thermal gradient ranging from 550-500ºC at the pluton-wall rock contact to 500-450ºC at ~100 m away from the pluton. These relatively flat thermal profiles could represent the true thermal gradient of the aureole rocks, or they may have been transposed by fluids advecting heat through the aureole rocks, or part of the thermal gradient may have been ‘lost’ during the extreme thinning of the aureole rocks (Nyman et al., 1995).

The Papoose Flat pluton and its aureole rocks are crosscut by a series of Mesozoic to Cenozoic near-vertical strike-slip faults that likely formed during cooling of the pluton. A NE-SW trending maximum principal compressive stress ($\sigma_1$) is inferred from the fault orientations (Nelson, 1962; Ross, 1969; Sylvester, 1969; Sylvester et al., 1978). The faults do not exhibit any convincing geometric relationships with the pluton itself and are regarded as forming in response to the larger-scale regional stress field (Sylvester, 1969). Finally, the White-Inyo Mountain Range exhumed as a single, coherent fault block (Stockli et al., 2003) in Miocene times.

### 3.2.2 Sample description

Sample PF77 was collected on the northwestern side of the Papoose Flat Pluton aureole in the Harkless quartzite at a structural distance of 28 m above the pluton-wall rock contact (Fig. 1b; Traverse E of Law et al., 1992; and Nyman et al., 1995). The Harkless quartzite has a strongly developed foliation and lineation, and is also characterized by strongly developed quartz *c*-axis and *a*-axis textures (Sylvester and Christie, 1968; Sylvester, 1969; Sylvester et al., 1978; Law et al., 1992). Two orthogonal sections (Fig. 1c) were therefore cut to investigate if these strongly developed crystallographic textures and structural fabric elements have influenced the distribution and development of void space at grain boundaries.

Section PF77_YZ was cut perpendicular to foliation and lineation (*Y-Z* section) and section PF77_XZ was cut perpendicular to the foliation and parallel to the lineation (*X-Z* section). Both sections are dominated by quartz (>90%), with minor muscovite, chlorite, rutile, and zircon (Fig. 1d-e). Quartz grains in both sections record extensive grain boundary migration II (GBM II) microstructures and, to a lesser degree, grain boundary migration I (GBM I) microstructures (terminology after Stipp et al., 2002). GBM I microstructures are formed when migrating quartz grain boundaries are pinned by a secondary phase, such as phyllosilicate (pink arrows Fig. 1d-e), wherein the spacing of the secondary phase controls the resultant quartz grain size. GBM II microstructures are formed when migrating quartz grain boundaries are not pinned by second phase particles (green arrows Fig. 1d-e) and resultant recrystallized grain sizes are larger.

### 3.2.3 Rationale for sample choice

In general, quartz *c*-axis textures from the Harkless quartzite indicate a dominantly plane strain non-coaxial deformation with a km-scale domanial distribution of top to the SE and top to the NW shear senses (Law et al., 1992). However, sample PF77 is characterized by a symmetrical cross girdle distributions of quartz *c*-axes (Law et al., 1992; their figure 15). These observations suggest that the location of the Harkless quartzite that was sampled experienced bulk coaxial deformation. Sample PF77 was chosen for this study because the inferred bulk coaxial strain eliminates some of the potential kinematic variables that might have complicated our interpretations of quartz microstructure and grain boundary processes.

In sample PF77 there is no microstructural evidence for relict sedimentary grains. The sample's grain shape lineation is parallel to lineation in the pluton, suggesting that the entire sample recrystallized during contact metamorphism while subject to intrusion-related deformation. There is no evidence for grain boundary bulging or retrograde metamorphism that would suggest that PF77 has experienced deformation or subsequent recrystallization following peak metamorphic conditions (Figure 1d-e). Taken together, these observations suggest that the microstructures and crystal fabrics in the Harkless quartzite samples developed very close to peak conditions of contact metamorphism and were not affected by later deformation or metamorphism, thus allowing us to study how peak temperature microstructures and preferred crystal orientation relate to the distribution of void space at grain boundaries.

## 3.3 ANALYTICAL METHODS

### 3.3.1 Electron backscattered diffraction (EBSD)

EBSD was used to characterize patterns of crystallographic orientation in the two orthogonal sections cut from sample PF77. EBSD analyses were performed using a Tescan MIRA3 LMU Field Emission Gun Scanning Electron Microscope (FEG-SEM) equipped with an Oxford Instruments Symmetry$^{TM}$ EBSD detector. EBSD analyses were acquired using an accelerating voltage of 25 kV and beam currents of 50-75 nA (see Prior et al., 1999 for a full description of acquisition methods). Large area maps of crystallographic texture (cf. Prior et al., 1999; Halfpenny et al., 2006) were produced using Oxford Instruments AZtecHKL acquisition and analysis software (version 4.3). The resultant orientation maps measured ~15 mm x 16 mm (PF77_YZ) and ~13.5 mm x 13 mm (PF77_XZ), allowing for the complete characterization of both GBM I and GBM II microstructures within the thin sections. In order to ensure a high-density of crystallographic orientation solutions within individual grains, a 5 µm step size was used during automated large area mapping. Quartz grains in both sections are almost all larger than 5 µm width, so this step size allows for multiple EBSD analyses per grain. Indexing rates for crystallographic orientations were high in these samples (> 95%), resulting in datasets comprising over 9 million (PF77_YZ) and 6 million (PF77_XZ) solutions per large area EBSD map.

### 3.3.2 Scanning electron microscopy imaging

Full thin-section backscattered electron (BSE) images were created for sections PF77_YZ and PF77_XZ using the Tescan MIRA3 LMU FEG-SEM within the Department of Earth and Environmental Sciences at Boston College. BSE maps were acquired using an accelerating voltage of 25 kV and beam currents of 10-25 nA. Additional BSE and secondary electron (SE) images were acquired using a 10 kV accelerating voltage using a FEI Quanta 600 FEG-SEM at the Virginia Tech Nanoscale Fabrication and Classification Laboratory.

### 3.3.3 EBSD data processing

EBSD data were processed using MTeX version 5.2 in MATLAB (Bachmann et al., 2010). Individual crystal orientations with median absolute deviation (MAD) values >1.0, which equates to a low confidence in the EBSD solution, were removed. Individual grains were reconstructed using the 'calcgrains' function in MTeX using a 10º misorientation cut-off relative to neighboring solutions. Pole figures were created for the mean orientation of each grain based on the orientation distribution function (ODF), or the three dimensional distribution of crystallographic orientation in Euler space (Wenk and Wilde, 1972; Ismaïl and Mainprice, 1998) using the 'calcODF' function with a halfwidth of 2.8º for PF77_YZ and 2.3º for PF77_XZ. The mean orientation of each individual grain was then plotted on lower hemisphere, equal area pole figures such that each grain is represented by a single mean orientation on the pole figure, which was subsequently contoured (see Fig. 2e,3e). This is an appropriate way to determine the orientation of each grain, as the individual crystal orientations within each grain rarely differ by >5º and there are very few grains that contain subgrain boundaries.

In both PF77_YZ and sample PF77_XZ, void spaces were identified on the full thin section BSE image. This analytical method allows us to detect grain boundary voids greater than ~150 nm, and we acknowledge that more detailed characterization would be necessary to detect smaller voids. Smaller open grain boundaries may be present, but would require TEM imaging, which is impractical for a thin-section scale survey such as this. As such, open grain boundaries are defined in this study as resolvable in the SEM-BSE image (150 nm). The voids were marked by plotting the normals to the grain boundaries on the EBSD band contrast image. The void spaces were then compared to maps of the crystal orientation of each adjacent grain, and were color coded with the following scheme:

red = the *a*-axis of one of the quartz grains on either side of the grain boundary is normal to the grain boundary (within 20º);
green = the *c*-axis of one of the quartz grains on either side of the grain boundary is normal to the grain boundary (within 10º);
blue = the *a*-axis of one grain is normal to the grain boundary and the *c*-axis of the other grain is normal to the grain boundary;
white = there is no major crystallographic axis of quartz normal to the grain boundary;
gray = the void is located at a subgrain boundary;
black = the grain is too small to determine its orientation with the EBSD data available.

For the quantification of relationships between void spaces and crystal orientation, only the red, green, pink, and white groups were considered. This assumes that the appropriate crystallographic axes of quartz are in the plane of the thin section and normal to the grain boundary, which may not always be the case (Randle, 2006). However, we compare the orientation data to the void spaces that we observe at the top of the 2D plane of the thin section, so this should not be a substantial issue for our data. Additionally, we assume that the grain boundaries themselves are randomly oriented in the third dimension, and we use orthogonal sections of the same rock to mitigate this challenge. The reader is directed to Supplemental Material Part I for the datasets showing the BSE images and the EBSD maps used to determine the crystallographic orientation of the quartz crystals on either side of the individual grain boundary voids.

The oriented void spaces were plotted on the EBSD band contrast image, which is a qualitative map of EBSD pattern quality that also reveals the grain microstructure (Fig. 4b,5b). The black areas on the band contrast image indicate points on the thin section where pattern quality was poor and the EBSD solver could not determine a crystallographic solution for that point. These regions of poor indexing typically indicate: (i) a grain boundary; (ii) the presence of a minor phase at that point that could not be indexed; or (iii) poor sample polish at that region. As a result, the black areas on the band contrast image nominally map out the grain boundaries of the sample, which are shown by the black lines in Figure 4b,5b. Where there is a grain boundary with no tick mark in Figure 4b,5b, no void space is detectable at that grain boundary in the accompanying BSE and SE images. The color-coded tick marks thus represent the grain boundaries that have void space and the crystal orientation of the quartz grain that is normal to the grain boundary.

## 3.4 RESULTS

### 3.4.1 Grain Orientations, Distributions, and Sizes

Figure 2a shows a map of the individual EBSD-determined crystallographic orientations that are parallel to the horizontal (Y) direction, measured in the YZ plane of section PF77_YZ. The predominance of red colored grains in the map corresponds to the preferred alignment of quartz *c*-axes parallel to the Y direction within the thin section sample. A map of the quartz grain boundaries is shown in Figure 2b, with the red box highlighting Area 1 which is examined in detail in Figure 4. These more detailed areas were chosen (in both orthogonal sections) because there are minimal phyllosilicate grains in these sections (dominantly GBM II microstructures), thus we were able to clearly find and measure quartz-quartz grain boundaries over a large (25 mm$^2$) area. Figure 2c shows a map of the grains that are color-coded based on the area of each grain. These grain areas are quantified in Figure 2d, which shows the relative proportion of each of 14 class sizes. The crystal size distribution is skewed so that the smallest grain size (grain area less than 2.5 x $10^4$ μm$^2$) represents almost 50% of the total area of the sample. The average grain area (N = 24,173 grains) is 10.29 x $10^3$ μm$^2$ and the average grain diameter is 134 μm. Pole figures contoured for multiples of uniform density (MUD) for the *c* [0001], *m* <$10\bar{1}0$>, and *a* <$11\bar{2}0$> crystal axes are shown in Figure 2e. The quartz *c*-axis pattern is typical of a Type II (Lister, 1977) cross girdle texture (consistent with plane strain coaxial deformation) viewed in a YZ section plane cut perpendicular to the lineation. See Law & Johnson (2010), their figure 10, for a review and summary of commonly occuring quartz *c*-axis textures viewed on orthogonal section planes.

Figure 3 shows the same types of information as Figure 2, but for the XZ section. The mean grain area of sample PF77_XZ is 9.73 x $10^3$ μm$^2$ and the mean diameter is 131 μm (N = 17, 204 grains). Similar to the crystal size distribution of section PF77_YZ, the grain area histogram for PF77_XZ shows a skew to the smaller grains, with the smallest grain size (grain area less than 2.5 x $10^4$ μm$^2$) comprising ~50% of the sample area. Figure 3e shows pole figures for the c [0001], m <$10\bar{1}0$>, and a <$11\bar{2}0$> crystal axes. The quartz *c*-axis pattern, here viewed on the XZ section plane, is a Type II cross girdle texture, and is nearly identical to the optically measured *c*-axis pole figure for the XZ section plane of sample PF77 previously reported in Law et al., (1992) (their figure 15).

### 3.4.2 Peak Pressure-Temperature Conditions of PF77

Peak *P-T* conditions were determined based on quartz recrystallization microstructures (Stipp et al., 2002), quartz *c*-axis fabric opening angle thermometers, measuring the opening angle (OA) between the maxima of the cross girdle fabrics (Kruhl, 1998; Morgan and Law, 2004; Law, 2014; Faleiros et al., 2016), and the appearance of pressure-sensitive minerals in the contact aureole. Contact metamorphism and plastic deformation were synchronous in the Harkless quartzite (Sylvester et al., 1978; Law et al., 1992; Nyman et al., 1995; Morgan et al., 1998), so peak deformation temperatures are essentially synchronous with formation of microstructures and crystal fabrics preserved in the sample.

In both sections PF77_YZ and PF77_XZ GMB II microstructures dominate. So, based on the Stipp et al. (2002) microstructural calibration, the deformation temperature for sample PF77 is estimated at > ~ 550ºC, assuming similar strain rates and degrees of hydrolytic weakening to the study area used by Stipp et al. (2002). The quartz *c*-axis opening angle is 71º (Fig. 3e). Based on the Kruhl (1998) quartz *c*-axis fabric opening angle thermometer, the deformation temperature is estimated at 560ºC ± 50ºC. Application of the Faleiros et al. (2016) opening angle thermometer (linear version) yields a deformation temperature estimated at 538ºC (Fig. 3e). Taken together, these temperature estimates suggest a likely peak temperature range of ~ 540-560ºC, in good agreement with the 500-550°C temperature of contact metamorphism indicated by calcite-dolomite thermometry in the inner part of the contact aureole (Nyman et al., 1995). The presence of andalusite in nearby pelitic aureole rocks (Nyman et al., 1995) places the maximum pressure conditions for sample PF77 at 4 kbar. Based on the above, in this study we assume peak *P-T* conditions of 550ºC and 3.5 kbar for sample PF77.

### 3.4.3 Correlation between intergranular voids and grain orientation

#### *3.4.3.1 Section PF77_YZ*

Figure 4a shows the mean crystallographic orientation of each grain in Area 1 of section PF77_YZ (as shown in Figure 2b) measured parallel to the sample Y direction (horizontal in section plane). Figure 4b shows the EBSD band contrast image for PF77_YZ Area 1 with tick marks that correspond to grain boundary segments with void space. There are far more grain boundary segments that do not have void space (no tick marks) than have void space (tick marks). Quantitatively, 494 of the 103,785 grain boundary segments in Area 1 of PF77_YZ show void space: less than 1% of the grain boundaries contain a void space in this 2D section plane. 321 of these void spaces (65%) have the *a*-axis of one of the grains on either side of the grain boundary oriented normal to the grain boundary, 89 voids (18%) have the *c*-axis normal to the grain boundary, and 84 (17%) of these void spaces have no major crystallographic directions normal to the grain boundaries (Table 1).

Figure 4c is a close-up BSE-SEM image of Inset A in Figures 4a-b. This shows an area of the thin section that lacks measurable void space. Figure 4d is a close-up BSE image of Inset B in Figure 4a-b with the same color coding as Figure 4b for the crystal orientation of grains surrounding the void space. The close-up BSE and SE images show dark contrast along the grain boundaries (BSE) and topography changes along the grain boundaries (SE), indicating that there is void space at grain boundaries.

Figure 4d shows the measurements of two void spaces across the grain boundary. These measurements (338 nm and 345 nm) are each the average of three measurements taken from the SEM images, and assume that the grain boundary is perpendicular to the surface of the thin section. If the grain boundary is oblique to the surface of the thin section, the measured grain boundary void would be larger than the true width of the grain boundary void. Thus, our measurements represent maximum apertures of void space at grain boundaries.

### *3.4.3.2 Section PF77_XZ*

Figure 5a shows the mean crystallographic orientation of each grain in Area 2 of section PF77_XZ measured parallel to the sample X direction (horizontal in section plane). Figure 5b shows the EBSD band contrast image of PF77_XZ Area 2, with tick marks mapping out the void spaces at grain boundaries. Of the 119,190 grain boundary segments in PF77_XZ, 441 grain boundary segments (<1%) contain measurable void space. Of these 441 void space measurements, 313 (71%) are oriented so that the *a*-axis in one of the quartz grains on either side of grain boundary is perpendicular to the grain boundary, 58 (13%) are oriented so that the *c*-axis of one of the grains is normal to the grain boundary, and 70 (16%) are oriented so that neither the *a* or *c* axes are normal to the grain boundary (Table 1).

### *3.4.3.3 Statistics*

We conducted a chi squared ($\chi^2$) test to determine if there is a statistically significant relationship between the measured void space and the orientation of adjacent quartz crystals. The details of how the expected (random) distribution was created are described in Supplemental Material Part II, and the results of our $\chi^2$ test are shown in Table 1. Our null hypothesis is that there is no relationship between the orientation of quartz and the distribution of void space. The $\chi^2$ statistic was calculated by:

$$\boldsymbol{X^2} = \frac{\boldsymbol{(Observed\ frequency - Expected\ frequency)^2}}{\boldsymbol{Expected\ frequency}}$$

$\chi^2$ is 610 for section PF77_YZ and 644 for section PF77_XZ (Table 1). Both of these values are greater than the critical $\chi^2$ for statistical significance (v = 9.210) for two degrees of freedom and

99% confidence (see analytical methods and data tables in Swan & Sandilands, 1995), so the null hypothesis is rejected. There is, therefore, a statistically significant relationship between the orientation of quartz and the presence of void space at grain boundaries, and there are more voids oriented normal to the *a*-axis of quartz than expected from a random distribution.

In calculating the expected distribution of void space, we accounted for likely human error in determining the orientation of the quartz crystal that was normal to the grain boundary. For the *c*-axis of quartz, we classify any orientation within 10º of the *c*-axis as parallel to the *c*-axis, and for the *a*-axis of quartz, we classify any orientation within 20º of the *a*-axis as parallel to the *a*-axis. We then conducted a sensitivity test to determine if changing the classification of angles parallel to the *a* and *c*-axes in our expected distribution effected the statistical significance of our data (Table 2). We altered the expected distribution of PF77_YZ multiple times and re-did the $X^2$ test to see if changing the expected distribution changed the results of the $X^2$ test. In all cases, the calculated $\chi^2$ is greater than the critical $\chi^2$ for statistical significance: the null hypothesis is rejected and there is still a statistically significant relationship between the orientation of quartz and the distribution of void space at grain boundaries.

## 3.5 DISCUSSION

### 3.5.1 Interpretation of the relationship between void space and host quartz crystal orientation

The strong correlation between grain orientation and (now) open void space requires some interpretation of when porosity formed in this sample. This porosity could theoretically develop during several tectono-metamorphic stages, including: (i) prograde contact metamorphism; (ii) peak metamorphic *P*-*T* conditions; (iii) exhumation, or (iv) the final stages of sample collection and preparation. In this section, we discuss whether or not it is possible for the void spaces to open up at each of these steps, starting with our favored interpretation of opening during exhumation, before outlining reasons why we believe that opening during the other processes is less likely.

The strong correlation between grain boundary voids and crystal orientation suggest that the void spaces at grain boundaries in the Harkless quartzite likely opened up as a result of volume decreases associated with an anisotropic elastic change in quartz crystal lattice dimensions during exhumation. During exhumation of an upper crustal rock, as temperature decreases, the molar volume of quartz will decrease (cooling contraction), but as pressure decreases, the molar volume of quartz will increase (decompression expansion) (Ackermann and Sorrell, 1974; Angel et al., 1997, 2017; Raz et al., 2002; Kruhl et al., 2013). Over this *P*-*T* range, the molar volume of quartz is more sensitive to changes in temperature than changes in pressure, thus the molar volume of quartz decreases (Figure 6a) (Raz et al., 2002). Traced from 550ºC and 3.5 kbar (peak *P*-*T* conditions for sample PF77) to the Earth's surface, the molar volume of quartz will decrease from 23.1 cm$^3$/mol at 550ºC and 3.5 kbar to 22.7 cm$^3$/mol at 25ºC and 1 bar (a 1.73% decrease, Figure 6a) (Raz et al., 2002; Angel et al., 2017).

This volume decrease is controlled by anisotropic elastic change in quartz crystal lattice dimensions (Figure 6b-c) (Ackermann and Sorrell, 1974; Angel et al., 1997, 2017; Raz et al., 2002). Raz et al., (2002) experimentally determined the changes in length of quartz single crystals cut parallel to the *a*-axis and to the *c*-axis as a simultaneous function of both *P* and *T* from 25-600ºC and 0-3.5 kbar. Upon cooling and exhumation from 550ºC and 3.5 kbar to 25ºC and 1 bar, the measured relative change in the length of the quartz crystal cut parallel to the *a*-axis is 0.7, while the measured relative change in length of the quartz crystal cut parallel to the *c*-axis is 0.45, so the *a*-axis decreases by ~1.7 times that of the *c*-axis (Raz et al., 2002) (Figure 6b-c). Thus, during exhumation the length of the *a*-axis will decrease by more than the length of the *c*-axis.

These differences in the elastic properties of quartz along the *a* and *c* axes may explain our results, which indicate that there are more void spaces when the *a*-axis of quartz is normal to the grain boundary than for any other orientation. Since the *a*-axis of quartz experiences greater contraction during exhumation than the *c*-axis, this may result in preferential opening of accommodating void spaces at appropriately orientated grain boundaries, shown schematically in Figure 7. Unfortunately, there are insufficient grain boundary measurements to quantitatively test here whether the size of grain boundary voids also correlates with *a*-axis and *c*-axis orientations, though this information would be instructive. It is also currently unclear why the void spaces opened up at exactly the microstructural positions observed, or why every grain boundary normal to the *a*-axis of the host quartz grains does not have associated void space. Further, there is no obvious organization of the void spaces into a characteristic spacing, unless this spacing is at a larger than thin section scale and thus went unnoticed here. It is likely that additional factors, such as the tensile yield strength of the grain boundaries, control whether or not a void space opens up at local grain boundaries (Raghami et al., 2020).

Our results and interpretations agree well with previous experimental, observational, and numerical studies on changes in the molar volume of quartz during exhumation. In experimental studies where granite (with a large proportion of quartz) was heated to 700ºC and then cooled, the thermal expansion upon heating and subsequent contraction upon cooling created a net porosity in the final sample that was manifested as cracks along grain boundaries (Zaraisky and Balashov, 1994), similar to our observations in the Harkless quartzite. In a study of 25 quartz grain boundaries via Focused Ion Beam (FIB) milling and TEM analyses, where most of the grain boundaries were open on the nanoscale, Kruhl et al., (2013) proposed a conceptual model in which volume decrease of quartz in a rock with a random quartz microstructure results in void spaces opening up at grain boundaries oriented normal to the *a*-axis, while other grain boundaries remained closed due to the confining pressure exerted by neighboring grains.

In three dimensional numerical modelling of grain boundary opening in a random quartz microstructure during cooling and decompression, (Raghami et al., 2020) concluded that: (i) the onset of cracking is a linear function of the yield stress of the grain boundaries, (ii) crack nucleation occurs along grain vertices and triple junctions, and (iii) the overall effects of a decrease in pressure or temperature on grain boundary cracks are nearly identical. This work highlights, as shown in our study, that porosity primarily forms along triple junctions and grain boundaries. The Raghami et al., (2020) numerical model also describes the points along an exhumation path at which cracking is most likely to occur as the tensile strength of grain boundaries is overcome. It is currently impossible to precisely determine the *P*-*T* conditions at which void space opened in natural samples such as those presented here.

In a synthesis by Lander et al., (2008) of natural examples, experimentally grown quartz, and numerical simulations of quartz cementation, the rate of quartz crystal growth along the *c*-axis drops (compared to other growth directions) after euhedral crystal faces develop. Thus, differences in the volume of quartz overgrowth cement (and the amount of porosity in sandstones) may be controlled by the relative growth rates along different orientations of quartz crystals (Lander and Laubach, 2015). While this represents a very different process than that inferred here for the Harkless quartzite, it reinforces the idea that the crystal orientation of quartz can influence the distribution of porosity in quartz-dominated lithologies.

It is highly unlikely that these voids in the Harkless quartzite represent primary porosity that formed during prograde or peak metamorphism. The Papoose Flat pluton was emplaced at depths of 12-15 km (Morgan et al., 1998; de Saint-Blanquat et al., 2001), and at crustal depths greater than ~3 km sandstones (the protolith material) contain minimal porosity (Galloway, 1974). Thus, we believe that it is unlikely that any true porosity created during prograde to peak metamorphism was retained within the Harkless quartzite during exhumation. Further, it is unclear to us what mechanism or process during prograde metamorphism would favor the creation of void spaces at specific crystallographic orientations.

There is a potential concern that void spaces may form during sample preparation, and we mitigated those concerns where possible in our study. The foliated sample was gently cleaved from the rock face using a hammer and chisel and applied stresses on the sample during extraction are likely to have been minimal. Similarly, cutting the sample with a rock saw is unlikely to have involved enough force to break open void spaces. The final stages of polishing of these samples used a 0.05 μm colloid alumina suspension. This colloidal Alumina suspension (50 nm) is less than the measured void space (~350 nm), and it is potentially possible that the final polishing stage may have increased the size of some of the void spaces. However, it is unlikely that this polishing stage opened any new void spaces because epoxy is present on grain boundaries in the thin section (Figure 1d-e), which suggests that void space at grain boundaries was present before the final polishing stages. Furthermore, the use of a colloidal alumina suspension for EBSD polishing does not result in chemical etching of grains, as is the case with colloidal silica suspensions.

### 3.5.2 Abundance and size of void spaces

While the exhumed Harkless quartzite does contain void spaces at grain boundaries (porosity) that correlate with the crystal orientation of the host quartz grains, less than 1% of the grain boundary segments in PF77_YZ and PF77_XZ contain void space. With a few assumptions, we can determine the fraction porosity in sample surfaces PF77_YZ and PF77_XZ. In both sample surfaces we can assume that the average void width is 0.3 µm (300 nm) and the average void length is 50 µm, so the average area of a void space (0.3 µm x 50 µm) is 16.7 $\mu m^2$. There are 493 void spaces in PF77_YZ Area 1, so the total area of void space (16.7 $\mu m^2$ void space x 493 voids) is 8233.1 $\mu m^2$. Since Area 1 is 25 $mm^2$, the fraction porosity in PF77_YZ is 0.000329. Following the same logic, for the 441 voids in PF77_XZ, the fraction porosity is 0.000295. If instead we assume that each void space is 100 µm long, the fraction porosity in PF77_YZ is 0.00066 and the fraction porosity in PF77_XZ is 0.00059. However, our average void space measurements may be confounded by a small data set, and we acknowledge that further, more detailed TEM based measurements on grain boundary voids may be necessary for more precise quantification of void space sizes and thus porosity.

These porosity values are small and broadly agree with studies that have used neutron scattering techniques to quantify three-dimensional porosity in exhumed metamorphic rocks. Estimates of porosity range from < 0.04 in a partially serpentinized olivine (Tutolo et al., 2016) to < 0.3 fraction porosity in a shallowly buried sandstone (Anovitz et al., 2018), and to < 0.1 fraction porosity in metamorphosed limestone (Anovitz et al., 2009). These measurements all demonstrate that there is minimal porosity present in exhumed metamorphic rocks, and the low total porosity values in turn suggest that it is highly unlikely that there is any significant interconnected porosity (i.e. permeability) in the exhumed samples analyzed.

In contrast, other work based on TEM imaging and numerical modelling of quartzite grain boundaries have found that most of the observed grain boundaries (N=25) in metamorphosed quartzites from the Ballachulish igneous complex aureole and the Aar Massif are open on the nanoscale (Kruhl et al., 2013; Raghami et al., 2020). The differences in the proportion of open grain boundaries between our study and that of Kruhl et al., (2013) are most likely due to a combination of factors such as: (i) the effect of a preferred orientation in our samples; (ii) different analytical techniques (EBSD & SEM versus TEM) used to quantify porosity, in which TEM investigation may be able to observe more open grain boundaries; and (iii) number of grain boundaries analyzed.

Despite the differences in the total number of grain boundaries voids in the Harkless quartzite, compared with the Ballachulish igneous complex aureole and Aar Massif studies, the measured size of grain boundary voids follows a trend across all three samples. The Ballachulish aureole, Aar Massif, and Harkless quartzite all reached similar peak pressure conditions (~3.0 kbar), but different peak temperature conditions. The Ballachulish aureole reached a peak *T* of 670ºC and contains grain boundary voids ranging from 150-500 nm, the Harkless quartzite reached 550ºC and contains 350 nm voids, and the Aar Massif has a peak *T* of 350ºC and contains 44-110 nm voids (Kruhl et al., 2013). Thus, there appears to be a relationship in which quartzites that reached a greater peak *T* contain larger grain boundary void space. This relationship between peak temperature and size of void space at grain boundaries may be the result of quartz grains that reached a greater temperature having a larger decrease in their molar volume between their peak *P-T* and exhumation to the Earth's surface, thus creating larger void spaces at grain boundaries. While the accuracy of these grain boundary void space measurements is potentially subject to both sample preparation techniques and the angle of the grain boundary relative to the thin section plane, this general trend implies that peak *P-T* conditions (and particularly peak *T* conditions) may play a more important role during exhumation in controlling the size of grain boundary voids of a quartzite than the metamorphic and deformation processes operating during the earlier prograde history.

### 3.5.3 Orientation of void spaces

As shown in the pole figures for PF77_YZ (Figure 2e) and PF77_XZ (Figure 3e), quartz crystals in PF77 have a strongly developed preferred orientation (Fig. 8a). Thus, it is important to investigate if the preferred orientation of the quartz crystals results in a preferred orientation of the grain boundary void spaces. Figure 8 shows rose diagrams for poles to grain boundaries exhibiting void spaces in PF77_YZ (Fig. 8c-e) and PF77_XZ (Fig. 8f-h). See Fig. 8b for orientation schematic. In PF77_YZ, the poles to the void spaces that correspond to the *c*-axis of at least one neighboring quartz crystal are dominantly horizontal (i.e. parallel to the sample Y direction), matching the orientation of the *c*-axes of quartz (Fig. 8c; a map of grain orientations is available in Supplemental Material). The poles to the void spaces that are oriented perpendicular to the *a*-axis of at least one neighboring grain do not have a strongly preferred orientation (Fig. 8d), consistent with the range of *a* axis orientations that emerge from any grains with their *c*-axis dipping into the plane of the thin section (as shown in Supplemental Material Part I). There is no preferred orientation of the void spaces that are oblique to the *a* or *c*-axes of the host quartz crystals in PF77_YZ (Fig. 8c).

In PF77_XZ, the poles to the orientation of grain boundaries exhibiting void spaces that correspond to the *c*-axis and the *a*-axis of quartz do not have a preferred orientation (Fig. 8f-g). The lack of preferred orientation in the *c*-axis voids is likely due to the fact that PF77_XZ has a *c*-axis point maxima oriented parallel to the sample Y direction (Fig. 3d, 8a), so there are relatively few *c*-axes lying within the XZ thin section plane. The lack of preferred orientation of the *a*-axis voids (Fig. 8g) is the result of the *a*-axes of quartz crystals being oriented in all directions in the thin section plane of PF77_XZ (as shown in Supplemental Material Part I). There does appear to be a preferred orientation in the void spaces that are oblique to the *a* or *c*-axes of the host quartz crystals in PF77_XZ, but the processes that formed these void spaces remain unknown. In general, the preferred orientations of the void spaces reflect (and is controlled by) the preferred orientation of quartz crystals in the Harkless quartzite, which is itself a function of deformation processes operating during prograde contact metamorphism.

None of the observed void spaces are oriented similarly to larger-scale faults and joints that formed during the final stages of pluton emplacement as a result of regional scale stress fields (Sylvester, 1969). Thus, the inferred regional stress field is unlikely to have exerted any significant control on their formation.

### 3.5.4 Fluid flow in the Harkless quartzite

There is considerable evidence for the presence and movement of fluids during emplacement of the Papoose Flat pluton, including calc-silicate skarn deposits in the contact aureole (Sylvester et al., 1978; Law et al., 1992) and fluid inclusions in the granitic pluton and gneissic rocks at its outer edge that are interpreted to have been trapped during the final stages of the pluton's cooling (Brauer, 1998). Sample PF77 contains numerous quartz-hosted fluid inclusions. Thus, it is likely that the grain boundary voids in the exhumed Harkless quartzite were once filled with a fluid that was expelled from the rock in the final stages of sample preparation. It is unlikely that the grain boundary voids in the Harkless quartzite represent true void spaces that are not filled with a fluid phase because it is unclear how these voids would remain open in the crust under a confining pressure, particularly as most of the exhumation history was well below the liquid-vapor curve for water.

The source of this fluid is likely either pre-existing intragranular fluid inclusions that migrated to grain boundaries or intergranular fluid inclusions that migrated along grain boundaries as the void spaces opened. Since grain boundary diffusion occurs at rates much faster than intragranular diffusion (Joesten, 1991; Dohmen and Milke, 2010), it is likely that the void spaces were filled with fluids that were originally intergranular fluid inclusions. However, the exact location of where this fluid was stored in the Harkless quartzite prior to the opening up of crystallographic controlled void spaces is not known. This process has previously been used to explain the presence of fluid inclusions along healed microcracks at grain boundaries in quartzites (Kronenberg et al., 1990), void space at quartz-quartz grain boundaries in pelitic schists and quartz-feldspar mylonites (Hiraga et al., 1999, 2001), and bubbles along quartz-quartz grain boundaries (White, 1973) and is the interpretation we favor for the grain boundary void spaces in the Harkless quartzite. These grain boundary void-hosted fluids were most likely expelled from the rock during sample and thin section preparation.

### 3.6 CONCLUSIONS

EBSD analysis of quartz crystallographic orientations and SEM observations of void space at quartz-quartz grain boundaries in two orthogonal sections of sample PF77 from the Harkless quartzite reveal that:

1. Void spaces are present at quartz-quartz grain boundaries. Further, the presence of voids correlates well with the orientation of at least one of the host quartz crystals on either side of the grain boundary, with more void spaces when the *a*-axis of a host quartz crystal is normal to the grain boundary than in any other orientation.

2. The void space at grain boundaries likely opened during exhumation because of the anisotropic elastic properties of quartz. During exhumation from peak *P-T* conditions of 550ºC and 3.5 kbar to the Earth's surface, the molar volume of quartz decreases anisotropically. The length of quartz's *a*-axis decreases by more than that of its *c*-axis during exhumation, and this process produces more void spaces at grain boundaries normal to the host quartz crystal *a*-axis than to the *c*-axis or any other orientation.
3. A preferred orientation of void spaces that are normal to either the *a*-axis or the *c*-axis of quartz host crystals correlates with the preferred orientation of the quartz crystals in PF77. No convincing relationship was found between the orientation of void spaces and any macro-scale structures in the aureole of the Papoose Flat pluton. Thus, the crystallographic orientation of quartz host crystals and the anisotropic elastic properties of these crystals is thought to control the distribution of void space at quartz-quartz grain boundaries in the Harkless quartzite.
4. It is likely that the observations and processes that we discuss here in the Harkless quartzite operate more generally during the exhumation of low *P*- medium *T* metamorphic rocks. These void spaces may control fluid migration (if connected), initial slip in fault systems, and the strength of the exhumed rocks.

## 3.7 REFERENCES

Ackermann, R.J., Sorrell, C.A., 1974. Thermal expansion and the high–low transformation in quartz. I. High temperature X-Ray studies. Journal of Applied Crystallography 7, 468–473. https://doi.org/10.1107/S0021889874010223

Angel, R.J., Allan, D.R., Miletich, R., Finger, L.W., 1997. The use of quartz as an internal pressure standard in high-pressure crystallography. Journal of Applied Crystallography 30, 461–466. https://doi.org/10.1107/S0021889897000861

Angel, R.J., Alvaro, M., Miletich, R., Nestola, F., 2017. A simple and generalised P–T–V EoS for continuous phase transitions, implemented in EosFit and applied to quartz. Contributions to Mineralogy and Petrology 172, 1–15. https://doi.org/10.1007/s00410-017-1349-x

Anovitz, L.M., Cole, D.R., Rother, G., Allard, L.F., Jackson, A.J., Littrell, K.C., 2013. Diagenetic changes in macro- to nano-scale porosity in the St. Peter Sandstone: An (ultra) small angle neutron scattering and backscattered electron imaging analysis. Geochimica et Cosmochimica Acta 102, 280–305. https://doi.org/10.1016/j.gca.2012.07.035

Anovitz, L.M., Freiburg, J.T., Wasbrough, M., Mildner, D.F.R., Littrell, K.., Pipich, V., Ilavsky, J., 2018. The effects of burial diagenesis on multiscale porosity in the St. Peter Sandstone: An imaging, small-angle, and ultra-small-angle neutron scattering analysis. Marine and Petroleum Geology 92, 352–371. https://doi.org/10.1016/j.marpetgeo.2017.11.004

Anovitz, L.M., Lynn, G.W., Cole, D.R., Rother, G., Allard, L.F., Hamilton, W.A., Porcar, L., Kim, M.H., 2009. A new approach to quantification of metamorphism using ultra-small and small angle neutron scattering. Geochimica et Cosmochimica Acta 73, 7303–7324. https://doi.org/10.1016/j.gca.2009.07.040

Austrheim, H., 1987. Eclogitization of lower crustal granulites by fluid migration through shear zones. Earth and Planetary Science Letters 81, 221–232.

Bachmann, F., Hielscher, R., Schaeben, H., 2010. Texture analysis with MTEX- Free and open source software toolbox. Solid State Phenomena 160, 63–68. https://doi.org/10.4028/www.scientific.net/SSP.160.63

Baxter, E.F., Asimow, P.D., Farley, K.A., 2007. Grain boundary partitioning of Ar and He.

Geochimica et Cosmochimica Acta 71, 434–451. https://doi.org/10.1016/j.gca.2006.09.011

Behrmann, J.H., 1985. Crystal plasticity and superplasticity in quartzite; A natural example. Tectonophysics 115, 101–129. https://doi.org/10.1016/0040-1951(85)90102-7

Billia, M.A., Timms, N.E., Toy, V.G., Hart, R.D., Prior, D.J., 2013. Grain boundary dissolution porosity in quartzofeldspathic ultramylonites: Implications for permeability enhancement and weakening of mid-crustal shear zones. Journal of Structural Geology 53, 2–14. https://doi.org/10.1016/j.jsg.2013.05.004

Brauer, N., 1998. Fluid inclusions as a monitor of progressive grain-scale deformation during cooling of the Papoose Flat Pluton, eastern California. Https://Vtechworks.Lib.vt.Edu/Handle/10919/36556.

Bruner, W.M., 1984. Crack growth during unroofing of crustal rocks: Effects on thermoelastic behavior and near-surface stresses. Journal of Geophysical Research 89, 4167–4184. https://doi.org/10.1029/jb089ib06p04167

Carlson, W.D., 2011. Porphyroblast crystallization: linking processes, kinetics, and microstructures. International Geology Review 53, 406–445. https://doi.org/10.1080/00206814.2010.496184

Carlson, W.D., 2010. Dependence of reaction kinetics on H2O activity as inferred from rates of intergranular diffusion of aluminium. Journal of Metamorphic Geology 28, 735–752. https://doi.org/10.1111/j.1525-1314.2010.00886.x

Carmichael, D.M., 1969. On the mechanism of prograde metamorphic reactions in quartz-bearing pelitic rocks. Contributions to Mineralogy and Petrology 20, 244–267. https://doi.org/10.1007/BF00377479

Chen, Y., Nabelek, P.I., 2017. The influences of incremental pluton growth on magma crystallinity and aureole rheology: numerical modeling of growth of the Papoose Flat pluton, California. Contributions to Mineralogy and Petrology 172, 1–16. https://doi.org/10.1007/s00410-017-1405-6

de Saint-Blanquat, M., Law, R.D., Bouchez, J.L., Morgan, S.S., 2001. Internal structure and emplacement of the Papoose Flat pluton: An integrated structural, petrographic, and magnetic susceptibility study. Bulletin of the Geological Society of America 113, 976–995. https://doi.org/10.1130/0016-7606(2001)113<0976:ISAEOT>2.0.CO;2

Dohmen, R., Milke, R., 2010. Diffusion in polycrystalline materials: grain boundaries, mathematical models, and experimental data. Reviews in Mineralogy & Geochemistry 72, 921–970. https://doi.org/10.2138/rmg.2010.72.21

Drury, M.R., Urai, J.L., 1990. Deformation-related recrystallization processes. Tectonophysics 112, 235–253.

Ernst, W.G., 1996. Petrochemical study of regional/contact metamorphism in metaclastic strata of the central White-Inyo Range, eastern California. Bulletin of the Geological Society of America 108, 1528–1548. https://doi.org/10.1130/0016-7606(1996)108<1528:PSORCM>2.3.CO;2

Ernst, W.G., Nelson, C.A., Hall, C.A., 1993. Geology and metamorphic mineral assemblages of Precambrian and Cambrian rocks of the central White-Inyo Range, eastern California. California Division of Mines and Geology, Map Sheet 46, 25 p.

Faleiros, F.M., Moraes, R., Pavan, M., Campanha, G.A.C., 2016. A new empirical calibration of the quartz c-axis fabric opening-angle deformation thermometer. Tectonophysics 671, 173–182. https://doi.org/10.1016/j.tecto.2016.01.014

Farver, J.R., Yund, R.A., 1999. Oxygen bulk diffusion measurements and TEM characterization of a natural ultramylonite: Implications for fluid transport in mica-bearing rocks. Journal of Metamorphic Geology 17, 669–683. https://doi.org/10.1046/j.1525-1314.1999.00223.x

Fusseis, F., Regenauer-Lieb, K., Liu, J., Hough, R.M., De Carlo, F., 2009. Creep cavitation can establish a dynamic granular fluid pump in ductile shear zones. Nature 459, 974–977. https://doi.org/10.1038/nature08051

Galloway, W.E., 1974. Deposition and diagenetic alteration of sandstone in northeast Pacific arc-related basins: Implications for graywacke genesis. Bulletin of the Geological Society of America 85, 379–390. https://doi.org/10.1130/0016-7606(1974)85<379:DADAOS>2.0.CO;2

Gilgannon, J., Poulet, T., Berger, A., Barnhoorn, A., Herwegh, M., 2020. Dynamic recrystallization can produce porosity in shear zones. Geophysical Research Letters 47, 1–10. https://doi.org/10.1029/2019GL086172

Griggs, D., 1967. Hydrolytic weakening of quartz and other silicates. Geophysical Journal of the Royal Astronomical Society 14, 19–31. https://doi.org/10.1111/j.1365-246X.1967.tb06218.x

Halfpenny, A., Prior, D.J., Wheeler, J., 2006. Analysis of dynamic recrystallization and nucleation in a quartzite mylonite. Tectonophysics 427, 3–14. https://doi.org/10.1016/j.tecto.2006.05.016

Hiraga, T., Anderson, I.M., Kohlstedt, D.L., 2004. Grain boundaries as reservoirs of incompatible elements in the Earth’s mantle. Nature 427, 699–703. https://doi.org/10.1038/nature02259

Hiraga, T., Nagase, T., Akizuki, M., 1999. The structure of grain boundaries in granite-origin ultramylonite studied by high-resolution electron microscopy. Physics and Chemistry of

Minerals 26, 617–623. https://doi.org/10.1007/s002690050226

Hiraga, T., Nishikawa, O., Nagase, T., Akizuki, M., 2001. Morphology of intergranular pores and wetting angles in pelitic schists studied by transmission electron microscopy. Contributions to Mineralogy and Petrology 141, 613–622. https://doi.org/10.1007/s004100100263

Hirth, G., Tullis, J., 1992. Dislocation creep regimes in quartz aggregates. Journal of Structural Geology 14, 145–159. https://doi.org/10.1016/0191-8141(92)90053-Y

Ismaïl, W. Ben, Mainprice, D., 1998. An olivine fabric database: An overview of upper mantle fabrics and seismic anisotropy. Tectonophysics 296, 145–157. https://doi.org/10.1016/S0040-1951(98)00141-3

Jaoul, O., Tullis, J., Kronenberg, A.K., 1984. The effect of varying water contents on the creep behavior of Heavitree quartzite. Journal of Geophysical Research 89, 4298–4312.

Joesten, R., 1991. Grain-boundary diffusion kinetics in silicate and oxide minerals. In: Ganguly, J. (Ed.), Diffusion, Atomic Ordering, and Mass Transport. Advances in Physical Geochemistry. Springer, New York, NY.

Konrad-Schmolke, M., O'Brien, P.J., Heidelbach, F., 2007. Compositional re-equilibration of garnet: the importance of sub-grain boundaries. European Journal of Mineralogy 19, 431–438. https://doi.org/10.1127/0935-1221/2007/0019-1749

Kostenko, O., Jamtveit, B., Austrheim, H., Pollok, K., Putnis, C., 2002. The mechanism of fluid infiltration in peridotites at Almklovdalen, western Norway. Geofluids 2, 203–215. https://doi.org/10.1046/j.1468-8123.2002.00038.x

Kronenberg, A.K., Segall, P., Wolf, G.H., 1990. Hydrolytic weakening and penetrative deformation within a natural shear zone. Geophysical Monograph Series 56, 21–36.

https://doi.org/10.1029/GM056p0021

Kronenberg, A.K., Tullis, J., 1984. Flow strengths of quartz aggregates: grain zize and pressure effects due to hydrolytic weakening. Journal of Geophysical Research 89, 4281–4297.

Kruhl, J.H., 1998. Reply: prism- and basal-plane parallel subgrain boundaries in quartz: a microstructural geothermobarometer. Journal of Metamorphic Geology 16, 142–146.

Kruhl, J.H., Wirth, R., Morales, L.F.G., 2013. Quartz grain boundaries as fluid pathways in metamorphic rocks. Journal of Geophysical Research: Solid Earth 118, 1957–1967. https://doi.org/10.1002/jgrb.50099

Lander, R.H., Larese, R.E., Bonnell, L.M., 2008. Toward more accurate quartz cement models: The importance of euhedral versus noneuhedral growth rates. American Association of Petroleum Geologists Bulletin 92, 1537–1563. https://doi.org/10.1306/07160808037

Lander, R.H., Laubach, S.E., 2015. Insights into rates of fracture growth and sealing from a model for quartz cementation in fractured sandstones. Bulletin of the Geological Society of America 127, 516–538. https://doi.org/10.1130/B31092.1

Law, R.D., 2014. Deformation thermometry based on quartz c-axis fabrics and recrystallization microstructures: A review. Journal of Structural Geology 66, 129–161. https://doi.org/10.1016/j.jsg.2014.05.023

Law, R.D., Johnson, M.R.W., 2010. Microstructures and crystal fabrics of the Moine Thrust zone and Moine Nappe: History of research and changing tectonic interpretations. Geological Society of London Special Publication Special Publication 335, 443–503. https://doi.org/10.1144/SP335.21

Law, R.D., Nyman, M., Morgan, S.S., Casey, M., 1992. The Papoose Flat Pluton of eastern California: A reassessment of its emplacement history in the light of new microstructural and crystallographic fabric observations. Transactions of the Royal Society of Edinburgh: Earth Sciences 83, 361–375. https://doi.org/10.1017/S0263593300008026

Lister, G.S., 1977. Crossed girdle c-axis fabrics in quartzites plastically deformed by plane strain and progressive simple shear. Tectonophysics 39.

Lloyd, G.E., 2000. Grain boundary contact effects during faulting of quartzite: An SEM/EBSD analysis. Journal of Structural Geology 22, 1675–1693. https://doi.org/10.1016/S0191-8141(00)00069-9

Lloyd, G.E., Kendall, J.M., 2005. Petrofabric-derived seismic properties of a mylonitic quartz simple shear zone: Implications for seismic reflection profiling. Geological Society of London Special Publication 240, 75–94. https://doi.org/10.1144/GSL.SP.2005.240.01.07

Mainprice, D., Lloyd, G.E., Casey, M., 1993. Individual orientation measurements in quartz polycrystals: advantages and limitations for texture and petrophysical property determinations. Journal of Structural Geology 15, 1169–1187. https://doi.org/10.1016/0191-8141(93)90162-4

Mainprice, D., Paterson, M.S., 1984. Experimental studies of the role of water in the plasticity of quartzites. Journal of Geophysical Research 89, 4257–4269.

Moore, J., Beinlich, A., Austrheim, H., Putnis, A., 2019. Stress orientation-dependent reactions during metamorphism. Geology 47, 151–154. https://doi.org/10.1130/G45632.1

Morgan, S.S., Law, R.D., 2004. Unusual transition in quartzite dislocation creep regimes and crystal slip systems in the aureole of the Eureka Valley-Joshua Flat-Beer Creek pluton, California: A case for anhydrous conditions created by decarbonation reactions. Tectonophysics 384, 209–231. https://doi.org/10.1016/j.tecto.2004.03.016

Morgan, S.S., Law, R.D., Nyman, M.W., 1998. Laccolith-like emplacement model for the

Papoose Flat pluton based on porphyroblast-matrix analysis. Bulletin of the Geological Society of America 110, 96–110. https://doi.org/10.1130/0016-7606(1998)110<0096:LLEMFT>2.3.CO;2

Nelson, C.A., 1962. Lower Cambrian-Precambrian succession, White-Inyo Mountains, California. Geological Society Of America Bulletin 73, 139–144.

Nelson, C.A., Oertel, G., Christie, J.M., Sylvester, A.G., 1978. Geologic map of Papoose Flat Pluton, Inyo Mountains, California with palinspastic map and cross sections. Geological Society of America, Boulder, CO.

Nyman, M.W., Law, R.D., Morgan, S.S., 1995. Conditions of contact metamorphism, Papoose Flat Pluton, eastern California, USA: implications for cooling and strain histories. Journal of Metamorphic Geology 13, 627–643. https://doi.org/10.1111/j.1525-1314.1995.tb00247.x

Prior, D.J., Boyle, A.P., Brenker, F., Cheadle, M.C., Day, A., Lopez, G., Peruzzo, L., Potts, G.J., Reddy, S., Spiess, R., Timms, N.E., Trimby, P., Wheeler, J., Zetterstrom, L., 1999. The application of electron backscatter diffraction and orientation constrast imaging in the SEM to textural problems in rocks. American Mineralogist 84, 1741–1759. https://doi.org/10.2138/am-1999-11-1204

Putnis, A., Austrheim, H., 2010. Fluid-induced processes: metasomatism and metamorphism. Geofluids 10, 254–269. https://doi.org/10.1111/j.1468-8123.2010.00285.x

Raghami, E., Schrank, C., Kruhl, J.H., 2020. 3D modelling of the effect of thermal-elastic stress on grain-boundary opening in quartz grain aggregates. Tectonophysics 774, 1–13. https://doi.org/10.1016/j.tecto.2019.228242

Randle, V., 2006. “Five-parameter” analysis of grain boundary networks by electron backscatter diffraction. Journal of Microscopy 222, 69–75. https://doi.org/10.1111/j.1365-

2818.2006.01575.x

Raz, U., Girsperger, S., Thompson, A.B., 2002. Thermal expansion, compressibility and volumetric changes of quartz obtained by single crystal dilatometry to 700°C and 3.5 kilobars (0.35 GPa). Schweizerische Mineralogische Und Petrographische Mitteilungen 82, 561–574. https://doi.org/10.3929/ethz-a-004392716

Rosenberg, C.L., Handy, M.R., 2005. Experimental deformation of partially melted granite revisited: Implications for the continental crust. Journal of Metamorphic Geology 23, 19–28. https://doi.org/10.1111/j.1525-1314.2005.00555.x

Ross, D.C., 1969. Descriptive petrography of three large granitic bodies in the Inyo Mountains, California. U.S. Geological Survey, Professional Paper 601, 47p.

Rowe, C.D., Lamothe, K., Rempe, M., Andrews, M., Mitchell, T.M., Di Toro, G., White, J.C., Aretusini, S., 2019. Earthquake lubrication and healing explained by amorphous nanosilica. Nature Communications 10, 320. https://doi.org/10.1038/s41467-018-08238-y

Sawyer, E.W., Cesare, B., Brown, M., 2011. When the continental crust melts. Elements 7, 229–234. https://doi.org/10.2113/gselements.7.4.229

Scheidl, K.S., Kurnosov, A., Trots, D.M., Boffa Ballaran, T., Angel, R.J., Miletich, R., 2016. Extending the single-crystal quartz pressure gauge up to hydrostatic pressure of 19 GPa. Journal of Applied Crystallography 49, 2129–2137. https://doi.org/10.1107/S1600576716015351

Stipp, M., Stünitz, H., Heilbronner, R., Schmid, S.M., 2002. Dynamic recrystallization of quartz: correlation between natural and experimental conditions. Geological Society, London, Special Publications 200, 171–190. https://doi.org/10.1144/GSL.SP.2001.200.01.11

Stockli, D.F., Dumitru, T.A., McWilliams, M.O., Farley, K.A., 2003. Cenozoic tectonic evolution of the White Mountains, California and Nevada. Bulletin of the Geological Society of America 115, 788–816. https://doi.org/10.1130/0016-7606(2003)115<0788:CTEOTW>2.0.CO;2

Swan, A.R.H., Sandilands, M., 1995. Introduction to Geological Data Analysis. Blackwell Science Ltd, Cambridge, MA.

Sylvester, A.G., 1969. A microfabric study of calcite, dolomite, and quartz around Papoose Flat pluton, California. Bulletin of the Geological Society of America 80, 1311–1328. https://doi.org/10.1130/0016-7606(1969)80[1311:SMSOCD]2.0.CO;2

Sylvester, A.G., Christie, J.M., 1968. The origin of crossed-girdle orientations of optic axes in deformed quartzites. The Journal of Geology 571–580.

Sylvester, A.G., Ortel, G., Nelson, C.A., Christie, J.M., 1978. Papoose Flat pluton: A granitic blister in the Inyo Mountains, California. Bulletin of the Geological Society of America 89, 1205–1219. https://doi.org/10.1130/0016-7606(1978)89<1205:PFPAGB>2.0.CO;2

Thomas, J.B., Watson, E.B., 2014. Diffusion and partitioning of magnesium in quartz grain boundaries. Contributions to Mineralogy and Petrology 168, 1–12. https://doi.org/10.1007/s00410-014-1068-5

Tutolo, B.M., Mildner, D.F.R., Gagnon, C.V.L., Saar, M.O., Seyfried, W.E., 2016. Nanoscale constraints on porosity generation and fluid flow during serpentinization. Geology 44, 103–106. https://doi.org/10.1130/G37349.1

Urai, J.L., Means, W.D., Lister, G.S., 1986. Dynamic recrystallization of rocks and minerals. In: Heard, H., Hobbs, B. (Eds.), Mineral and Rock Deformation: Laboratory Studies, the Paterson Volume. American Geophysical Union, Washington, DC, 161–200.

Wenk, H., Wilde, W., 1972. Orientation distribution fabrics for 3 Yule marble fabrics. In: Heard, H.C., Borg, I.Y., Carter, N.L., Raleigh, C.B. (Eds.), Flow and Fracture of Rocks: American Geophysical Union Geophysical Monograph. 83–94. https://doi.org/https:// doi .org /10 .1029 /GM016p0083

White, J.C., White, S.H., 1981. On the structure of grain boundaries in tectonites. Tectonophysics 78, 613–628. https://doi.org/10.1007/978-94-009-7870-6_8

White, S.H., 1973. Dislocations and bubbles in vein quartz. Nature 244, 47–49.

Zaraisky, G.P., Balashov, V.N., 1994. Thermal decompaction of rocks. In: Shmulovich, W.I., Yardley, B.W.D., Gonchar, G.G. (Eds.), Fluids in the Crust: Equilibrium and Transport Properties. Chapman & Hall, London, 253–284.

## 3.8 ACKNOWLEDGEMENTS

The authors acknowledge use of the facilities and the assistance of Steve McCartney at the Nanoscale Characterization and Fabrication Laboratory at Virginia Tech. Ryan Pollyea is thanked for discussions on statistical methods. Jorn Kruhl, Amicia Lee, and an anonymous reviewer are thanks for helpful and constructive reviews. The authors thank Stephen Laubach for editorial handling of this paper. Members of the Metamorphic Processes Group at Virginia Tech are thanked for helpful discussions on various parts of this project.

## 3.9 FIGURES

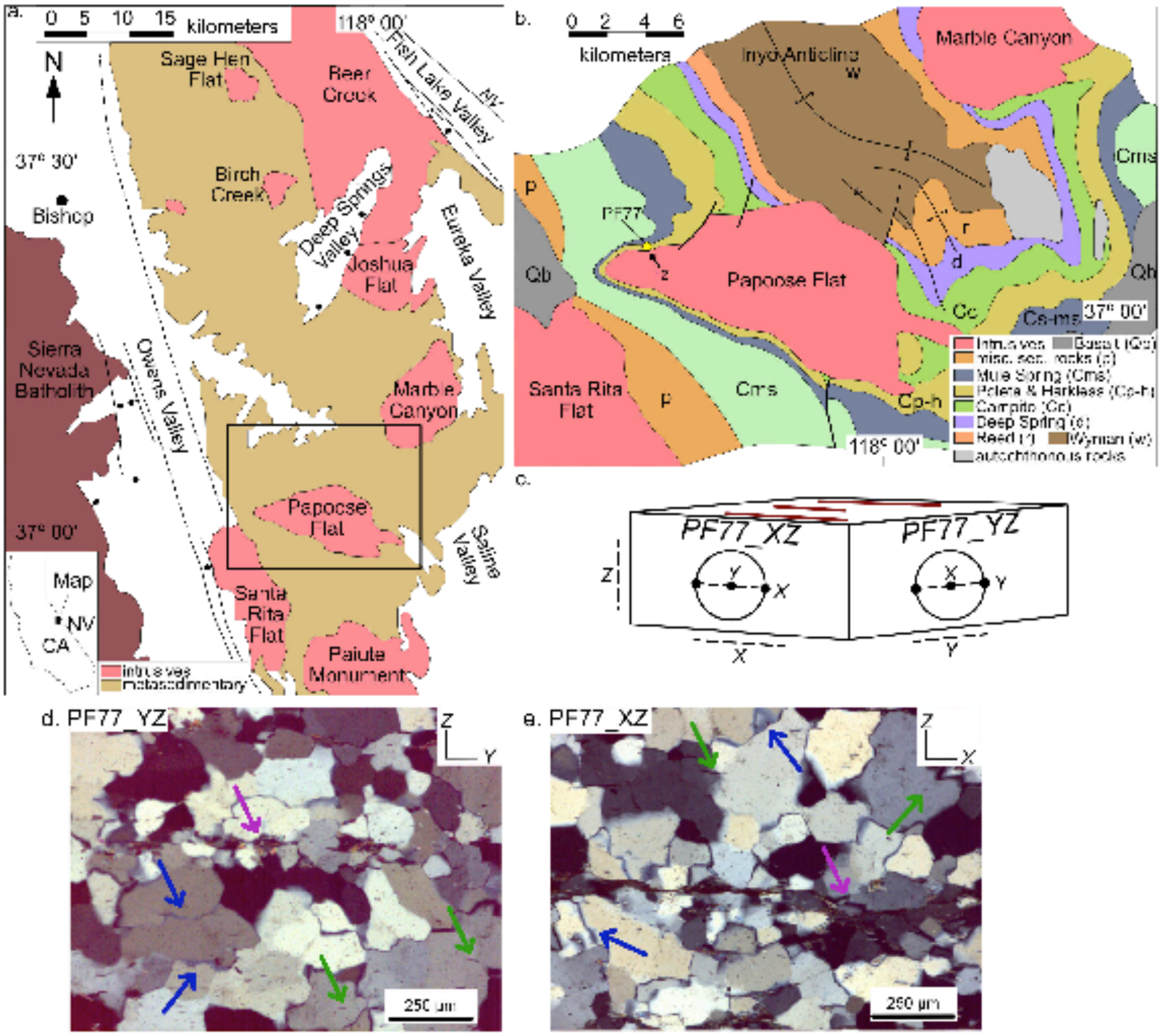

Figure 2.1. **Geologic map, orientation of orthogonal sections, and photomicrographs of sample PF77. (a)** Simplified geologic map of Mesozoic intrusions (pink) and metasedimentary rocks (tan) in the White-Inyo Range, showing location of Papoose Flat Pluton. To the west, the White-Inyo Range is bounded by normal faults in Owens Valley and to the east it is bounded by normal and dextral strike-slip faults in the Fish Lake, Eureka, and Saline valleys. Figure modified from Law et al., (1992). **(b)** Geologic map of the area surrounding Papoose Flat Pluton, showing extreme attenuation of stratigraphic units around the western edge of the pluton. The

location of sample PF77 and the local trend and plunge of lineation are indicated. Qb = Quaternary basalt; p = miscellaneous Middle Cambrian and younger sedimentary rocks; Cms = Mule Spring Formation; Cs-ms = Saline Valley and Mule Spring formations; Cp-h = Poleta and Harkless formations; Cc = Campito Formation; d = Deep Spring Formation; r = Reed Formation; w = Wyman Formation; unlabeled gray masses = autochthonous rocks beneath thrust of Jackass Flat. Figure is modified from: http://sylvester.faculty.geol.ucsb.edu/PAPOOSE/PFpages/PFgeolmap1.html **(c)** Box diagram showing how sample PF77 was cut: PF77-YZ is cut perpendicular to the foliation and lineation (*Y-Z* section) and PF77-XZ is cut perpendicular to the foliation and parallel to the lineation (*X-Z* section). **(d)** Photomicrograph of PF77-YZ showing GBM I (pink arrow) and GBM II (green arrow) recrystallization regime microstructures. Blue arrow shows epoxy at grain boundaries, which is evidence for original void space at the grain boundaries. **(e)** Photomicrograph of PF77-XZ showing GBM I (pink arrow) and GBM II (green arrow) recrystallization regime microstructures. Blue arrow shows epoxy at grain boundaries.

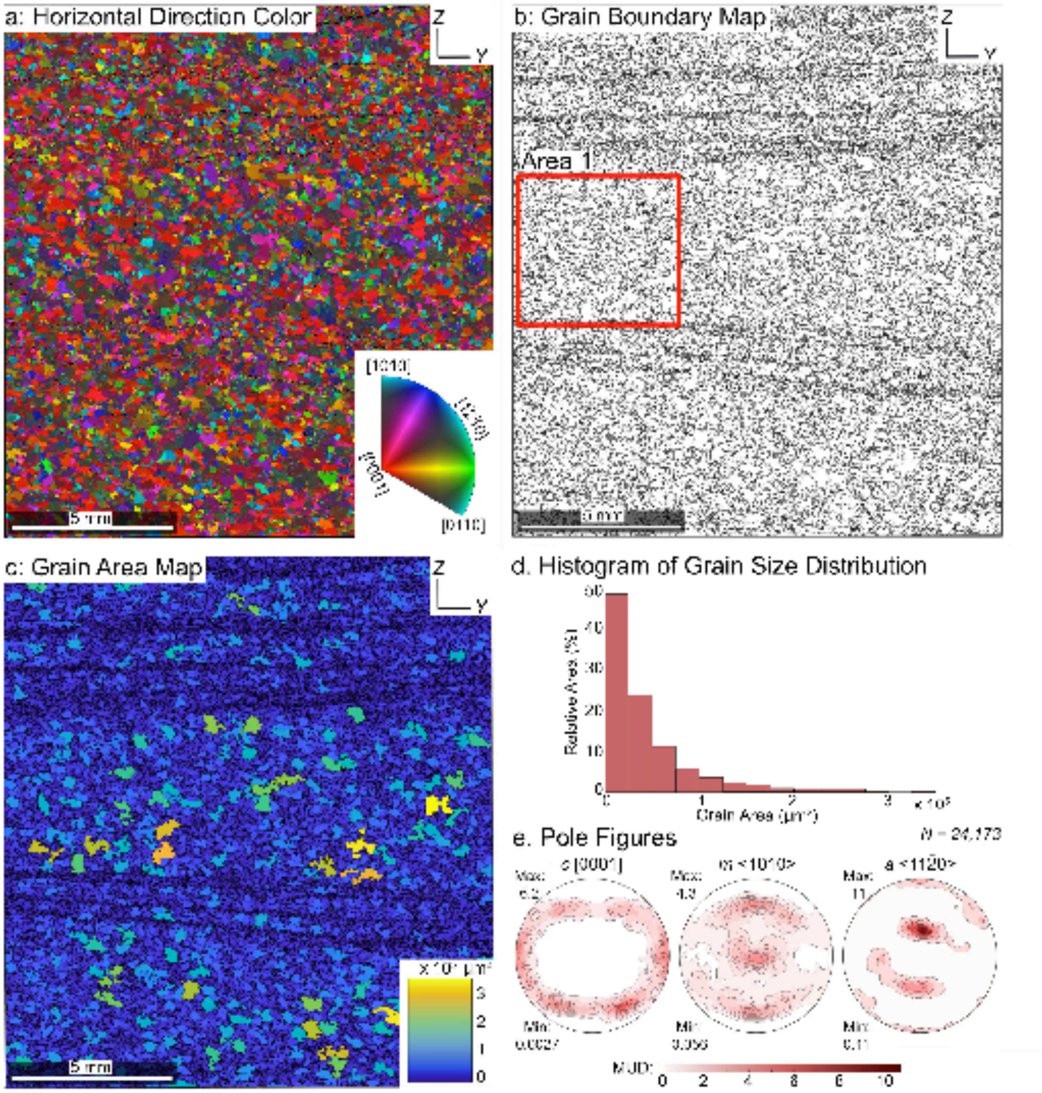

Figure 2.2. **Overview of section PF77-YZ.** (a) Representative EBSD map shown in quartz inverse pole figure coloring in crystal reference frame (see inset). Colors denote the quartz crystallographic axis oriented parallel to the horizontal direction of the mapped region (Y direction in sample coordinates). **(b)** Map of grain boundaries calculated with a 10º misorientation angle cutoff. Location of Area 1 (Fig. 4) is highlighted by red box. **(c)** Map of grain size distribution (grain area). **(d)** Histogram of grain size (measured in area) distribution. See text for explanation. **(e)** Lower hemisphere, equal area pole figures. The contoured coloring

represents multiples of uniform density (MUD) for the corresponding Orientation Distribution Function of each pole figure, with the maximum and minimum value for each pole figure noted. Contouring based on 24,173 grains, with one point per grain.

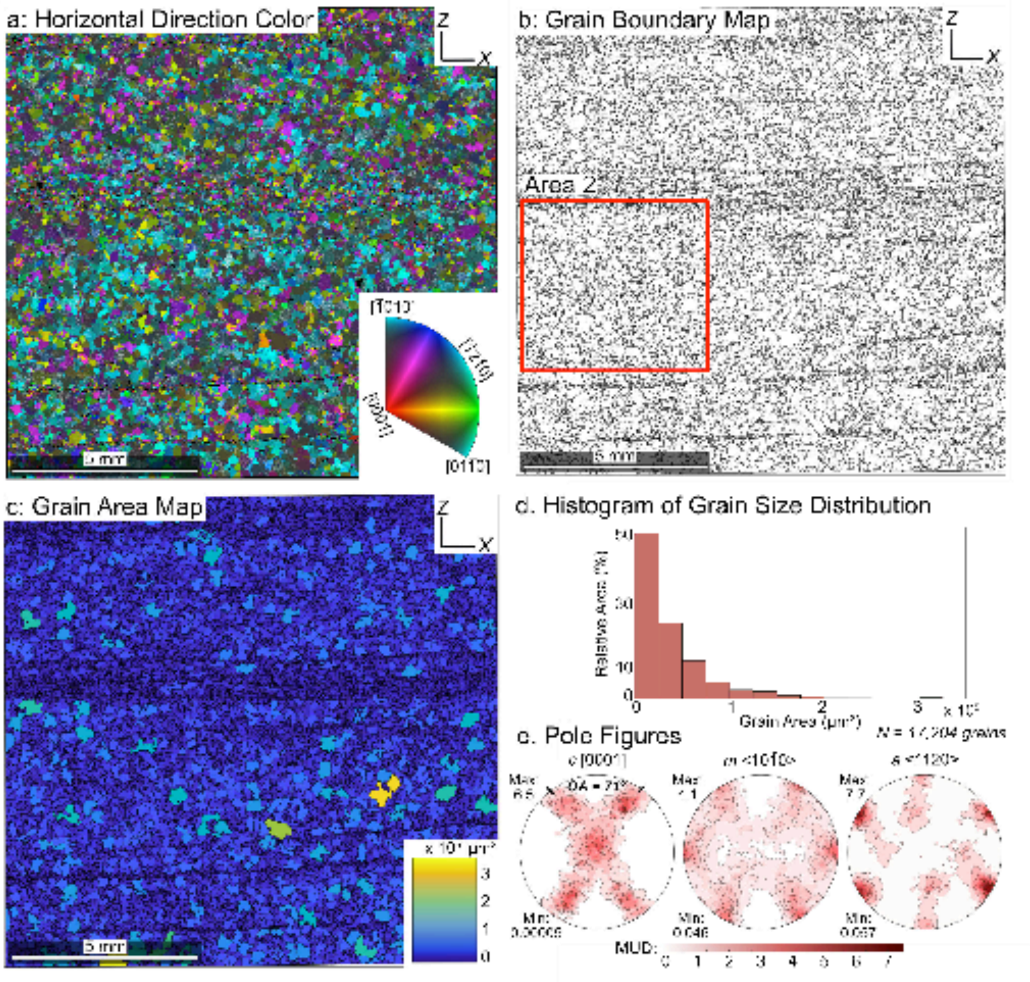

Figure 2.3. **Overview of section PF77-XZ.** (a) Representative EBSD map shown in quartz inverse pole figure coloring in the crystal reference frame (see inset). Colors denote the quartz crystallographic axis oriented parallel to the horizontal direction of the mapped region (X direction in sample coordinates). (b) Map of grain boundaries, calculated with a 10º misorientation angle cutoff. Location of Area 2 (Fig. 5) is highlighted by red box. (c) Map of grain size distribution (grain area). (d) Histogram of grain size (measured in area) distribution.

See text for explanation. (e) Lower hemisphere, equal area pole figure plots. The contoured coloring represents multiples of uniform density (MUD) for the corresponding Orientation Distribution Function of each pole figure with the maximum and minimum value for each pole figure noted. Contouring based on 17,204 grains, with one point per grain. Opening angle (OA) (measured from tick marks) of quartz c-axis fabric = 71º.

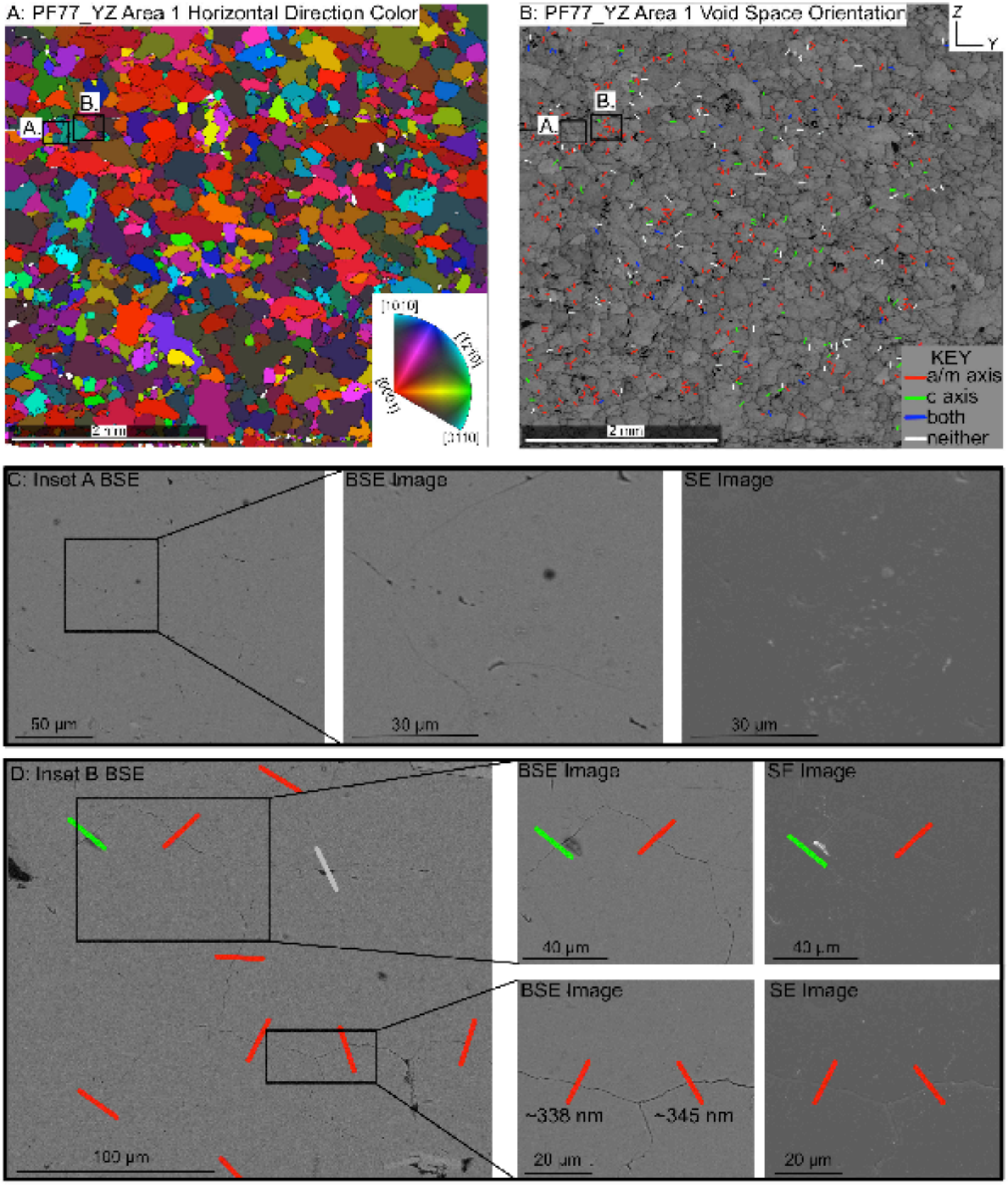

Figure 2.4. **Orientation and void space data for PF77-YZ Area 2.** (a) Representative EBSD map shown in inverse quartz pole figure coloring in crystal reference frame (see inset) for the mean orientation of each grain. Colors denote the quartz crystallographic axis oriented parallel to

the horizontal direction of the mapped region (Y direction in sample coordinates). (b) EBSD band contrast image showing the grains (gray) and grain boundaries (black). Grain boundaries with void spaces are color coded based on the crystallographic orientation of one of the grains on either side of the grain boundary, where gray = subgrain boundary, black = very small grain, red = *a*-axis normal to the grain boundary, green = *c*-axis normal to the grain boundary, blue = both an *a*-axis and a c-axis normal to the grain boundary, and white = neither the *a*-axis or the *c*-axis normal to the grain boundary. (c) Inset region A: BSE image, showing no measurable void space at grain boundaries. Zoomed in BSE and SE images of the black box show no measurable void space at grain boundaries. (d) Inset region B: BSE image, with two sub-regions that are shown in more detail. Color coding for the orientation of grains on either side of the void space as in panel b. Detailed BSE and SE images reveal void space at grain boundaries.

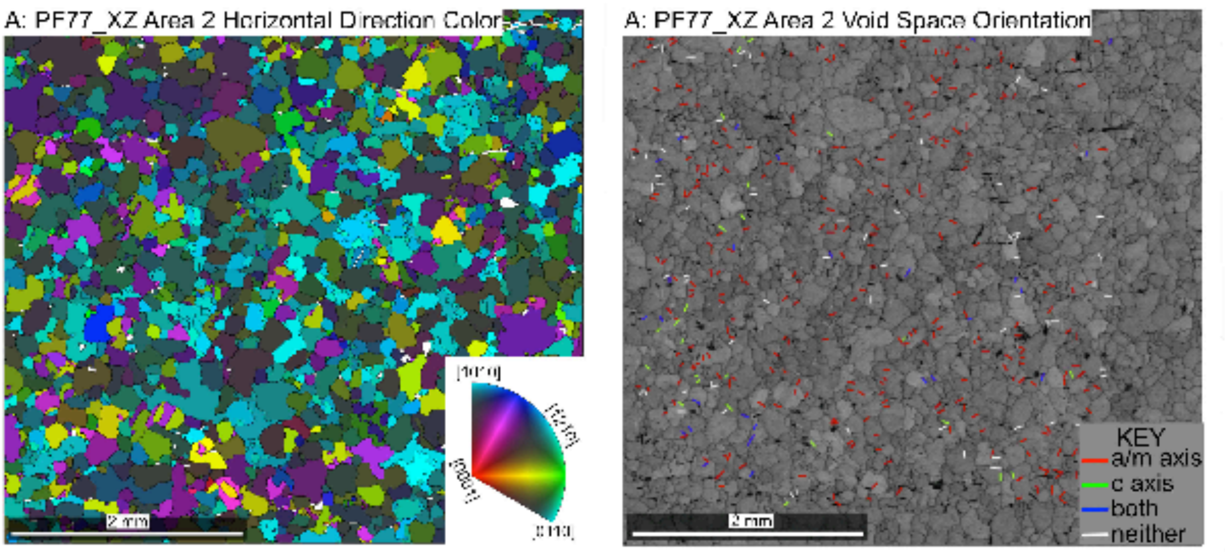

Figure 2.5. **Orientation and void space data for PF77-XZ Area 2.** (a) Representative EBSD map shown in inverse pole figure coloring in the crystal reference frame (see inset) for the mean orientation of each grain. Colors denote the quartz crystallographic axis oriented parallel to the horizontal direction of the mapped region (X direction in sample coordinates). (b) EBSD band

contrast image showing the grains (gray) and grain boundaries (black). The grain boundaries with void spaces are color coded based on the crystallographic orientation of one of the grains on either side of the grain boundary, where gray = subgrain boundary, black = very small grain, red = *a*-axis normal to the grain boundary, green = *c*-axis normal to the grain boundary, blue = both an *a*-axis and a *c-axis* normal to the grain boundary, and white = neither the *a*-axis or the c-axis normal to the grain boundary.

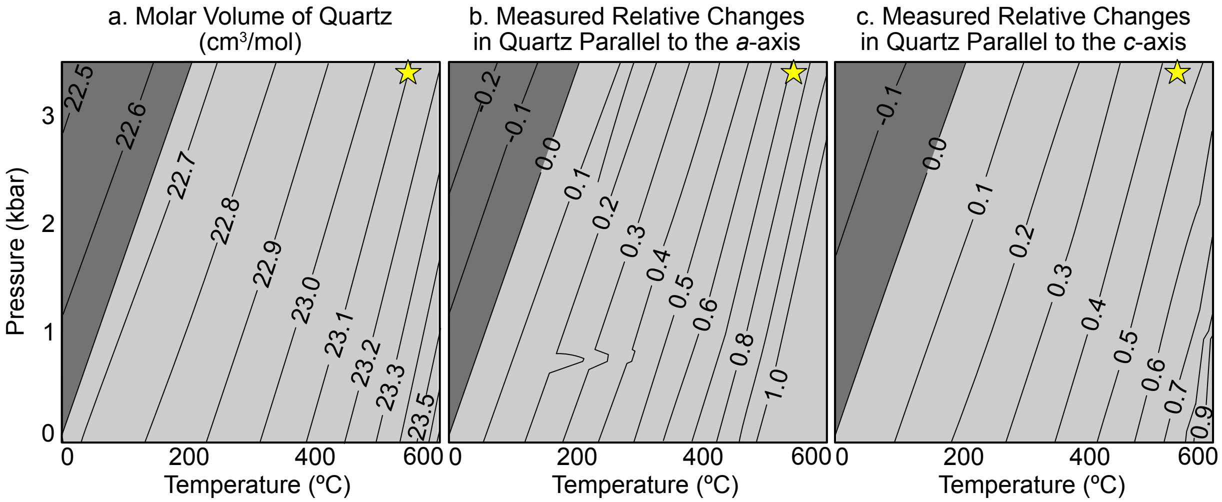

Figure 2.6. **Molar volume and relative lengths of the *a*- and *c*-axes of quartz over the *P-T* range of interest.** All data are from Raz et al., (2002). Star represents peak *P-T* conditions of PF77. Dark gray shading (left side of *P-T* diagram) represents *P-T* space in which the molar volume of quartz and relative length of *a*- and *c*-axes are *less* at elevated *P-T* conditions than at 25ºC and 1 bar (volume increase during exhumation). Light gray shading (right side of *P-T* diagram) represents 'area' of *P-T* space in which the molar volume of quartz and relative length of *a*- and *c*-axes are *greater* at elevated *P-T* conditions than at 25ºC and 1 bar (volume decrease during exhumation). (a) Molar volume of quartz. (b) Relative changes (percent) in length

(compared to length at 25ºC and 1 bar) of a quartz crystal measured parallel to the *a*-axis. (c) Relative changes (percent) in length of a quartz crystal measured parallel to the *c*-axis.

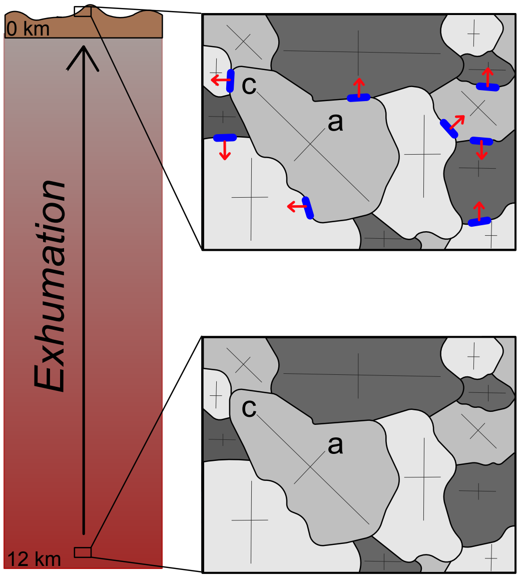

Figure 2.7. **Schematic diagram** (not to scale) showing how grain boundary voids may open during exhumation of a quartzite. Anisotropic contraction of quartz during exhumation results in greater decrease in the length of the *a*-axis than the *c*-axis (shown by red arrows). This preferentially opens void space at grain boundaries adjacent to specific crystal orientations, as shown in blue.

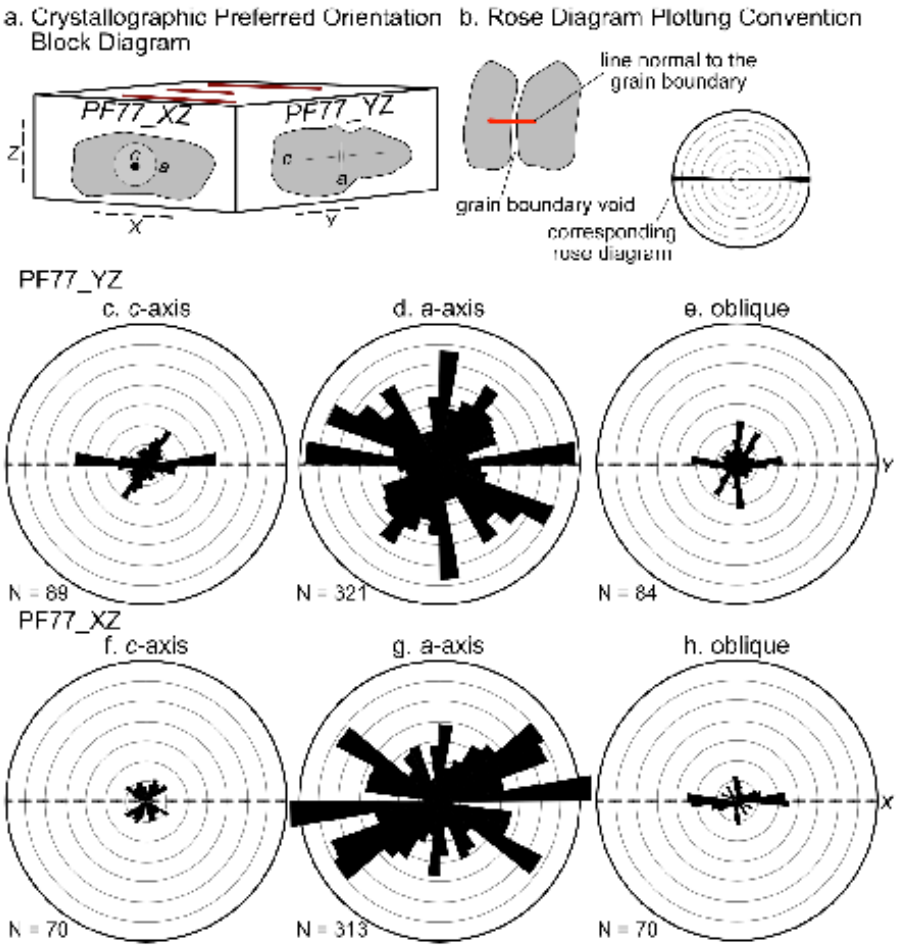

Figure 2.8. **Poles to grain boundary void spaces plotted on rose diagrams.** All rose diagrams have the same scale in which circles of increasing diameter represent 5, 10, 15 .. 35 grain boundary voids. (a) Orientation of the majority of quartz crystals in PF77_YZ and PF77_XZ (c-axes oriented parallel to sample Y direction and associated a-axes lying in basal crystal plane oriented parallel to sample XZ plane; cf. Fig. 3e), plotted on a block diagram with *a-axes* and *c*-axes of each crystal noted. (b) Rose diagram plotting convention showing a schematic of a grain boundary void space, the line normal to the grain boundary, and the corresponding rose diagram line for that void space. (c-e) Orientation of voids normal to the *c*-axis*,* *a*-axis, and oblique to all major crystallographic axes of quartz in YZ section plane; sample Y direction is horizontal in

each rose diagram. (f-g) Orientation of voids normal to the *c*-axis*, a*-axis, and oblique to all major crystallographic axes of quartz in XZ section plane; sample X direction is horizontal in each rose diagram.

## 3.10 TABLES

Table 3.1. Number of void spaces correlating with orientation of quartz grains compared to a random distribution of void spaces, and $X^2$ statistical test calculation.

| Orientation (color) | Observed Frequency (measured) | Expected Frequency (random distribution) | $X^2$ Value |
|---|---|---|---|
| ***Sample PF77_YZ*** | | | |
| a axis (red) | 321 | 110 | 406 |
| c axis (green) | 89 | 55 | 21 |
| None (white) | 84 | 329 | 183 |
| Total | 494 | 494 | 610 |
| ***Sample PF77_XZ*** | | | |
| a axis (red) | 313 | 98 | 472 |
| c axis (green) | 58 | 49 | 2 |
| None (white) | 70 | 294 | 171 |

| | | | |
|---|---|---|---|
| Total | 441 | 441 | 644 |

Table 3.2. Sensitivity test for changing the expected distribution and resulting $X^2$ statistic

| Orientation (color) | Observed Frequency (measured) | Expected Frequency (random distribution) | $X^2$ Value | |
|---|---|---|---|---|
| ***Sample PF77_YZ $X^2$ Test #1: within 10º of c axis, within 20º of a/m axis*** | | | | |
| a/m axis (red) | 321 | 110 | 406 | |
| c axis (green) | 89 | 55 | 21 | |
| None (white) | 84 | 329 | 183 | |
| Total | 494 | 494 | 610 | Calculated $X^2$ > Critical $X^2$ |
| ***Sample PF77_YZ $X^2$ Test #2: within 10º of c axis, within 10º of a/m axis*** | | | | |
| a/m axis (red) | 321 | 55 | 1290 | |
| c axis (green) | 89 | 55 | 21 | |
| None (white) | 84 | 384 | 235 | |
| Total | 494 | 494 | 1546 | Calculated $X^2$ > Critical $X^2$ |
| ***Sample PF77_YZ $X^2$ Test #3: within 20º of c axis, within 10º of a/m axis*** | | | | |
| a/m axis (red) | 321 | 55 | 1290 | |

| | | | | |
|---|---|---|---|---|
| c axis (green) | 89 | 110 | 4 | |
| None (white) | 84 | 329 | 183 | |
| Total | 494 | 493 | 1477 | Calculated $X^2$ > Critical $X^2$ |

***Sample PF77_YZ $X^2$ Test #4: within 20° of c axis, within 20° of a/m axis***

| | | | | |
|---|---|---|---|---|
| a/m axis (red) | 321 | 110 | 406 | |
| c axis (green) | 89 | 110 | 4 | |
| None (white) | 84 | 274 | 132 | |
| Total | 494 | 494 | 542 | Calculated $X^2$ > Critical $X^2$ |

***Sample PF77_YZ $X^2$ Test #5: within 5° of c axis, within 5° of a/m axis***

| | | | | |
|---|---|---|---|---|
| a/m axis (red) | 321 | 27 | 3140 | |
| c axis (green) | 89 | 27 | 138 | |
| None (white) | 84 | 439 | 287 | |
| Total | 494 | 494 | 3565 | Calculated $X^2$ > Critical $X^2$ |

# Chapter 4: The (Chemical) Potential for Understanding Overstepped Garnet Nucleation and Growth

Nagurney, A.B.[1], Caddick, M.J.[1], Dragovic, B.[2], Busse, K.M.[3]

[1] *Department of Geosciences, Virginia Tech, 926 West Campus Drive, Blacksburg, VA, 24060 USA,* [2] *School of Earth, Ocean, and Envirnment, Unviersity of South Carolina, 700 Sumter Street, Columbia, SC 29208, USA,* [3]*ExxonMobil 22777 Springwoods Village Parkway, Spring, TX, 77389, USA*

This chapter is *In Press* (2021) at American Mineralogist).

https://doi.org/10.2138/am-2020-7354

## 4.1 ABSTRACT

Overstepping of porphyroblast-forming reactions has been shown to occur in regional, contact, and subduction zone metamorphism, calling into question the paradigm that metamorphic mineral reactions occur at or very close to thermodynamic equilibrium. These overstepped reactions result from the fact that nucleation and growth of new phases requires a thermodynamic driving force, or a *departure* from equilibrium. We use phase equilibria modeling to elucidate the energetic consequences of overstepped garnet nucleation and growth by comparing the chemical potentials of garnet-forming oxide components (MnO, CaO, FeO, MgO, $Al_2O_3$) in two sets of calculations: one in which Gibbs free energy is minimized and one in which the minimization proceeds under identical conditions but in the forced absence of garnet. We focus on twelve examples from the literature which have previously described garnet nucleation as minimally overstepped (garnet nucleation at the *P-T* of initial garnet stability) or garnet nucleation as more substantially overstepped (garnet nucleation at *P-T* conditions greater than initial garnet stability). For a small *P-T* interval above nominal garnet-in reactions, differences in the chemical potentials between the two calculations are commonly minimal. In all tested examples calculated using two versions of the THERMOCALC thermodynamic dataset, the chemical potential of $Al_2O_3$ ($\mu_{Al2O3}$) diverges between garnet-bearing and garnet-absent calculations at greater *P-T* conditions than that of MnO, CaO, FeO and MgO. The *P-T* interval between thermodynamic garnet-in and the point at which $\mu_{Al2O3}$ differs substantially between the two sets of calculations appears to be a function of bulk-rock MnO content, reemphasizing the role that small quantities of MnO play in the apparent stability of garnet in calculated phase equilibria. These results highlight the importance of considering multiple thermodynamic datasets, the location of the garnet-in curve, and the abundance of mineral phases in the

discussion of overstepped metamorphic reactions. The results have implications for determining kinetic barriers to crystal nucleation and growth, and considering the most appropriate way of defining ‘garnet-in’ for samples that have experienced overstepping.

## 4.2 INTRODUCTION

The equilibrium paradigm in metamorphic petrology, in which minerals and fluids continually react with changing pressure (*P*) and temperature (*T*) to achieve the lowest possible Gibbs free energy configuration, has resulted in many significant advances in our understanding of metamorphic and tectonic processes (e.g. Thompson 1957; Essene 1982; Spear and Selverstone 1983; Powell et al. 1998; Kerrick and Connolly 2001; White and Powell 2002; Hacker et al. 2003). Within this paradigm, if the stability of a new phase would decrease the Gibbs free energy (*G*) of the system following a change in *P* and *T* conditions, the departure from equilibrium needed to form that new phase is considered to be negligible and it will nucleate and grow without kinetic barriers. This assumption of equilibrium is consistent with the metamorphic facies principle (Eskola 1915, 1920), which led to the interpretation of evolving metamorphic conditions using natural mineral compositions and textural information, and facilitated the integration of metamorphic constraints within a tectonic framework. However, recent examples have highlighted rocks in which it appears that deviations from the equilibrium state may have been substantial (>50ºC and >1 kbar), (e.g. Dragovic et al. 2012; Spear et al. 2014; Wolfe and Spear 2018).

Overstepped reactions, typically identified in the metamorphic rock record as cases in which the initial occurrence of a mineral appears to have been at *P-T* conditions significantly greater than its thermodynamically-defined initial stability, have been well-documented (e.g. Ridley and Thompson 1986; Chernoff and Carlson 1997, 1999; Waters and Lovegrove 2002;

Zeh and Holness 2003; Wilbur and Ague 2006; Pattison and Tinkham 2009; Pattison et al. 2011; Ague and Carlson 2013; Spear et al. 2014; Carlson et al. 2015a; Castro and Spear 2016; Spear and Wolfe 2018). An alternative observation, of the persistence of phases such as chloritoid, garnet and staurolite beyond the nominal *P-T* limit of their stability, can also be made but is less commonly associated with 'reaction overstepping' (Waters and Lovegrove 2002; Pattison and Tinkham 2009; Pattison & Spear 2018). Broadly, overstepped reactions in the rock record are interpreted to be a consequence of the fact that while pressure, temperature, and bulk composition are the primary controls on metamorphic paragenesis, kinetic impediments to the nucleation of minerals in metamorphic rocks may be substantial and significant (e.g. Ridley and Thompson 1986; Rubie 1998).

The degree of reaction overstepping depends partly on the free energy change of the reaction which, if controlled by temperature, is directly related to its entropy ($S$) (e.g. Fyfe et al. 1958; Ridley and Thompson 1986; Pattison and Tinkham 2009; Pattison et al. 2011). This suggests that devolatilization reactions with a significant change in entropy ($\Delta S_{\mathrm{rxn}}$) should experience 'smaller temperature oversteps' than solid-solid reactions with relatively smaller $\Delta S_{\mathrm{rxn}}$ (Ridley and Thompson 1986). However, it appears from comparisons of calculated phase equilibria with natural samples that despite commonly forming from high entropy devolatilization reactions involving breakdown of chlorite, micas, and amphiboles, the nucleation of garnet is frequently overstepped. This has been observed in rocks from contact (e.g. Waters and Lovegrove 2002; Pattison and Tinkham 2009), regional (e.g. Spear et al. 2014; Wolfe and Spear 2017), and subduction (e.g. Dragovic et al. 2012, 2015; Castro and Spear 2016) metamorphic settings and contrasts with other cases in which maintenance of rock-wide thermodynamic equilibrium has been well-demonstrated (e.g. George and Gaidies 2017).

Improved understanding of the conditions and kinetics of garnet nucleation and growth is necessary because garnet is a useful mineral for understanding prograde to peak metamorphic processes. This follows in part from its stability over a wide range of protolith compositions, possible crustal and mantle *P-T* conditions, and from the compositional variations that it and accompanying phases experience during evolving metamorphic conditions, hence its extensive application in quantitative thermobarometry (e.g. Tracy et al. 1976; Ghent 1976; Ferry and Spear 1978; Hodges and Spear 1982; Spear and Selverstone 1983; Spear et al. 1984; St-Onge 1987; Florence and Spear 1991; Konrad-Schmolke et al. 2006; Caddick and Thompson 2008; Moynihan and Pattison 2013). As garnet can also be dated isotopically, this improved understanding can potentially lead to better determination of the rates of tectonic processes (Duchêne et al. 1997; Scherer et al. 2000; Pollington and Baxter 2010; Baxter and Scherer 2013; Dragovic et al. 2015; Baxter et al. 2017; Seman et al. 2017) These examples highlight the importance of making accurate predictions about the likely departures from equilibrium preserved in garnet crystals from a variety of settings.

Here, we study metapelitic samples in which previous work has identified that garnet nucleation and growth were overstepped to varying extents, from minimally (i.e. crystals record evidence of growth at approximately the conditions of thermodynamically calculated garnet-in curves for that bulk-rock composition) to more significantly (i.e. initial growth several tens of degrees hotter or several kbars pressure higher than calculated garnet-in). For each sample, we initially calculate the energetic differences between a thermodynamic system in which we minimize free energy and a system that is otherwise identical but in which we prohibit garnet stability. We then examine the differences in the calculated chemical potentials of thermodynamic components (MnO, CaO, FeO, MgO, $Al_2O_3$) between the garnet-present and garnet-absent systems. Our work aims to reveal some of the macro-energetic consequences of overstepped garnet nucleation and growth, while also highlighting possible factors that lead to apparently overstepped metamorphic reactions in pseudosection calculations.

## 4.3 THEORETICAL BACKGROUND

### 4.3.1 Processes of Crystallization

Several sequential and simultaneous processes are required in order for a metamorphic crystal to nucleate and grow. These can be summarized as: i) breakdown of reactant phases to liberate nutrient components; ii) transport of these nutrients through the intergranular medium, typically in solution within grain boundary fluids but also through solid-state diffusion; iii) homogenous or heterogeneous crystal nucleation; iv) crystal growth via the attachment of atoms or molecules onto the crystal nucleus or surface (e.g. Kretz 1966, 1974; Carmichael 1969; Fisher 1978; Walther and Wood 1984; Ridley and Thompson 1986; Rubie 1986; Carlson 1989, 2011). Each of these processes is inherently complex in natural rocks, but can be understood through the application of appropriate simplifications and rate laws (e.g. Wood and Walther 1983; Walther and Wood 1984; Lasaga 1986; Ridley and Thompson 1986; Lasaga and Rye 1993; Rimstidt 2014). Although these steps most likely coincide in a rock matrix (Carlson 2011), failure of any one of the processes can lead to a (temporary) absence of the product mineral within the rock mass. Sustained failure of one or more of these processes over metamorphic timescales can lead to apparent reaction overstepping, in which an otherwise thermodynamically stable mineral at a given $P$ or $T$ is absent.

Classical views of crystallization in geologic environments include the homogeneous nucleation model, wherein nuclei form via interactions between atoms in solution (Christian 1975). In metamorphic rocks it may be more appropriate to consider heterogeneous nucleation, wherein nuclei develop on pre-existing substrates, thereby lowering interfacial energy (Nielsen 1964; Mullin 1992). Regardless of the nucleation mechanism, a specific molecular cluster size is necessary for a nucleus to mature into an energetically stable crystal. This nucleation step thus exerts a finite requirement on the amount of overstepping for any given reaction (Ridley and Thompson 1986). Few studies have directly quantified the energies required for nucleation in metamorphic rocks (e.g. Rubie et al. 1990; Hacker et al. 1992; Liu and Yund 1993; Rubie 1998; Milke and Heinrich 2002). However, several previous studies have focused on calculating macroscale (rock-wide) energetic differences between rocks containing a particular mineral, typically garnet, and rocks at the same *P*-*T* but lacking that phase (e.g. Waters and Lovegrove 2002; Pattison and Tinkham 2009; Pattison et al. 2011; Spear et al. 2014; Castro and Spear 2016).

Crystal growth can proceed after this nucleation step, with the rate of growth subject to several criteria. Crystal growth rate can be controlled by element supply, itself a function of reactant mineral breakdown and transport dynamics (i.e. by a diffusion control) or by the energetics of attachment (i.e. by an interface control). Again, each of the processes can be rate-limiting, with a high probability that each one dominated the evolution of some rocks, but played a smaller role in others. Furthermore, one process may be rate-limiting for large parts of the metamorphic history of a rock, but may proceed rapidly during certain phases of crystallization.

For the case of diffusion control, the mobility of the slowest diffusing crystal-building component is likely to control the kinetics and spatial distribution of crystal growth. For example, the local availability of aluminum has been hypothesized as a barrier to garnet crystal growth (e.g. Carmichael 1969; Carlson 2002, 2011; Ketcham and Carlson 2012; Kelly et al. 2013a, 2013b). This is a complex function of the heterogeneous distribution of aluminum in the protolith matrix and the limited solubility of aluminum-bearing species in geologic fluids on grain boundaries (e.g. Manning 2007; Newton and Manning 2007; Carlson 2010, 2011; Carlson et al. 2015b). Such diffusion controlled growth can lead to spatially-ordered porphyroblast distributions (e.g. Hirsch et al. 2000, Carlson 2011; Ketcham & Carlson 2012; Kelly et al. 2013a,b).

In the interface controlled case, the rate of attachment of individual atoms on to the surface of growing crystals controls the net rate of crystal growth (Carlson 2011; Gaidies et al. 2011). The equal availability of nutrients throughout the rock matrix at any given time will result in uniform growth rates and compositional zoning of crystals within a population (Ague and Carlson 2013), with resulting rock textures exhibiting near-random distributions of porphyroblasts (Carlson 2011; Gaidies et al. 2015).

## Application of Equilibrium Thermodynamics to Metamorphic Rocks

Gibbs free energy calculations for metamorphic rocks have helped develop our understanding of the evolution of the Earth's lithosphere. Experimental and empirical constraints on activity-composition (*a-X*) models for minerals and fluids have been integrated with datasets of end-member thermodynamic properties (e.g. Berman 1988; Holland and Powell 1998, 2003, 2004, 2011, Powell et al. 1998, 2014; White et al. 2014; Green et al. 2016). Coupled with thermodynamic modeling software, this has resulted in the widespread calculation of pseudosections (or isochemical phase diagrams) to reveal stable mineral assemblages, abundances, and compositions over a range of metamorphic *P-T* conditions. Comparisons of calculated phase equilibria with natural samples have resulted in a deeper understanding of the *P-T* evolution of metamorphic rocks (e.g. Spear 1993; Tinkham and Ghent 2005; Konrad-Schmolke et al. 2006; Gaidies et al. 2008; Groppo et al. 2009), but have also revealed some challenges to the assumption of whole-rock chemical equilibrium (e.g. Pattison et al. 2011; Guevara and Caddick 2016; Palin et al. 2016; Lanari and Engi 2017; Spear and Wolfe 2018).

Multiple approaches have been proposed for better understanding the development of rocks experiencing deviations from true thermodynamic equilibrium and calculating the compositions of newly-formed phases that will grow after a period of overstepping. This follows from the acknowledgement that the nucleation of new minerals requires departures from thermodynamic equilibrium and energetic driving forces for nucleation (e.g. Rumble 1976; Joesten 1977; Powell 1978). This energetic driving force, or reaction affinity, can be calculated by comparing the energetics of systems containing and prohibiting the stability of a particular phase at a given *P* and *T* (e.g. Pattison et al. 2011; Carlson et al. 2015a). There are three general approaches to calculating the energetics of systems in which the stability of a phase is prohibited. First, one can assume that all other phases in the rock freely equilibrate to the composition that results in the lowest Gibbs free energy of that system and that the composition of garnet grown following an overstep is the same as the equilibrium composition of garnet at that *P-T* condition if overstepping had not occurred (described as the 'Method 1' calculation of reaction affinity by Pattison et al. (2011)). A second assumption is that the matrix is entirely unreactive in the region of overstepping, so that the compositions of all phases in the rock are fixed in the overstepped interval (Method 2 of Pattison et al. (2011)). A third intermediate approach, often termed the parallel tangent method, is to assume that the compositions of matrix phases can change in the overstepped-region but that the composition of garnet that would grow following overstepping is that which would lower the chemical potential of each thermodynamic component equally (Method 3 of Pattison et al. (2011)).

### 4.3.2 Challenges Associated with Applying Equilibrium Thermodynamics to Metamorphic Rocks

Current challenges associated with phase equilibria modelling include: i) making appropriate choices about bulk rock composition and equilibration volume, ii) ascribing appropriate uncertainties to results, and iii) determining the best way to quantify the *P-T* conditions at which minerals nucleate. Careful consideration of 'effective bulk compositions' (Tracy 1982) can help to reduce some of the disparities between calculated rock assemblages and the natural rock record. This is typically implemented by modifying measured rock compositions to remove unreactive phases (e.g. Spear 1988; Marmo et al. 2002; Evans 2004; Konrad-Schmolke et al. 2005; Zuluaga et al. 2005; Caddick et al. 2007; McCarron et al. 2019), by progressively modifying assumed length-scales of chemical equilibrium and calculating 'local compositions' accordingly (e.g. Guevara and Caddick 2016; Lanari and Engi 2017), or by modifying bulk composition so that appropriate mineral compositions are calculated at *P-T* conditions that have been independently constrained (Spear and Wolfe 2018). Each of these calculation methods involves its own set of assumptions about the length scale of equilibrium, reactivity of phases, and transport of material, and will likely result in a different effective bulk composition. Additionally, the choice of equilibration volume and method for determining the bulk composition (the geologic uncertainty) leads to uncertainties in the calculated equilibria (Palin et al. 2016). Finally, there are uncertainties associated with the mineral and fluid end-members and *a-X* models involved in a calculation (Powell and Holland 2008). The propagated uncertainty on the size and position of each calculated mineral assemblage field, and on the abundances and compositions of co-existing phases, depends on the uncertainties on each calculated phase, and is still poorly quantified in most cases.

Several methods have been used to determine the *P-T* of garnet nucleation from phase equilibria, with each method having its own benefits and challenges. First, the composition of garnet calculated in a pseudosection at any *P-T* may be assumed to relate directly to the composition of garnet that would exist in a natural rock at that *P-T* condition. Thus isopleths calculated for garnet compositions measured from natural crystal cores (expressed as $X_{\mathrm{alm}}$, $X_{\mathrm{sps}}$, $X_{\mathrm{grs}}$, $X_{\mathrm{pyp}}$) are thought to reveal the *P-T* of early garnet growth (e.g. Tinkham and Ghent 2005), in what we hereafter refer to as the 'garnet core isopleth intersection' method. This method has been widely used, but has been questioned for cases in which elastic thermobarometry on inclusions in garnet imply trapping at *P-T* conditions well above those of initial garnet stability in a pseudosection (e.g. Spear et al. 2014; Castro and Spear 2016).

Alternatively, the parallel tangent method has been proposed as a more appropriate way to determine the conditions of garnet nucleation following overstepping, by calculating the garnet composition which would lead to the greatest reduction of Gibbs free energy following a defined interval of overstepping (Thompson and Spaepen 1983; Hillert and Rettenmayr 2003; Hillert 2008; Gaidies et al. 2011; Pattison et al. 2011; Spear et al. 2014). In this case, it is assumed that the chemical potentials of each garnet-forming thermodynamic component would be reduced by the same amount upon garnet nucleation, solving to find the garnet composition at a given *P* and *T* that would achieve this. This method has currently been applied to few samples (rocks from the Sikkim, Himalaya, Sifnos, Greece, the Eastern Vermont terrane, and the Nelson Aureole: Gaidies et al. 2011; Pattison et al. 2011; Spear et al. 2014; Castro and Spear 2016; George and Gaidies 2017; Spear and Wolfe 2018; Wolfe and Spear 2018), and it is unclear how well a methodology that was derived to study homogeneous nucleation in binary metallic melts

(Thompson and Spaepen 1983) translates to heterogenous nucleation in metamorphic rocks (see Gaidies et al. 2011 for a discussion on some of the challenges of this method).

With careful consideration of the associated challenges, equilibrium-based thermodynamics can be utilized to study the energetic consequences of overstepped garnet nucleation and growth. Here, we use equilibrium thermodynamics to elucidate the way that the chemical potentials of rock forming components are affected by the failure of garnet to nucleate. We show that chemical potentials of each garnet-forming component behave differently between a garnet-present and garnet-absent phase equilibria calculation. While previous works have used calculated chemical potential gradients to study metamorphic textures (e.g. White et al. 2008; Stipska et al. 2010; Powell et al. 2019), we stress that our phase equilibria calculations do not reveal anything about the atomistic mechanisms of crystal nucleation and growth in natural rocks. Instead, by studying the evolution of chemical potential by the failure of garnet to nucleate and grow, we can explore the role that each component has on the energetics of the system.

## 4.4 CHOICE OF SAMPLES

We use twelve well-described samples from the literature that have been shown to have experienced various extents of overstepping of garnet-in reactions. Five representative examples are described in detail in the main text. Details of the remaining seven are presented as Supplemental Material, with their results summarized in the main text. For detailed descriptions of the geologic setting for each of these samples, the reader is directed to the original studies describing the samples. The apparent *P-T* of garnet nucleation and previously reported extent of overstepping for each of these samples are summarized in Table 1.

### 4.4.1 Examples with Minimal Overstepping (<10ºC and 0.5 kbar)

Sample 24-99 is a sample from the garnet zone of the Lesser Himalaya in Sikkim (Dasgupta et al. 2009; Anczkiewicz et al. 2014; Gaidies et al. 2015; George and Gaidies 2017; George et al. 2018). Previous work suggests that the *P-T* of garnet nucleation (determined by garnet core isopleths) occurred at the garnet-in curve, (Gaidies et al. 2015) and subsequent calculations of the *P-T* of garnet nucleation using the parallel tangent method determined an overstep of <10ºC and 0.4 kbar (George and Gaidies 2017), indicating that the departure from equilibrium during garnet nucleation was negligible.

Sample 35F03 is from the Rappold Complex of the Austroalpine Crystalline Basement of the eastern European Alps (Gaidies et al. 2008). Previous work on this sample suggested that the *P-T* of garnet nucleation (determined by the intersection of garnet core isopleths) occurred at or close to the *P-T* of initial garnet stability, suggesting minimal overstepping (Gaidies et al. 2008).

Additional samples (described in more detail Supplemental Material Part I) that experienced little apparent overstepping are W122, from the Danba Structural Culmination of eastern Tibet (Weller et al. 2013) and DM_06_128 from the Kootenay Arc of British Columbia (Moynihan and Pattison 2013).

### 4.4.2 Examples with Apparent Overstepping (>10ºC and 0.5 kbar)

Sample TM549a is from the eastern flank of the Strafford Dome in the regional Barrovian sequence of eastern Vermont, and has been cited as providing evidence that overstepping may be important in regional metamorphic terranes (Spear et al. 2014). Thermo-barometric constraints for TM549a indicate that garnet nucleation occurred at 450-500ºC and 4-5 kbar (Menard and Spear 1994). Spear et al. (2014) used quartz-in-garnet barometry to determine the entrapment pressure of quartz inclusions in garnet cores, calculating an isochore extending from 440ºC at 6.7 kbar to 580ºC at 9.0 kbar, contrasting significantly with the earlier thermo-barometric results. While these varying *P-T* estimates lead to different interpretations of the amount of overstepping of the garnet-in reaction, Spear et al. (2014) quantify the overstepping of the garnet nucleation to be 10ºC and 0.6 kbar.

Sample AV26A is from the Pomfret Dome, southeastern Vermont (Bell et al. 2013). It formed during the Appalachian Taconic Orogeny, when over-thrusting of thick tectonic sheets resulted in porphyroblast nucleation at 550ºC and 8.0 kbar, consistent with 30ºC and 1.5 kbar of overstepping (Bell et al. 2013). Analysis of inclusion trail geometries reveals that garnet only nucleated and grew during the start of crenulation-forming deformation events and nucleation was controlled by microlithologic domains developed during deformation (Bell et al. 2013).

Sample 93-CW-4 is from the Nelson Contact Aureole, British Columbia (Pattison and Vogl 2005; Tomkins and Pattison 2007; Pattison and Tinkham 2009; Gaidies et al. 2011; Pattison et al. 2011). Closely-spaced mineral isograds and chemical zoning in garnet suggest that garnet nucleation was delayed until the rocks reached temperatures coincident with the stability of higher-grade porphyroblasts (staurolite and andalusite; Pattison and Tinkham 2009). Garnet nucleation was initially calculated to be overstepped by 30ºC (Pattison and Tinkham 2009). Gaidies et al. (2011) reported overstepping of 6-17ºC, which equates to the maximum driving force for garnet nucleation occurring at 545ºC and 3.5 kbar, the *P-T* conditions of nucleation that we use in this study.

Additional samples experiencing apparent overstepping (described in Supplemental Material Part I) are 12TM16 from the Grenvillian Flinton Group of southeastern Ontario (McCarron et al. 2014), ED34 from the Menderes Massif of southwest Turkey (Etzel et al. 2019), D13-75 from the Central Himalayan metamorphic core (Iaccarino et al. 2017), TH203B from the Albion Mountains of Idaho (Kelly et al. 2015), and SSFM307-7G from the Funeral Mountains, California (Craddock Affinati et al. 2020).

## 4.5 METHODS

### 4.5.1 Calculation of Phase Equilibria

Equilibrium mineral assemblages were re-calculated for these samples, using the thermodynamic modeling program Perple_X, version 6.8.3 (Connolly 1990, 2005). Calculations initially used the 'ds5.5' update to the Holland and Powell (1998) internally consistent dataset and the following solution models: biotite (Powell and Holland 1999), chlorite (Holland et al. 1998), chloritoid, garnet, staurolite (Holland and Powell 1998), ilmenite (ideal), muscovite (Coggon and Holland 2002), and plagioclase (Fuhrman and Lindsley 1988). ds5.5 was used to maintain consistency with the original literature, with phase equilibria for all but one of the samples that we study here originally calculated with ds5.5. The only exception is Eastern Vermont sample TM549a (Spear et al. 2014), with the original calculations using the modified thermodynamic dataset from Spear and Pyle (2010). We also recalculated five examples using the updated 'ds6.2' (Holland & Powell 2011) and *a-X* models from (White et al. 2014a), to compare the effects of thermodynamic data on pseudosection topologies and $\Delta\mu_{\text{component}}$ calculations. While several comparisons between ds5.5 and revised dataset ds6.2 are now available (White et al. 2014a; Pattison and DeBuhr 2015; Guevara and Caddick 2016; Lanari and Duesterhoeft 2019; Waters 2019; Starr et al. 2020), additional comparison is useful here, as it will shed light on whether the chemical potential trends that we observe above are applicable more broadly, or are artifacts of the specific *a-X* models chosen. The bulk composition and garnet core compositions for all samples are listed in Supplemental Material Part II.

Calculations utilized the chemical system MnO–$Na_2O$–CaO–$K_2O$–FeO–MgO–$Al_2O_3$–$SiO_2$±$TiO_2$, with $H_2O$ in excess. $TiO_2$ was only included when deemed appropriate by the authors of the original works, in an attempt to maintain consistency. Ferric iron content was not reported in the source papers for any of these samples, so all iron was considered ferrous.

Two pseudosections were calculated for each sample. We first calculated the lowest possible free energy mineral-fluid configuration (i.e. a conventional pseudosection), hereafter termed the true equilibrium calculation or TEC and shown in Figure 1A for a hypothetical sample. This found the identity, abundances and compositions of stable phases as a function of *P* and *T* (see methodology in Connolly and Kerrick 1987; Connolly 1990, 2005). We then recalculated phase equilibria using the same input data, but prohibiting the stability of garnet by excluding its end-members. This calculation, defined here as the Metastable Calculation (MSC) and shown in Figure 1B, involves the assumption that in the forced absence of garnet stability, all other phases will react to reach an alternate lowest Gibbs free energy configuration of the system. As seen in Figure 1B (and in all cases described below), at the *P-T* conditions at which the garnet core isopleths intersect, the only difference in the mineral assemblages between the TEC and MSC is the lack of garnet in the MSC. At temperatures substantially above garnet-in in the TEC, additional differences in mineral assemblage do occur, but these *P-T* regions are not relevant to this study.

### 4.5.2 Chemical Potential Calculations

Chemical potentials ($\mu_{\text{component}}$) define the compositional dependence of the Gibbs free energy and are calculated here to understand the energetic consequences of the failure of garnet to nucleate at garnet-in (defined as the curve in *P-T* space along which garnet first appears in the TEC). At any *P-T* point, a Gibbs free energy versus composition (*G-X*) diagram can be used to visualize stable mineral assemblages (Figure 1C; Gibbs 1928; Joesten 1977; Powell 1978; Spear 1993), with the lowest energy tangent line determining the stable phases at that condition (e.g. Phase X and Phase Z in Figure 1C). The chemical potential of each component can then be defined by the intersection of the tangent with the Y-axes (Figure 1C; Gibbs 1928; Joesten 1977; Powell 1978; Spear 1993). This can be extended to three or more dimensions, with the number of stable phases and chemical potentials increasing accordingly (e.g. Figure 1D).

Chemical potentials were extracted from the Perple_X output for the TEC and MSC of each sample. The differences in chemical potentials between the TEC and MSC at a range of *P* and *T* conditions were then calculated, e.g. for MgO:

$$\Delta\mu_{MgO} = \mu_{MgO}{}^{TEC} - \mu_{MgO}{}^{MSC} \quad (1)$$

Figure 1E shows variations in $\Delta\mu_{component}$ versus temperature for the theoretical example in Figure 1A-B along a simple 1-D burial and heating path (shown in Figure 1A). As in all examples described below, the *P-T* path was determined by defining the shortest possible path between garnet-in in the TEC and the *P-T* point at which garnet core isopleths intersect in that diagram. This provides a consistent method for determining the *P-T* path for each sample. At *P-T* conditions below initial garnet stability in the TEC (515ºC and 4.1 kbar), both calculations are energetically identical, so $\Delta\mu = 0$ for all components (Figure 1E). At greater *P* and *T*, garnet is stable in the TEC but absent in the MSC, so the two systems have increasingly different energetic configurations. In Figure 1E, $\mu_{MnO}$, $\mu_{CaO}$, and $\mu_{FeO}$ become increasingly negative towards greater *T*, implying that the partial molar free energy of MnO, CaO, and FeO, is lowered by the stability of garnet in the TEC. A positive $\Delta\mu_{component}$, as is the case for MgO in Figure 1E, would imply that the partial free energy of that component is increased by the stability of garnet in the TEC. If $\Delta\mu_{component}$ is zero at any condition greater than initial garnet stability in the TEC, as is the case for $\Delta\mu_{Al2O3}$ up to 550ºC & 4.5 kbar in Figure 1E, then one would infer that the partial free energy of that component in that system is not affected by the stability of garnet. $\Delta\mu_{Na2O}$, $\Delta\mu_{K2O}$, and $\Delta\mu_{TiO2}$ also experience a deviation upon initial garnet stability in the TEC, but are not discussed further here.

Calculated mineral assemblage fields, phase abundances and phase compositions are all subject to propagated uncertainties on thermodynamic data and bulk compositions (Powell & Holland 2008; Palin et al. 2016). However, each of our calculations use the same mineral end-members and thermodynamic data, so some of the absolute errors cancel, and the relative uncertainty between the TEC and MSC for each example is regarded as small (Hodges and McKenna 1987; Powell and Holland 2008; Palin et al. 2016; Hernández-Uribe and Palin 2019). Thus, the uncertainties on chemical potentials calculated from the TEC and MSC for each sample calculated in each dataset would also result in a small relative uncertainty.

### 4.5.3 Garnet Composition Calculation

Our calculations follow Method 1 of Pattison et al. (2011), determining the energetics associated with the failure of garnet to nucleate by comparing two possible equilibrium systems. The *P-T* conditions of garnet nucleation were constrained by the intersection of isopleths in the TEC calculation, for the purpose of simple comparison with the source papers in which these samples were originally described. Use of the parallel tangent method would instead lead to the calculation of different garnet compositions following overstepping, likely leading to larger apparent oversteps (Pattison et al. 2011; Spear et al. 2014; George and Gaidies 2017). Relevant data for the calculation of the trapping conditions of inclusions in garnet are generally lacking for the samples in this study.

It is important to be able to equate measured garnet crystal core compositions with the composition with which garnet first grew. In three of the samples that we use, garnet core compositions were specifically taken from the centers of the carefully-chosen largest garnet crystals in the rock matrix (Rappold Complex Sample 35E03 from Gaidies et al. (2008); Sikkim Sample 24-99 from Gaidies et al. (2015); Nelson Aureole Sample 93-CW-4 from Gaidies et al. (2011)). In the other examples, we have to assume that the garnet crystals were near-centrally sectioned. We also assume that minimal diffusional modification occurred during or after garnet growth, which is probably appropriate for these samples that reached no greater than low-to-mid amphibolite facies conditions (e.g. Yardley 1978).

## 4.6 RESULTS

Results for all twelve samples calculated with ds5.5 are summarized in Table 2. Comparisons between the published pseudosections, our recalculations, and the rock samples are described in Supplemental Material Part III and differences are minor. Samples 24-99 (Sikkim, Himalaya), 35F03 (Rappold Complex), AV26A (Pomfret Dome, Vermont), TM549A (Eastern Vermont), and 93-CW-4 (Nelson Aureole) are described in detail below, with samples W122 (Eastern Tibet), DM_06_128 (Kootenay Arc), 12TM16 (Southeastern Ontario), ED34 (Southwest Turkey), D13-75 (Central Himalaya), TH203B (Albion Mountains), and SSFM307-7G (Funeral Mountains), described in Supplemental Material Part IV (Supplemental Figures 1-7).

Results for the five samples calculated with ds6.2 are summarized in Table 3. Comparisons of pseudosections calculated with ds5.5 and ds6.2 are highlighted below for three examples: Sikkim, Pomfret Dome, and Nelson Aureole. Two additional examples (Rappold Complex and Eastern Vermont) and a discussion of the broad differences between ds5.5 and ds6.2 calculations are provided in Supplemental Material Part V and Supplemental Material Figures 8 & 9.

### 4.6.1 Behavior of Chemical Potentials in Examples with Minimal Overstepping

#### *4.6.1.1 Sikkim, Himalaya: Sample 24-99*

In the ds5.5 calculation, isopleths calculated for the preserved core compositions of garnet intersect in the TEC at 526ºC and 5.0 kbar, which is coincident with the *P-T* of garnet-in (Figure 2A). Differences in the chemical potentials calculated between the TEC and MSC emerge at garnet-in, producing negative $\Delta\mu_{MnO}$, $\Delta\mu_{FeO}$, and $\Delta\mu_{Al2O3}$ and positive $\Delta\mu_{MgO}$ (Figure 2C). $\Delta\mu_{CaO}$ becomes negative 4ºC after garnet-in, essentially coincident with the *P-T* conditions at which the garnet core isopleths intersect (Figure 2C).

Using ds6.2, garnet core isopleths intersect at 525ºC and 5.2 kbar, which is consistent with essentially no overstepping (3ºC and 0.3 kbar; Figure 2D). At all *P-T* conditions greater than garnet-in in the TEC, $\Delta\mu_{MnO}$ is negative and $\Delta\mu_{MgO}$ is positive (Figure 2F). $\Delta\mu_{Al2O3}$, $\Delta\mu_{FeO}$, and $\Delta\mu_{CaO}$ are initially zero, becoming negative after a short interval, at the *P-T* point essentially consistent with garnet core isopleth intersections (Figure 2F).

The topologies of the pseudosections calculated with each thermodynamic dataset are broadly similar (compare Figure 2A-B with Figure 2D-E), with the main difference being that biotite is stable in ds5.5 calculations at temperatures greater than ~550ºC (Figure 2A), but is stable over the entire *P-T* range of the ds6.2 pseudosection (Figure 2D). However, in both the ds5.5 and ds6.2 calculations, biotite is present at the peak *T* conditions of the sample 565ºC (Figure 2, peak *T* from Gaidies et al. 2015). Thus, both the ds5.5 and ds6.2 calculations yield appropriate assemblages at peak metamorphic conditions.

$\Delta\mu_{MnO}$ is negative and $\Delta\mu_{MgO}$ is positive at *P-T* conditions greater than initial garnet stability in calculations using both datasets (Figure 2C, 2F). $\Delta\mu_{Al2O3}$, $\Delta\mu_{CaO}$, and $\Delta\mu_{FeO}$ are negative in calculations using both datasets. In ds5.5, $\Delta\mu_{Al2O3}$ and $\Delta\mu_{FeO}$ are negative directly above garnet-in, with $\Delta\mu_{CaO}$ becoming negative 4ºC above garnet-in. The pattern is similar in the ds6.2 calculation, though displaced to a slightly higher temperature. In both datasets, $\Delta\mu$ of all components diverges from zero at a *P-T* approximately coincident with the garnet core isopleth intersection.

#### *4.6.1.2 Rappold Complex: Sample 35F03*

Along the inferred *P-T* path in the ds5.5 calculation, garnet-in is at 531ºC and 4.4 kbar (Figure 3A). Garnet core isopleths do not intersect as tightly in this sample, though spessartine and grossular contents intersect at 531ºC and 4.4 kbar, suggesting little to no overstepping. Again, at *P-T* conditions directly above garnet-in, $\Delta\mu_{CaO}$ and $\Delta\mu_{MgO}$ become positive and $\Delta\mu_{MnO}$, $\Delta\mu_{FeO}$, and $\Delta\mu_{Al2O3}$ become increasingly negative (Figure 3C). There is no *P-T* interval above garnet-in at which $\Delta\mu$ of any examined component remains at zero.

### 4.6.2 Behavior of Chemical Potentials in Examples with Apparent Overstepping

#### *4.6.2.1 Eastern Vermont: Sample TM549A*

The intersection of garnet core isopleths is at 540ºC and 5.8 kbar, suggesting a minimum 35ºC and 1.5 kbar overstep (Figure 4A). Within this apparent overstepped region, $\Delta\mu_{MnO}$ and $\Delta\mu_{CaO}$ become negative and $\Delta\mu_{MgO}$ becomes positive directly after garnet-in (Figure 4C). $\Delta\mu_{FeO} = 0$ for the first 6ºC above garnet-in, before becoming negative. $\Delta\mu_{Al2O3}$ is initially zero, becoming negative at 541ºC and 5.8 kbar, essentially coincident with the *P-T* at which the garnet core isopleths intersect.

Pressure has also been estimated in this sample by quartz-in-garnet elastic barometry. Results from Spear et al. (2014) suggest that, if we assume a temperature of 540ºC, garnet nucleation occurred at 8.0 kbar (their Figure 8). We calculated the $\Delta\mu_{component}$ values along a vector that connects garnet-in in our pseudosection to this *P-T* estimate (Figure 4A,D). At all *P-T* conditions above garnet-in along this vector $\Delta\mu_{MnO}$ and $\Delta\mu_{CaO}$ are negative and $\Delta\mu_{MgO}$ is positive. $\Delta\mu_{FeO}$ becomes negative at 499ºC and 5.1 kbar, and $\Delta\mu_{Al2O3}$ is the final component to experience a deviation between the TEC and MSC at 521ºC and 6.5 kbar (Figure 4D).

*4.6.2.2 Pomfret Dome, Vermont: Sample AV26A*

In the ds5.5 calculation, Garnet core isopleths for this sample intersect at 540ºC and 7.4 kbar, 38ºC and 2.3 kbar above the closest segment of the garnet-in curve (Figure 5A). Along a simple *P-T* path between these points, a) $\Delta\mu_{MnO}$ is negative at all *P-T* conditions above garnet-in (Figure 5C), b) $\Delta\mu_{CaO}$ and $\Delta\mu_{MgO}$ are both initially zero, deviating at 504ºC and 5.2 kbar, c) $\Delta\mu_{FeO}$ is initially zero, becoming negative at 514ºC and 5.8 kbar, and d) $\Delta\mu_{Al2O3}$ is zero until 530ºC and 6.7 kbar, then becoming negative (Figure 5C). All chemical potentials experience a deviation between the TEC and MSC prior to the *P-T* conditions where the garnet core isopleths intersect.

Using ds6.2, garnet core isopleths intersect at 548ºC and 7.8 kbar (Figure 5D), equating to an approximately 38ºC and 2.3 kbar overstep (Figure 5D). $\Delta\mu_{MnO}$ and $\Delta\mu_{CaO}$ are negative and $\Delta\mu_{MgO}$ is positive at all conditions greater than garnet-in (Figure 5F). $\Delta\mu_{FeO}$ becomes negative after 518ºC and 6.0 kbar and $\Delta\mu_{Al2O3}$ becomes negative at 520ºC and 6.1 kbar.

The topologies of the ds5.5 and ds6.2 pseudosections are again very similar, containing biotite, chlorite, garnet, muscovite, plagioclase, and quartz in the field where the garnet core isopleths intersect. These intersections also occur at very similar conditions in both calculations and yield identical apparent oversteps in each case. With both datasets, $\Delta\mu$ of all components deviates from zero at or before the *P-T* point at which garnet core isopleths intersect, and in both ds5.5 and ds6.2 $\Delta\mu_{Al2O3}$ is the final component to experience a difference between the TEC and MSC.

### *4.6.2.3 Nelson Aureole, British Columbia: Sample 93-CW-4*

In this ds5.5 example, the calculated garnet core isopleths do not intersect (Figure 6A). We thus assume garnet nucleation at 545ºC and 3.5 kbar, as previously calculated by Gaidies et al. (2011) (their Figure 6B). This coincides with the equilibrium staurolite-in reaction (Figure 6A), so the stability of staurolite was also suppressed in the MSC calculation (Figure 6B). Chemical potential differences generally run parallel to garnet-in reactions unless additional phases such as andalusite are calculated in the TEC (Figure 6C-G). Our choice of an isobaric heating *P-T* path for this contact metamorphic setting is thus unlikely to have a significant effect on the trends in the $\Delta\mu$ calculations. At *P-T* conditions greater than garnet-in in the TEC, $\Delta\mu$ of all components other than MnO is zero for at least an additional 10˚C. $\Delta\mu_{Al2O3}$ diverges last, becoming negative at 528˚C (Figure 6H).

Isopleths for measured garnet core compositions do not intersect in the ds6.2 calculations, where the composition of garnet also never reaches the measured manganese contents of crystal cores ($X_{sps} = 0.31$), hence the $X_{sps}$ isopleth is not shown in Figure 7A. We thus assume, as in the ds5.5 calculation for this sample, that the *P-T* conditions of garnet nucleation are 545ºC and 3.5 kbar. Along a heating path, $\Delta\mu_{MgO}$ immediately becomes positive at *P-T* conditions greater than garnet-in, while $\Delta\mu_{MnO}$ becomes negative (Figure 7C), $\Delta\mu_{CaO}$ is negative above 448ºC, $\Delta\mu_{FeO}$ is negative above 525ºC, and $\Delta\mu_{Al2O3}$ becomes negative after 539ºC, at slightly lower *T* conditions than assumed garnet nucleation in this sample.

Several significant differences exist between the ds5.5 and ds6.2 pseudosections for this sample (Figures 6 & 7). The stability fields of both garnet and zoisite are expanded in ds6.2 relative to the ds5.5 calculations, which is consistent with other studies (White et al. 2014a; Waters 2019). No substantial differences are apparent in the stability of other phases, including staurolite, with an initial stability at ~545ºC and 3.5 kbar in both cases. As a result of this expanded garnet stability field, there is a greater $\Delta T$ of overstepping in the ds6.2 calculation.

The chemical potential trends are similar in ds5.5 and ds6.2 calculations. In both cases, $\Delta\mu_{MnO}$ immediately becomes negative at the *P-T* of initial garnet stability (Figure 6H, 7C), $\Delta\mu_{Al2O3}$ is the final component to experience a difference, and the *P-T* at which that occurs is nearly coincident with the *P-T* point at which Gaidies et al. (2011) calculated garnet nucleation. There is, however, a greater temperature interval where $\Delta\mu_{Al2O3} = 0$ in the ds6.2 calculation, resulting from the expanded garnet stability field in ds6.2.

## 4.7 DISCUSSION

### 4.7.1 Interpretation of Chemical Potential Calculations

Our calculations show that the chemical potentials of all garnet-forming components typically experience a difference between the TEC and MSC prior to the *P-T* conditions at which garnet nucleates, as inferred from garnet core isopleth intersections.

For samples 24-99 (Sikkim), 35F03 (Rappold Complex), W122 (Eastern Tibet) and DM_06_128 (Kootenay Arc), the garnet core isopleths intersect at effectively the *P-T* of garnet-in. This can be interpreted as lack of garnet overstepping, agreeing with previous interpretations of these samples (Gaidies et al. 2008, 2015; George and Gaidies 2017). In these examples, $\Delta\mu_{all\ components} \neq 0$ at conditions immediately up-temperature and pressure of garnet-in in the TEC (Figures 2, 3, Supplemental Figures 1-2,8).

In contrast, calculations using both tested datasets for samples 93-CW-4 (Nelson Aureole), AV26A (Pomfret Dome), and TM549a (Eastern Vermont), and calculations using ds5.5 for samples 12TM16 (Southeastern Ontario), ED34 (Southwest Turkey), D13-75 (Central Himalaya), TH203B (Albion Mountains), and SSFM307-7G (Funeral Mountains) show that $\Delta\mu$ of at least one component is zero immediately up temperature of garnet-in. This is represented schematically in Figure 8, in which a hypothetical simplified three-component system is drawn with tangent planes that represent the lowest free energy of the TEC (gray) and the MSC (yellow). In this case, *P-T* conditions exist above garnet-in at which $\mu_{Al2O3}$ is identical in the TEC and MSC, despite differences in $\mu_{MgO}$ and $\mu_{FeO}$ (Figure 8B-C). In the eight overstepped examples shown in this paper $\Delta\mu_{Al2O3}$ is the final component to experience a deviation between the TEC and MSC (Tables 2 & 3).

For certain components (MgO in all examples and CaO for samples 35F03 and 12TM16), $\Delta\mu_{component}$ is positive at *P-T* conditions greater than the TEC's garnet-in. Geometrically, this is shown in Figure 8, in which the tangent planes evolve so that the TEC tangent plane (gray) has a greater $\mu_{MgO}$ than the MSC tangent plane (yellow), resulting in a positive $\Delta\mu_{MgO}$ (Figure 8B-C). This is related to the preferential partitioning of MgO into other phases such as chlorite and biotite at lower to middle amphibolite-facies temperatures (e.g. Ferry and Spear 1978; Holland et al. 1998; Vidal 1999; Lanari et al. 2014). We stress here that while chemical potential gradients drive diffusion in natural systems, the positive $\Delta\mu$ values in our calculations should not be interpreted as diffusional gradients driving MgO and CaO away from a garnet nucleus, with these calculations having no spatial context.

### 4.7.2 The Key Role of $Al_2O_3$

In the eight examples where overstepping appears to have been significant (Eastern Vermont, Pomfret Dome, Nelson Aureole, Southeastern Ontario, Southwest Turkey, Central Himalaya, Albion Mountains, and Funeral Mountains), $\Delta\mu_{Al2O3}$ persists at or very close to zero until substantially greater *P-T* than the TEC's garnet-in (Table 2). This reflects the evolution of TEC and MSC tangent planes (Figure 8B-C). For three out of the eight overstepped examples (Eastern Vermont, Central Himalaya, and Funeral Mountains), the *P-T* location at which $\Delta\mu_{Al2O3}$ first diverges from zero is at the *P-T* at which the garnet core isopleths intersect. In the Pomfret Dome example, $\Delta\mu_{Al2O3}$ becomes negative 10ºC below the *P-T* of the garnet core isopleth intersection. In the four remaining examples (Southeastern Ontario, Southwest Turkey, Nelson Aureole, and Albion Mountains), $\Delta\mu_{Al2O3}$ diverges >10ºC below the point at which the garnet core isopleths intersect.

It is unlikely that $\Delta\mu_{Al2O3}$ consistently being the final component to diverge between the TEC and MSC results from the choice of *P-T* path. In the 2D graph of $\Delta\mu_{Al2O3}$ (Figure 6G), most possible heating paths would lead to a similar result for $\Delta\mu_{Al2O3}$. In the Eastern Vermont example, where we described the evolution of $\Delta\mu$ along two different *P-T* paths (Figure 4C,D), $\Delta\mu_{Al2O3}$ is the final component to experience a deviation between the TEC and MSC in both cases. The coincidence of $\Delta\mu_{Al2O3} \neq 0$ and the *P-T* of garnet nucleation is more robust for the garnet core isopleth intersection (Figure 4C) than the quartz-in-garnet barometry determination (Figure 4D), indicating that this relationship is partially dependent on the method of determining the *P-T* of garnet nucleation.

In all five examples using ds6.2, $\Delta\mu_{Al2O3}$ is the final component to experience a difference between the TEC and MSC (Table 3). In the Sikkim, Rappold Complex, and Nelson Aureole samples, this deviation in $\Delta\mu_{Al2O3}$ occurs within 10ºC of the *P-T* at which the garnet core isopleths intersect. Once again, this suggests that the calculated equilibrium garnet composition at the *P-T* at which $\Delta\mu_{\text{all components}}$ diverge from zero coincides with the preserved compositions of appropriate natural garnet crystal cores.

### 4.7.3 The Role of $X_{MnO}$ in Pseudosection Calculations

The only difference between examples calculated within any given dataset is the bulk-rock composition (compositions are listed in Supplemental Material Part II). In general, samples with lower bulk rock MnO content display the least apparent overstepping of garnet nucleation.

Figure 9 shows TEC and MSC versions of a $T$-$X_{MnO}$ diagram for sample AV26A (Bell et al. 2013) in which the *x* axis ranges from 0 to 0.2 wt.% MnO, with other components fixed in the ratio reported by Bell et al. (2013). The temperature at which garnet stability is first calculated scales inversely with the bulk rock MnO content. At 0.05 wt.% MnO there is a <10ºC difference between garnet-in and $\Delta\mu_{Al2O3} \neq 0$, at 0.10 wt.% MnO, the temperature difference between garnet-in and $\Delta\mu_{Al2O3} \neq 0$ is 35ºC, and at 0.15 wt.% MnO the temperature difference between garnet-in and $\Delta\mu_{Al2O3} \neq 0$ is >75ºC (Figure 9C). Thus, as the bulk-rock MnO content increases, the temperature of garnet-in decreases, and a substantial window opens between garnet-in and the initial decrease of $\Delta\mu_{Al2O3}$. Thus, if $\Delta\mu_{Al2O3} \neq 0$ can be used as an approximate indicator of *P-T* conditions at which garnet nucleation is likely, then rocks with a greater bulk rock MnO might be expected to exhibit more pronounced apparent overstepping of garnet-in reactions. This results from high MnO contents lowering the calculated temperature of garnet-in reactions without significantly changing the equilibrium garnet composition at higher temperatures (Symmes and Ferry 1992; Mahar et al. 1997; Tinkham et al. 2001; Caddick and Thompson 2008; White et al. 2014b).

Due to the challenges of experimentally creating Mn end-member phases, thermodynamic data for Mn end-members were either calculated based on natural partitioning data in well-equilibrated natural rock samples or estimated based on experimental constraints for other end-members (Mahar et al. 1997) and estimated Margules parameters (White et al. 2014b). Therefore, the uncertainties on the equilibria for Mn-bearing phases are likely greater than the uncertainties on end members with more robust experimental constraints. The strong dependence of garnet-in on the MnO bulk rock content may partially be a function of poorly constrained thermodynamic data or may be impacted by the sequestration of MnO by accessory phases (McCarron et al. 2019). Simply recalculating phase equilibria in a MnO-free system is not an appropriate way to mitigate this phenomenon, with the calculated initial stability of garnet then moving to higher *P*-*T* than suggested by independent constraints (e.g. White et al. 2014b).

It is also clear that immediately up-pressure and -temperature of calculated garnet-in reactions, calculated volume abundances of garnet in the TEC are extremely small (labeled in panel A of Figures 2-7). In the examples from Sikkim (ds5.5 & ds6.2) and the Rappold Complex (ds6.2), garnet core isopleths intersect at a point at which 0.5% of the calculated rock volume is garnet in the TEC. None of the other calculations suggest core isopleth intersections at conditions at which the TEC predicts the stability of much more than 1% garnet. This suggests that while the *P*-*T* range of garnet stability appears large, very low abundances of garnet would be expected over much of this range. Even if garnet is stable in a natural rock, abundances of less than 0.5% may not be readily detected in thin section. It is thus important to carefully interrogate the calculated abundances of phases while interpreting pseudosection results.

## 4.8 IMPLICATIONS

Examples used in this paper are consistent with previous observations that suggest that overstepping of garnet-in reactions occurs in a variety of metamorphic settings (e.g. Pattison and Tinkham 2009; Gaidies et al. 2011; Pattison et al. 2011; Dragovic et al. 2012; Spear et al. 2014; Carlson et al. 2015; Castro and Spear 2016; Wolfe and Spear 2017; Spear and Wolfe 2018). It is thus important to consider: i) the tectonic implications of overstepping, ii) the utility of these chemical potential calculations, iii) the definition of the garnet-in curve, and iv) interrogation of the thermodynamic data.

Comparison of the amount of overstep and geochronological constraints on the duration of garnet growth provide important evidence that overstepping can influence interpretations of tectonic processes. In an example from Sifnos, Greece, garnet experienced a large overstepping of ~100ºC and 7 kbar during subduction, then grew cm-sized crystals in <<1.0 Myr (Dragovic et al. 2012). Other samples in Sifnos experienced an apparently smaller overstep and grew 3–5 cm crystals over ~8 Myr (Dragovic et al. 2015). In the regionally metamorphosed Eastern Vermont terrane (geographically near the samples described by Bell et al. (2013) and Spear et al. (2014)), garnet crystals nucleated after a ~35 ˚C overstep (Dragovic et al. 2018) and then grew up to ~2.5 cm in diameter in 3.8 ± 2.2 Myr during regional metamorphism (Gatewood et al. 2015). In the Cascades Crystalline Core, garnet experienced ~30-40ºC of overstepping and then grew over a period of < 6 Myr (Stowell et al. 2011). Thus, it appears that examples with extreme overstepping may subsequently result in very rapid garnet growth, while moderate overstepping results in slower garnet growth rates. This follows from the fact that nucleation rate is a function of the amount of temperature overstep and that the kinetics of intergranular transport are dependent on the absolute temperature of the system (e.g. Waters & Lovegrove 2002). Thus, if a system is overstepped at high temperature, eventual crystal nucleation will be followed by efficient transport to the nuclei. This link between overstepping and the duration of garnet growth has potentially important implications for understanding the pulsed or continuous nature of metamorphism and its associated fluid generation.

In the minimally overstepped examples, there is an immediate difference in the chemical potential of all components at garnet-in. In the more significantly overstepped examples, there is an ‘area’ of *P-T* space in which $\Delta\mu_{Al2O3} = 0$, but garnet is nominally stable. Thus, the calculation of chemical potentials in the TEC and MSC may be used as a first order approximation to assess whether a rock experienced substantially overstepped garnet-in reactions.

Much of the previous discussion about overstepped garnet nucleation and growth has focused on improving methodologies to determine the *P-T* of garnet nucleation and comparing and contrasting the *P-T* of garnet nucleation constrained by different methodologies. Our work highlights that this discussion of overstepping must also include: i) consideration of the factors controlling the position of garnet-in curves, and ii) interrogation of additional information inherent in pseudosection calculations.

The garnet-in curve is generally defined as the *P-T* at which garnet first becomes thermodynamically stable in the TEC. Alternatively, we can explore the consequences of approximating garnet-in as the *P-T* at which $\Delta\mu_{Al2O3} \neq 0$. If that were the case, then all of the overstepped examples explored here would have lower apparent oversteps. For the three examples (Eastern Vermont, Central Himalaya, Funeral Mountains) in which $\Delta\mu_{Al2O3} \neq 0$ aligns with the *P-T* at which the garnet core isopleths intersect, this would lead to an interpretation that those rocks are not overstepped.

In many of our examples, the modal abundance of garnet calculated at *P*-*T* conditions immediately greater than garnet-in is < 0.5%. It is unclear if this would always be detected in a thin section point count (see Howarth (1998) for a discussion on the likely probabilities and errors associated with point counting). This leads to an interesting discrepancy between field, petrographic, and pseudosection calculations. For example, in the Nelson Aureole, Pattison & Tinkham (2009) calculate initial garnet stability in the pseudosection to be at 527ºC. Based on thermal modelling of the Nelson Batholith and associated contact aureole, this should occur 2300 meters from the batholith. However, the isograd is mapped in the field (based on the first visible presence of garnet) at 1400 meters from the batholith. Thus, there are 900 meters (equating to 30ºC) of section in which garnet has been calculated to be thermodynamically stable, but has not been recognized in the field or in thin section. Our pseudosection recalculations for this locality suggest that rocks would only contain 0.5% garnet by volume at *P*-*T* conditions immediately greater than garnet-in. This may not be readily detected without study of numerous thin sections and hand specimens, and in many cases, it may thus be more appropriate to redefine an 'effective garnet-in' as the *P*-*T* conditions at which a more substantial garnet fraction would be stable.

## 4.9 REFERENCES

Ague, J.J., and Carlson, W.D. (2013) Metamorphism as garnet sees it: The kinetics of nucleation and growth, equilibration, and diffusional relaxation. Elements, 9, 439–445.

Anczkiewicz, R., Chakraborty, S., Dasgupta, S., Mukhopadhyay, D., and Kołtonik, K. (2014) Timing, duration and inversion of prograde Barrovian metamorphism constrained by high resolution Lu-Hf garnet dating: A case study from the Sikkim Himalaya, NE India. Earth and Planetary Science Letters, 407, 70–81.

Baxter, E.F., and Scherer, E.E. (2013) Garnet geochronology: Timekeeper of tectonometamorphic processes. Elements, 9, 433–438.

Baxter, E.F., Caddick, M.J., and Dragovic, B. (2017) Garnet: A Rock-Forming Mineral Petrochronometer. Reviews in Mineralogy &Geochemistry, 83, 469–533.

Bell, T.H., Rieuwers, M.T., Cihan, M., Evans, T.P., Ham, A.P., and Welch, P.W. (2013) Inter-relationships between deformation partitioning, metamorphism and tectonism. Tectonophysics, 587, 119–132.

Berman, R.G. (1988) Internally consistent thermodynamic data for minerals in the system Na2O-K2O-CaO-MgO-FeO-Fe2O-SiO2-TiO2-H2O-CO2. Journal of Petrology, 29, 445–552.

Caddick, M.J., and Thompson, A.B. (2008) Quantifying the tectono-metamorphic evolution of pelitic rocks from a wide range of tectonic settings: Mineral compositions in equilibrium. Contributions to Mineralogy and Petrology, 156, 177–195.

Caddick, M.J., Bickle, M.J., Harris, N.B.W., Holland, T.J.B., Horstwood, M.S.A., Parrish, R.R., and Ahmad, T. (2007) Burial and exhumation history of a Lesser Himalayan schist: Recording the formation of an inverted metamorphic sequence in NW India. Earth and Planetary Science Letters, 264, 375–390.

Caddick, M.J., Konopásek, J., and Thompson, A.B. (2010) Preservation of garnet growth zoning and the duration of prograde metamorphism. Journal of Petrology, 51, 2327–2347.

Carlson, W.D. (1989) The significance of intergranuar diffusion to the mechanisms and kinetics of porphyroblast crystallization. Contribution to Mineralogy and Petrology, 103, 1–24.

——— (2002) Scales of disequilibrium and rates of equilibration during metamorphism. American Mineralogist, 87, 185–204.

——— (2010) Dependence of reaction kinetics on H2O activity as inferred from rates of intergranular diffusion of aluminium. Journal of Metamorphic Geology, 28, 735–752.

——— (2011) Porphyroblast crystallization: linking processes, kinetics, and microstructures. International Geology Review, 53, 406–445.

Carlson, W.D., Pattison, D.R.M., and Caddick, M.J. (2015a) Beyond the equilibrium paradigm: How consideration of kinetics enhances metamorphic interpretation. American Mineralogist, 100, 1659–1667.

Carlson, W.D., Hixon, J.D., Garber, J.M., and Bodnar, R.J. (2015b) Controls on metamorphic equilibration: the importance of intergranular solubilities mediated by fluid composition. Journal of Metamorphic Geology, 33, 123–146.

Carmichael, D.M. (1969) On the mechanism of prograde metamorphic reactions in quartz-bearing pelitic rocks. Contributions to Mineralogy and Petrology, 20, 244–267.

Castro, A.E., and Spear, F.S. (2016) Reaction overstepping and re-evaluation of peak P–T conditions of the blueschist unit Sifnos, Greece: implications for the Cyclades subduction zone. International Geology Review, 59, 1–15.

Chernoff, C.B., and Carlson, W.D. (1997) Disequilibrium for Ca during growth of pelitic garnet. Journal of Metamorphic Geology, 15, 421–438.

——— (1999) Trace element zoning as a record of chemical disequilibrium during garnet growth. Geology, 27, 555–558.

Christian, J.W. (1975) The Theory of Transformations in Metals and Alloys, 1–586 p. Pergamon Press.

Coggon, R., and Holland, T.J.B. (2002) Mixing properties of phengitic micas and revised garnet-phengite thermobarometers. Journal of Metamorphic Geology, 20, 683–696.

Connolly, J.A.D. (1990) Multivariable phase diagrams: an algorithm based on generalized thermodynamics. American Journal of Science, 290, 666–718.

Connolly, J.A.D. (2005) Computation of phase equilibria by linear programming: A tool for geodynamic modeling and its application to subduction zone decarbonation. Earth and Planetary Science Letters, 236, 524–541.

Connolly, J.A.D., and Kerrick, D.M. (1987) An algorithm and computer program for calculating composition phase diagrams. CALPHAD, 11, 1–55.

Craddock Affinati, S., Hoisch, T.D., Wells, M.L., and Vervoort, J.D. (2020) Pressure-temperature-time paths from the Funeral Mountains, California, reveal Jurassic retroarc underthrusting during early Sevier orogenesis. GSA Bulletin, 132, 1–19.

Dasgupta, S., Chakraborty, S., and Neogi, S. (2009) Petrology of an inverted Barrovian sequence of metapelites in Sikkim Himalaya, India: Constraints on the tectonics of inversion. American Journal of Science, 309, 43–84.

Dragovic, B., Samanta, L.M., Baxter, E.F., and Selverstone, J. (2012) Using garnet to constrain the duration and rate of water-releasing metamorphic reactions during subduction: An example from Sifnos, Greece. Chemical Geology, 314–317, 9–22.

Dragovic, B., Baxter, E.F., and Caddick, M.J. (2015) Pulsed dehydration and garnet growth during subduction revealed by zoned garnet geochronology and thermodynamic modeling, Sifnos, Greece. Earth and Planetary Science Letters, 413, 111–122.

Dragovic, B., Gatewood, M.P., Baxter, E.F., and Stowell, H.H. (2018) Fluid production rate during the regional metamorphism of a pelitic schist. Contributions to Mineralogy and Petrology, 173, 1–16.

Duchêne, S., Blichert-Toft, J., Luais, B., Télouk, P., Lardeaux, J.M., and Albarède, F. (1997) The Lu-Hf dating of garnets and the ages of the Alpine high-pressure metamorphism. Nature, 387, 586–589.

Eskola, P. (1915) On the relations between the chemical and mineralogical composition in the metamorphic rocks of the Orijarvi region. Bull. Comm. Geol. Finlande.

——— (1920) The mineral facies of rocks. Norsk. Geol. Tidsskr., 6, 143–194.

Essene, E.J. (1982) Geologic thermometry and barometry. In Characterization of Metamorphism through Mineral Equilbria: Mineralogical Society of America pp. 153–206.

Etzel, T.M., Catlos, E.J., Ataktürk, K., Lovera, O.M., Kelly, E.D., Çemen, I., and Diniz, E. (2019) Implications for thrust-related shortening punctuated by extension from P-T paths and geochronology of garnet-bearing schists, southern (Çine) Menderes Massif, SW Turkey. Tectonics, 38, 1974–1998.

Evans, T.P. (2004) A method for calculating effective bulk composition modification due to crystal fractionation in garnet-bearing schist: Implications for isopleth thermobarometry. Journal of Metamorphic Geology, 22, 547–557.

Ferry, J.M., and Spear, F.S. (1978) Experimental calibration of the partitioning of Fe and Mg between biotite and garnet. Contributions to Mineralogy and Petrology, 66, 113–117.

Fisher, G.W. (1978) Rate laws in metamorphism. Geochimica et Cosmochimica Acta, 42, 1035–1050.

Florence, F.P., and Spear, F.S. (1991) Effects of diffusional modification of garnet growth zoning on P-T path calculations. Contributions to Mineralogy and Petrology, 107, 487–500.

Fuhrman, M.L., and Lindsley, D.H. (1988) Ternary-feldspar modeling and thermometry. American Mineralogist, 73, 201–215.

Fyfe, W.S., Turner, F.J., and Verhoogen, J. (1958) Kinetics of Metamorphic Reactions. In Metamorphic Reactions and Metamorphic Facies p. 80. Geological Society of America.

Gaidies, F., Krenn, E., De Capitani, C., and Abart, R. (2008) Coupling forward modelling of garnet growth with monazite geochronology: An application to the Rappold Complex (Austroalpine crystalline basement). Journal of Metamorphic Geology, 26, 775–793.

Gaidies, F., Pattison, D.R.M., and de Capitani, C. (2011) Toward a quantitative model of metamorphic nucleation and growth. Contributions to Mineralogy and Petrology, 162, 975–993.

Gaidies, F., Petley-Ragan, A., Chakraborty, S., Dasgupta, S., and Jones, P. (2015) Constraining the conditions of Barrovian metamorphism in Sikkim, India: P-T-t paths of garnet crystallization in the Lesser Himalayan Belt. Journal of Metamorphic Geology, 33, 23–44.

Gatewood, M.P., Dragovic, B., Stowell, H.H., Baxter, E.F., Hirsch, D.M., and Bloom, R. (2015) Evaluating chemical equilibrium in metamorphic rocks using major element and Sm-Nd isotopic age zoning in garnet, Townshend Dam, Vermont, USA. Chemical Geology, 401, 151–168.

George, F.R., and Gaidies, F. (2017) Characterisation of a garnet population from the Sikkim Himalaya: insights into the rates and mechanisms of porphyroblast crystallisation. Contributions to Mineralogy and Petrology, 172, 1–22.

George, F.R., Gaidies, F., and Boucher, B. (2018) Population-wide garnet growth zoning revealed by LA-ICP-MS mapping: implications for trace element equilibration and syn-kinematic deformation during crystallisation. Contributions to Mineralogy and Petrology, 173, 1–24.

Ghent (1976) Plagioclase-garnet-Al2SiO5-quartz: a potential geobarometer-geothermometer. American Mineralogist, 61, 710–714.

Gibbs, J.W. (1928) Thermodynamics. Green Longmans, New York.

Green, E.C.R., White, R.W., Diener, J.F.A., Powell, R., Holland, T.J.B., and Palin, R.M. (2016)

Activity–composition relations for the calculation of partial melting equilibria in metabasic rocks. Journal of Metamorphic Geology, 34, 845–869.

Groppo, C., Beltrando, M., and Compagnoni, R. (2009) The P-T path of the ultra-high pressure Lago Di Cignana and adjoining high-pressure meta-ophiolitic units: Insights into the evolution of the subducting Tethyan slab. Journal of Metamorphic Geology, 27, 207–231.

Guevara, V.E., and Caddick, M.J. (2016) Shooting at a moving target: Phase equilibria modelling of high-temperature metamorphism. Journal of Metamorphic Geology, 34, 209–235.

Hacker, B.R., Kirby, S.H., and Bohlen, S.R. (1992) Time and metamorphic petrology: Calcite to aragonite experiments. Science, 258, 110–112.

Hacker, B.R., Abers, G.A., and Peackcock, S.M. (2003) Subduction factory 1. Theoretical mineralogy, densities, seismic wave speeds, and H2O contents. Journal of Geophysical Research, 108, 1–26.

Hernández-Uribe, D., and Palin, R.M. (2019) Catastrophic shear-removal of subcontinental lithospheric mantle beneath the Colorado Plateau by the subducted Farallon slab. Scientific Reports, 9, 1–10.

Hillert, M. (2008) Phase equilibria, phase diagrams, and phase transformations: their thermodynamic basis, 2nd ed. Cambridge University Press, Cambridge.

Hillert, M., and Rettenmayr, M. (2003) Deviation from local equilibrium at migrating phase interfaces. Acta Materialia, 51, 2803–2809.

Hodges, K.V., and McKenna, L.W. (1987) Realistic propagation of uncertainties in geologic thermobarometry. American Mineralogist, 72, 671–680.

Hodges, K.V., and Spear, F.S. (1982) Geothermometry, geobarometry and the Al2SiO5 triple point at Mt. Moosilauke, New Hampshire. American Mineralogist, 67, 1118–1134.

Holland, T.J.B., and Powell, R. (1998) An internally consistent thermodynamic data set for phases of petrological interest. Journal of Metamorphic Geology, 16, 309–343.

——— (2003) Activity-compositions relations for phases in petrological calculations: An asymetric multicomponent formulation. Contributions to Mineralogy and Petrology, 145, 492–501.

——— (2004) An internally consistent thermodynamic data set for phases of petrological interest. Journal of Metamorphic Geology, 16, 309–343.

Holland, T.J.B., and Powell, R. (2011) An improved and extended internally consistent thermodynamic dataset for phases of petrological interest, involving a new equation of state for solids. Journal of Metamorphic Geology, 29, 333–383.

Holland, T.J.B., Baker, J., and Powell, R. (1998) Mixing properties and activity-composition relationships of chlorites in the system MgO-FeO-Al2O3-SiO2-H2O. European Journal of Mineralogy, 10, 395–406.

Howarth, R.J. (1998) Improved point estimates of uncertainty in proportions, point-counting, and pass-fail test results. American Journal of Science, 298, 594–607.

Iaccarino, S., Montomoli, C., Carosi, R., Massonne, H.J., and Visonà, D. (2017) Geology and tectono-metamorphic evolution of the Himalayan metamorphic core: Insights from the Mugu Karnali transect, Western Nepal (Central Himalaya). Journal of Metamorphic Geology, 35, 301–325.

Joesten, R. (1977) Evolution of mineral assemblage zoning in diffusion metasomatism. Geochimica et Cosmochimica Acta, 41, 649–670.

Kelly, E.D., Carlson, W.D., and Ketcham, R.A. (2013a) Crystallization kinetics during regional metamorphism of porphyroblastic rocks. Journal of Metamorphic Geology, 31, 963–979.

——— (2013b) Magnitudes of departures from equilibrium during regional metamorphism of porphyroblastic rocks. Journal of Metamorphic Geology, 31, 981–1002.

Kelly, E.D., Hoisch, T.D., Wells, M.L., Vervoort, J.D., and Beyene, M.A. (2015) An Early Cretaceous garnet pressure–temperature path recording synconvergent burial and exhumation from the hinterland of the Sevier orogenic belt, Albion Mountains, Idaho. Contributions to Mineralogy and Petrology, 170, 1–22.

Kerrick, D.M., and Connolly, J.A.D. (2001) Metamorphic devolatilization of subducted oceanic metabasalts: Implications for seismicity, arc magmatism and volatile recycling. Earth and Planetary Science Letters, 189, 19–29.

Ketcham, R.A., and Carlson, W.D. (2012) Numerical simulation of diffusion-controlled nucleation and growth of porphyroblasts. Journal of Metamorphic Geology, 30, 489–512.

Konrad-Schmolke, M., Handy, M.R., Babist, J., and O’Brien, P.J. (2005) Thermodynamic modelling of diffusion-controlled garnet growth. Contributions to Mineralogy and Petrology.

Konrad-Schmolke, M., Babist, J., Handy, M.R., and O’Brien, P.J. (2006) The physico-chemical properties of a subducted slab from garnet zonation patterns (Sesia Zone, western Alps). Journal of Petrology, 47, 2123–2148.

Kretz, R. (1966) Interpretation of the shape of mineral grains in metamorphic rocks. Journal of Petrology, 7, 68–94.

Kretz, R. (1974) Some models for the rate of crystallization of garnet in metamorphic rocks. Lithos, 7, 123–131.

Lanari, P., and Duesterhoeft, E. (2019) Modeling metamorphic rocks using equilibrium thermodynamics and internally consistent databases: Past achievements, problems and perspectives. Journal of Petrology, 60, 19–56.

Lanari, P., and Engi, M. (2017) Local bulk composition effects on metamorphic mineral assemblages. Reviews in Mineralogy & Geochemistry, 83, 55–93.

Lanari, P., Wagner, T., and Vidal, O. (2014) A thermodynamic model for di-trioctahedral chlorite from experimental and natural data in the system MgO-FeO-Al2O3-SiO2-H2O: applications to P-T sections and geothermometry. Contributions to Mineralogy and Petrology, 167, 1–19.

Lasaga, A.C. (1986) Metamorphic reaction rate laws and development of isograds. Mineralogical Magazine, 50, 359–373.

Lasaga, A.C., and Rye, D.M. (1993) Fluid flow and chemical kinetics in metamorphic systems. American Journal of Science, 293, 361–404.

Liu, M., and Yund, R.A. (1993) Transformation kinetics of polycrystalline aragonite to calcite: New experimental data, modelling, and implications. Contributions to Mineralogy and Petrology, 114, 465–478.

Mahar, E.M., Baker, J.M., Powell, R., Holland, T.J.B., and Howell, N. (1997) The effect of Mn on mineral stability in metapelites. Journal of Metamorphic Geolgoy, 15, 223–238.

Manning, C.E. (2007) Solubility of corundum + kyanite in H2O at 700°C and 10 kbar: Evidence for Al-Si complexing at high pressure and temperature. Geofluids, 7, 258–269.

Marmo, B.A., Clarke, G.L., and Powell, R. (2002) Fractionation of bulk rock composition due to porphyroblast growth: Effects on eclogite facies mineral equilibria, Pam Peninsula, New Caledonia. Journal of Metamorphic Geology, 20, 151–165.

McCarron, T., Gaidies, F., McFarlane, C.R.M., Easton, R.M., and Jones, P. (2014) Coupling thermodynamic modeling and high-resolution in situ LA-ICP-MS monazite geochronology: evidence for Barrovian metamorphism late in the Grenvillian history of southeastern Ontario. Mineralogy and Petrology, 108, 741–758.

McCarron, T., McFarlane, C.R.M., and Gaidies, F. (2019) The significance of Mn-rich ilmenite and the determination of P-T paths from zoned garnet in metasedimentary rocks from the western Cape Breton Highlands, Nova Scotia. Journal of Metamorphic Geology, 37, 1171–1192.

Menard, T., and Spear, F.S. (1994) Metamorphic P-T paths from calcic pelitic schists from the Strafford Dome, Vermont, USA. Journal of Metamorphic Geology, 12, 811–826.

Milke, R., and Heinrich, W. (2002) Diffusion-controlled growth of wollastonite rims between quartz and calcite: Comparison between nature and experiment. Journal of Metamorphic Geology, 20, 467–480.

Moynihan, D.P., and Pattison, D.R.M. (2013) An automated method for the calculation of P-T paths from garnet zoning, with application to metapelitic schist from the Kootenay Arc, British Columbia, Canada. Journal of Metamorphic Geology, 31, 525–548.

Mullin (1992) Crystallization, 3rd ed. Butterworth, Heinemann, Oxford.

Newton, R.C., and Manning, C.E. (2007) Solubility of grossular, Ca3Al2Si3O12, in H2O-NaCl solutions at 800 °C and 10 kbar, and the stability of garnet in the system CaSiO3-Al2O3-H2O-NaCl. Geochimica et Cosmochimica Acta, 71, 5191–5202.

Nielsen, A.E. (1964) Kinetics of Precipitation. Pergamon Press.

Palin, R.M., Weller, O.M., Waters, D.J., and Dyck, B. (2016) Quantifying geological uncertainty in metamorphic phase equilibria modelling; A Monte Carlo assessment and implications for tectonic interpretations. Geoscience Frontiers, 7, 591–607.

Pattison, D.R.M., and DeBuhr, C.L. (2015) Petrology of metapelites in the Bugaboo aureole, British Columbia, Canada. Journal of Metamorphic Geology, 33, 437–462.

Pattison, D.R.M., and Spear, F.S. (2018) Kinetic control of staurolite-Al2SiO5mineral assemblages: Implications for Barrovian and Buchan metamorphism. Journal of Metamorphic Geology, 36, 667–690.

Pattison, D.R.M., and Tinkham, D.K. (2009) Interplay between equilibrium and kinetics in prograde metamorphism of pelites: an example from the Nelson aureole, British Columbia. Journal of Metamorphic Geology, 27, 249–279.

Pattison, D.R.M., and Vogl, J.J. (2005) Contrasting sequences of metapelitic mineral-assemblages in the aureole of the tilted Nelson Batholith, British Columbia: Implications for phase equilibria and pressure determination in andalusite-sillimanite-type settings. Canadian Mineralogist, 43, 51–88.

Pattison, D.R.M., de Capitani, C., and Gaidies, F. (2011) Petrological consequences of variations in metamorphic reaction affinity. Journal of Metamorphic Geology, 29, 953–977.

Pollington, A.D., and Baxter, E.F. (2010) High resolution Sm-Nd garnet geochronology reveals the uneven pace of tectonometamorphic processes. Earth and Planetary Science Letters, 293, 63–71.

Powell, R. (1978) Equilibrium Thermodynamics in Petrology: An Introduction, 1–294 p. Harper & Row Publishers, New York.

Powell, R., and Holland, T.J.B. (1999) Relating formulations of the thermodynamics of mineral solid solutions: Activity modeling of pyroxenes, amphiboles, and micas. American Mineralogist, 84, 1–14.

Powell, R., and Holland, T.J.B. (2008) On thermobarometry. Journal of Metamorphic Geolgoy, 26, 155–179.

Powell, R., Holland, T.J.B., and Worley, B. (1998) Calculating phase diagrams involving solid solutions via non-linear equations, with examples using THERMOCALC. Journal of Metamorphic Geology, 16, 577–588.

Powell, R., White, R.W., Green, E.C.., Holland, T.. B., and Diener, J.F.. (2014) On parameterizing thermodynamic descriptions of minerals for petrological calculations. Journal of Metamorphic Geology, 32, 245–260.

Powell, R., Evans, K.A., Green, E.C.R., and White, R.W. (2019) The truth and beauty of chemical potentials. Journal of Metamorphic Geology, 37, 1007–1019.

Ridley, J., and Thompson, A.B. (1986) The role of mineral kinetics in the development of metamorphic microtextures. Advances in Physical Geochemistry, 5, 154–193.

Rimstidt, J.D. (2014) Geochemical Rate Models. Cambridge University Press, New York.

Rubie, D.C. (1986) The catalysis of mineral reactions by water and restrictions on the presence of aqueous fluid during metamorphism. Mineralogical Magazine, 50, 399–415.

——— (1998) Disequilibrium during metamorphism: The role of nucleation kinetics. Geological Society, London, Special Publications, 138, 199–214.

Rubie, D.C., Tsuchida, Y., Yagi, T., Utsumi, W., Kikegawa, T., Shimomura, O., and Brearley, A.J. (1990) An in situ X ray diffraction study of the kinetics of the Ni2SiO4 olivine-spinel transformation. Journal of Geophysical Research, 95, 15829–15844.

Rumble, D. (1976) The use of mineral solid solutions to measure chemical potential gradients. American Mineralogist, 61, 1167–1174.

Scherer, E.E., Cameron, K.L., and Blichert-Toft, J. (2000) Lu-Hf garnet geochronology: Closure temperature relative to the Sm-Nd system and the effects of trace mineral inclusions.

Geochimica et Cosmochimica Acta, 64, 3413–3432.

Seman, S., Stockli, D.F., and McLean, N.M. (2017) U-Pb geochronology of grossular-andradite garnet. Chemical Geology, 460, 106–116.

Spear, F.S. (1988) Metamorphic fractional crystallization and internal metasomatism by diffusional homogenization of zoned garnets. Contributions to Mineralogy and Petrology, 99, 507–517.

Spear, F.S. (1993) Metamorphic Phase Equilibria and Pressure-Temperature-Time Paths. Mineralogical Society of America, Washington, DC.

Spear, F.S., and Pyle, J.M. (2010) Theoretical modeling of monazite growth in a low-Ca metapelite. Chemical Geology, 273, 111–119.

Spear, F.S., and Selverstone, J. (1983) Quantitative P-T paths from zoned minerals: Theory and tectonic applications. Contributions to Mineralogy and Petrology, 83, 348–357.

Spear, F.S., and Wolfe, O.M. (2018) Evaluation of the effective bulk composition (EBC) during growth of garnet. Chemical Geology, 491, 39–47.

Spear, F.S., Selverstone, J., Hickmott, D., Crowley, P., and Hodges, K.V. (1984) P-T paths from garnet zoning: A new technique for deciphiering tectonic process in crystalline terranes. Geology, 12, 87–90.

Spear, F.S., Thomas, J.B., and Hallett, B.W. (2014) Overstepping the garnet isograd: A comparison of QuiG barometry and thermodynamic modeling. Contributions to Mineralogy and Petrology, 168.

St-Onge, M.R. (1987) Zoned poikiloblastic garnets: P-T paths and syn-metamorphic uplift through 30 km of structural depth, Wopmay Orogen, Canada. Journal of Petrology, 28, 1–21.

Starr, P.G., Pattison, D.R.M., and Ames, D.E. (2020) Mineral assemblages and phase equilibria of metabasites from the prehnite–pumpellyite to amphibolite facies, with the Flin Flon Greenstone Belt (Manitoba) as a type example. Journal of Metamorphic Geology, 38, 71–102.

Stipska, P., Powell, R., White, R.W., and Baldwin, J.A. (2010) Using calculated chemical potential relationships to account for coronas around kyanite: An example from the Bohemian Massif. Journal of Metamorphic Geology, 28, 97–116.

Stowell, H., Bulman, G., Tinkham, D., and Zuluaga, C. (2011) Garnet growth during crustal thickening in the Cascades Crystalline Core, Washington, USA. Journal of Metamorphic Geology, 29, 627–647.

Symmes, G.H., and Ferry, J.M. (1992) The effect of whole-rock MnO content on the stability of garnet in pelitic schists during metamorphism. Journal of Metamorphic Geology, 10, 221–237.

Thompson, C.V., and Spaepen, F. (1983) Homogeneous crystal nucleation in binary metallic melts. Acta Metall., 31, 2021–2027.

Thompson, J.B. (1957) The graphical analysis of mineral assemblages in pelitic schists. American Mineralogist, 42, 841–858.

Tinkham, D.K., and Ghent, E.D. (2005) Estimating P-T conditions of garnet growth with isochemical phase-diagram sections and the problem of effective bulk-composition. Canadian Mineralogist, 43, 35–50.

Tinkham, D.K., Zuluaga, C.A., and Stowell, H.H. (2001) Metapelite phase equilibria modeling in MnNCKFMASH: The effect of variable Al2O3 and MgO/(MgO+FeO) on mineral stability. Geological Materials Research, 3, 1–42.

Tomkins, H.S., and Pattison, D.R.M. (2007) Accessory phase petrogenesis in relation to major phase assemblages in pelites from the Nelson contact aureole, southern British Columbia. Journal of Metamorphic Geology, 25, 401–421.

Tracy, R.J. (1982) Compositional zoning and inclusions in metamorphic minerals. Characterization of Metamorphism through Mineral Equilbria: Mineralogical Society of America, 10, 355–397.

Tracy, R.J., Robinson, P., and Thompson, A.B. (1976) Garnet composition and zoning in the determination of temperatuer and pressure of metamorphism, central Massachusetts. American Mineralogist, 61, 762–775.

Vidal, O. (1999) Calibration and testing of an empirical chloritoid-chlorite Mg-Fe thermometer and thermodynamic data for daphnite. Journal of Metamorphic Geology, 17, 25–39.

Walther, J. V., and Wood, B.J. (1984) Rate and mechanism in prograde metamorphism. Contributions to Mineralogy and Petrology, 88, 246–259.

Waters, D.J. (2019) Metamorphic constraints on the tectonic evolution of the High Himalaya in Nepal: the art of the possible. Geological Society, London, Special Publications, 483, 325–375.

Waters, D.J., and Lovegrove, D.P. (2002) Assessing the extent of disequilibrium and overstepping of prograde metamorphic reactions in metapelites from the Bushveld Complex aureole, South Africa. Journal of Metamorphic Geology, 20, 135–149.

Weller, O.M., St-Onge, M.R., Waters, D.J., Rayner, N., Searle, M.P., Chung, S.L., Palin, R.M., Lee, Y.H., and Xu, X. (2013) Quantifying Barrovian metamorphism in the Danba Structural Culmination of eastern Tibet. Journal of Metamorphic Geology, 31, 909–935.

White, R.W., and Powell, R. (2002) Melt loss and the preservation of granulite facies mineral assemblages. Journal of Metamorphic Geology, 20, 621–632.

White, R.W., Powell, R., and Baldwin, J.A. (2008) Calculated phase equilibria involving chemical potentials to investigate the textural evolution of metamorphic rocks. Journal of Metamorphic Geology, 26, 181–198.

White, R.W., Powell, R., Holland, T.J.B., Johnson, T.E., and Green, E.C.R. (2014a) New mineral activity-composition relations for thermodynamic calculations in metapelitic systems. Journal of Metamorphic Geology, 32, 261–286.

White, R.W., Powell, R., and Johnson, T.E. (2014b) The effect of Mn on mineral stability in metapelites revisited: new a-x relations for manganese-bearing minerals. Journal of Metamorphic Geology, 32, 809–828.

Whitney, D.L., and Evans, B.W. (2010) Abbreviations for names of rock-forming minerals. American Mineralogist, 95, 185–187.

Wilbur, D.E., and Ague, J.J. (2006) Chemical disequilibrium during garnet growth: Monte Carlo simulations of natural crystal morphologies. Geology, 34, 689–692.

Wolfe, O.M., and Spear, F.S. (2018) Determining the amount of overstepping required to nucleate garnet during Barrovian regional metamorphism, Connecticut Valley Synclinorium. Journal of Metamorphic Geology, 36, 79–94.

Wood, B.J., and Walther, J. V. (1983) Rates of hydrothermal reactions. Science, 222, 413–415.

Yardley, B.W.D. (1978) Genesis of the Skagit Gneiss migmatites, Washington, and the distinction between possible mechanisms of migmatization. Geological Society of America Bulletin, 89, 941–951.

Zeh, A., and Holness, M.B. (2003) The effect of reaction overstep on garnet microtextures in metapelitic rocks of the Ilesha Schist Belt, SW Nigeria. Journal of Petrology, 44, 967–991.

Zuluaga, C., Stowell, H.H., and Tinkham, D.K. (2005) The effect of zoned garnet on metapelite pseudosection topology and calculated metamorphic P-T paths. American Mineralogist, 90, 1619–1628.

## 4.10 ACKNOWLEDGEMENTS

ABN acknowledges funding from the Virginia Tech ICTAS Doctoral Scholars Program. BD and MJC acknowledge support from NSF award OIA 1545903 (to M. Kohn, S. Penniston-Dorland, and M. Feineman). Harold Stowell, Oliver Wolfe, Jacob Forshaw, and an anonymous reviewer are thanked for constructive and helpful reviews. We thank Callum Hetherington for his handling of this paper as Associate Editor and David Pattison is thanked for comments on an earlier version of this manuscript. Members of the Metamorphic Processes Group at Virginia Tech are thanked for discussions on this project and Victor Guevara and Calvin Mako are thanked for detailed comments.

## 4.11 FIGURES

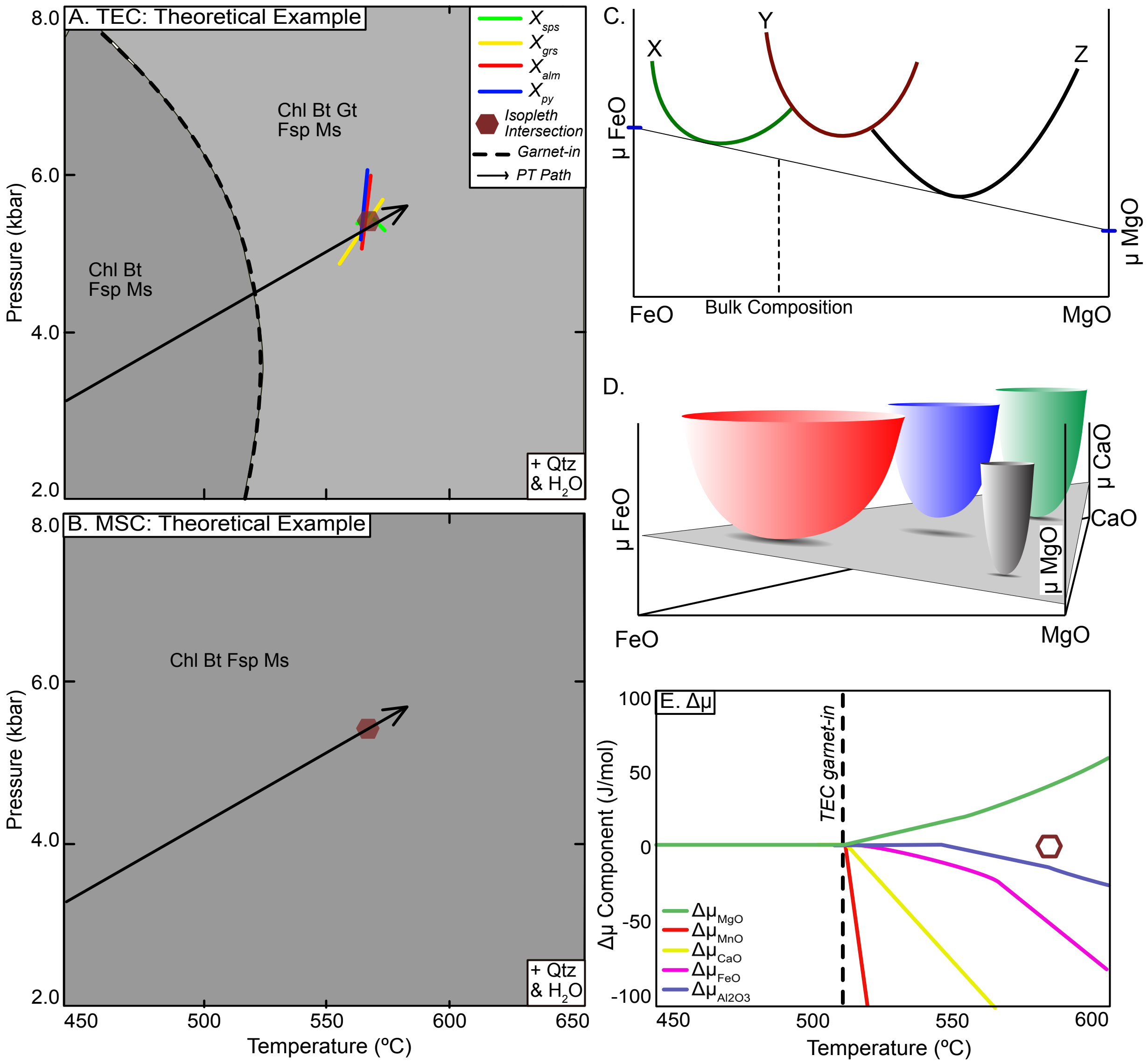

Figure 4.1. **Overview of the methodologies applied in this paper.** A. Schematic TEC pseudosection for a theoretical pseudosection (hypothetical bulk composition), with mineral abbreviations from Whitney & Evans (2010). Bold dashed line indicates the bounds of garnet stability. Compositional isopleths corresponding to measured garnet core compositions are shown in green ($X_{sps}$), yellow ($X_{grs}$), red ($X_{alm}$), and blue ($X_{prp}$). Maroon hexagon indicates the intersection of the garnet core isopleths and thus apparent garnet nucleation. Arrow represents

the shortest vector from garnet-in to this *P-T* condition. B. MSC pseudosection for the same hypothetical bulk composition, yielding an identical assemblage but without garnet. C. Free-energy–composition (*G-X*) diagram showing stable minerals X and Z and the tangent that defines the chemical potentials of MgO and FeO in a two-component system. D: *G-X* diagram showing stable minerals W, X and Z and the tangent plane in a three-component system. E: Differences in the chemical potential of oxide components between the calculations shown in A and B along the *P-T* path shown. in A and B (i.e. $\Delta\mu_{MgO} = \mu_{MgO\ TEC} - \mu_{MgO\ MSC}$).

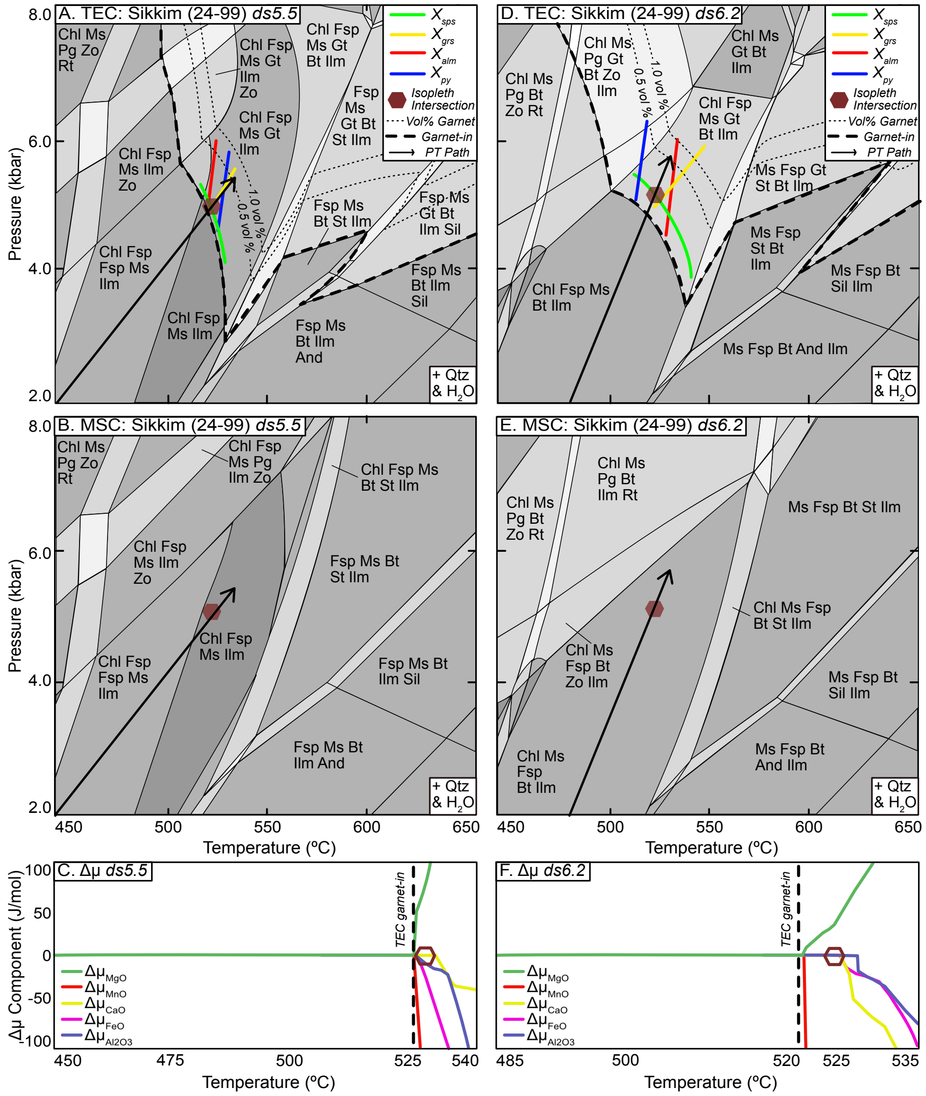

Figure 4.2. A. TEC pseudosection for sample 24-99 (Sikkim, Himalaya) calculated with ds5.5. B. MSC pseudosection for sample 24-99. C. $\Delta\mu_{\text{component}}$ along the *P-T* path shown in A & B. D. TEC pseudosection for sample 24-99 (Sikkim, Himalaya) calculated with ds6.2. E. MSC pseudosection for sample 24-99. C. $\Delta\mu_{\text{component}}$ along the *P-T* path shown in D & E.

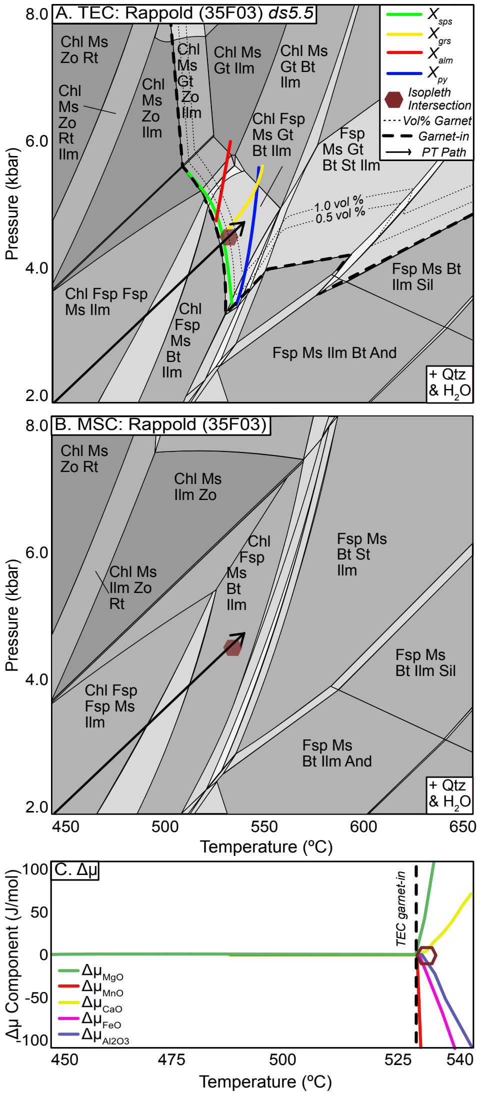

Figure 4.3. A. TEC pseudosection for sample 35F03 (Rappold Complex) calculated with ds5.5. B. MSC pseudosection for sample 35F03. C. $\Delta\mu_{component}$ along the *P*-*T* path shown in A & B.

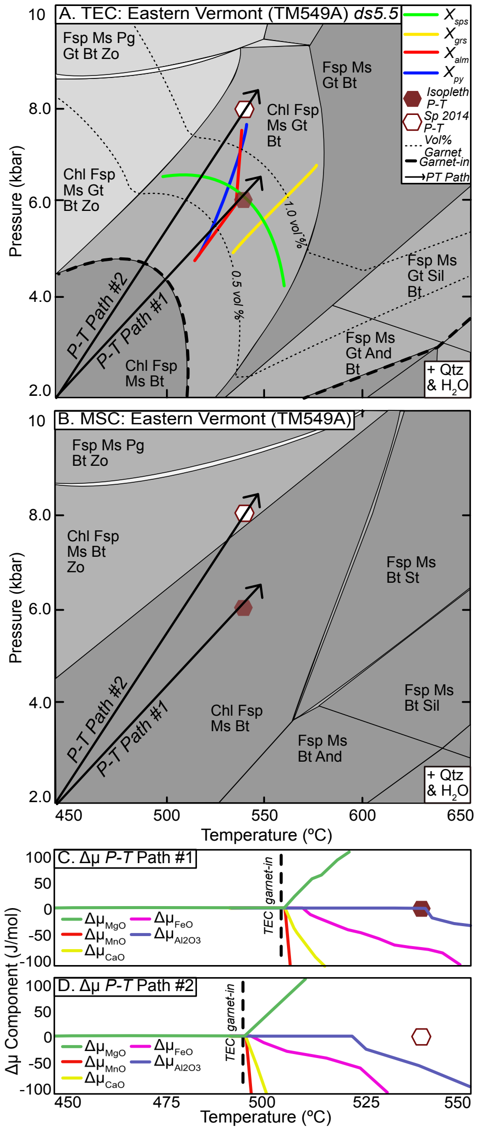

Figure 4.4. A. TEC pseudosection for sample TM549A (Eastern Vermont) calculated with ds5.5. B. MSC pseudosection for sample TM549A. C. $\Delta\mu_{\text{component}}$ along *P-T* path #1 shown in A & B. D. $\Delta\mu_{\text{component}}$ along *P-T* path #2 shown in A & B.

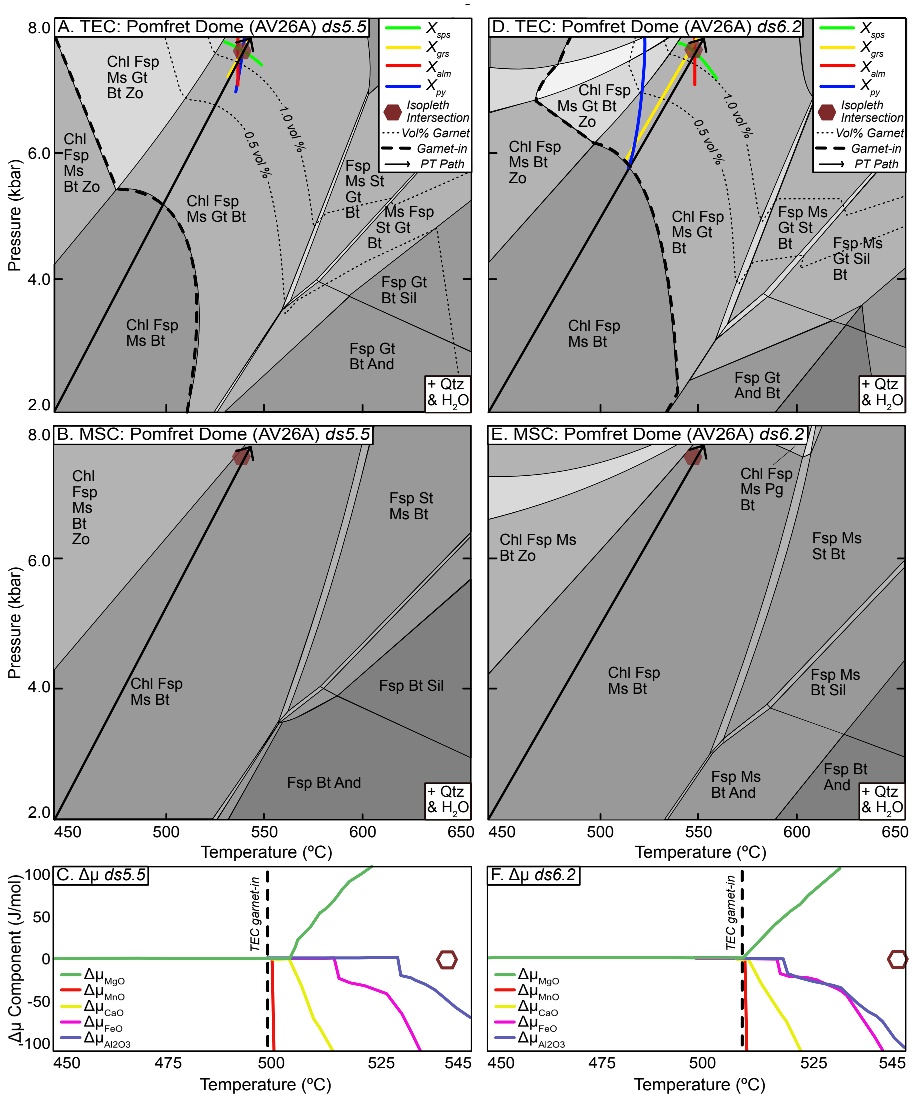

Figure 4.5. A. TEC pseudosection for sample AV26A (Pomfret Dome) calculated with ds5.5. B. MSC pseudosection for sample AV26A. C. $\Delta\mu_{\text{component}}$ along the *P-T* path shown in A & B. D. TEC pseudosection for sample AV26A (Pomfret Dome) calculated with ds6.2. E. MSC pseudosection for sample AV26A. F. $\Delta\mu_{\text{component}}$ along the *P-T* path shown in A & B.

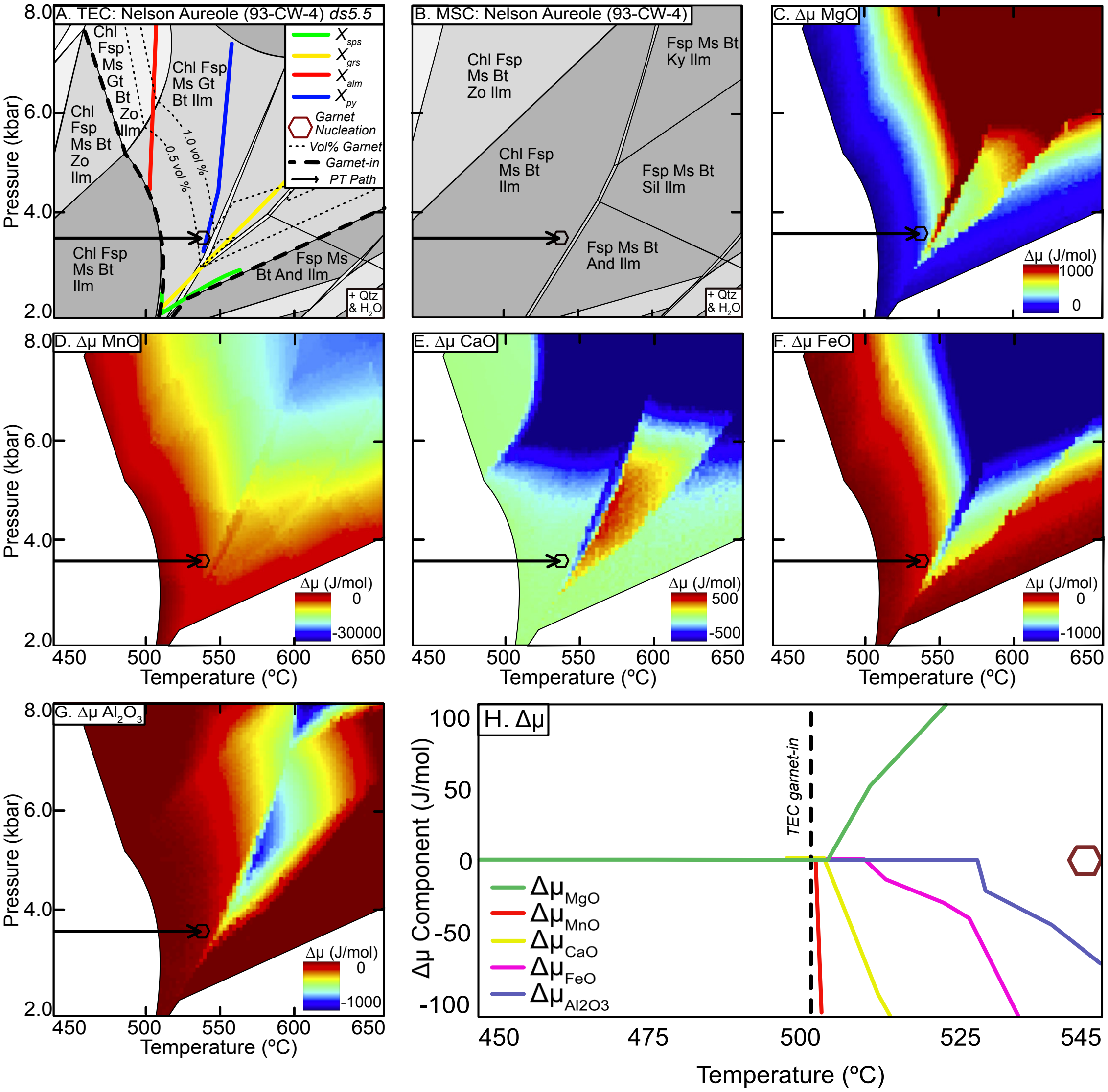

Figure 4.6. A. TEC pseudosection for sample 93-CW-4 (Nelson Aureole), calculated with ds5.5. B. MSC pseudosection for sample 93-CW-4. C-G. $\Delta\mu_{MgO}$, $\Delta\mu_{MnO}$, $\Delta\mu_{FeO}$ $\Delta\mu_{CaO,}$ and $\Delta\mu_{Al2O3}$ as functions of *P* and *T*. H. $\Delta\mu_{component}$ along the heating path shown in A-G.

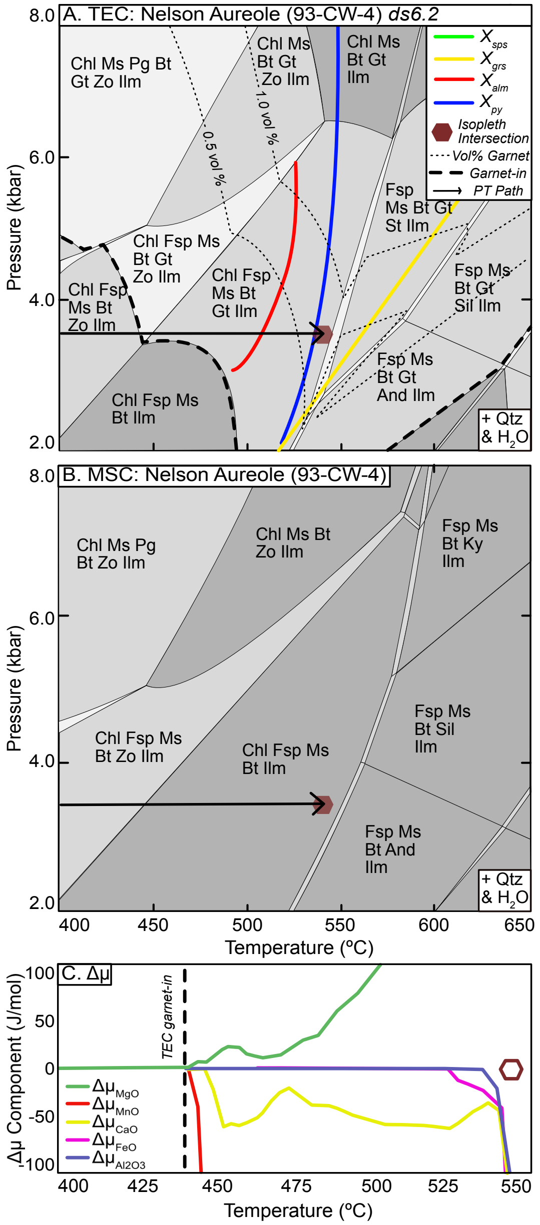

Figure 4.7. A. TEC pseudosection for sample 93-CW-04 (Nelson Aureole) calculated with ds6.2. B. MSC pseudosection for sample 93-CW-04. C. $\Delta\mu_{\text{component}}$ along the *P*-*T* path shown in A & B.

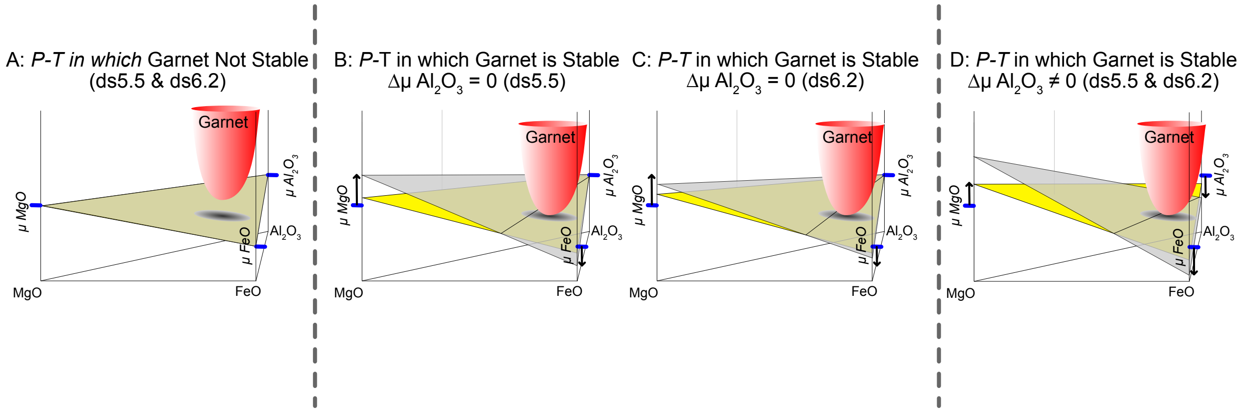

Figure 4.8. A: Schematic three component *G-X* diagram at *P-T* conditions where garnet is not stable in the TEC. Gray triangle is the tangent plane through stable phases whose *G-X* surfaces have been removed for clarity. B. *G-X* diagram at *P-T* conditions where garnet is stable in the TEC but has been prohibited in the MSC (yellow tangent plane). $\mu_{MgO}$ and $\mu_{FeO}$ are different between the TEC and MSC but $\Delta\mu_{Al2O3}$ is the same in each. C. Further increase in $\Delta\mu_{MgO}$ and $\Delta\mu_{FeO}$ without developing $\Delta\mu_{Al2O3}$. D. A *G-X* diagram for *P-T* conditions at which the chemical potentials of all three components differ between the TEC and MSC.

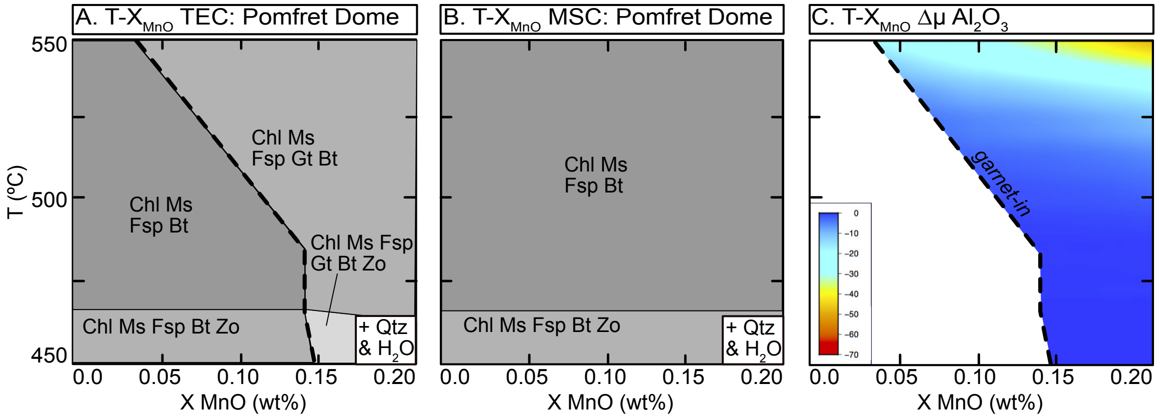

Figure 4.9. A. *T-X*$_{MnO}$ TEC diagram for sample AV26A at *P* = 5.0 kbar. *X* axis ranges from 0.0 wt% MnO to 0.2 wt% MnO. Dashed line denotes garnet-in. B. *T-X*$_{MnO}$ MSC diagram for sample AV26A at *P* = 5.0 kbar. C. *T-X*$_{MnO}$ diagram contoured for $\Delta\mu_{Al2O3}$ (J/mol).

## 4.12 TABLES

Table 4.1 Comparison of amount of overstepping reported in the literature and that calclated in this study using the THERMOCALC ds5.5 thermodynamic dataset. ** = sample described in main text. * =sample described in Supplemental Material

| | | | **Reported in the Literature** | | **This Study (ds5.5)** | |
|---|---|---|---|---|---|---|
| Location | Sample # | Original Source | *P-T* of Garnet Nucleation | Amount of Apparent Overstep | *P-T* of Garnet Nucleation | Amount of Apparent Overstep |
| | | **Examples with Minimal Overstepping (<10°C and 0.5 kbar)** | | | | |
| Sikkim, Himalaya ** | 24-99 | Gaidies et al. 2015 | 520°C 4.5 kbar | 0°C 0 kbar | 526°C 5.0 kbar | 0°C 0 kbar |
| Rappold Complex ** | 35F03 | Gaidies et al. 2008 | 530°C 5.2 kbar | 0°C 0 kbar | 531°C 4.4 kbar | 0°C 0 kbar |
| Eastern Tibet * | W122 | Weller et al. 2013 | not reported | not reported | 547°C 4.9 kbar | 0°C 0 kbar |
| Kootenary Arc * | DM_06_128 | Moyniham & Pattison 2013 | 500°C 5.2 kbar | <10°C <0.5 kbar | 491°C 5.0 kbar | 4°C 0.2 kbar |
| | | **Examples with Apparent Overstepping (>10°C and 0.5 kbar)** | | | | |
| Eastern Vermont ** | TM549a | Spear et al. 2014 | 540°C 8.0 kbar | 10°C 0.6 kbar | 540°C 5.8 kbar | 35°C 1.5 kbar |
| Pomfret Dome ** | AV26A | Bell et al. 2013 | 550°C 8.0 kbar | 30°C 1.5 kbar | 540°C 7.4 kbar | 38°C 2.3 kbar |
| Nelson Aureole ** | 93-CW-4 | Gaidies et al. 2011 | 545°C 3.5 kbar | 30°C 0 kbar | 545°C 3.5 kbar | 43°C 0 kbar |
| Southeastern Ontario * | 12TM16 | McCarron et al. 2014 | 512°C 4.0 kbar | 32°C 1.1 kbar | 530°C 4.4 kbar | 34°C 1.0 kbar |
| Southwest Turkey * | ED34 | Etzel et al. 2019 | 565°C 6.0 kbar | 25°C 0.8 kbar | 550°C 6.3 kbar | 26°C 1.2 kbar |
| Central Himalaya * | D13-75 | Iaccarino et al. 2017 | 520°C 5.5 kbar | 30°C 0.7 kbar | 530°C 5.4 kbar | 22°C 1.0 kbar |
| Albion Mountains * | TH203B | Kelly et al. 2015 | 550°C 5.1 kbar | 50°C 0.7 kbar | 550°C 6.3 kbar | 43°C 1.9 kbar |
| Funeral Mountains * | SSFM307-7G | Craddock-Affinati et al. 2020 | 550°C 6.1 kbar | >50°C >2 kbar | 552°C 7.1 kbar | 34°C 1.7 kbar |

Table 4.2 Summary of Results for 12 Samples Calculated Using THERMOCALC ds5.5. ** = sample described in main text. * =sample described in Supplemental Material.

| Location | *P-T* of Garnet Isograd | *P-T* of Garnet Nucleation | Amount of Apparent Overstep | First Component(s) whose Δμ ≠ 0 | *P-T* Conditions Where First Δμcomponent ≠ 0 | Δ*T* & Δ*P* Between *P-T* of Garnet-in and *P-T* Where First Component(s) ≠ 0 | Final Component(s) whose Δμ ≠ 0 | *P-T* Conditions Where Last Δμcomponent ≠ 0 | Δ*T* & Δ*P* Between *P-T* of Garnet-in and *P-T* Where Last Component(s) ≠ 0 |
|---|---|---|---|---|---|---|---|---|---|
| **Examples with Minimal Overstepping (<10ºC and 0.5 kbar)** | | | | | | | | | |
| Sikkim, Himalaya ** | 526ºC 5.0 kbar | 526ºC 5.0 kbar | 0ºC 0 kbar | MnO, MgO, $Al_2O_3$, FeO | 526ºC 5.0 kbar | 0ºC 0 kbar | CaO | 530ºC 5.2 kbar | 4ºC 0.2 kbar |
| Rappold Complex ** | 531 ºC 4.4 kbar | 531ºC 4.4 kbar | 0ºC 0 kbar | MnO, MgO, $Al_2O_3$, FeO, CaO | 531ºC 4.4 kbar | 0ºC 0 kbar | N/A | N/A | N/A |
| Eastern Tibet * | 547ºC 4.9 kbar | 547ºC 4.9 kbar | 0ºC 0 kbar | MnO, MgO, FeO, CaO | 547ºC 4.9 kbar | 0ºC 0 kbar | $Al_2O_3$ | 549ºC 4.9 kbar | 2ºC 0 kbar |
| Kootenary Arc * | 487ºC 4.8 kbar | 491ºC 5.0 kbar | 4ºC 0.2 kbar | MnO, MgO, FeO, CaO | 487ºC 4.8 kbar | 0ºC 0 kbar | $Al_2O_3$ | 492ºC 5.1 kbar | 5ºC 0.3 kbar |
| **Examples with Apparent Overstepping (>10ºC and 0.5 kbar)** | | | | | | | | | |
| Eastern Vermont ** | 505 ºC 4.3 kbar | 540ºC 5.8 kbar | 35ºC 1.5 kbar | MnO, MgO, CaO | 505ºC 4.3 kbar | 0ºC 0 kbar | $Al_2O_3$ | 541ºC 5.8 kbar | 36ºC 1.5 kbar |
| Pomfret Dome ** | 502 ºC 5.1 kbar | 540ºC 7.4 kbar | 38ºC 2.3 kbar | MnO | 502ºC 5.1 kbar | 0ºC 0 kbar | $Al_2O_3$ | 530ºC 6.7 kbar | 28ºC 1.6 kbar |
| Nelson Aureole ** | 502 ºC 3.5 kbar | 545ºC 3.5 kbar | 43ºC 0 kbar | MnO | 502ºC 3.5 kbar | 0ºC 0 kbar | $Al_2O_3$ | 528ºC 3.5 kbar | 26ºC 0 kbar |
| Southeastern Ontario * | 496 ºC 3.4 kbar | 530ºC 4.4 kbar | 34ºC 1.0 kbar | MnO, MgO | 496ºC 3.4 kbar | 0ºC 0 kbar | $Al_2O_3$ | 513ºC 3.8 kbar | 17ºC 0.4 kbar |
| Southwest Turkey * | 524 ºC 5.1 kbar | 550ºC 6.3 kbar | 26ºC 1.2 kbar | MnO, MgO | 524ºC 5.1 kbar | 0ºC 0 kbar | $Al_2O_3$, CaO | 532ºC 5.5 kbar | 8ºC 0.4 kbar |
| Central Himalaya * | 508 ºC 4.4 kbar | 530ºC 5.4 kbar | 22ºC 1.0 kbar | MnO, FeO, MgO, CaO | 508ºC 4.4 kbar | 0ºC 0 kbar | $Al_2O_3$ | 532ºC 5.5 kbar | 24ºC 1.1 kbar |
| Albion Mountains * | 507 ºC 4.4 kbar | 550ºC 6.3 kbar | 43ºC 1.9 kbar | MnO, MgO, CaO | 507ºC 4.4 kbar | 0ºC 0 kbar | $Al_2O_3$ | 532ºC 5.5 kbar | 25ºC 1.1 kbar |
| Funeral Mountains * | 518 ºC 5.4 kbar | 552ºC 7.1 kbar | 34ºC 1.7 kbar | MnO, MgO | 518ºC 5.4 kbar | 0ºC 0 kbar | $Al_2O_3$ | 551ºC 7.0 kbar | 33ºC 1.6 kbar |

Table 4.3 Summary of Results for 5 Samples Calculated with THERMOCALC ds6.2 ** = sample described in main text. * =sample described in Supplemental Material.

| Location | *P-T* of Garnet Isograd | *P-T* of Garnet Nucleation | Amount of Apparent Overstep | First Component(s) whose Δμ ≠ 0 | *P-T* Conditions Where First Δμcomponent ≠ 0 | Δ*T* & Δ*P* Between *P-T* of Garnet-in and *P-T* Where First Component(s) ≠ 0 | Final Component(s) whose Δμ ≠ 0 | *P-T* Conditions Where Last Δμcomponent ≠ 0 | Δ*T* & Δ*P* Between *P-T* of Garnet-in and *P-T* Where Last Component(s) ≠ 0 |
|---|---|---|---|---|---|---|---|---|---|

|  |  |  |  |  |  |  |  |  |  |
|---|---|---|---|---|---|---|---|---|---|
| **Examples with Minimal Overstepping (<10ºC and 0.5 kbar)** |  |  |  |  |  |  |  |  |  |
| Sikkim, Himalaya ** | 522ºC 4.9 kbar | 525ºC 5.2 kbar | 3ºC 0.3 kbar | MnO, MgO | 522ºC 4.9 kbar | 0ºC 0 kbar | $Al_2O_3$ | 528ºC 5.5 kbar | 6ºC 0.6 kbar |
| Rappold Complex * | 525ºC 4.4 kbar | 537ºC 4.9 kbar | 12ºC 0.5 kbar | MnO | 525ºC 4.4 kbar | 0ºC 0 kbar | $Al_2O_3$ | 541ºC 5.0 kbar | 16ºC 0.6 kbar |
| **Examples with Apparent Overstepping (>10ºC and 0.5 kbar)** |  |  |  |  |  |  |  |  |  |
| Eastern Vermont * | 505ºC 4.3 kbar | 550ºC 6.3 kbar | 45ªC 2.0 kbar | MnO | 505ºC 4.3 kbar | 0ºC 0 kbar | $Al_2O_3$ | 531ºC 5.4 kbar | 26ºC 1.1 kbar |
| Pomfret Dome ** | 510ºC 5.5 kbar | 548ºC 7.8 kbar | 38ºC 2.3 kbar | MnO, MgO, CaO | 510ºC 5.5 kbar | 0ºC 0 kbar | $Al_2O_3$ | 520ºC 6.1 kbar | 10ºC 0.6 kbar |
| Nelson Aureole ** | 443ºC 3.5 kbar | 545ºC 3.5 kbar | 102ºC 0 kbar | MnO, MgO | 443ºC 3.5 kbar | 0ºC 0 kbar | $Al_2O_3$ | 539ºC 3.5 kbar | 96ºC 0 kbar |

# Chapter 5: Metamorphism of the southwestern Meguma Terrane, Nova Scotia, Canada

Nagurney, A.B.[1], Caddick, M.J.[1]

[1] *Department of Geosciences, Virginia Tech, 926 West Campus Drive, Blacksburg, VA, 24060 USA,*

This chapter will be submitted to the Journal of Metamorphic Geology.

## 5.1 ABSTRACT

We present data on the metamorphic pressure and temperature conditions experienced by rocks of the Meguma Terrane, Nova Scotia, also utilizing three-dimensional microstructural data on one sample to better constrain the mechanisms that controlled its garnet crystallization. Inverse and forward thermodynamic modeling place peak *P-T* conditions at ~650ºC and 4.5 kbar in the southwestern Meguma Terrane. Interpretation of these results with petrographic observations and previous *P-T* constraints across the terrane suggest that the southwestern Meguma Terrane was likely at amphibolite facies during the Devonian NeoAcadian orogeny (405-395 Ma) and that the intrusion of granitic plutons at ~373 Ma likely drove metamorphic recrystallization locally. The 3D size, shape, and location of garnet crystals in one sample reveal that the rate limiting step for garnet crystallization was likely the diffusion of aluminum through the intergranular matrix. Nucleation was aided by epitaxial overgrowth onto a muscovite substrate. Integration of our data on the 3D location and size of garnet crystals, the metamorphic heating rate, and the role of epitaxy in garnet crystallization with data from other studies helps provide a more holistic understanding of garnet crystallization. This has implications for understanding metamorphic and tectonic processes during the formation of the Appalachian Mountains and for understanding the atomic-scale mechanisms controlling garnet crystallization during metamorphism.

## 5.2 INTRODUCTION

Integrating pressure-temperature (*P-T*) constraints on metamorphism with studies of metamorphic porphyroblast crystallization can provide a holistic understanding of metamorphic petrogenesis. This is especially useful in areas in which it appears that the resulting pattern of mineral assemblages may be a function of polymetamorphism. Petrographic textures, inverse and forward thermodynamic modeling, and 3D microstructural information can all be utilized to unravel metamorphic histories, and then interpreted to constrain past tectonic processes. This study applies these methodologies to amphibolite facies rocks of the southwestern Meguma Terrane, Nova Scotia, interrogating the metamorphic rock record to better understand the relative effects of regional metamorphism versus contact metamorphic heating during terrane accretion in the Appalachian orogen.

The Meguma Terrane is the most outboard terrane of the Appalachian Orogen and it accreted on to the Avalon Terrane to the west 405-395 Ma during the Neoacadian Orogeny (Taylor and Schiller 1966; Keppie and Dallmeyer 1995; Waldron et al. 2009; van Staal and Barr 2012). From 405-345 Ma it underwent a multi-stage history including: i) regional metamorphism during terrane accretion, ii) granitic plutonism driven by slab delamination, iii) contact metamorphic overprint of the previously regionally metamorphosed rocks, and iv) uplift and cooling. However, it is currently unclear which areas of the resulting metamorphic pattern are the result of regional metamorphism, contact metamorphism, or a combination of the two.

*P*-*T* constraints on metamorphism can provide insight into past tectonic processes. This follows from the fact that different tectonic processes can result in metamorphic rocks that experience different *P*-*T* paths through the crust (Spear et al. 1984; Thompson and England 1984; Pattison et al. 1999; Wakabayashi 2004; Wells et al. 2012; Hillenbrand et al. 2021). It is, however, often difficult to infer a unique path for complex rocks, with evidence of early conditions of prograde metamorphism being particularly poorly preserved. Furthermore, application of multiple methods of thermobarometry sometimes reveals significant disparities, raising questions about the processes and length-scales of equilibration. Although quantification of metamorphic *P*-*T* conditions has systematically re-affirmed the concept of the metamorphic facies for over forty years, quantitative understanding of the competition between the atomic-scale processes that facilitate or retard metamorphic equilibration is still lacking. This is especially important to understand in minerals, such as garnet, whose composition can record: i) the *P-T* evolution of metamorphic rocks and ii) the timing and duration of metamorphism (Caddick and Kohn 2013; Baxter et al. 2017).

Understanding of the 3D size, shape, and location of garnet porphyroblasts can provide a more holistic understanding of metamorphic porphyroblast crystallization and be interpreted to infer, for example, the rate limiting step for garnet growth (Kretz 1966, 1974; Carlson 1989, 2011; Carlson and Denison 1992; Ketcham 2005; Whitney et al. 2008; Hirsch 2008; Ketcham and Carlson 2012; Kelly et al. 2013a, 2013b; Gaidies et al. 2015, 2020; George and Gaidies 2017). These methods typically reveal that one of two end member scenarios acted as the rate limiting step for garnet crystallization: interface-controlled nucleation and growth (ICNG), in which the rate limiting step is the attachment of particles on to the surface of a garnet crystal, and diffusion-controlled nucleation and growth (DCNG), in which the intergranular diffusion of nutrients to the growing porphyroblast is rate limiting (Carlson 2011). It is likely that both processes can control porphyroblast crystallization, with some rocks showing strong evidence for ICNG (Gaidies et al. 2011, 2015) and others clearly being controlled by DCNG (Hirsch 2008; Ketcham and Carlson 2012; Kelly et al. 2013b, 2013a). However, the specific factors that control when a rock will fall into either regime are still poorly enough constrained that forward models of complex rock textures are still difficult to attain.

The relatively straightforward model of DCNG versus ICNG may be complicated by fact that garnet has also been shown to preferentially crystallize epitaxially on muscovite (Spiess et al. 2007; Moore et al. 2015; George and Gaidies 2020; Nagurney et al. 2021). This suggests that the distribution of both reactant (nutrient-providing) minerals and potential substrate (template-providing) minerals may play an important role in garnet crystallization, but connections between this and the dominance of either diffusion or interface-controlled growth are not well understood.

Here, we integrate new *P-T* data with previous constraints on the metamorphism of the Meguma Terrane, interpreting them in the context of previously-described tectonic models for microcontinent accretion to better constrain tectonic processes during the NeoAcadian orogen. We also study the 3D size, shape, and distribution of garnet crystals in a single sample to interpret: (i) the general controls of whether garnet crystallizes via DCNG or ICNG, and (ii) how consideration of both epitaxial nucleation and models for DCNG or ICNG can provide a more holistic understanding of garnet crystallization.

## 5.3 GEOLOGIC BACKGROUND

The Appalachian Orogen in Canada is the result of a series of microcontinent accretions from the Cambrian (515 Ma) through the Permian (275 Ma) that culminated in the continent-continent collision that formed supercontinent Pangaea (e.g. Wilson 1966; Williams 1979; Williams and Hatcher 1982; van Staal et al. 2009; Hibbard et al. 2010; van Staal and Barr 2012). The Meguma Terrane is the most eastward expression of the Appalachian Orogen in Canada, and is bounded to the west by the Avalon Terrane (Fig. 1A). The Meguma Terrane is comprised of a thick (>11 km) sequence of Cambrian to Lower Ordovician metasediments divided into the lower (primarily sandstone) Goldenville Group and upper (dominantly shale) Halifax Group (White and Barr 2010) that were likely originally deposited in a rift basin (Waldron et al. 2009). The contact between the Goldenville and Halifax groups is defined by the Mn-rich sulphidic Mosher's Island formation, which at higher metamorphic grades contains spessartine garnet coticule layers (Schenk 1997; White and Barr 2010; Waldron and White 2011).

During the Devonian Neoacadian Orogeny (415-395 Ma), the Meguma microcontinent was thrust over the Avalon Terrane to the west (van Staal and Barr 2012), resulting in regional greenschist facies metamorphism and northeast-southwest trending folding of the Meguma Terrane (Reynolds et al. 1973, 2012; Dallmeyer and Keppie 1986, 1988; Keppie and Dallmeyer 1987, 1995; Muecke et al. 1988; Hicks et al. 1999). At 373 Ma, upwelling of heat and magma from the mantle, either the result of delamination or the Meguma terrane overriding a hot spot (Keppie and Dallmeyer 1995; Murphy et al. 1999; Moran et al. 2007), melted the Meguma crust. This recrystallized to form a series of granitoid plutons: the South Mountain Batholith, Port Mouton Pluton, Shelburne Pluton, and Barrington Passage Pluton (e.g. Clarke et al. 1997; Clarke et al. 2015; Clarke et al. 2000; Currie et al. 1998; Jamieson et al. 2012; McKenzie & Clarke 1975; Pattison et al. 1999; Reynolds et al. 1987; Tate & Clarke 1997). U-Pb monazite, titanite, and zircon geochronology of those plutons tightly constrain their formation to 373 Ma (Keppie and Dallmeyer 1995; Tate and Clarke 1995; Currie et al. 1998; Keppie and Krogh 1999).

Metamorphic grade generally increases to the southwest in the Meguma terrane, reaching amphibolite facies (Fig. 1B) (Taylor and Schiller 1966; Raeside and Jamieson 1992; Hwang 1997; Currie et al. 1998; Pattison et al. 1999; Pattison and Spear 2018). Of the granitoid plutons, only the South Mountain Batholith has a distinct contact metamorphic aureole. The contact aureole is <3 km wide, recording *P-T* conditions ~650ºC at 2.5-3.0 kbar (Jamieson et al. 2012; Hilchie and Jamieson 2014). The areas surrounding the Shelburne and Port Mouton plutons reached ~520-620ºC at ~4.5 kbar (Currie et al. 1998). The presence of late stage cordierite in metasediments surrounding the Shelburne Pluton suggests a polymetamorphic path for these rocks: it is likely that these rocks followed a clockwise *P-T* path in which a higher pressure (staurolite bearing) assemblage was overprinted by a later, lower pressure (cordierite bearing) event (Pattison et al. 1999). Both the Shelburne Pluton and Port Mouton Pluton contain pegmatites associated with the granitoid intrusions, but there is no pegmatite associated with the Barrington Passage Pluton (Currie et al. 1998).

The formation of extensive gold, copper, and other economic mineral deposits was contemporaneous with 373 Ma plutonism (Kontak et al. 1990a; Kontak and Kerrich 1997; Carruzzo et al. 2004). These mineral deposits are associated with quartz veins, indicating substantial fluid movement during the Devonian (Kontak et al. 1990a). Thus, aqueous fluid availability and movement may have played an important role in the metamorphism of the Meguma Terrane (Pattison et al. 1999). Post plutonism and metamorphism, the Meguma Terrane underwent rapid exhumation. Based on $^{40}Ar/^{39}Ar$ age spectra of biotite, the central Meguma Terrane cooled to below 300ºC by 368-360 Ma, and the southern Meguma Terrane cooled below 300ºC by 345 Ma (Dallmeyer and Keppie 1988; Keppie and Dallmeyer 1995).

It is not currently known whether amphibolite facies metamorphic rocks in the southwestern Meguma terrane are the result of regional metamorphism during the Neoacadian Orogeny, a contact metamorphic overprint from the intruding granitic plutons, or a combination of both. Understanding the drivers of metamorphism in the Meguma terrane has important implications for the metamorphic and tectonic evolution of eastern North America, as well as our understanding of the drivers of metamorphism during microcontinent collision. To investigate this, we performed microstructural analyses and determined the *P-T* conditions of metamorphism in a suite of samples from the area around the Barrington Passage Pluton (Fig. 1C). This specific field area was chosen because it preserves the largest difference in metamorphic grade over a relatively small (< 10 km) field distance, allowing for investigation of the relative effects of regional versus contact metamorphism on the Meguma terrane metasediments. This detailed *P-T* study of the Barrington Passage area was then compared to previous *P-T* constraints across the Meguma Terrane, which allowed us to determine the broader effects of regional versus contact metamorphism across the terrane. This, in turn, allowed us to integrate these *P-T* constraints with previous tectonic models for the formation of the Meguma Terrane.

## 5.4 METHODS

Element mapping of garnet and quantitative major element compositional analyses were performed on an ARL-SEMQ electron probe microanalyzer (EPMA) at Concord University and a CAMECA SX-50 EPMA at Virginia Tech. X-ray maps were created using both energy dispersive and wavelength dispersive spectrometry (EDS and WDS, respectively). Natural and synthetic samples were used as standards. Quantitative spot analyses used a 15-20 kV accelerating voltage, 20 nA beam current, and ~5 μm spot size. Whole rock major element analysis was performed at the Department of Earth and Environment at Franklin and Marshall College using a Malvern PANalytical Zetium X-ray fluorescence (XRF) vacuum spectrometer, following methods described by Boyd and Mertzman (1987). The presence of extremely large (~10 cm scale) andalusite porphyroblasts in many samples results in extreme compositional heterogeneity on the hand-sample scale, so XRF bulk rock composition is only presented for one sample without these porphyroblasts (2018PPGrt_01).

Metamorphic *P-T* conditions were determined by a combination of thermodynamic forward modeling, Ti-in-biotite thermometry, garnet-biotite thermometry, and garnet-aluminosilicate-plagioclase (GASP) barometry. Isochemical phase diagrams (pseudosections) were calculated in the $MnO-Na_2O-CaO-K_2O-FeO-MgO-Al_2O_3-SiO_2-H_2O-TiO_2$ system using Perple_X 6.8.3 (Connolly 2005) and the tds6.2 (‘hp11’) thermodynamic dataset (Holland and Powell 2011), with solution models for biotite, chlorite, chloritoid, cordierite, garnet, muscovite, and staurolite from White et al., (2014) (White et al. 2014) and feldspar from Holland and Powell (2003) (Holland and Powell 2003). Ilmenite was modeled as an ideal ilmenite- geikielite-pyrophanite ternary solution.

The three-dimensional location, size, and shape of garnet crystals in 2018PPGrt_01 was characterized using an NSI CT Scanner at the University of Texas, Austin. The scan used 150 kV and 0.24 mA X-Ray source, an aluminum filter, and a Perkin Elmer detector. 2D slices with voxel size of 24.9 μm were acquired and rendered into the 3D image. Post reconstruction, a beam hardening and ring correction was applied to the data. The size and location of individual garnet crystals were found using Blob3D (Ketcham et al. 2005) and utilized to make the crystal size distribution (CSD). The 3D location and size of garnet porphyroblasts were statistically analyzed using Reduce3D (Hirsch 2011).

## 5.5 RESULTS

### 5.5.1 Petrographic and field observations

Samples 2018PPGrt_01, 2018PPGrt_03A, 2018PPAnd_01A, 2018PPAnd_02A, 2018PPAnd_03, and 400RR were collected from coastal outcrops, quarries, road and river cuts.

Sample 2018PPGrt_01 is a metapelite from the Mosher’s Island Formation that contains garnet and staurolite porphyroblasts in a fine-grained matrix of chlorite, muscovite, biotite, quartz, feldspar, and ilmenite. Garnet porphyroblasts are euhedral (~300 μm in diameter) and contain quartz inclusions in the core and mantle, but the rims are relatively inclusion-free (Fig. 2A-B). Staurolite porphyroblasts contain abundant inclusions of garnet, quartz, and ilmenite (Fig. 2A-B). Chlorite, muscovite, and ilmenite define the $S_1$ foliation. Garnet and staurolite both overgrow the $S_1$ foliation.

Sample 2018PPAnd_03 contains garnet, staurolite, biotite, and andalusite porphyroblasts in a matrix of quartz, plagioclase, muscovite and ilmenite. Garnet porphyroblasts are ~400 µm in diameter and contain minor quartz inclusions. Staurolite porphyroblasts are anhedral and contain quartz inclusions. It appears that, in some places, staurolite replaced biotite to create a pseudomorphic texture. Biotite porphyroblasts are ~600 µm in diameter and are deformed. Andalusite overgrows all minerals except for muscovite, which defines the foliation and wraps around all of porphyroblasts.

Sample 2018PPGrt_03A is a metapelite that contains garnet, staurolite, and andalusite porphyroblasts in a matrix of biotite, quartz, and feldspar (Fig. 2C). Ilmenite is also present in this sample and muscovite occurs as late-stage overgrowths. Andalusite porphyroblasts contain inclusions of randomly aligned biotite and muscovite, garnet, quartz, and ilmenite. Staurolite porphyroblasts contain garnet, quartz, and ilmenite conclusions. Staurolite also contains inclusion free areas that likely represent staurolite overgrowing former biotite grains through a different growth reaction (Farber et al. 2014). The former biotite grains appear to be randomly oriented, which suggest that biotite was not defining a foliation in the rock prior to the crystallization of staurolite (Fig. 2C). Textural relationships between staurolite and andalusite suggest that staurolite formed first. Garnet porphyroblasts are ~500 µm in diameter and contain quartz and ilmenite inclusions. There is no clear foliation preserved by inclusions in andalusite. The matrix surrounding garnet, staurolite, and andalusite porphyroblasts exhibits an $S_1$ foliation defined primarily by the alignment of biotite. The $S_1$ foliation wraps around the garnet, staurolite, and andalusite porphyroblasts, suggesting that garnet, staurolite, and andalusite predate the $S_1$ foliation. Muscovite crystals cross cut this foliation and are themselves deformed, suggesting another stage of deformation, post $S_1$.

Sample 2018PPAnd_01A was collected from the Mosher's Island Formation. It contains a layer of spessartine garnet crystals that has previously been reported as indicative of the Mosher's Island Formation across the southwestern Meguma Terrane (White and Barr 2010). The rest of the sampled outcrop contains 5-7 cm long andalusite porphyroblasts that are randomly oriented (Fig. 2D), but andalusite in Sample 2018PPAnd_01A occurs as 5-7 cm crystals. The sample also contains garnet and biotite, coexisting with matrix muscovite, feldspar, quartz, ilmenite, chlorite, and sillimanite. Garnet, biotite, quartz, and ilmenite are present as inclusions in the andalusite porphyroblasts (Fig. 2E). Those garnet and biotite crystals themselves contain quartz inclusions. Quartz defines an $S_1$ foliation in garnet that is continuous with quartz inclusions in andalusite. Muscovite defines an $S_2$ foliation that wraps around the andalusite, garnet, and biotite porphyroblasts. The $S_1$ foliation in the garnet crystals is at a high angle to the $S_2$ muscovite-defined foliation. Chlorite replaces biotite and garnet. Minor fibrolite sillimanite is only found around biotite crystals.

Sample 2018PPAnd_02A is very similar to 2018PPAnd_01A, but with dramatically larger (5-7 cm long), randomly oriented andalusite porphyroblasts. 2018PPAnd_02A contains 'biotite box' structures in andalusite that are clear in hand sample and thin section (Fig. 2F) and are absent from sample 2018PPAnd_01A. The 'biotite box' is defined as the rectaungular-like alignment of biotite inside andalusite crystals. Inside the biotite box, the andalusite contains garnet (~250 μm), quartz, biotite, and ilmenite inclusions. Ilmenite defines the $S_1$ foliation here. There is minor biotite inside the biotite box. Both inside and outside the biotite box, garnet crystals contain fluid inclusions and quartz inclusions in their cores and mantles, but the rims are inclusion free (Fig. 2G). Outside of the andalusite porphyroblast, muscovite defines the $S_2$

foliation, wrapping around the andalusite porphyroblasts. There is also minor fibrolite sillimanite present around biotite crystals.

Sample 400RR was collected from the edge of the Barrington Passage Pluton. It contains garnet, cordierite, biotite, muscovite, quartz, plagioclase, sillimanite, chlorite and ilmenite (Fig. 2H-I). Garnet contains quartz inclusions in its core, but has relatively inclusion poor mantle and rims (Fig. 2H). Sillimanite occurs as inclusions in quartz and as fibrolite surrounding biotite, quartz, and cordierite. Quartz grain boundaries have 120º triple junctions (Fig. 2I). Biotite occurs as > 500 µm crystals as well as smaller crystals (< 200 µm) at these quartz triple junctions, and as inclusions in cordierite. Minor amounts of muscovite and chlorite are present, with chlorite–biotite relationships suggesting that chlorite is a retrograde product.

### 5.5.2 Garnet composition

The largest garnets were element mapped via EDS or WDS (Fig. 3). Quantitative analysis was then conducted by EPMA on traverses through those garnet crystals (Fig. 3). Garnet composition is reported as $X_{alm}$ = (Fe/(Fe+Ca+Mg+Mn)), $X_{grs}$ (Ca/(Fe+Ca+Mg+Mn)), $X_{prp}$ = (Mg/(Fe+Ca+Mg+Mn)), and $X_{sps}$ = (Mn/(Fe+Ca+Mg+Mn)). Garnet zoning is consistent in all samples except 400RR characterized by rimward decrease in $X_{sps},$ decrease or no zoning in $X_{grs},$ rim wards increase in $X_{alm},$ and increase or no zoning in $X_{prp},$ which is consistent with prograde zoning (Tracy et al. 1976). 400RR is unzoned in $X_{alm},$ $X_{grs},$ and $X_{prp}$ and shows a small increase in $X_{sps}$ from core to rim.

### 5.5.3 *P-T* Conditions of Metamorphism

*P-T* conditions of metamorphism were determined with phase equilibria modeling for sample 2018PPGrt_01 and inverse thermobarometry for all samples. Phase equilibria were not calculated for other samples because of difficulties calculating an appropriate reactive bulk-rock composition for rocks with decimeter-scale andalusite porphyroblasts. Garnet-biotite thermometry used both the Caddick and Thompson (2008) and Ferry and Spear (1978) calibrations, Ti-in-biotite thermometry used the (Henry et al. 2005) calibration, GASP barometry used the Hodges and Spear (1982) calibration, and garnet-cordierite barometry followed Treloar (1981). Where ranges of temperatures are given below, they refer to, for instance, multiple garnet–biotite pair analyses from within a sample.

**2018PPGrt_01:** An isochemical phase diagram for 2018PPGrt_01 was constructed using the measured XRF bulk rock composition and is shown in Fig. 4A. The peak *P-T* conditions of the rock were determined by comparing the observed mineral assemblage in thin section (biotite + chlorite + garnet + muscovite + plagioclase + quartz + staurolite) to be calculated stability fields of those minerals. The assemblage biotite + chlorite + garnet + muscovite + plagioclase + quartz + staurolite is calculated to be stable from 530ºC and 3.0 kbar to 560ºC and 5.0 kbar (denoted by the black box in Fig. 4A-E). The *P-T* conditions of garnet nucleation were determined by calculating isopleths (lines of constant composition) appropriate for the measured composition of garnet crystal cores in this sample. This was done for three garnet crystals in the sample, with minimal differences in the composition of the measured crystals. The garnet core isopleths intersect at 495ºC and 3.7 kbar, which is our inferred *P-T* of garnet nucleation in this sample.

The calculated abundances (volume %) of both garnet and staurolite are shown in Fig. 4D-E. The measured amount of garnet in the rock sample is 1 volume %, and the measured amount of staurolite is 6 volume %. The calculated abundance of garnet within the peak field (black box in Fig. 4D) ranges from 0.9-2.0 volume %, which is in good agreement with the sample. Staurolite ranges from 2-16 volume % within the peak assemblage field (Fig. 4E), with the measured amount of staurolite in the rock (6 volume %) falling within this range.

A second phase diagram was calculated for an effective bulk composition in which a volume-averaged composition of garnet was removed from the initial bulk rock composition. Calculated isopleths for the measured composition of garnet rims in sample 2018PPGrt_01 intersect at 545ºC and 4.8 kbar, which falls within the peak assemblage field (Fig. 4E). The apparent *P*-*T* conditions of growth of garnet crystal core and rim can then be used to determine a metamorphic heating rate for this sample, based on estimates for the duration of Neoacadian Orogeny. Depending on the length of the orogeny (405-395 Ma or 405-373 Ma), this equates to 50ºC of metamorphic heating over a 10-30 million year duration, resulting in a hearing rate of 1.6-5 ºC/Myr.

**2018PPAnd_03:** The range of temperatures calculated via Ti-in-biotite thermometry is 459-470ºC (Fig. 5A). Garnet biotite thermometry yields temperatures of 485ºC based on the Ferry and Spear (1978) calibration and 553ºC from the Caddick and Thompson (2008) calibration (Fig. 5B). The presence of andalusite and staurolite in this rock places the peak pressure at 3.5-4.0 kbar, based on thermodynamic calculations of coexisting staurolite and andalusite assemblages from (Pattison and Spear 2018).

**2018PPGrt_03A:** Ti-in-biotite thermometry gives temperatures ranging from 549-601ºC (Fig. 5A). The Ferry and Spear (1978) garnet biotite thermometer yields 512ºC while the Caddick and Thompson (2008) calibration suggests 576ºC (Fig. 5B). GASP barometry using the Hodges and Spear (1982) calibration returns a pressure of 2.6. kbar (Fig. 5C). The presence of coexisting staurolite and andalusite is consistent with a peak temperature of 550-600ºC and a likely pressure range of 3.5-4.0 kbar (Pattison and Spear 2018).

**2018PPAnd_01A:** Ti-in-biotite thermometry results range from 578-627ºC (Fig. 5A), with garnet-biotite thermometry yielding temperatures of 526-604ºC using the Ferry and Spear (1978) calibration and 584-660ºC using the Caddick and Thompson (2008) calibration (Fig. 5B). The presence of andalusite places the peak pressure at < 4 kbar.

**2018PPAnd_02A:** Ti-in-biotite thermometry yields temperatures of 569-614ºC (Fig. 5A). Temperatures from garnet-biotite thermometry range from 454-545ºC or 530-602ºC, using the Ferry and Spear (1978) and Caddick and Thompson (2008) calibrations, respectively (Fig. 5B). GASP barometry returns pressures of 4.1-5.1 kbar using the Hodges and Spear (1982) calibration (Fig. 5C). Once again, the presence of andalusite suggests that this rock likely reach peak pressures of 4.0 kbar.

**400RR:** The range of temperatures from Ti-in-biotite thermometry is 572-660ºC (Fig. 5A), with garnet-biotite thermometry results of 516ºC using the Ferry and Spear (1978) calibration and 594ºC using the Caddick and Thompson (2008) calibration (Fig. 5B). A peak pressure of 3.4 kbar was calculated using the Treloar (1981) garnet-cordierite barometer (Fig. 5C).

## 5.6 GARNET X-RAY CT DATA

### 5.6.1 Garnet Crystal Size Distribution

A ~13 mm$^3$ volume of 2018PPGrt_01 was analyzed for the shape, size, and distribution of garnet crystals (Fig. 6). The 9866 garnet crystals within that volume account for 0.83% of the rock volume. The crystal size distribution (CSD) of those garnet crystals is shown in Fig. 7. Garnet crystals have an average radius of 126 µm, within minimum and maximum radii of 53 µm and 445 µm. However, the 445 µm radius garnet crystal appears to be an outlier, with the next largest garnet crystal in the sample having a radius of 339 µm. The averaged sphere-normalized surface to volume ratio is 1.28. If all garnet crystals in the population are considered, the skew is 1.34, reducing to 0.91 if the 445 µm radius crystal is not considered. Overall conclusions are the same regardless of whether this largest crystal is considered or omitted, with the dataset skewing to the right.

A right skewed CSD that consists of many small garnet crystals, in this case with an average radii of 126 µm, is generally interpreted as reflecting a rock with a high initial nucleation rate (i.e. effectively a single event of nucleation) that slows down over time (Hirsch 2008; Kelly et al. 2013a). It is likely that most crystals nucleated over a short interval, and then subsequent grew, which results in lots of small crystals.

The range of crystal sizes in the CSD is likely due to a variety of competing factors including: heating rate, critical temperature for garnet nucleation, and the rate of diffusion of Al through the intergranular matrix (Hirsch 2008). It is also possible that the distribution of trace elements in the rock, the presence of Mn-rich ilmenite, the properties of grain boundaries, and/or the availability of suitable nucleation sites may play a role in controlling the available nucleation sites for garnet to crystallize on (Daniel and Spear 1998, 1999; Moore et al. 2015; Gaidies 2017; George et al. 2018; McCarron et al. 2019; Rubatto et al. 2020), add in my paper when it is published.

### 5.6.2 Spatial Statistics and Indices

Statistical indices and correlation functions can be utilized to analyze the 3D size and location of garnet porphyroblasts, and that information can be interpreted to understand the mechanisms controlling the crystallization of garnet (Denison et al. 1997; Hirsch et al. 2000). The calculated values of the indices and correlation functions for the CT scanned sample are compared to a null hypothesis window calculated via a Monte Carlo simulation. The null hypothesis window represents an interface controlled garnet nucleation and growth scenario in which perfectly spherical garnet crystals grow in a homogeneous matrix. If the data plots outside the null hypothesis window, garnet crystals can be interpreted to be clustered or ordered compared to a random distribution of garnet crystals. Then interpretations as to whether garnet nucleated and grew via an interface-controlled or diffusion-controlled mechanism can be made.

**Correlation Functions (scale dependent):** The L' function is a measurement of how many garnet crystals are within a certain distance of each other. It is used to test for short range ordering and nucleation suppression (Fig. 8A). For 2018PPGrt_01, up to the mean nearest neighbor distance, the L' Function is less than the values for a random distribution, indicating ordering. This is consistent with interpretations of diffusion-controlled nucleation and growth.

The pair correlation function (PCF) also measures the number of garnet crystals that are within a certain distance of a center crystal. However, unlike the L' function, it is a measure of crystal centers that are at a certain distance from the center crystal (versus inside a distance with the L' function) (Fig. 8B). 2018PPGrt_01 shows ordering at distances less than the average nearest neighbor pair, which is interpreted as diffusion-controlled nucleation and growth.

The mark correlation function (MCF) also measures the number of crystals at a certain distance from each other, but unlike the PCF also considers the size (radii) of the garnet crystals (Fig. 8C). At test distances less than the mean nearest neighbor pair, the MCF value is less than that for a random distribution, again consistent with interpretations of diffusion-controlled nucleation and growth.

The correlation statistics are interpreted such that garnet in 2018PPGrt_01 formed via a diffusion-controlled nucleation and growth mechanism.

Varying geometric assumptions and the resulting differences in nearest neighbor distances have also been shown to affect the L' function, PCF, and MCF (Petley-Ragan et al. 2016). However, this is more likely to occur in situations in which the porphyroblasts investigated are ellipsoidal, and does not apply to our garnet crystals, in which a circular assumption for crystal shape is valid.

**Statistical Indices (scale independent):** Statistical indices can be used to characterize the ordering, clustering, and impingement of crystals in the sample and can be used to make interpretations about the mechanisms controlling garnet crystallization (Denison et al. 1997; Whitney et al. 2008). The ordering and clustering indices are a test of the distances between crystal centers. The ordering index is a nearest neighbor test in which the mean nearest neighbor distance for each crystal is divided by the predicted value for a random distribution. Here a value for 1/ordering index > 1 equates to a clustered distribution and a value for 1/ordering index < 1 is an ordered distribution. Our data has a 1/ordering index of > 1 indicating a clustered distribution (Fig. 8D). The clustering index (Carlson and Denison 1992), or the random point index, measures the presence of crystal centers in comparison to a random distribution of crystal centers in which a clustering index < 1 = ordered and > 1 = clustered. Our data shows that the clustering index falls within the null hypothesis region which suggests the location of crystal centers does not deviate from a random distribution of crystal centers (Fig. 8D). The impingement index (Carlson 1989) which factors in the center location and radii of crystals, is a measured ratio of the amount of interpenetration of crystals to that of a random distribution. A value > 1 = a clustered distribution and a value < 1 = an ordered distribution. The impingement index here is < 1 indicating an ordered distribution (Fig. 8D).

In summary, the statistical indices show for the 3D distribution of garnet crystals the distribution of crystal centers is random, but the nearest neighbor distances between crystals are more clustered than expected for a random distribution. Further, the amount of impingement is less than expected for a random distribution. These statistical indices are difficult to interpret.

Any single value can provide evidence for clustering or ordering, but a single measurement is ambiguous (Denison et al. 1997). In this case, it may be more appropriate to use scale dependent correlation functions to interpret the 3D size and location of garnet crystals, which allow for a more robust statistical analysis (Hirsch et al. 2000), and from that the garnet population in 2018PPGrt_01 is interpreted to have formed via a diffusion controlled nucleation and growth scenario.

### 5.6.3 Summary of Controls on Garnet Crystallization

It is possible to integrate the breadth of microstructural and compositional data for 2018PPGrt_01 to produce a comprehensive understanding of garnet nucleation and growth in this sample. First, it is likely that the majority of garnet crystals (even maybe all of them) nucleated in a single event. This is supported by two lines of evidence. First, the CSD shows a narrow right skew, which is commonly interpreted as a single nucleation event (Kretz 1974; Hirsch et al. 2000; Kelly et al. 2013a). Second, the composition of the garnet crystal cores is relatively similar between all measured garnet crystals. Composition data from four garnet crystals show a very small range of garnet core compositions with $X_{sps}$: 0.33-0.38, $X_{grs}$: 0.11-0.13, $X_{alm}$: 0.47-0.51, and $X_{prp}$: 0.026-0.027. This can be interpreted as all garnet crystals nucleating from the same chemical matrix. This is in contrast to a progressive nucleation scenario in which smaller garnet crystals would be expected to have lower $X_{sps}$ because Mn is sequestered into earlier forming garnet crystals (Finlay and Kerr 1979; Daniel and Spear 1999; Spear and Daniel 2003; Gatewood et al. 2015).

Further, garnet nucleated by templating on preexisting muscovite crystals in this sample (Nagurney et al. 2021). Muscovite is abundant in this sample and therefore provided plentiful nucleation sites for garnet. Thus, the availability of nucleation sites is likely not a limiting factor in the crystallization of garnet. This agrees well with the fact that the 3D spatial statistical analyses of garnet are interpreted such that the rate limiting step of garnet crystallization is likely the diffusion of Al through the intergranular matrix (Fig. 8,9).

## 5.7 DISCUSSION

### 5.7.1 Kinetics of Garnet Crystallization

The crystallization kinetics of garnet are the result of a series of likely simultaneous steps, which include: breakdown of reactant phases, intergranular transport, nucleation, and crystal growth (Carmichael 1969; Finlay and Kerr 1979; Ridley and Thompson 1986). The rate of these processes, is controlled, to some degree by the heating rate of the rock. In metapelites, it appears that garnet in rocks with heating rates >100 ºC/Ma are more likely to be controlled by interfacial processes (Gaidies et al. 2011, 2015; George and Gaidies 2017), while garnet in rocks with lower heating rates ~10 ºC/Ma are likely to be controlled by diffusion (Kelly et al. 2013b; this study).

The role heating rate on the resulting garnet CSD has been studied for interface and diffusion controlled growth separately (Gaidies et al. 2011; Ketcham and Carlson 2012). In numerical simulations of interface controlled crystal nucleation and growth, Gaidies et al. (2011) show that as heating rate increases, the resulting CSD will produce more smaller garnet crystals. An increased heating rate will also decrease the time available for crystal growth resulting in a decrease in the chemical fractionation into garnet, thus extending the temperature range and rate of garnet nucleation (Gaidies et al. 2011). Alternatively, in numerical simulations of diffusion controlled nucleation and growth, an increased heating rate results in fewer, larger crystals (Ketcham and Carlson 2012). However, these numerical simulations do not allow us to quantitatively compare the effects of heating rate on if garnet grows via DCNG or ICNG.

Yet, the effect of heating rate on ICNG versus DCNG can the qualitatively understood. Faster heating rates likely promote faster intergranular diffusion (Yardley 1978). Therefore, the supply of nutrient elements, such as Al, can easily move to the site of the growing porphyroblast, and diffusion is not likely to be the rate limiting step for metamorphism. In the case of slower heating rates, intergranular diffusion is likely slower, resulting in it controlling the overall rate of garnet crystallization.

Further, garnet has shown to crystallize via epitaxial nucleation on muscovite in samples that show interface controlled (Nelson Aureole) and diffusion controlled (2018PPGrt_01, this study) garnet growth (Nagurney et al. 2021). This suggests that while heating rate can influence the 3D size and position of garnet crystals, it does not control the atomic scale processes of how a garnet nucleus templates onto the crystal structure of muscovite. Epitaxial nucleation occurs regardless of the heating rate and distribution of Al through the intergranular matrix. Yet, whether a garnet nucleus forming on a muscovite crystal matures into a macroscale porphyroblast is likely strongly influenced by the heating rate of the rock.

### 5.7.2 Peak *P-T* Conditions Across the SW Meguma Terrane

Figure 9 combines work from this study as well as previous studies (Bourque 1985; Wetzell 1985; Misner 1986; Peskleway 1986; Mahoney 1996; Currie et al. 1998; Jamieson et al. 2012) quantifying *P-T* conditions across the Meguma Terrane. In general, there is an increase in *P-T* conditions from the NE (in the contact aureole of the South Mountain Batholith) to the SW (surrounding the Barrington Passage Pluton). It is possible that this range of peak *P-T* conditions is the result of the current surface of the Meguma Terrane being buried deeper in the SW than the NE ~400-360 Ma. The Meguma Terrane then underwent differential uplift and erosion to the surface expression that exists today. This follows from the fact that post peak metamorphism the majority of the Meguma Terrane cooled through 300ºC by 360 Ma, but SW Meguma Terrane cooled through 300ºC ~345 Ma (Keppie and Dallmeyer 1995). If the SW Meguma Terrane was buried deeper than the NE (at the current erosion level), then it would take more time to cool through 300ºC. Thus, broadly, the increasing metamorphic grade to the SW in the Meguma Terrane could be the result of a regional metamorphic sequence that has been differentially uplifted and eroded.

Alternatively, the relatively small (<2 kbar) differences in pressure across the Meguma Terrane (Fig. 9) could be the result of various barometers and their uncertainties. Peak pressures were obtained from a combination of GASP barometry, garnet-cordierite barometry, pseudosection modeling, and TWQ. All of these methodologies have an uncertainty ~±0.5-1.0 kbar. If those uncertainties are expanded, most of the pressure data falls within 4.0 ± 0.5 kbar, which would suggest that the Meguma Terrane is not a regional metamorphic sequence that has been differentially uplifted and eroded. Instead, this would suggest that there is increased metamorphic heating to the southwest, but the entire terrane was at similar depth (pressure). In this case the argon cooling ages (Keppie and Dallmeyer 1995) can be interpreted such that the More quantitative *P-T* data, especially in the 'biotite' zone (Fig. 9) is necessary to resolve this.

### 5.7.3 Polymetamorphic Metamorphic *P-T* Path in the SW Meguma Terrane

More important to the tectonic story of the Meguma Terrane than the potential differences in pressure is the evidence of polymetamorphism in the area of the Barrington Passage Pluton and Shelburne Pluton in the SW Meguma Terrane. First, sample 2018PPGrt_01 is ~10 km from the Barrington Passage Pluton at it reached 590ºC and 4.5 kbar. It is unlikely that a granitic pluton could provide enough heat to a rock ~10 km away for that rock to reach those *P-T* conditions (citation about heat transfer in the crust?). Thus, it is likely that 2018PPGrt_01 formed as the result of the regional (previously described as ‘greenschist facies’) event prior to the intrusion of the Barrington Passage Pluton.

Second, in samples collected from the Pubnico Point peninsula there are petrographic indicators of polymetamorphism. Some samples contain multiple foliations (Fig. 2), which could be interpreted as multiple deformational and/or metamorphic events. Additionally, the presence of the ‘biotite box structures’ in the 5-7 cm long andalusite crystals 2018PPAnd_02A may provide textural evidence of metamorphism (Fig. 2F). These boxes could represent andalusite forming via the reaction: muscovite + staurolite + quartz = biotite + andalusite + garnet + $H_2O$ (or staurolite + chlorite = biotite + andalusite + $H_2O$). The andalusite inside the ‘biotite box’ could represent former staurolite that andalusite has pseudomorphed. The alignment of biotite in the box structure around the andalusite may have formed in that way due to epitaxial nucleation or transport limited diffusion.

Outside the biotite box (and in 2018PPAnd_01A which also contains ~6 cm andalusite porphyroblasts, but no biotite box structures), andalusite is likely forming from a reaction that does not contain staurolite such as. Due to the large size of these andalusite crystals and the presence of fluid inclusions in garnet (Fig. 2G), it is likely that an input of an aqueous fluid may have catalyzed/driven this reaction. The likely source of this fluid and heat was the nearby Barrington Passage Pluton. Taken together, this suggests that these rocks were already at staurolite grade prior to the intrusion of the Barrington Passage Pluton and fluids and heat from the Barrington Passage Pluton drove the next stage of metamorphic reactions

Third, andalusite appears to be the final porphyroblast to grow and it appears to be overgrowing everything (Fig. 2). This later stage andalusite in the Barrington Passage area can be compared to the later stage cordierite in the Shelburne area (see Fig. 9 for geographic location of areas). There, later stage cordierite was the result of a polymetamorphic *P-T* path in which rocks with a Ms + St + Bt assemblage were heated up during exhumation and formed later stage cordierite, with the presence of cordierite at least partially controlled by the Mg/(Mg + Fe) ratio of the rock (Pattison et al. 1999).

It is possible that the later stage cordierite event in the Shelburne area is related to the later stage andalusite event in the Barrington Passage area. The regional distribution of andalusite and cordierite is likely controlled by the *P-T* conditions of the rocks. Quantitative *P-T* constraints suggest that the peak *P-T* conditions in the Shelburne area were slightly less (1-1.5 kbar) than the Barrington Passage area. This 1-1.5 kbar difference can result in cordierite forming in lower *P* (1.0-3.0) rocks and andalusite forming in higher *P* (2.5-3.5 kbar) rocks (Pattison et al. 1999). It is unlikely that either bulk rock composition or fluid availability controls the regional distribution of cordierite versus andalusite in this area as i) there is ample evidence for regional fluid infiltration in both areas (fluid inclusions in Fig. 2) (Hwang 1997) and ii) both the Goldenville and Halifax formations crosscut the distribution of metamorphic minerals (Barr and White 2012).

Therefore, it is possible that the growth of the later stage porphyroblasts was driven by the heat from the Barrington Passage and Shelburne plutons. If this is the case, then it is likely that the SW Meguma Terrane was already at amphibolite facies (at least garnet-staurolite grade) metamorphic conditions prior to the intrusion of the plutons. The SW Meguma Terrane therefore followed a polymetamorphic *P-T* path in which it reached amphibolite facies during the previously described regional ‘greenschist facies’ event prior to the intrusion of the plutons and then heat from the plutons drove the formation of the later stage porphyroblasts.

This polymetamorphic *P-T* path may also explain the distribution of staurolite + andalusite in some rocks across the Pubnico Point area. Staurolite + andalusite assemblages occur over a relatively narrow window of *P-T* space. Kinetic factors such as the delayed breakdown of staurolite resulting in persistence of staurolite to greater *T* are often utilized to interpret this coexistence (Pattison and Spear 2018). However, it appears that in the southwestern Meguma Terrane, polymetamophism is a likely explanation for the St + And assemblages.

### 5.7.4 Regional Tectonic Implications

This interpretation of a polymetamorphic *P-T* path in the southwestern Meguma Terrane requires an assessment of the tectonic implications of that for Neoacadian Orogeny and formation of the northern Appalachians. To the west, the Meguma Terrane was thrust over the Avalon Terrane (Greenough et al. 1999; van Staal and Barr 2012). Convergence is dextral to oblique and accommodated along the Cobequid-Chedabucto fault system. Geophysical imaging reveals a northwest dipping subduction zone below Meguma (Keen et al. 1991). This subduction zone likely represents the leading edge of Gondwana (van Staal and Barr 2012). The dip of the subducting slab was likely shallow either due to the presence of a mantle plume (Murphy et al. 1999) or the subduction of younger and hotter oceanic lithosphere (maybe Keppie & Dallmeyer reference here?), which can lead to flat slab subduction.

Flat slab subduction generally results in a cold forearc with minimal volcanic activity (Dumitru et al. 1991; Gutscher 2002). This is in contrast to the high volume granitic plutonism and metamorphism observed in the Meguma Terrane. However, break off of the slab or delamination of the lower lithosphere can provide both the input of heat and material needed to heat up the crust to form those metamorphic and plutonic rocks (Tate 1995; Tate and Clarke 1995, 1997; Clarke et al. 1997; Currie et al. 1998). Flat slab subduction and subsequent delamination of the lower lithosphere and/or slab breakoff can explain the pattern of metamorphism and plutonism in the Meguma Terrane (Keppie and Dallmeyer 1995; Moran et al. 2007). The general younging trend of plutons from the South Mountain Batholith southwest to the offshore Seal Isle Pluton provide evidence for increased magmatism due to the roll back of the subducting slab prior to the collision of Gondwana (Moran et al. 2007).

Thus, the collision of Meguma with Avalon combined with flat slab subduction below the Meguma Terrane were likely responsible for the initial regional metamorphism in the Meguma Terrane. Slab break off and upwelling of the lithosphere then melted the Meguma crust, which recrystallized to from granitic plutons, releasing heat and fluids into the surrounding rocks and further metamorphosing them (Keppie and Dallmeyer 1995; Moran et al. 2007).

### 5.8 CONCLUSIONS

This paper presents a regional *P-T* study of the Meguma Terrane and, utilizing one sample from this area, discusses the controls on garnet crystallization kinetics during metamorphism. The Meguma Terrane reached mid amphibolite facies during the Neoacadian orogeny, prior to the intrusion of granitic plutons ~373 Ma. The heat from the plutons then locally drove porphyroblast growth, resulting in a polymetamorphic *P-T* path across some of the southwestern Meguma Terrane. This suggests that during microcontinent collision, the resulting metamorphism may be a complex interplay between regional metamorphism and contact heating from intruding plutons.

In sample 2018PPGrt_01, garnet porphyroblasts likely crystallized in one event in and the rate limiting step for their crystallization was likely the intergranular diffusion of aluminum. Combined with previous studies on garnet crystallization kinetics, this suggests that heating rate may be an important control in determining if garnet crystallizes via an interface or diffusion-controlled mechanism. However, it appears that independent of heating rate, garnet crystallizes by epitaxially nucleating on muscovite.

## 5.9 REFERENCES

Barr, S.M., and White, C.E. (2012) The New Meguma: Stratigraphy, Metemorphisim, Paleontology, and Provenance.

Baxter, E.F., Caddick, M.J., and Dragovic, B. (2017) Garnet: A Rock-Forming Mineral Petrochronometer. Reviews in Mineralogy & Geochemistry, 83, 469–533.

Bourque, A.D. (1985) Migmatization and metamorphism associated with the Barrington Passage Pluton Shelburne and Yarmouth Counties, Nova Scotia. Acadia University Wolfeville, Nova Scotia.

Boyd, F.R., and Mertzman, S.A. (1987) Composition of structure of the Kaapvaal lithosphere, southern Africa. In Magmatic Processes- Physiochemical Principles, B.O. Mysen, Ed., The Geochemical Society, Special Publication #1 pp. 13–24.

Caddick, M.J., and Kohn, M.J. (2013) Garnet: Witness to the evolution of destructive plate boundaries. Elements, 9, 427–432.

Caddick, M.J., and Thompson, A.B. (2008) Quantifying the tectono-metamorphic evolution of pelitic rocks from a wide range of tectonic settings: Mineral compositions in equilibrium. Contributions to Mineralogy and Petrology, 156, 177–195.

Carlson, W.D. (1989) The significance of intergranuar diffusion to the mechanisms and kinetics of porphyroblast crystallization. Contribution to Mineralogy and Petrology, 103, 1–24.

——— (2011) Porphyroblast crystallization: linking processes, kinetics, and microstructures. International Geology Review, 53, 406–445.

Carlson, W.D., and Denison, C. (1992) Mechanisms of porphyroblast crystallization: Results from high-resolution computed x-ray tomography. Science, 257, 1236–1239.

Carmichael, D.M. (1969) On the mechanism of prograde metamorphic reactions in quartz-bearing pelitic rocks. Contributions to Mineralogy and Petrology, 20, 244–267.

Carruzzo, S., Kontak, D.J., Clarke, D.B., and Kyser, T.K. (2004) An integrated fluid-mineral stable-isotope study of the granite-hosted mineral deposits of the New Ross area, South Mountain Batholith, Nova Scotia, Canada: Evidence for multiple reservoirs. Canadian Mineralogist, 42, 1425–1441.

Clarke, D.B., Macdonald, M.A., and Tate, M.C. (1997) The Nature of Magmatism in the Appalachian Orogen. In A. Sinha, J.B. Whalen, and J.P. Hogan, Eds., Geological Society of America Memoir Vol. 191.

Clarke, D.B., Fallon, R., and Heaman, L.M. (2000) Interaction among upper crustal, lower crustal, and mantle materials in the Port Mouton pluton, Meguma Lithotectonic Zone, southwest Nova Scotia. Canadian Journal of Earth Sciences, 37, 579–600.

Clarke, D.B., MacDonald, M.A., and Tate, M.C. (2015) Late Devonian mafoc-felsic magmatism in the Meguma Zone, 31, 2015.

Connolly, J.A.D. (2005) Computation of phase equilibria by linear programming: A tool for geodynamic modeling and its application to subduction zone decarbonation. Earth and Planetary Science Letters, 236, 524–541.

Currie, K.L., Whalen, J.B., Davis, W.J., Longstaffe, F.J., and Cousens, B.L. (1998) Geochemical evolution of peraluminous plutons in southern Nova Scotia, Canada-a pegmatite-poor suite. Lithos, 44, 117–140.

Dallmeyer, R.D., and Keppie, J.D. (1986) Polyphase late Paleozoic tectonothermal evolution of the southwestern Meguma Terrane, Nova Scotia: evidence from 40Ar/39Ar mineral ages1.

Canadian Journal of Earth Sciences, 24, 1242–1254.

Dallmeyer, R.D., and Keppie, J.D. (1988) Superposed Late Paleozoic thermal events in the southwestern Meguma Terrane , Nova Scotia. Maritime Sediments and Atlantic Geology, 124, 157–169.

Daniel, C.G., and Spear, F.S. (1998) Three-dimensional patterns of garnet nucleation and growth. Geology, 26, 505–506.

Daniel, C.G., and Spear, F.S. (1999) The clustered nucleation and growth processes of garnet in regional metamorphic rocks from north-west Connecticut, USA. Journal of Metamorphic Geology, 17, 503–520.

Denison, C., Carlson, W.D., and Ketcham, R.A. (1997) Three-dimensional quantitative textural analysis of metamorphic rocks using high-resolution computed X-ray tomography: Part I. Methods and techniques. Journal of Metamorphic Geology, 15, 29–44.

Dumitru, T.A., Gans, P.B., Foster, D.A., and Miller, E.L. (1991) Refrigeration of the western Cordilleran lithosphere during Laramide shallow-angle subduction. Geology, 19, 1145–1148.

Farber, K., Caddick, M.J., and John, T. (2014) Controls on solid-phase inclusion during porphyroblast growth: insights from the Barrovian sequence (Scottish Dalradian). Contributions to Mineralogy and Petrology, 168, 1–17.

Ferry, J.M., and Spear, F.S. (1978) Experimental calibration of the partitioning of Fe and Mg between biotite and garnet. Contributions to Mineralogy and Petrology, 66, 113–117.

Finlay, C.A., and Kerr, A. (1979) Garnet growth in a metapelite from the Moinian rocks of Northern Sutherland, Scotland. Contributions to Mineralogy and Petrology, 71, 185–191.

Gaidies, F. (2017) Nucleation in geological materials. EMU Notes in Mineralogy, 16, 347–371.

Gaidies, F., Pattison, D.R.M., and de Capitani, C. (2011) Toward a quantitative model of metamorphic nucleation and growth. Contributions to Mineralogy and Petrology, 162, 975–993.

Gaidies, F., Petley-Ragan, A., Chakraborty, S., Dasgupta, S., and Jones, P. (2015) Constraining the conditions of Barrovian metamorphism in Sikkim, India: P-T-t paths of garnet crystallization in the Lesser Himalayan Belt. Journal of Metamorphic Geology, 33, 23–44.

Gaidies, F., Morneau, Y.E., Petts, D.C., Jackson, S.E., Zagorevski, A., and Ryan, J.J. (2020) Major and trace element mapping of garnet: Unravelling the conditions, timing and rates of metamorphism of the Snowcap assemblage, west-central Yukon. Journal of Metamorphic Geology, 1–32.

Gatewood, M.P., Dragovic, B., Stowell, H.H., Baxter, E.F., Hirsch, D.M., and Bloom, R. (2015) Evaluating chemical equilibrium in metamorphic rocks using major element and Sm-Nd isotopic age zoning in garnet, Townshend Dam, Vermont, USA. Chemical Geology, 401, 151–168.

George, F.R., and Gaidies, F. (2017) Characterisation of a garnet population from the Sikkim Himalaya: insights into the rates and mechanisms of porphyroblast crystallisation. Contributions to Mineralogy and Petrology, 172, 1–22.

George, F.R., and Gaidies, F. (2020) Simultaneous operation of opposing reaction mechanisms: The influence of matrix heterogeneity on post-kinematic garnet crystallisation in an inverted metamorphic sequence. Journal of Metamorphic Geology, 38, 743–769.

George, F.R., Gaidies, F., and Boucher, B. (2018) Population-wide garnet growth zoning revealed by LA-ICP-MS mapping: Implications for trace element equilibration and syn-kinematic deformation during crystallisation. Contributions to Mineralogy and Petrology, 173, 1–24.

Greenough, J.D., Krogh, T.E., Kamo, S.L., Owen, J.V., and Ruffman, A. (1999) Precise U-Pb dating of Meguma basement xenoliths: new evidence for Avalonian underthrusting. Canadian Journal of Earth Sciences, 36, 15–22.

Gutscher, M.A. (2002) Andean subduction styles and their effect on thermal structure and interplate coupling. Journal of South American Earth Sciences, 15, 3–10.

Henry, D.J., Guidotti, C. V., and Thomson, J.A. (2005) The Ti-saturation surface for low-to-medium pressure metapelitic biotites: Implications for geothermometry and Ti-substitution mechanisms. American Mineralogist, 90, 316–328.

Hibbard, J., van Staal, C., and Rankin, D. (2010) Comparative analysis of the geological evolution of the northern and southern Appalachian orogen: Late Ordovician-Permian. From Rodinia to Pangea: the lithotectonic record of the Appalachian region: Geological Society of America Memoir 206, 206, 51–69.

Hicks, R.J., Jamieson, R.A., and Reynolds, P.H. (1999) Detrital and metamorphic (super 40) Ar/ (super 39) Ar ages from muscovite and whole-rock samples, Meguma Supergroup, southern Nova Scotia. Canadian Journal of Earth Sciences, 36, 23–32.

Hilchie, L.J., and Jamieson, R.A. (2014) Graphite thermometry in a low-pressure contact aureole, Halifax, Nova Scotia. Lithos, 208, 21–33.

Hillenbrand, I.W., Williams, M.L., Li, C., and Gao, H. (2021) Rise and fall of the Acadian altiplano : Evidence for a Paleozoic orogenic plateau in New England. Earth and Planetary Science Letters, 560, 116797.

Hirsch, D.M. (2008) Controls on porphyroblast size along a regional metamorphic field gradient. Contributions to Mineralogy and Petrology, 155, 401–415.

——— (2011) Reduce3D: A tool for three-dimensional spatial statistical analysis of crystals. Geosphere, 7, 724–732.

Hirsch, D.M., Ketcham, R.A., and Carlson, W.D. (2000) An evaluation of spatial correlation functions in textural analysis of metamorphic rocks. Geologic Materials Research, 2, 1–42.

Hodges, K.V., and Spear, F.S. (1982) Geothermometry, geobarometry and the Al2SiO5 triple point at Mt. Moosilauke, New Hampshire. American Mineralogist, 67, 1118–1134.

Holland, T.J.B., and Powell, R. (2003) Activity-compositions relations for phases in petrological calculations: An asymetric multicomponent formulation. Contributions to Mineralogy and Petrology, 145, 492–501.

Holland, T.J.B., and Powell, R. (2011) An improved and extended internally consistent thermodynamic dataset for phases of petrological interest, involving a new equation of state for solids. Journal of Metamorphic Geology, 29, 333–383.

Hwang, S.-G. (1997) Regional-scale metasomatism of Al, K, and Na during staurolite-andalusite grade contact metamorphism, in the southwestern Nova Scotia, Canada. Journal of the Petrological Society of Korea, 6, 52–64.

Jamieson, R.A., Hart, G.G., Chapman, G.G., Tobey, N.W., and Murphy, B.J.B. (2012) The contact aureole of the South Mountain Batholith in Halifax, Nova Scotia: geology, mineral assemblages, and isograds. Canadian Journal of Earth Sciences, 49, 1280–1296.

Keen, C.E., Maclean, B.C., and Kay, W.A. (1991) A deep seismic reflection profile across the Nova Scotia continental margin, offshore eastern Canada. Canadian Journal of Earth Sciences, 28, 1112–1120.

Kelly, E.D., Carlson, W.D., and Ketcham, R.A. (2013a) Crystallization kinetics during regional metamorphism of porphyroblastic rocks. Journal of Metamorphic Geology, 31, 963–979.

——— (2013b) Magnitudes of departures from equilibrium during regional metamorphism of porphyroblastic rocks. Journal of Metamorphic Geology, 31, 981–1002.

Keppie, J.D., and Dallmeyer, R.D. (1987) Dating transcurrent terrane accretion: an example from the Meguma and Avalon composite terranes in the northern Appalachians. Tectonics, 6, 831–847.

Keppie, J.D., and Dallmeyer, R.D. (1995) Late Paleozoic collision, delamination, short-lived magmatism, and rapid denudation in the Meguma Terrance (Nova Scotia, Canada): constraints from 40Ar/39Ar isotopic data. Canadian Journal of Earth Sciences, 659, 644–659.

Keppie, J.D., and Krogh, T.E. (1999) U - Pb Geochronology of Devonian Granites in the Meguma Terrane of Nova Scotia , Canada : Evidence for Hotspot Melting of a Neoproterozoic Source. Journal of Geology, 107, 555–568.

Ketcham, R.A. (2005) Computational methods for quantitative analysis of three-dimensional features in geological specimens. Geosphere, 1, 32–41.

Ketcham, R.A., and Carlson, W.D. (2012) Numerical simulation of diffusion-controlled nucleation and growth of porphyroblasts. Journal of Metamorphic Geology, 30, 489–512.

Ketcham, R.A., Meth, C., Hirsch, D.M., and Carlson, W.D. (2005) Improved methods for quantitative analysis of three-dimensional porphyroblastic textures. Geosphere, 1, 42–59.

Kontak, D.J., and Kerrich, R. (1997) An isotopic (C, O, Sr) study of vein gold deposits in the Meguma Terrane, Nova Scotia: Implication for source reservoirs. Economic Geology, 92, 161–180.

Kontak, D.J., Smith, P.K., Reynolds, P., and Taylor, K. (1990) Geological and 40Ar/39Ar geochronological constraints on the timing of quartz vein formation in Meguma Group lode-gold deposits, Nova Scotia. Atlantic Geology, 26, 201–227.

Kretz, R. (1966) Interpretation of the shape of mineral grains in metamorphic rocks. Journal of Petrology, 7, 68–94.

Kretz, R. (1974) Some models for the rate of crystallization of garnet in metamorphic rocks. Lithos, 7, 123–131.

Mahoney, K.L. (1996) The contact aureole of the South Mountain Batholith, Nova Scotia. Acadia University Wolfville, Nova Scotia.

McCarron, T., McFarlane, C.R.M., and Gaidies, F. (2019) The significance of Mn-rich ilmenite and the determination of P-T paths from zoned garnet in metasedimentary rocks from the western Cape Breton Highlands, Nova Scotia. Journal of Metamorphic Geology, 37, 1171–1192.

McKenzie, C.B., and Clarke, D.B. (1975) Petrology of the South Mountain Batholith, Nova Scotia. Canadian Journal of Earth Sciences, 1218, 1209–1218.

Misner, A.R. (1986) Metamorphism of the northern part of the Shelburne metamorphic complex Shelburne and Yarmouth counties, Nova Scotia. Acadia University Wolfeville, Nova Scotia.

Moore, S.J., Cesare, B., and Carlson, W.D. (2015) Epitaxial nucleation of garnet on biotite in the polymetamorphic metapelites surrounding the Vedrette di Ries intrusion (Italian Eastern Alps). European Journal of Mineralogy, 27, 5–18.

Moran, P.C., Barr, S.M., White, C.E., and Hamilton, M.A. (2007) Petrology, age, and tectonic setting of the Seal Island Pluton, offshore southwestern Nova Scotia. Canadian Journal of Earth Sciences, 44, 1467–1478.

Muecke, G.K., Elias, P., and Reynolds, P.H. (1988) Hercynian/Alleghanian overprinting of an acadian terrane:40Ar/39Ar studies in the Meguma zone, Nova Scotia, Canada. Chemical Geology: Isotope Geoscience Section, 73, 153–167.

Murphy, J.B., Survey, G., Street, B., Ka, O., Keppie, J.D., Geología, I. De, Nacional, U., and México, A. De (1999) Middle to late Paleozoic Acadian orogeny in the northern Appalachians : A Laramide-style plume-modified orogeny ? Geology, 27, 653–656.

Nagurney, A.B., Caddick, M.J., Pattison, D.R.M., and Michel, F.M. (2021) Preferred orientations of garnet porphyroblasts reveal previously cryptic templating during nucleation. Scientific Reports, 1–9.

Pattison, D.R.M., and Spear, F.S. (2018) Kinetic control of staurolite-Al2SiO5mineral assemblages: Implications for Barrovian and Buchan metamorphism. Journal of Metamorphic Geology, 36, 667–690.

Pattison, D.R.M., Spear, F.S., and Cheney, J.T. (1999) Polymetamorphic origin of muscovite + cordierite + staurolite + biotite assemblages: Implications for the metapelitic petrogenetic grid and for P-T paths. Journal of Metamorphic Geology, 17, 685–703.

Peskleway, C.D. (1986) The paragenesis and metamorphic significance of cordierite in NW Nova Scotia. Acadia University, Wolfeville, Nova Scotia.

Petley-Ragan, A., Gaidies, F., and Pattison, D.R.M. (2016) A statistical analysis of the distribution of cordierite and biotite in hornfels from the Bugaboo contact aureole: Implications for the kinetics of porphyroblast crystallization. Journal of Metamorphic Geology, 34, 85–101.

Raeside, R., and Jamieson, R.A. (1992) Low-pressure metamorphism of the Meguma Terrane, Nova Scotia. Geological Association of Canada- Mineralogical Association of Canada Joint Annual Meeting, Wolfville ’92, Field Excursion C-5: Guidebook, 25 pp.

Reynolds, P.H., Kublick, E.E., and Muecke, G.K. (1973) Potassium–Argon Dating of Slates from the Meguma Group, Nova Scotia. Canadian Journal of Earth Sciences, 10, 1059–1067.

Reynolds, P.H., Elias, P., Muecke, G.K., and Grist, A.M. (1987) Thermal history of the southwestern Meguma zone , Nova Scotia , from an 40Ar / 39Ar and fission track dating study of intrusive rocks. Canadian Journal of Earth Sciences, 24, 1952–1965.

Reynolds, P.H., White, C.E., Barr, S.M., Muir, C.M., and Hibbard, J. (2012) $^{40}$ Ar– $^{39}$ Ar ages for detrital white mica in Meguma terrane, Nova Scotia, Canada: implications for provenance of the Goldenville and Halifax groups. Canadian Journal of Earth Sciences, 49, 781–795.

Ridley, J., and Thompson, A.B. (1986) The role of mineral kinetics in the development of metamorphic microtextures. Advances in Physical Geochemistry, 5, 154–193.

Rubatto, D., Burger, M., Lanari, P., Hattendorf, B., Schwarz, G., Neff, C., Keresztes Schmidt, P., Hermann, J., Vho, A., and Günther, D. (2020) Identification of growth mechanisms in metamorphic garnet by high-resolution trace element mapping with LA-ICP-TOFMS. Contributions to Mineralogy and Petrology, 175, 61.

Schenk, P.E. (1997) Events and sea-level changes on Gondwana's margin: the Meguma Zone (Cambrian to Devonian) of Nova Scotia, Canada. Geological Society of America Bulletin, 103, 512–521.

Spear, F.S., and Daniel, C.G. (2003) Three-dimensional imaging of garnet porphyroblast sizes and chemical zoning: Nucleation and growth history in the garnet zone. Geological Materials Research, 1, 1–44.

Spear, F.S., Selverstone, J., Hickmott, D., Crowley, P., and Hodges, K.V. (1984) P-T paths from garnet zoning: A new technique for deciphiering tectonic process in crystalline terranes. Geology, 12, 87–90.

Spiess, R., Groppo, C., and Compagnoni, R. (2007) When epitaxy controls garnet growth. Journal of Metamorphic Geology, 25, 439–450.

Tate, M., and Clarke, D. (1995) Petrogenesis and regional tectonic significance of Late Devonian mafic intrusions in the Meguma Zone, Nova Scotia. Canadian Journal of Earth Sciences, 32, 1883–1898.

Tate, M., and Clarke, D.B. (1997) Compositional diversity among Late Devonian peraluminous granitoid intrusions in the Meguma Zone of Nova Scotia, Canada. Lithos, 39, 179–194.

Tate, M.C. (1995) The relationship between Late Devonian mafic intrusions and peraluminous granitoid generation in the Meguma lithotectonic zone, Nova Scotia, Canada. Dalhousie University.

Taylor, F., and Schiller, E. (1966) Metamorphism of the Meguma group of Nova Scotia. Canadian Journal of Earth Sciences, 3, 959–974.

Thompson, A.B., and England, P.C. (1984) Pressure - temperature - time paths of regional metamorphism II. their inference and interpretation using mineral assemblages in metamorphic rocks. Journal of Petrology, 25, 929–955.

Tracy, R.J., Robinson, P., and Thompson, A.B. (1976) Garnet composition and zoning in the determination of temperatuer and pressure of metamorphism, central Massachusetts. American Mineralogist, 61, 762–775.

Treloar, P.J. (1981) Garnet-biotite-cordierite thermometry and barometry in the Cashel thermal aureole, Connemara, Ireland. Mineralogical Magazine, 44, 183–189.

van Staal, C.R., and Barr, S.M. (2012) Lithospheric architecture and tectonic evolution of the Canadian Appalachians and associated Atlantic margin. In Tectonic Styles in Canada: the LITHOPROBE Perspective Vol. Geological, pp. 41–95.

van Staal, C.R., Whalen, J.B., Valverde-Vaquero, P., Zagorevski, A., and Rogers, N. (2009) Pre-Carboniferous, episodic accretion-related, orogenesis along the Laurentian margin of the northern Appalachians. Geological Society, London, Special Publications, 327, 271–316.

Wakabayashi, J. (2004) Tectonic mechanisms associated with P-T paths of regional metamorphism: Alternatives to single-cycle thrusting and heating. Tectonophysics, 392, 193–218.

Waldron, J., White, C., Barr, S., Simonetti, A., and Heaman, L. (2009) Provenance of the Meguma terrane, Nova Scotia: rifted margin of early Paleozoic Gondwana. Canadian Journal of Earth Sciences, 46, 1–8.

Waldron, J.W.F., and White, C.E. (2011) Discussion of Geochemical signature of Ordovician Mn-rich sedimentary rocks on the Avalonian shelf. Canadian Journal of Earth Sciences, 48, 703–718.

Wells, M.L., Hoisch, T.D., Cruz-Uribe, A.M., and Vervoort, J.D. (2012) Geodynamics of synconvergent extension and tectonic mode switching: Constraints from the Sevier-Laramide orogen. Tectonics, 31, 1–20.

Wetzell, B.D. (1985) Metamorphism of the Port La Tour area, Nova Scotia. Acadia University Wolfeville, Nova Scotia.

White, C.E., and Barr, S.M. (2010) Lithochemistry of the Lower Paleozoic Goldenville and Halifax groups, southwestern Nova Scotia, Canada: Implications for stratigraphy, provenance, and tectonic setting of the Meguma terrane. Geological Society of America Memoir, 206, 347–366.

White, R.W., Powell, R., Holland, T.J.B., Johnson, T.E., and Green, E.C.R. (2014) New mineral activity-composition relations for thermodynamic calculations in metapelitic systems.

Journal of Metamorphic Geology, 32, 261–286.

Whitney, D.L., Goergen, E.T., Ketcham, R.A., and Kunze, K. (2008) Formation of garnet polycrystals during metamorphic crystallization. Journal of Metamorphic Geology, 26, 365–383.

Williams, H. (1979) Appalachian Orogen in Canada. Canadian Journal of Earth Sciences, 16, 792–807.

Williams, H., and Hatcher, R.D. (1982) Suspect terranes and accretionary history of the Appalachian orogen. Geology, 10, 530–536.

Wilson, J.T. (1966) Did the Atlantic Close and Then Re-Open? Nature, 212, 901–903.

Yardley, B.W.D. (1978) Genesis of the Skagit Gneiss migmatites, Washington, and the distinction between possible mechanisms of migmatization. Geological Society of America Bulletin, 89, 941–951.

## 5.10 ACKNOWLEDGEMENTS

Lowell Moore and Stephen Kuehn are thanked for help with EPMA analyses and Stan Mertzman is thanked for XRF analyses. Rob Raeside provided sample 400RR_01. Sandra Barr is thanked for assistance in the field. Members of the Metamorphic Processes Group at Virginia Tech are thanked for helpful discussions on various aspects of this project. Jessie Maisano is thanked for help with CT scanning.

## 5.11 FIGURES

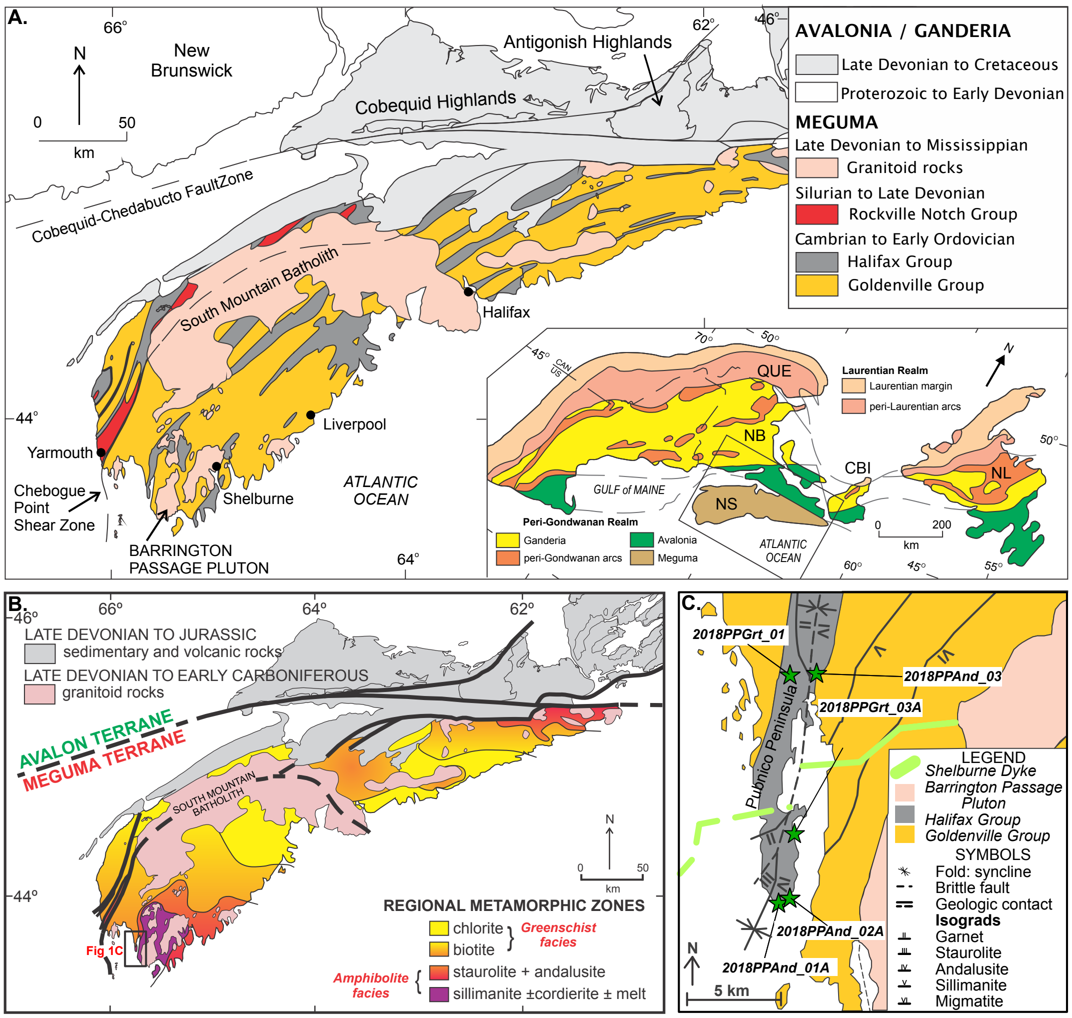

Figure 5.1: A: Geologic map (after White 2010) of the southwestern Meguma Terrane (location shown in inset) showing the Cambrian-Ordovician Halifax and Goldenville Groups and granitic intrusions (pink). B: Metamorphic map (after White 2010) of the southwestern Meguma Terrane, showing a general increase in metamorphic grade to the southwest. Location of C is shown with a black square. C: Close up of field locality near the Barrington Passage Pluton (from White 2003). Sample locations are shown with green stars.

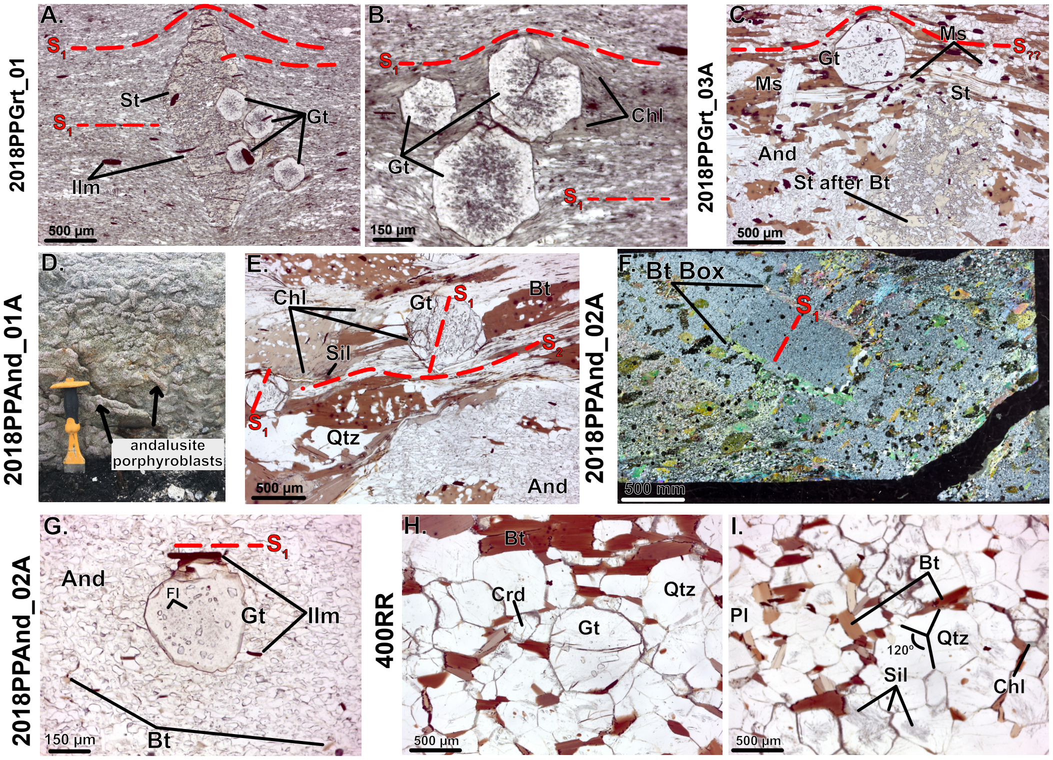

Figure 5.2: Representative petrographic and field photos. A-B: 2018PPGrt_01, C: 2018PPGrt_03A, D-E: 2018PPAnd_01A, F-G: 2018PPAnd_02A, H-I: 400RR.

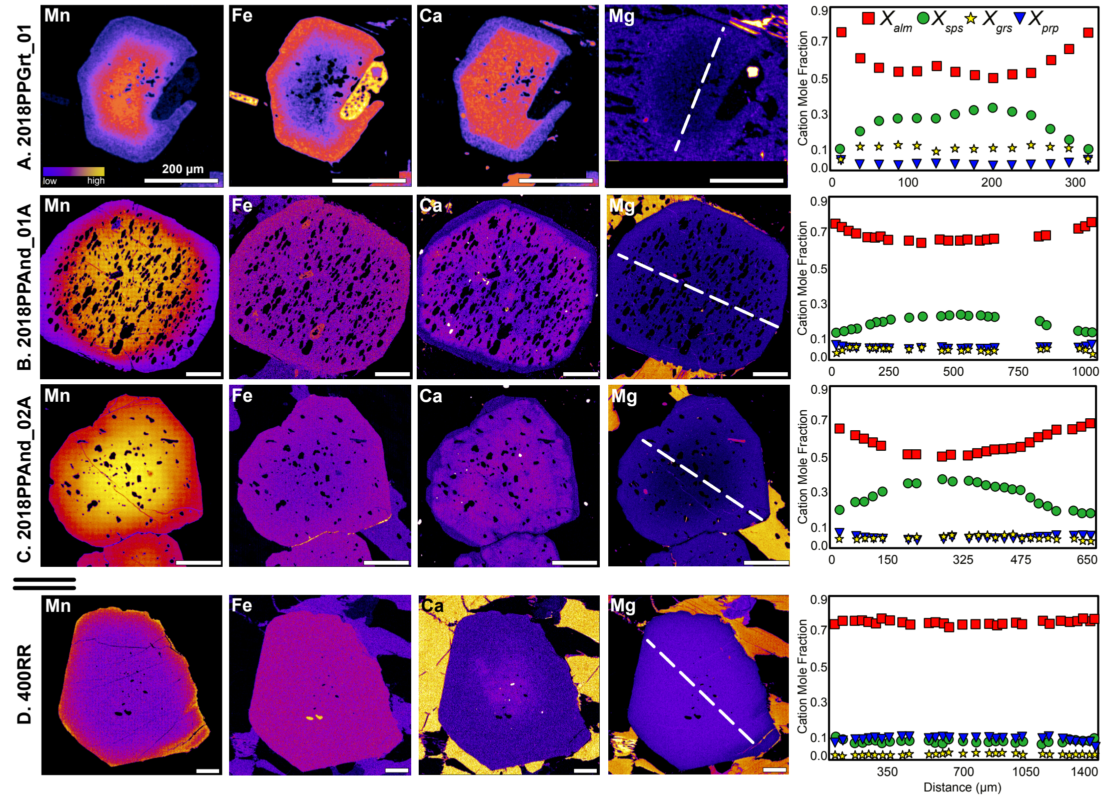

Figure 5.3: Garnet compositional maps and quantitative traverses for select garnet crystals in each sample. Location of traverse is shown in white dashed line on the Mg element map. A: 2018PPGrt_01, B: 2018PPAnd_01A, C: 2018PPAnd_02A, D: 400RR.

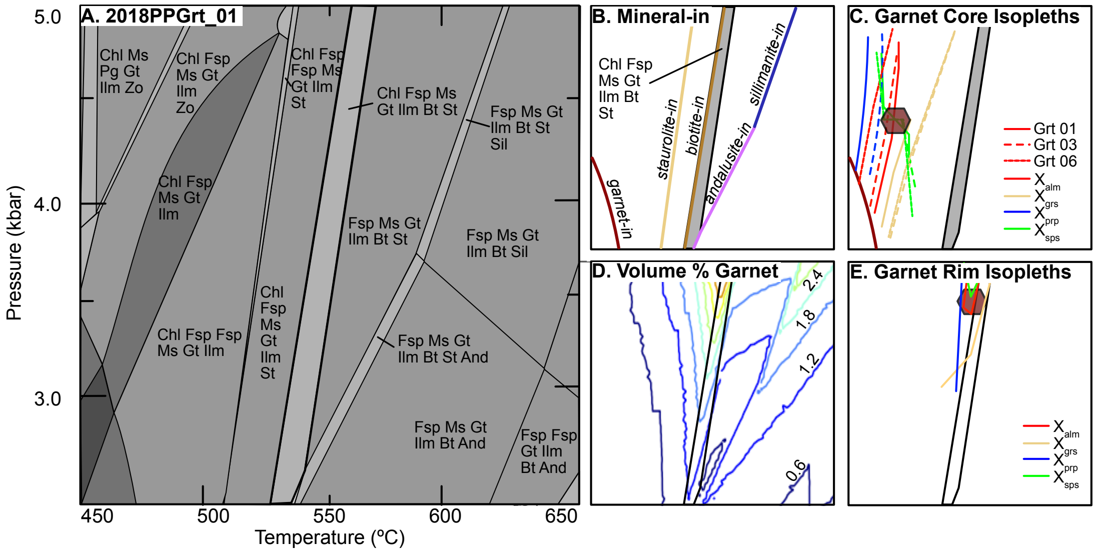

Figure 5.4: A: *P-T* pseudosection for 2018PPGrt_01. Black box indicates field (Bt+Chl+Grt+Ilm+Ms+Qtz+Pl+St) that corresponds to the mineralogy of the sample. B: Simplified version of A to highlight the major mineral-in fields. C: Garnet core compositional isopleths shown for 3 garnet crystals in 2018PPGrt_01. The intersection of these isopleths is the assumed *P-T* of garnet nucleation. D: Volume percent of garnet. Peak field (black outline) contains 0.9-2.0 volume % garnet, which is consistent with the 1 volume % garnet measured in the sample. E: Garnet rim isopleths for an effective bulk composition (see text and Appendix XX for explanation).

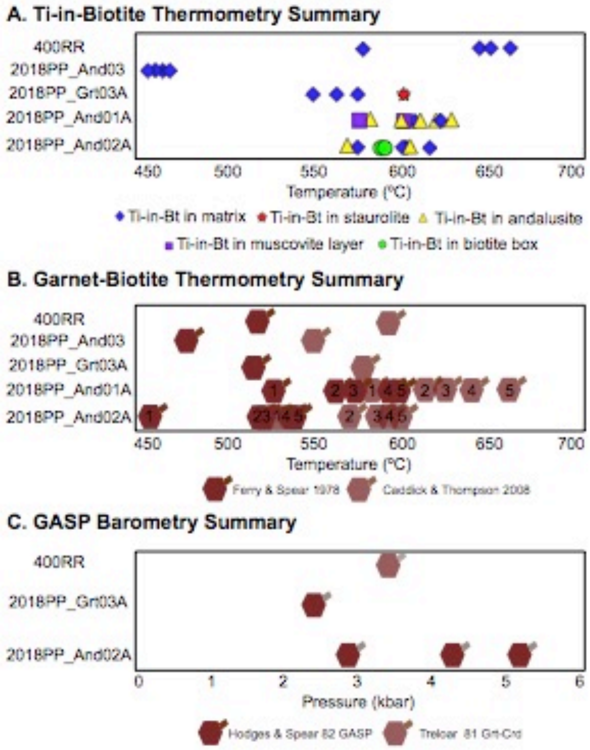

Figure 5.5: Summary of *P-T* Results. A: Temperatures from Ti-in-biotite thermometry (Henry et al. 2005) colored for microstructural position in the thin section. B: Garnet-biotite thermometry

(Ferry and Spear 1978; Caddick and Thompson 2008) for select garnet-biotite pairs. C: GASP barometry (Hodges and Spear 1982) for garnet-plagioclase pairs and garnet-cordierite barometry (Treloar 1981).

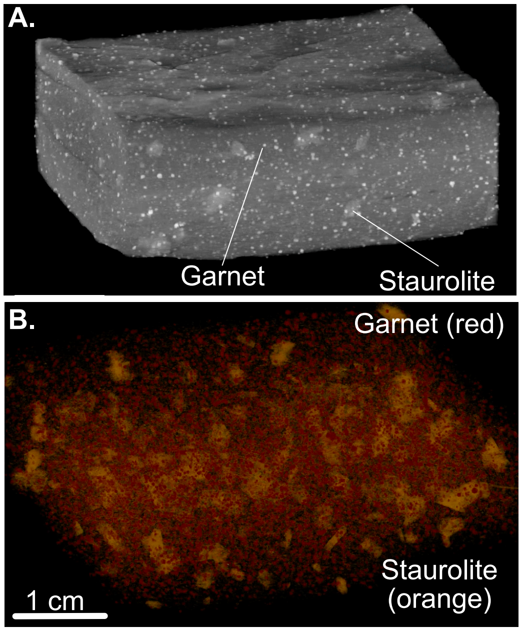

Figure 5.6: Overview of CT scan of 2018PPGrt_01. A: Gray scale image of the scanned volume showing garnet and staurolite porphyroblasts. B: False color image of the sample showing only garnet (maroon) and staurolite (orange) porphyroblasts.

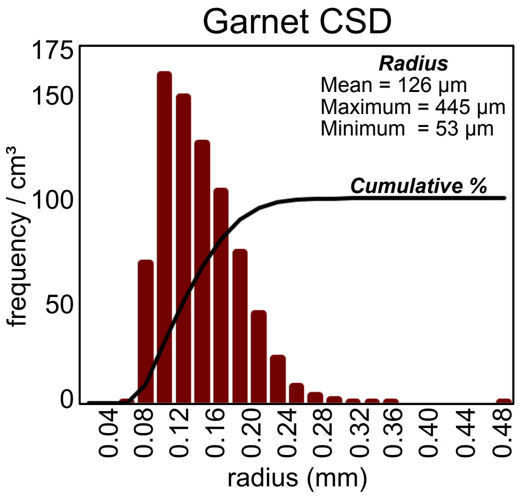

Figure 5.7: Garnet crystal size distribution (CSD) for 2018PPGrt_01. Y-axis is measured in frequency of garnet crystals / cm$^3$ scanned rock volume.

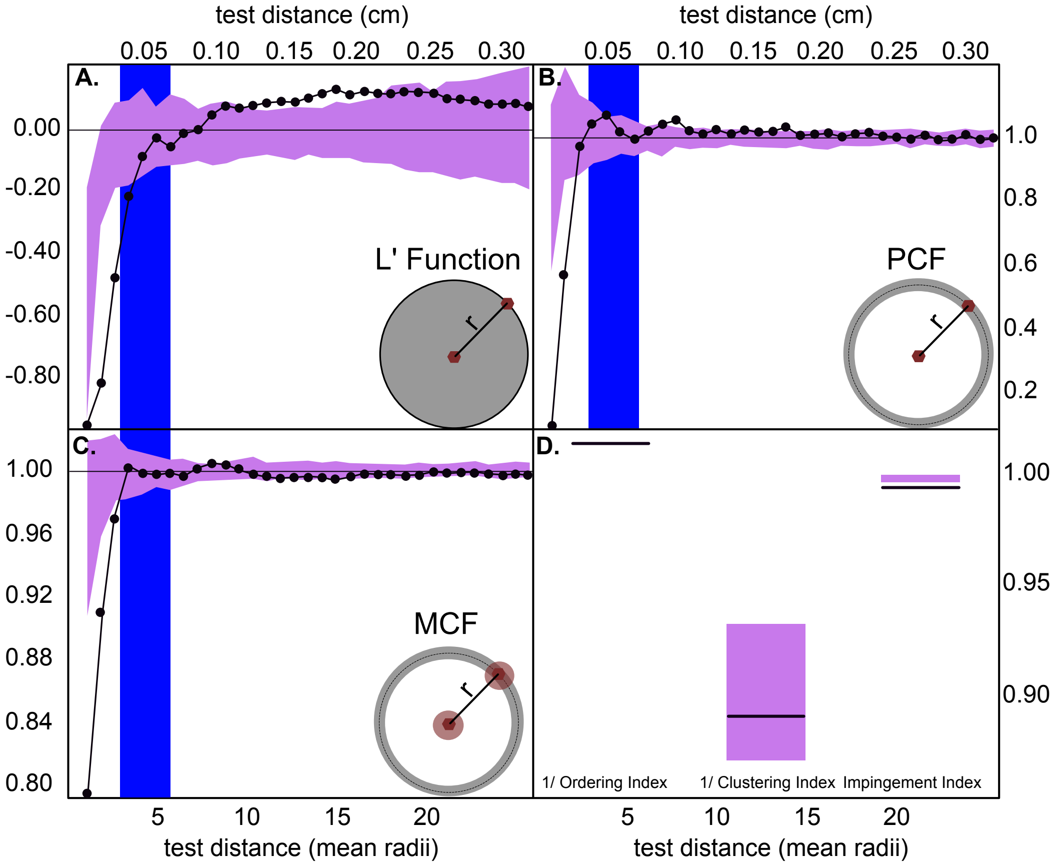

Figure 5.8: Correlation functions and statistical indices for the garnet crystal population in 2018PPGrt_01. A-C: L’ function, pair correlation function (PCF), and mark correlation function (MCF). Blue line is the mean nearest neighbor distance (± 1 standard deviation) between garnet crystals in 2018PPGrt_01. Pink shaded area represents the results of 100 Monte Carlo analyses of interface-controlled growth. For all functions, up to the nearest mean neighbor distance, the results for 2018PPGrt_01 plot below the interface-controlled window. This is interpreted as the garnet crystals being ordered and forming via diffusion-controlled nucleation and growth. D: Statistical indices (clustering index, ordering index, and impingement index).

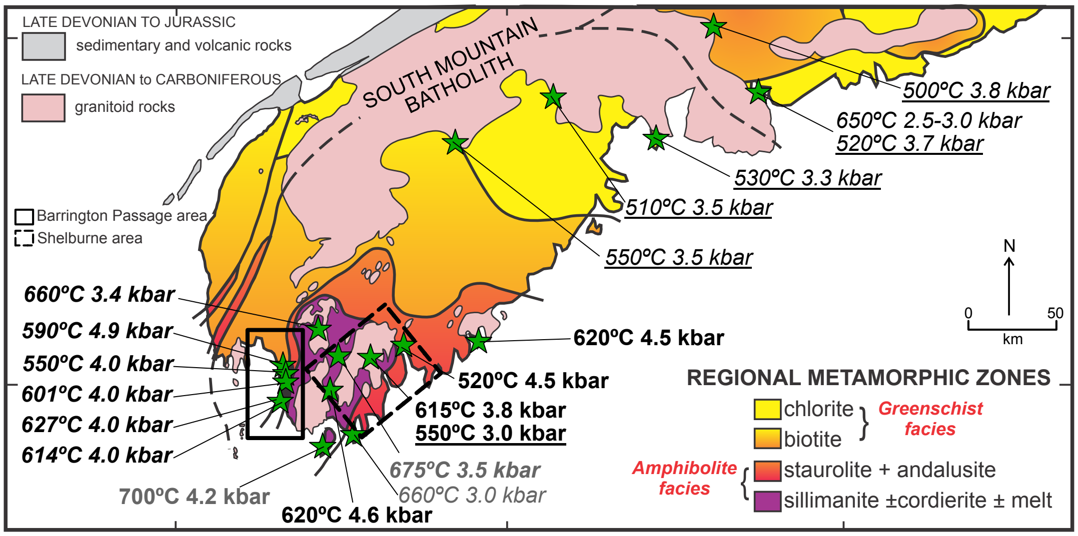

***From: This study,*** **Currie et al. 1998;** *Jamieson et al. 2012;* **White 1984;** **Borque 1985,** ***Misner 1986;*** *Wentzell 1986;* *Mahoney 1996*

Figure 5.9: Summary of *P-T* conditions from the Meguma terrane, Nova Scotia.

# Chapter 6: Conclusions

## 6.1 SUMMARY OF WORK

This PhD dissertation explored two broad themes: i) the microstructural controls on metamorphic processes in the crust and ii) the processes that control mineral crystallization during metamorphism. As a part of these two themes, several associated topics are explored including: the extent to which equilibrium versus kinetics control metamorphic petrogenesis, the properties of grain boundaries in metamorphic rocks, and the metamorphic and tectonic evolution of the Meguma Terrane, Nova Scotia.

It is clear that kinetic processes such as: reactant breakdown, diffusional transport, nucleation, and crystal growth play an important role in controlling the evolution of some metamorphic rocks (Kretz 1973; Ridley and Thompson 1986; Carlson 2011; Carlson et al. 2015; Pattison and Spear 2018). Yet, there are other examples that highlight that metamorphism may occur at near equilibrium conditions (Gatewood et al. 2015; George and Gaidies 2017; Catlos et al. 2018).

This dissertation explored this topic in two ways. First, Chapter 4 examined the differences between overstepped (i.e. likely containing kinetics barriers to nucleation) and non-overstepped (i.e. likely containing minimal kinetic barriers to nucleation) rocks in the thermodynamic modeling of a suite of previously described samples. There are differences in the trends in the evolution of the chemical potentials of garnet-forming reactants between the overstepped and non-overstepped scenarios. This highlights that equilibrium thermodynamic modeling may be used to further explore, and potentially predict, the extent to which kinetic factors may control the crystallization of garnet during metamorphism.

Second, one sample, 2018PPGrt_01, is explored in Chapter 2 & 5 as a case study to study garnet crystallization. To achieve this, multiple analyses were applied, with the goal of describing a comprehensive model of garnet nucleation and growth in this rock. Comparison of equilibrium thermodynamic models to quantitative constraints of garnet composition in the natural sample reveals that garnet likely nucleated at the *P-T* conditions of garnet-in, experiencing minimal overstepping. Interpretation of EBSD analysis reveals that garnet likely crystallized by nucleated on the crystal structure of muscovite. Muscovite is abundant in this rock, thus providing ample nucleation sites, which allow for garnet nucleation with minimal kinetic barriers and therefore at close to equilibrium conditions. Finally, interpretation of the analysis of the 3D spatial distribution of garnet crystals reveals that the growth of garnet was likely controlled by the diffusion of Al through the intergranular matrix. This follows from the fact that while garnet nucleates on muscovite, it is the breakdown of chlorite that likely provides Al for the garnet crystal to grow. Therefore, there needs to be diffusion between the breaking down chlorite and garnet growing on muscovite, and it is this diffusional step that controls the overall rate of garnet crystallization.

Next, SEM and TEM imaging are utilized to characterize the properties of grain boundaries in metamorphic rocks in Chapter 3 and Appendix A. Grain boundaries are important sites of diffusional transport and mineral nucleation in metamorphic rocks, and thus characterizing grain boundaries may provide insights into these processes. However, the properties of grain boundaries evolve from the peak *P-T* conditions of the rock to when the rock is in the hands of excited metamorphic petrologists. In both quartz-quartz and garnet-quartz grain boundaries there is a non-random distribution of void space at grain boundaries, which formed during exhumation. Thus, not all grain boundaries preserve characteristics of peak metamorphic

*P-T* conditions. While it is possible to characterize grain boundaries in metamorphic rocks on the nanoscale, care must be taken to link the properties of grain boundaries to the appropriate geologic process the rock has undergone.

The Meguma Terrane is the most outboard terrane of the Appalachian orogen, and its metamorphic and tectonic history is poorly constrained. As such, I worked to produce new *P-T* data and integrated that with previous *P-T* constraints to better understanding its metamorphic and tectonic evolution (Chapter 5). At the crustal level exposed on the surface today, metamorphic grade increases to the SW. This suggests that it is possible that the southwestern Meguma Terrane was buried deeper ~400-350 Ma than the northeast and since then, it has undergone differential uplift and erosion. This suggests that the entire Meguma Terrane could represent a regional metamorphic sequence that formed when the Meguma Terrane was thrust over the Avalon Terrane to the west ~405-395 Ma during the Neoacadian orogeny. Localized areas of higher metamorphic grade are likely driven by heat from nearby granitic plutons that intruded ~373 Ma.

Work in this dissertation highlights how the microstructure (or orientation and distribution of minerals) can control both the crystallization of metamorphic minerals and the distribution of porosity in metamorphic rocks. Further, the mechanisms controlling garnet crystallization are investigated via two different approaches. First, numerous examples of terranes in which garnet is varyingly overstepped are used to provide examples of how thermodynamic modeling can be used to better understand garnet nucleation and growth. Second, a case study of one sample from the Mosher's Island Formation, Nova Scotia reveals a comprehensive understanding of garnet crystallization in that sample. Taken together, these examples highlight how taking a holistic approach (either with a large sample size or multiple analyses on one sample) can provide important information on the processes controlling garnet crystallization during metamorphism.

## 6.2 FUTURE WORK

This dissertation work has inspired some future work. Here are some topics that may be addressed by researchers in the future.

*What are the best places to characterize prograde grain boundaries?* One challenge in this study of grain boundaries was the fact that the properties of grain boundaries were found to change during exhumation, making it challenging to study processes such as mineral crystallization and re-equilibration. The rocks studied here underwent relatively slow uplift and exhumation, therefore allowing the properties of grain boundaries to change during exhumation. It therefore may be necessary to study metamorphic rocks with different exhumation paths that better understand grain boundary characteristics. One option includes Kilbourne Hole in the southwestern United States, which is a volcano that erupts crustal xenoliths, exposing fresh and young metamorphic rocks (Cipar et al. 2020). Does this extremely fast exhumation mechanism reduce the changes in the properties of grain boundaries within metamorphic rocks? If future studies plan on characterizing the properties of grain boundaries in metamorphic rocks, it will be important to think about how the exhumation path may affect the grain boundaries. Erupted xenoliths may be one way to mitigate this challenge.

*What is the timing of metamorphism in the Meguma Terrane?* While we provide *P-T* and microstructural data to support our interpretation that much of the metamorphism in the southwestern Meguma terrane is a result of regional metamorphism ~405-395 Ma with localized recrystallization ~373 Ma, garnet geochronology could be utilized to place an age on the metamorphism of the Meguma Terrane. Either Sm-Nd or Lu-Hf garnet geochronology would place a constraint on the timing of amphibolite facies metamorphism (Duchêne et al. 1997; Baxter and Scherer 2013; Baxter et al. 2017). Further, a targeted study dating different crystal sizes of garnet (Skora et al. 2009; Smit et al. 2013) or zoned garnet geochronology (Pollington and Baxter 2010; Dragovic et al. 2012) may provide greater insights into the timing and duration of metamorphism during the formation of the Meguma Terrane. Additionally, more *P-T* and age constraints from the Shelburne and Port Mouton pluton areas (Hwang 1997; Clarke et al. 1998) is likely necessary. This area provides an important link between the contact aureole of the South Mountain Batholith near Halifax, which has clear quantitative *P-T* constraints (Jamieson et al. 2012) and our work in the southwestern Meguma Terrane. Understanding the timing and conditions of metamorphism in this area could provide important constraints on the relative heating effects of regional versus contact metamorphism in the Meguma Terrane.

*What is the extent of fluid infiltration in the Meguma Terrane?* In the area surrounding the Barrington Passage Tonalite, there is evidence for fluid infiltration during metamorphism. Large (10 cm) andalusite crystals that contain garnet crystals with $H_2O$ bearing fluid inclusions suggest that water may play an important role in the metamorphic petrogenesis of these rocks. However, the geographic extent of fluid infiltration and the source of the fluid are not known. A regional, broad scale study of oxygen isotopes in garnet (Valley 1986; Raimondo et al. 2012; Vho et al. 2020) could provide critical information about the source (magmatic or metamorphic) and extent to which fluid infiltration drove the metamorphism in the Meguma Terrane.

*What is the best approach to study interface versus diffusion controlled garnet growth?* One fundamental question remaining is: what metamorphic conditions and textures promote the equilibrium versus kinetic controls during metamorphism? What extent does heating rate, distribution of reactant minerals, matrix mineral homogeneity/heterogeneity, time at peak *P-T* conditions, etc. play in whether garnet forms via ICNG or DCNG? One approach to look at this may be to create a database of the likely factors that control metamorphic textural evolution and the resulting mechanism (ICNG or DCNG) for all known samples in which this has been studied. That may produce some clear trends as to which variables should be more closely studied and which variables may exert a stronger control on the textural evolution of garnet. This could also be used in the future to produce a better computational model of garnet crystallization, leading to a predictive model of garnet nucleation and growth.

*Does epitaxial nucleation of garnet occur in metabasites?* This dissertation provides an interpretation that garnet likely crystallizes via epitaxial nucleation on muscovite crystals during regional and contact metamorphism of pelitic rocks. However, does that occur in other rock types? Garnet also forms in subduction zones commonly from protolith compositions that are more basaltic in nature. The crystallization of garnet releases water from dehydration reactions, which may be a source of earthquakes in subduction zones (Hacker et al. 2003). Thus, it is important to be able to constrain the crystallization of garnet in subduction zones. However, it is not currently known what processes control garnet crystallization there. A similar approach as utilized in this study (i.e. combining EBSD, atomic scale crystal structure models, and X-Ray CT data) may be able to answer this question.

*What about staurolite?* Staurolite forms at greater *P-T* conditions than garnet, and previous work suggests that it may form in epitaxial relationships with kyanite (Cesare and Grobety 1995) and that there may be kinetic impediments to its crystallization (Pattison et al. 2011; Pattison and Spear 2018). Yet, the kinetics of staurolite crystallization are poorly constrained. This could be investigated via: i) EBSD of staurolite and other minerals in the rock to test if staurolite may crystallize via epitaxial or topotaxial relationships and ii) CT data on the 3D size, location, shape, and orientation of staurolite to test to see if it crystallizes via DCNG or ICNG. Results from these analyzes may provide important constraints, more broadly, on mineral crystallization kinetics during metamorphism.

*What are the uncertainties on pseudosection calculations?* The uncertainties on any given mineral-in or mineral-out reaction in a pseudosection is ±50ºC and 1 kbar (Palin et al. 2016). However, that number is based on the uncertainties in the calculation of the bulk rock composition used in forward modeling. What is less understood, as of now, is the uncertainties within mineral assemblage fields. For example, if garnet-in can shift ±50ºC what does that mean for the amount of garnet and other minerals in that calculation and their compositions? Understanding questions like this may prove important to interpreting pseudosection calculations.

Some of the work described here is currently ongoing, while other work will likely occur in the future.

## 6.3 REFERENCES

Baxter, E.F., and Scherer, E.E. (2013) Garnet geochronology: Timekeeper of tectonometamorphic processes. Elements, 9, 433–438.

Baxter, E.F., Caddick, M.J., and Dragovic, B. (2017) Garnet: A rock-forming mineral petrochronometer. Reviews in Mineralogy & Geochemistry, 83, 469–533.

Carlson, W.D. (2011) Porphyroblast crystallization: linking processes, kinetics, and microstructures. International Geology Review, 53, 406–445.

Carlson, W.D., Pattison, D.R.M., and Caddick, M.J. (2015) Beyond the equilibrium paradigm: How consideration of kinetics enhances metamorphic interpretation. American Mineralogist, 100, 1659–1667.

Catlos, E.J., Lovera, O.M., Kelly, E.D., Ashley, K.T., Harrison, T.M., and Etzel, T. (2018) Modeling High-Resolution Pressure-Temperature Paths Across the Himalayan Main Central Thrust (Central Nepal): Implications for the Dynamics of Collision. Tectonics, 37, 2363–2388.

Cesare, B., and Grobety, B. (1995) Epitaxial replacement of kyanite by staurolite: A TEM study of the microstructures. American Mineralogist, 80, 78–86.

Cipar, J.H., Garber, J.M., Kylander-Clark, A.R.C., and Smye, A.J. (2020) Active crustal differentiation beneath the Rio Grande Rift. Nature Geoscience, 13, 758–763.

Clarke, D.B., Henry, A.S., and White, M.A. (1998) Exploding xenoliths and the absence of ‘elephants’ graveyards’ in granite batholiths. Journal of Structural Geology, 20, 1325–1343.

Dragovic, B., Samanta, L.M., Baxter, E.F., and Selverstone, J. (2012) Using garnet to constrain the duration and rate of water-releasing metamorphic reactions during subduction: An example from Sifnos, Greece. Chemical Geology, 314–317, 9–22.

Duchêne, S., Blichert-Toft, J., Luais, B., Télouk, P., Lardeaux, J.M., and Albarède, F. (1997) The Lu-Hf dating of garnets and the ages of the Alpine high-pressure metamorphism. Nature, 387, 586–589.

Gatewood, M.P., Dragovic, B., Stowell, H.H., Baxter, E.F., Hirsch, D.M., and Bloom, R. (2015) Evaluating chemical equilibrium in metamorphic rocks using major element and Sm-Nd isotopic age zoning in garnet, Townshend Dam, Vermont, USA. Chemical Geology, 401, 151–168.

George, F.R., and Gaidies, F. (2017) Characterisation of a garnet population from the Sikkim Himalaya: insights into the rates and mechanisms of porphyroblast crystallisation. Contributions to Mineralogy and Petrology, 172, 1–22.

Hacker, B.R., Peacock, S.M., Abers, G. a., and Holloway, S.D. (2003) Subduction factory 2. Are intermediate-depth earthquakes in subducting slabs linked to metamorphic dehydration reactions? Journal of Geophysical Research, 108, 2030.

Hwang, S.-G. (1997) Regional-scale metasomatism of Al, K, and Na during staurolite-andalusite grade contact metamorphism, in the southwestern Nova Scotia, Canada. Journal of the Petrological Society of Korea, 6, 52–64.

Jamieson, R.A., Hart, G.G., Chapman, G.G., Tobey, N.W., and Murphy, B.J.B. (2012) The contact aureole of the South Mountain Batholith in Halifax, Nova Scotia: geology, mineral assemblages, and isograds. Canadian Journal of Earth Sciences, 49, 1280–1296.

Keppie, J.D., and Dallmeyer, R.D. (1995) Late Paleozoic collision, delamination, short-lived magmatism, and rapid denudation in the Meguma Terrance (Nova Scotia, Canada): constraints from 40Ar/39Ar isotopic data. Canadian Journal of Earth Sciences, 659, 644–659.

Kretz, R. (1973) Kinetics of the crystallization of garnet at two localities near Yellowknife. Canadian Mineralogist, 12, 1–20.

Moran, P.C., Barr, S.M., White, C.E., and Hamilton, M.A. (2007) Petrology, age, and tectonic setting of the Seal Island Pluton, offshore southwestern Nova Scotia. Canadian Journal of Earth Sciences, 44, 1467–1478.

Murphy, J.B., Survey, G., Street, B., Ka, O., Keppie, J.D., Geología, I. De, Nacional, U., and México, A. De (1999) Middle to late Paleozoic Acadian orogeny in the northern Appalachians : A Laramide-style plume-modified orogeny ? Geology, 27, 653–656.

Palin, R.M., Weller, O.M., Waters, D.J., and Dyck, B. (2016) Quantifying geological uncertainty in metamorphic phase equilibria modelling; A Monte Carlo assessment and implications for tectonic interpretations. Geoscience Frontiers, 7, 591–607.

Pattison, D.R.M., and Spear, F.S. (2018) Kinetic control of staurolite-Al2SiO5mineral assemblages: Implications for Barrovian and Buchan metamorphism. Journal of Metamorphic Geology, 36, 667–690.

Pattison, D.R.M., de Capitani, C., and Gaidies, F. (2011) Petrological consequences of variations in metamorphic reaction affinity. Journal of Metamorphic Geology, 29, 953–977.

Pollington, A.D., and Baxter, E.F. (2010) High resolution Sm-Nd garnet geochronology reveals the uneven pace of tectonometamorphic processes. Earth and Planetary Science Letters, 293, 63–71.

Raimondo, T., Clark, C., Hand, M., Cliff, J., and Harris, C. (2012) High-resolution geochemical record of fluid-rock interaction in a mid-crustal shear zone: A comparative study of major element and oxygen isotope transport in garnet. Journal of Metamorphic Geology, 30, 255–280.

Ridley, J., and Thompson, A.B. (1986) The role of mineral kinetics in the development of metamorphic microtextures. Advances in Physical Geochemistry, 5, 154–193.

Skora, S., Lapen, T.J., Baumgartner, L.P., Johnson, C.M., Hellebrand, E., and Mahlen, N.J.

(2009) The duration of prograde garnet crystallization in the UHP eclogites at Lago di Cignana, Italy. Earth and Planetary Science Letters, 287, 402–411.

Smit, M.A., Scherer, E.E., and Mezger, K. (2013) Lu-Hf and Sm-Nd garnet geochronology: Chronometric closure and implications for dating petrological processes. Earth and Planetary Science Letters, 381, 222–233.

Valley, J.W. (1986) Stable isotope geochemistry of metamorphic rocks. Reviews in Mineralogy & Geochemistry, 16, 445–489.

Vho, A., Lanari, P., Rubatto, D., and Hermann, J. (2020) Tracing fluid transfers in subduction zones: An integrated thermodynamic and δ18O fractionation modelling approach. Solid Earth, 11, 307–328.

# Appendix A: Garnet-Quartz Grain Boundary Data

Appendix A presents 7 figures and 1 table that may be formatted into a paper in the future (either on their own or combined with new work). This work aims to characterize garnet-quartz grain boundaries in the nanoscale.

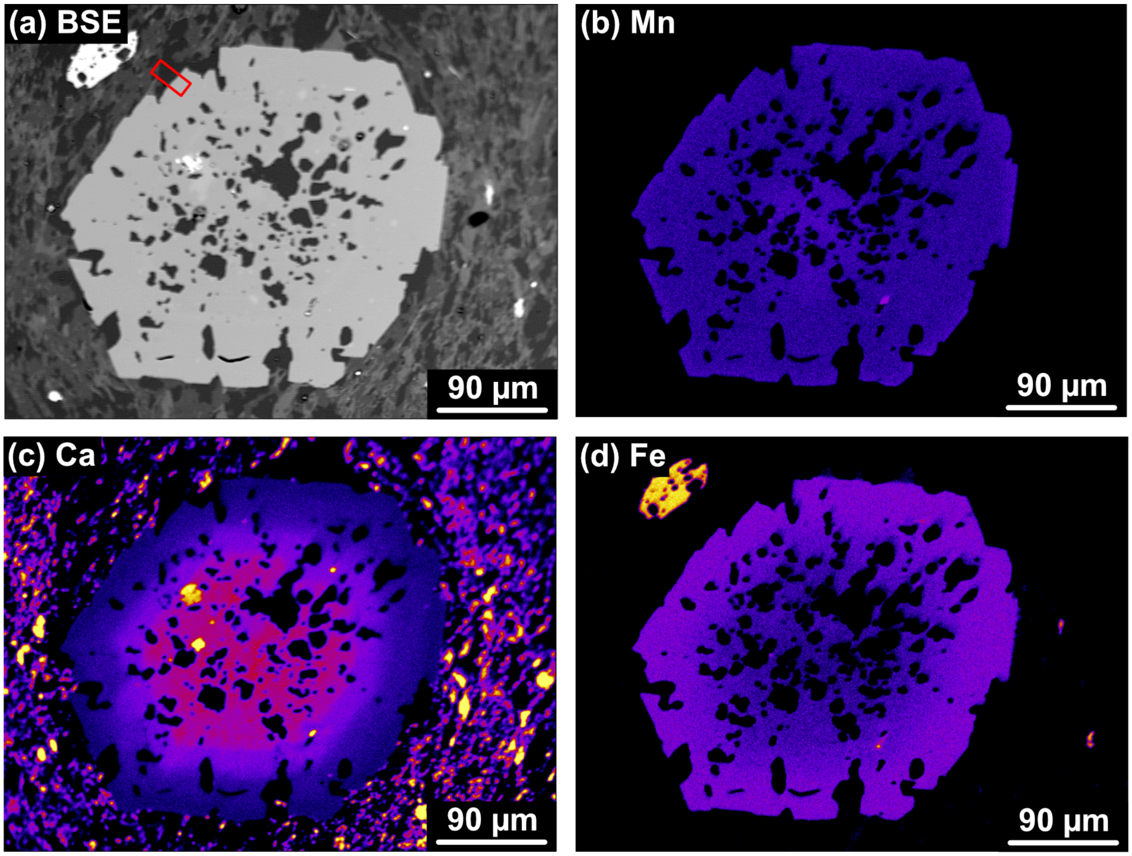

Figure 1. **08-CW-7A BSE and EDS images.** (a) BSE image showing location of garnet-quartz grain boundary used for TEM analysis in red box. (b) Mn. (c) Ca. (d) Fe.

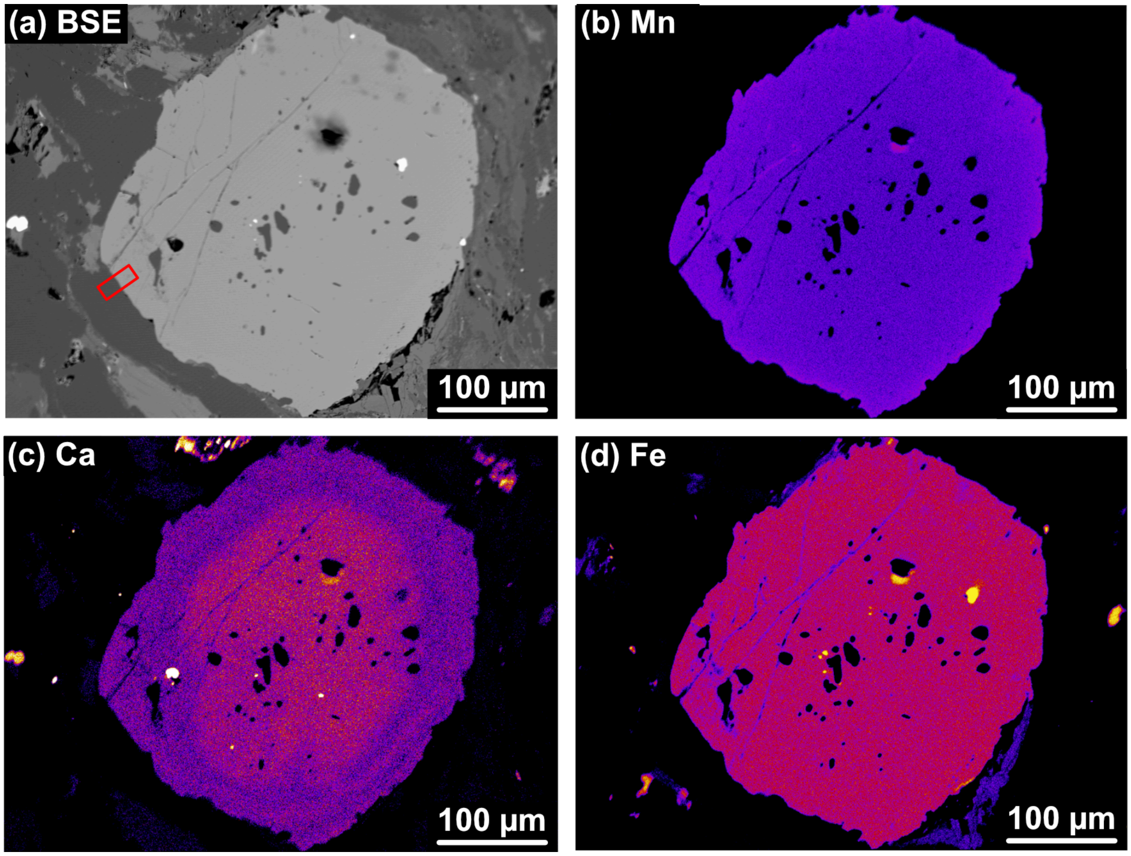

Figure 2. **93-CW-19A BSE and EDS images.** (a) BSE image showing location of garnet-quartz grain boundary used for TEM analysis in red box. (b) Mn. (c) Ca. (d) Fe.

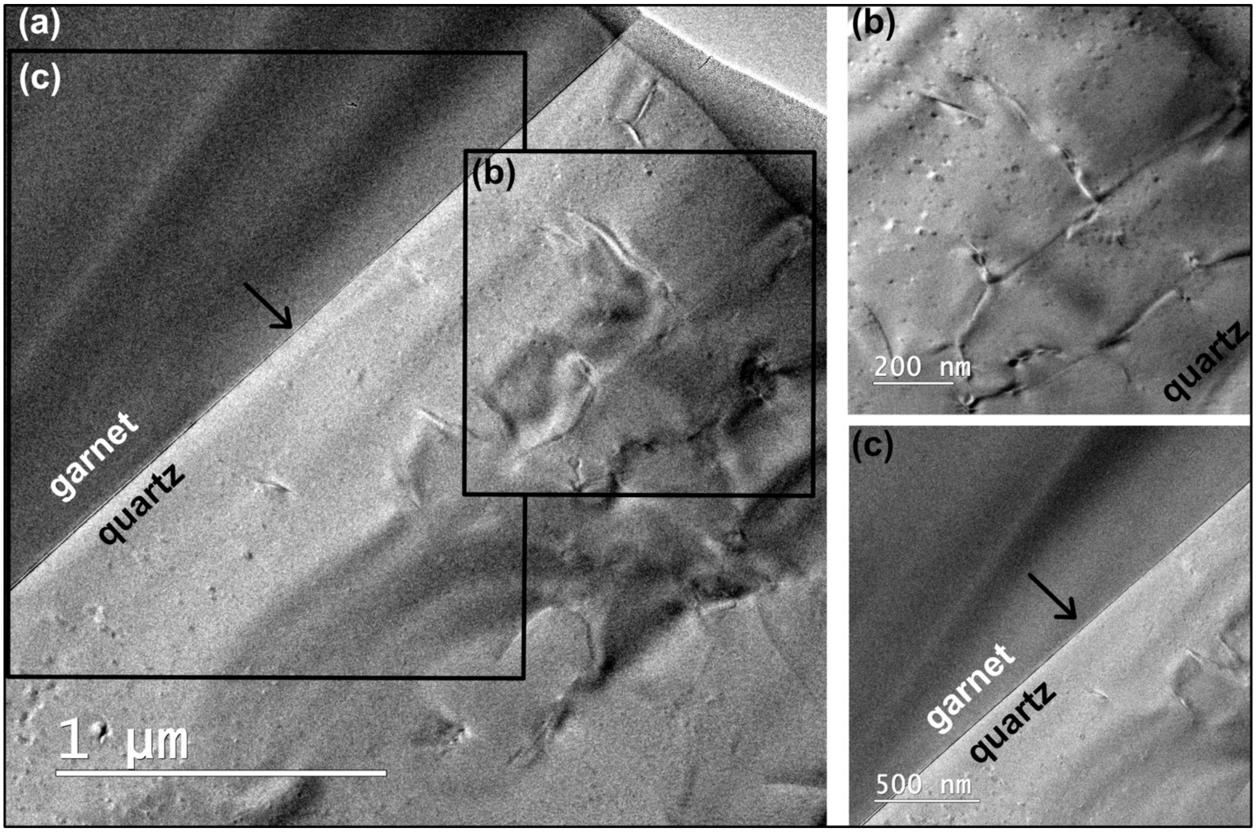

Figure 3. **08-CW-7A Garnet-Quartz TEM Images.** (a) Overview of garnet quartz grain boundary. Garnet is free of dislocations while quartz contains a network of dislocations. Arrow denotes the interface between garnet and quartz. It is a straight line and there is no observable void space. (b) Close up of nanoscale quartz structure showing dislocations in the quartz structure. Speckles are due to beam damage. (c) Close up of the interface between garnet and quartz. There are no dislocations in quartz attached to the grain boundary.

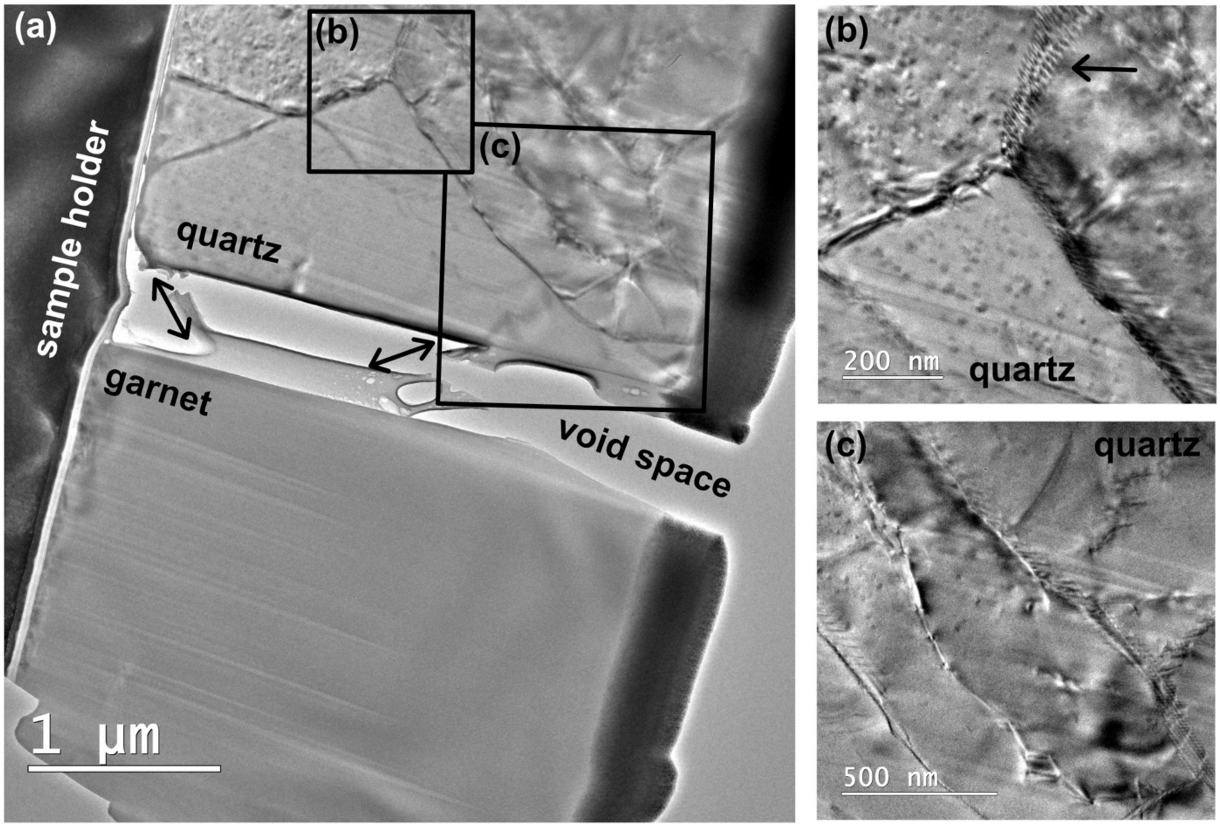

Figure 4. **08-CW-19A Garnet-Quartz TEM Images.** (a) Overview of garnet quartz grain boundary. Garnet is free of dislocations while quartz contains a subgrain boundary (shown in detail in b) and a network of dislocations (shown in detail in c). There is void space between the garnet and the quartz. There is a microstructure (shown with arrows) that was likely connected the garnet and quartz grains prior to damage during TEM analysis. (b) Close up of subgrain boundary in quartz showing dislocations that form the subgrain boundary. Speckles are due to beam damage. (c) Close up of nanoscale quartz structure showing dislocations in the quartz structure.

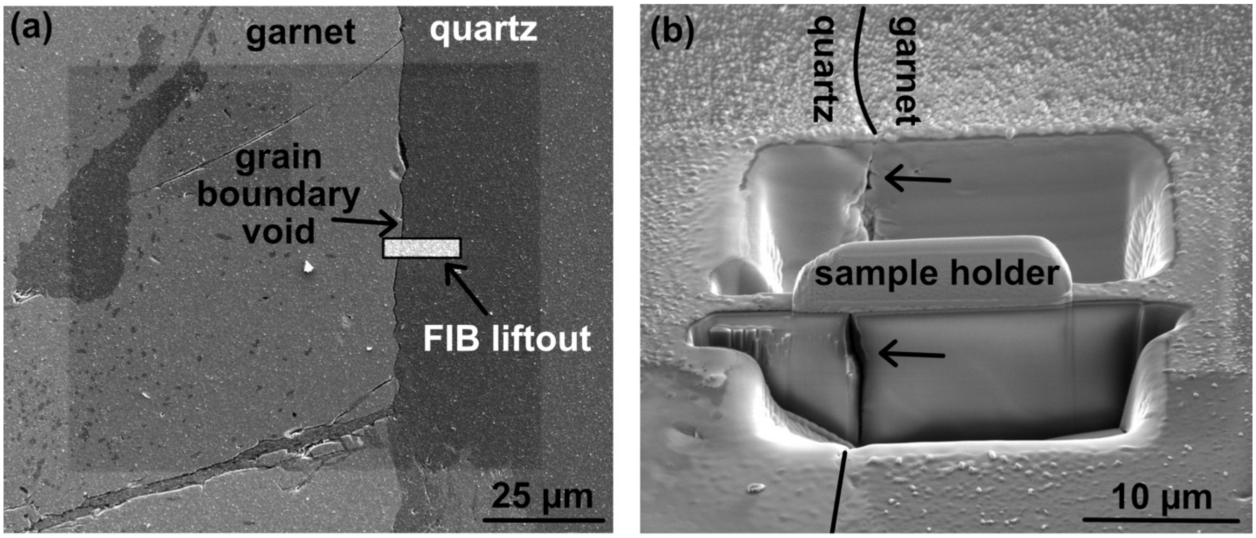

Figure 5. **93-CW-19A FIB Liftout.** (a) SEM BSE image of garnet and quartz. Location of FIB liftout is shown in black box with white interior. There is void space (noted by darker contrast in BSE image) along the garnet-quartz interface. (b) FIB ion milled garnet-quartz grain boundary. The trace of the grain boundary on the surface of the thin section is noted with a black line. Black arrows note the location of grain boundary voids in three dimensions.

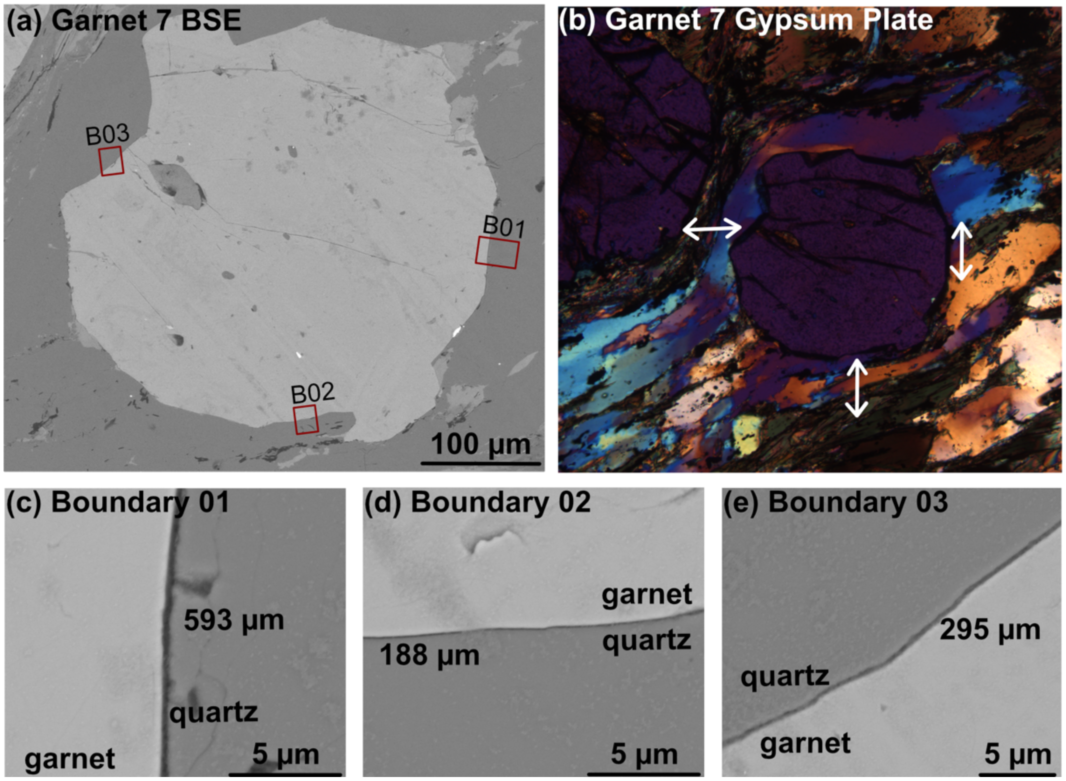

Figure 6. **93-CW-19A Garnet 7.** (a) BSE image showing location three measured garnet- quartz grain boundaries. (b) Photomicrograph of Garnet 7 with gypsum plate. Arrows show the orientation of the quartz c-axis for the 3 noted quartz grains in (a). (c-e) BSE images of garnet-quartz grain boundaries with measured grain boundary widths noted.

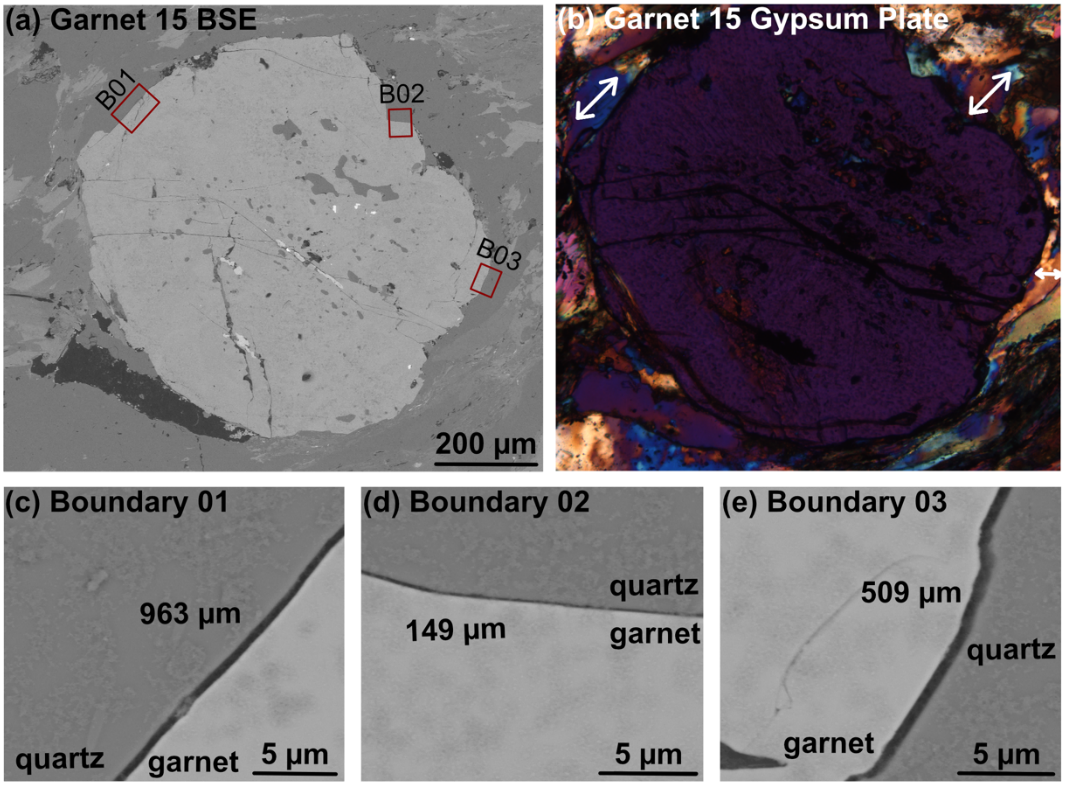

Figure 7. **93-CW-19A Garnet 15.** (a) BSE image showing location three measured garnet-quartz grain boundaries. (b) Photomicrograph of Garnet 15 with gypsum plate. Arrows show the orientation of the quartz c-axis for the 3 noted quartz grains in (a). (c-e) BSE images of garnet-quartz grain boundaries with measured grain boundary widths noted.

Table 1: Measured grain boundary widths, angle of grain boundary relative to the thin section plane, and orientation of quartz c axis relative grain boundary.

| | Average Measured Grain Bounday Width (nm) | Angle of Grain Boundary Relative to Thin Section Plane | **Quartz C Axis Orientation** |
|---|---|---|---|
| **Grt01 Boundary01** | 348 | | sub perpendicular |
| **Grt01 Boundary02** | 463 | | Unsure |

| | | |
|---|---|---|
| **Grt02 Boundary01** | 320 | Unsure |
| **Grt04 Boundary01** | 245 | pub perpendicular |
| **Grt07 Boundary01** | 593 | parallel |
| **Grt07 Boundary02** | 188 | perpendicular |
| **Grt07 Boundary03** | 295 | sub perpendicular |
| **Grt08 Boundary01** | 191 | perpendicular |
| **Grt08 Boundary02** | 221 | parallel |
| **Grt13 Boundary01** | 401 | sub perpendicular |
| **Grt15 Boundary01** | 963 | parallel |
| **Grt15 Boundary02** | 149 | perpendicular |
| **Grt15 Boundary03** | 509 | perpendicular |
| **Grt24 Boundary01** | 349 | sub perpendicular |
| **Grt24 Boundary02** | 261 | perpendicular |
| **Grt28 Boundary01** | 213 | sub perpendicular |
| **Grt28 Boundary02** | 217 | perpendicular |
| **Grt28 Boundary03** | 217 | perpendicular |
| **Grt29 Boundary01** | 59 | perpendicular |
| **Grt29 Boundary02** | 0 | perpendicular |
| **Average** | 310 | |

# Appendix B: Supplemental Material to Chapter 2

## Preferred Orientation of Garnet Porphyroblasts Reveals Previously Cryptic Templating During Nucleation

(online Supplementary Material)

Alexandra B. Nagurney*[1], Mark J. Caddick[1], David R.M. Pattison[2], F. Marc Michel[1]

[1] Department of Geosciences, Virginia Tech, Blacksburg VA, USA
[2]Department of Geosciences, University of Calgary, Calgary, Canada
*corresponding author: nagurney@vt.edu

**Geographic Coordinates of Samples**
08-CW-7A: 11U 0488607, 5467169
08-CW-7.5: 11U 0488662, 5467267
2018PPGrt_01: N 43.1373 W 65.7871

**Geologic Maps:**
Figure S1: Geologic Map of the Nelson Aureole (redrawn from Pattison and Tinkham, (2009))

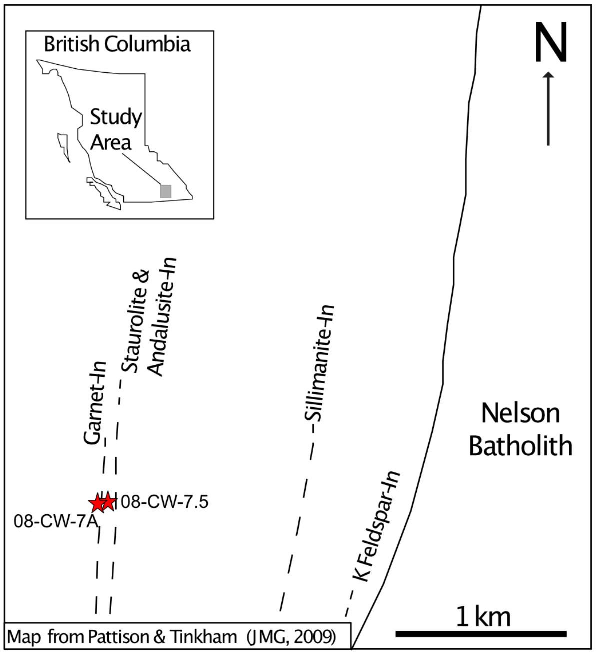

Figure S2: Geologic Map of southwestern Nova Scotia (redrawn from Currie et al., (1998)).

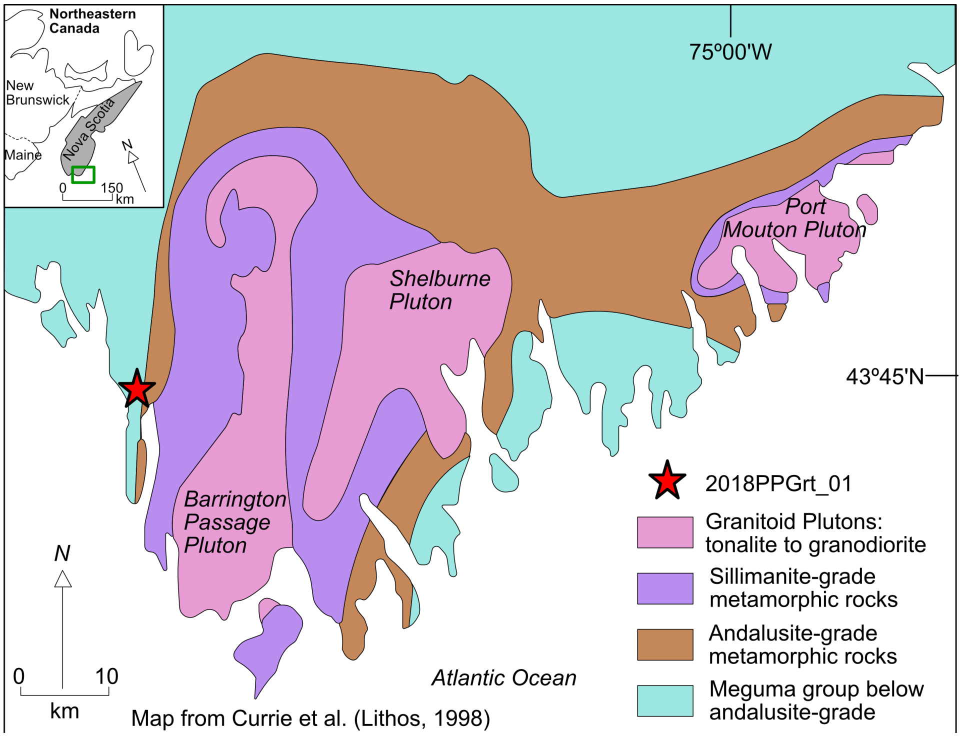

## Geologic Background

The Nelson aureole is comprised of graphitic, sulfidic, argillaceous Triassic-Jurassic aged Ymir Group sediments that were regionally metamorphosed to greenschist facies and developed a regional $S_1$ foliation prior to the intrusion of the Jurassic Nelson batholith. This intrusion further metamorphosed the Ymir Group sediments surrounding the Nelson batholith creating a contact aureole (Pattison and Vogl, 2005). Both 08-CW-7.5 and 08-CW-7A contain biotite, chlorite, garnet, muscovite, plagioclase, and quartz, garnet overgrows the foliation, and peak *P*-*T* conditions are ~530ºC and 3.5 kbar (Pattison and Vogl, 2005; Pattison and Tinkham, 2009). The Cambrian-aged Mosher's Island formation is a manganese-rich siltstone to slate that was metamorphosed to greenschist-amphibolite facies during the Devonian collision of the Meguma Terrane with North America during the Acadian Orogeny (Schiller and Taylor, 1966; Currie et al., 1998; White and Barr, 2010). Sample 2018PPGrt_01 contains biotite, chlorite, garnet, muscovite, plagioclase, staurolite, and quartz, and garnet overgrows the foliation. In both localities, syn-intrusive garnet growth has previously been interpreted to postdate regional metamorphism (and foliation development) (Taylor and Schiller, 1966; Pattison and Vogl, 2005; Pattison and Tinkham, 2009; White and Barr, 2010).

**Figure S3-** Petrography of Nelson Aureole and Mosher's Island Formation samples.

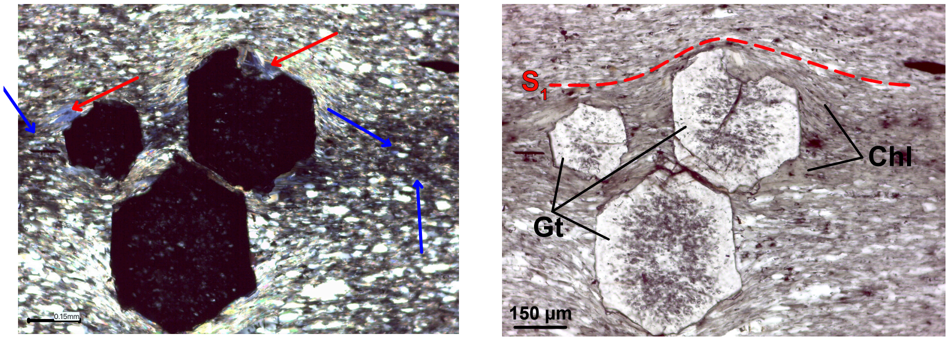

XPL photomicrograph of Mosher's Island formation showing select examples of prograde chlorite (blue arrows) which was identified as being in line with the foliation. Retrograde chlorite (red arrows) is characterized as having a texture in which it appears to be replacing garnet porphyroblasts. Here chlorite is replacing garnet which is breaking down.

PPL photomicrograph of Mosher's Island formation showing garnet and chlorite. The foliation is horizontal and is deflected by the growth of garnet.

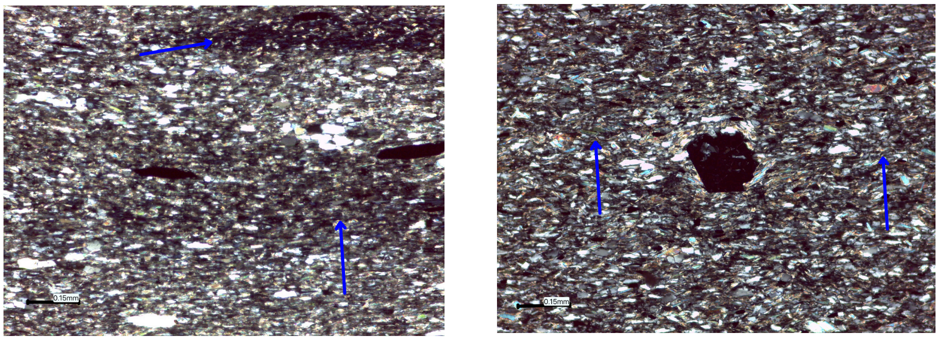

XPL photomicrograph of Mosher's Island formation showing more examples of prograde chlorite (areas highlighted by the blue arrows) in the matrix. Matrix phases include: quartz, plagioclase, chlorite, muscovite, biotite, and ilmenite.

XPL photomicrograph of Nelson aureole sample showing select examples of prograde chlorite (blue arrows) which was identified as being in line with the foliation. There is no clearly identifiable retrograde chlorite in this sample.

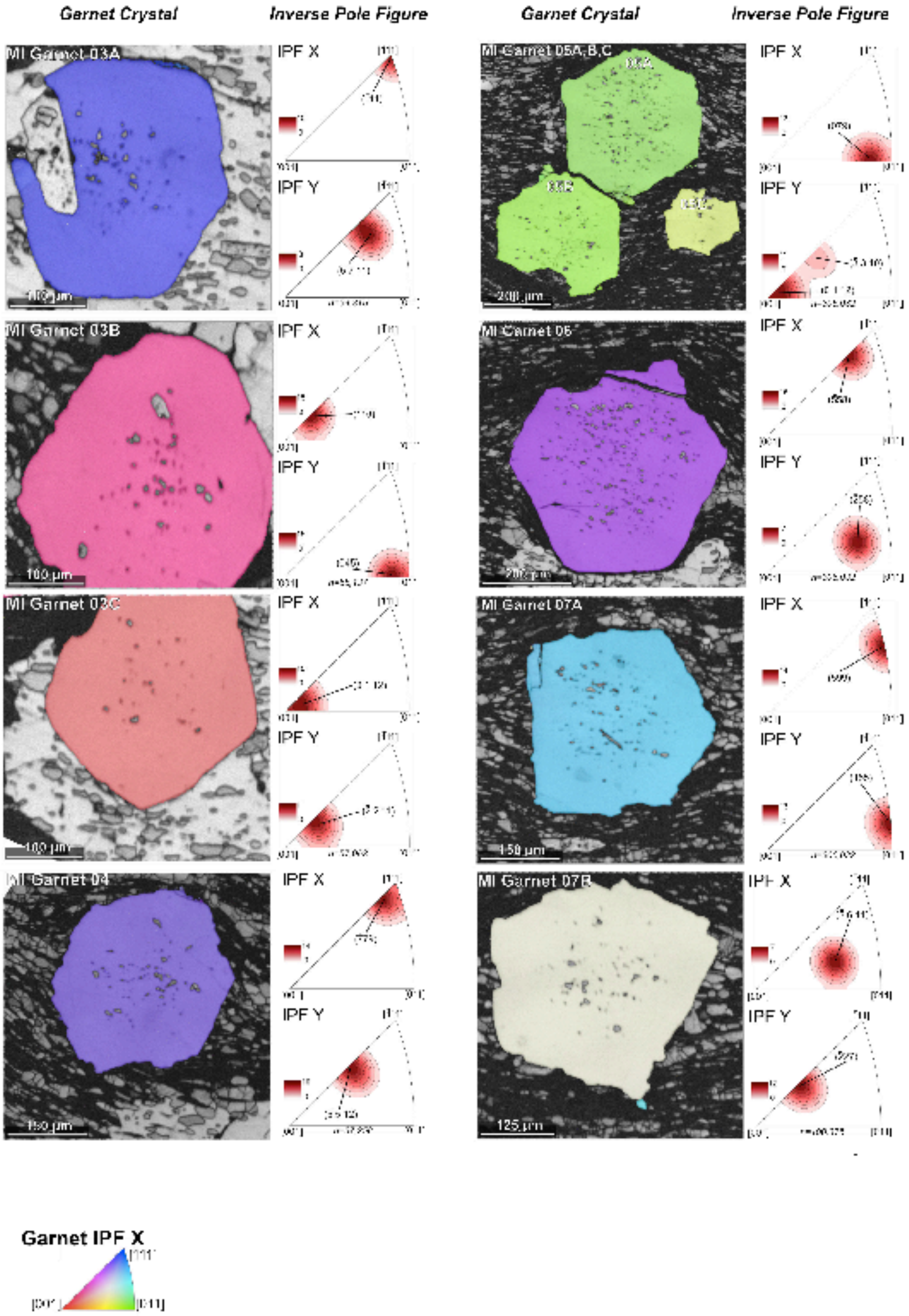
Garnet Crystal
Inverse Pole Figure
Garnet Crystal
Inverse Pole Figure
MI Garnet 03A
100 µm
MI Garnet 03B
100 µm
MI Garnet 03C
100 µm
MI Garnet 04
150 µm
MI Garnet 05A,B,C
05A
05B
05C
200 µm
MI Garnet 06
200 µm
MI Garnet 07A
150 µm
MI Garnet 07B
125 µm
IPF X
IPF Y
[111]
[001]
[011]
Garnet IPF X
[111]
[001]
[011]

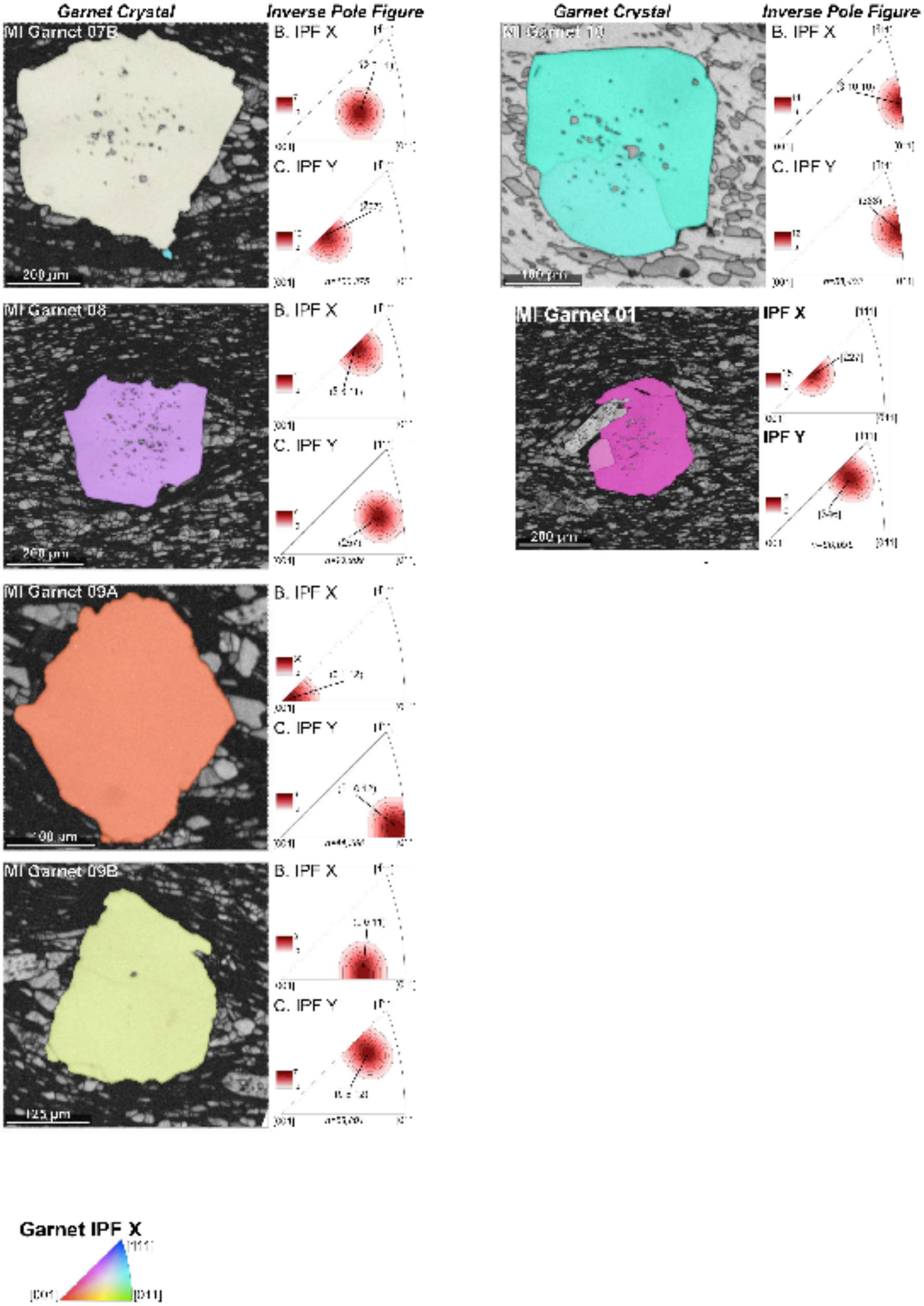
Garnet Crystal
Inverse Pole Figure
MI Garnet 07B
B. IPF X
C. IPF Y
200 µm
MI Garnet 08
B. IPF X
C. IPF Y
200 µm
MI Garnet 09A
B. IPF X
C. IPF Y
MI Garnet 09B
B. IPF X
C. IPF Y
125 µm
Garnet Crystal
Inverse Pole Figure
MI Garnet 10
B. IPF X
C. IPF Y
100 µm
MI Garnet 01
IPF X
IPF Y
200 µm
[001]
[011]
[111]
Garnet IPF X
[111]
[001]
[011]

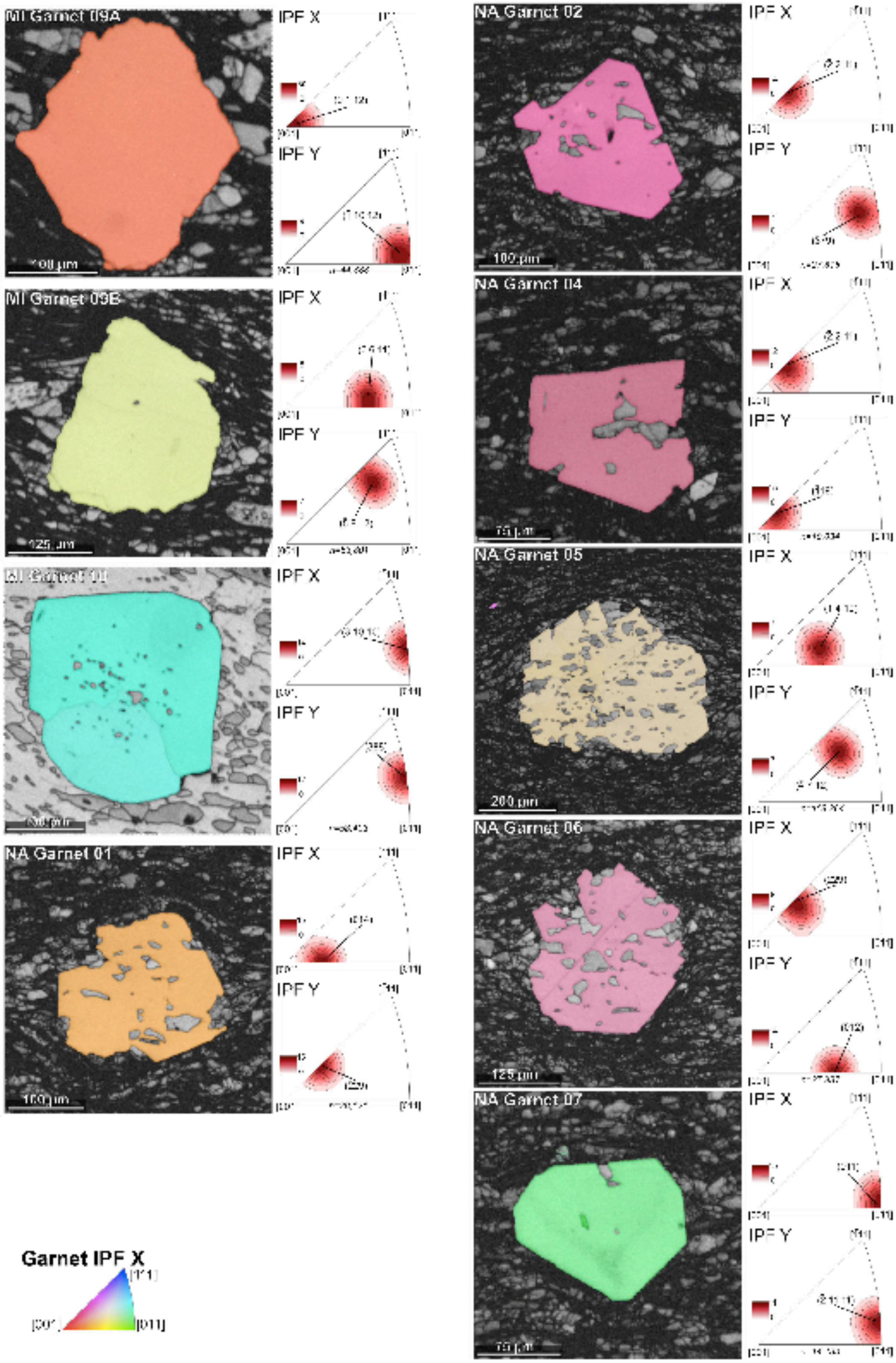
MI Garnet 09A
100 µm
IPF X
IPF Y
MI Garnet 09B
125 µm
IPF X
IPF Y
MI Garnet 10
100 µm
IPF X
IPF Y
NA Garnet 01
150 µm
IPF X
IPF Y
NA Garnet 02
100 µm
IPF X
IPF Y
NA Garnet 04
75 µm
IPF X
IPF Y
NA Garnet 05
200 µm
IPF X
IPF Y
NA Garnet 06
125 µm
IPF X
IPF Y
NA Garnet 07
75 µm
IPF X
IPF Y
Garnet IPF X
[111]
[001]
[011]

**Table S1:** Summary of EBSD results. For each crystal, the corresponding plane to the directions of garnet that are parallel to the X (horizontal, parallel foliation), Y, (vertical, perpendicular to the foliation), and Z (perpendicular to thin section plane, parallel to foliation) are plotted. All crystal planes have been grouped into their corresponding best fit planes (see Fig. 3B). Table shows corresponding crystal plane, crystal plane group, and the angular difference between the two.
The angular difference was calculated using the equation between planes for a cubic crystal like:

$$\cos \Phi = \frac{h_1 h_2 + k_1 k_2 + l_1 l_2}{\sqrt{h_1^2 + k_1^2 + l_1^2} * \sqrt{h_2^2 + k_2^2 + l_2^2}}$$

where Φ = the angle between planes and hkl are the crystal planes in garnet.
The best fit plane was chosen as the mean orientation of all the planes in the cluster.

| | X | | | Y | | | Z |
|---|---|---|---|---|---|---|---|
| Garnet Number | Crystal Plane | Crystal Plane Group | Angular Difference (°) | Crystal Plane | Crystal Plane Group | Angular Difference (°) | Crystal Plane |
| Mosher's Island Formation | | | | | | | |
| Garnet 01 | {-2 2 7} | {-1 1 6} | 8.74 | {-3 4 6} | {-3 4 6} | 0 | {0 7 10} |
| Garnet 03A | {-1 1 1} | {-7 7 9} | 7.01 | {-5 7 11} | {-3 4 6} | 1.97 | {-1 10 10} |
| Garnet 03B | {-1 1 6} | {-1 1 6} | 0 | {0 4 5} | {-2 11 11} | 9.68 | {-3 8 10} |
| Garnet 03C | {0 1 12} | {-1 1 6} | 10.45 | {-2 2 11} | {-2 2 11} | 0 | {0 2 9} |
| Garnet 04 | {-7 7 9} | {-7 7 9} | 0 | {-5 5 12} | {-3 4 6} | 10.4 | {-1 7 7} |
| Garnet 05A | {0 7 9} | {0 7 9} | 0 | {0 1 12} | {-2 2 11} | 11.55 | {-1 6 8} |
| Garnet 05B | {0 7 9} | {0 7 9} | 0 | {-3 4 12} | {-2 2 11} | 8.58 | {-5 7 9} |
| Garnet 05C | {0 5 8} | {0 7 9} | 5.87 | {-1 1 8} | {-2 2 11} | 4.4 | {-1 3 5} |
| Garnet 06 | {-5 5 8} | {-7 7 9} | 6.25 | {-2 5 8} | {-3 4 6} | 10.74 | {-5 11 11} |
| Garnet 07A | {-5 9 9} | {-7 7 9} | 11.94 | {-1 5 5} | {-2 11 11} | 0.72 | {-2 5 12} |
| Garnet 07B | {-2 6 11} | {0 7 9} | 12.94 | {-2 2 7} | {-2 2 11} | 7.59 | {-3 3 7} |
| Garnet 08 | {-6 6 11} | {-7 7 9} | 10.08 | {-2 5 7} | {-3 4 6} | 9.67 | {-2 4 9} |
| Garnet 09A | {0 1 12} | {-1 1 6} | 10.45 | {-1 10 12} | {-2 11 11} | 6.34 | {0 5 6} |
| Garnet 09B | {0 6 11} | {0 7 9} | 9.27 | {-5 8 12} | {-3 4 6} | 3.47 | {-6 11 12} |
| Garnet 10 | {-3 10 10} | {0 7 9} | 13.89 | {-3 8 8} | {-3 4 6} | 13.21 | {0 1 3} |
| Nelson Aureole | | | | | | | |
| 7.5 Garnet 01 | {0 1 4} | {-1 1 6} | 10.39 | {-2 2 9} | {-2 2 11} | 3.03 | {0 1 5} |
| 7.5 Garnet 02 | {-2 2 11} | {-1 1 6} | 1.15 | {-3 7 9} | {-3 4 6} | 8.79 | {0 4 5} |
| 7.5 Garnet 04 | {-2 2 11} | {-1 1 6} | 1.15 | {-1 1 9} | {-2 2 11} | 5.49 | {-1 2 9} |
| 7.5 Garnet 05 | {-1 4 10} | {-1 1 6} | 12.89 | {-4 7 12} | {-3 4 6} | 7.29 | {-3 7 10} |
| 7.5 Garnet 06 | {-2 2 9} | {-1 1 6} | 4.19 | {0 1 2} | {0 1 2} | 0 | {-3 4 8} |

| | | | | | | | |
|---|---|---|---|---|---|---|---|
| 7.5 Garnet 07 | {0 1 1} | {0 7 9} | 7.13 | {-2 11 11} | {-2 11 11} | 0 | {0 1 12} |
| 7A Garnet 05** | {-1 4 5} | {0 7 9} | 8.91 | {-7 7 10} | {-7 7 10} | 0 | {-4 5 10} |

** Indicates sample that is shown in the main text.

**Figure S5:** The following figure shows the EBSD generated phase maps for all 22 analyzed garnet crystals as well as pole figures for garnet, chlorite, and muscovite. All of the garnet crystals indexed very well >1,000 analyses per grain. Most of the chlorite and muscovite crystals indexed well, with a few exceptions. Pole figures are only presented for samples that have >100 points for chlorite and muscovite. For most samples the $(001)_{chl,ms}$ planes are parallel to the trace of the foliation. Where that is not the case, this is due to:

1. All of the orientation data is from one ‘oddly oriented’ grain that is not representative of the dominant rock foliation (NA Garnet 05).
2. Certain grains were mis indexed: there were a few cases in which staurolite was improperly indexed as muscovite, thus the muscovite pole figure is not representative of the actual muscovite in the rock (MI Garnet 03, MI Garnet 03C).
3. Muscovite or chlorite is an inclusion in ilmenite, thus not representing the dominant orientation of muscovite or chlorite in the rock (MI Garnet 03, MI Garnet 09B).
4. The muscovite and chlorite have been deflected by staurolite (which grew after garnet) and thus does not represent the orientation of chlorite and muscovite during garnet crystallization (MI Garnet 04, MI Garnet 06).

The degree of preferred orientation in the (100) and (010) muscovite and chlorite planes are likely a function of the number of grains analyzed. For example, NA Garnet 04 has a strong preferred orientation for (100) and (010) muscovite, but the associated phase map shows that only 1 muscovite grain was indexed, thus the degree of preferred orientation in those orientations is a function of the number of grains analyzed.

**Figure S5**

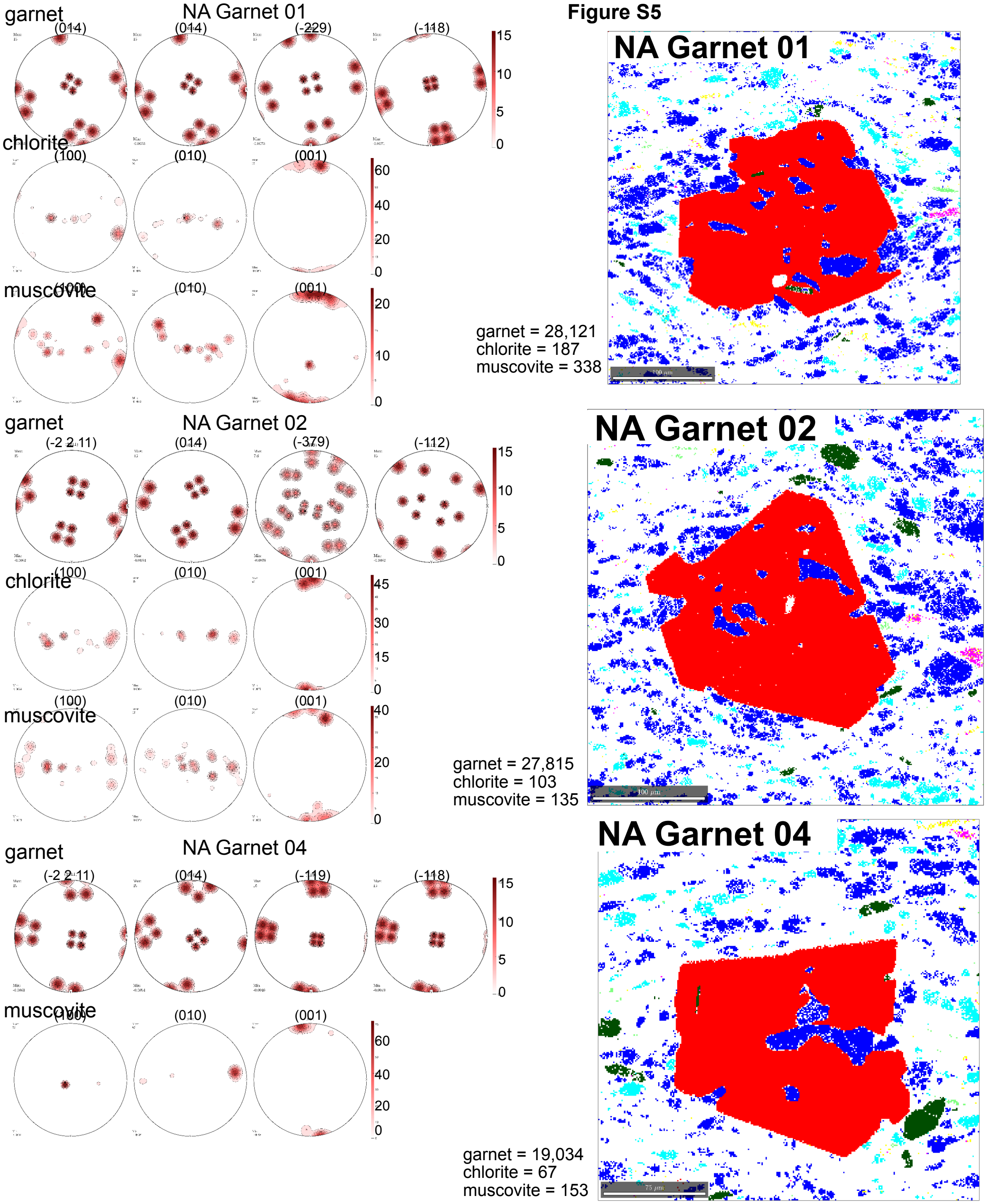

garnet = 28,121
chlorite = 187
muscovite = 338

garnet = 27,815
chlorite = 103
muscovite = 135

garnet = 19,034
chlorite = 67
muscovite = 153

Color Coding:
🟥 Garnet 🟩 Chlorite
🟦 Quartz 🟨 Muscovite
🟩 Ilmenite 🟪 Biotite
🟫 Staurolite 🟦 Plagioclase

Foliation is always oriented horizontal, unless deflected by the subsequent growth of staurolite.

**Figure S5 cont**

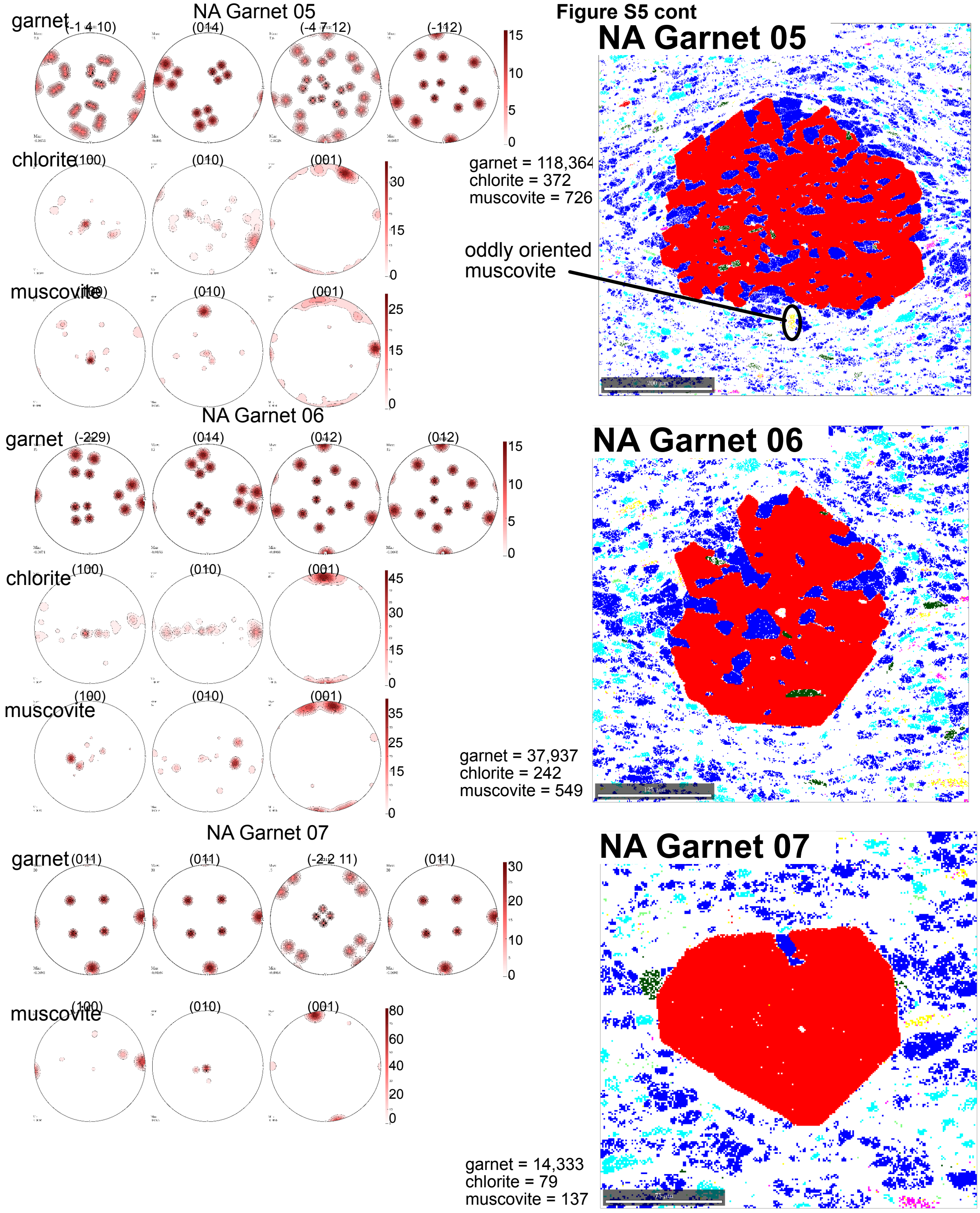

Color Coding:

🟥Garnet 🟩Chlorite
🟦Quartz 🟨Muscovite
🟩Ilmenite 🟪Biotite
🟫Staurolite 🟦Plagioclase

Foliation is always oriented horizontal, unless deflected by the subsequent growth of staurolite.

**Figure S5 cont**

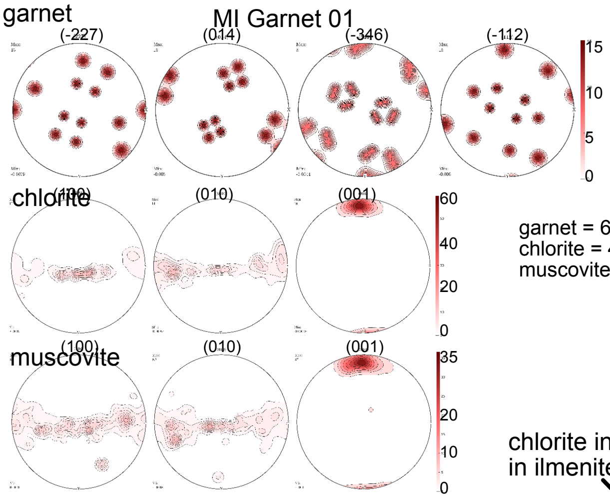

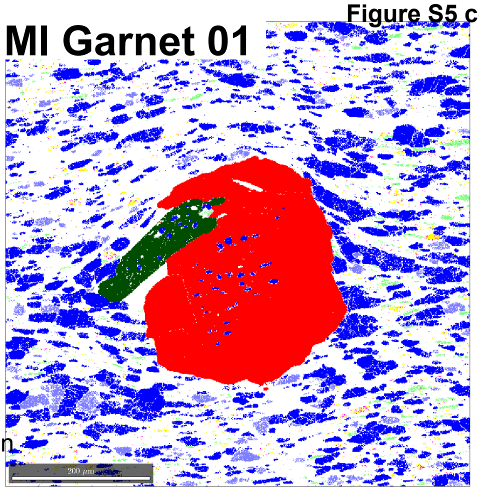

garnet = 66,695
chlorite = 4853
muscovite = 3626

chlorite inclusion
in ilmenite

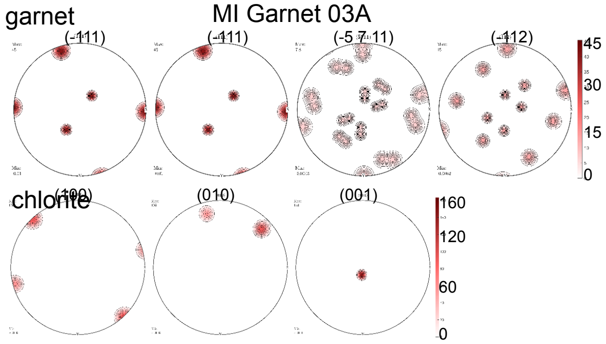

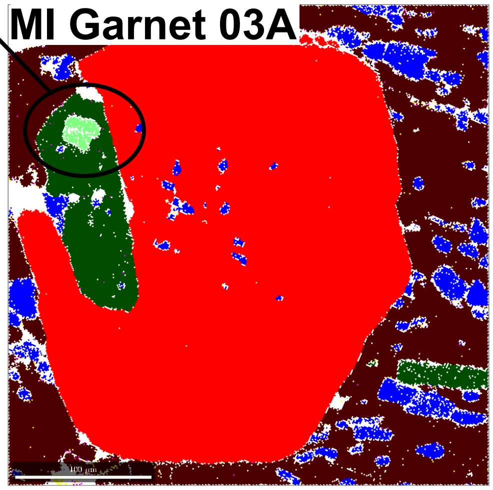

garnet = 64,315
chlorite = 353
muscovite = 246

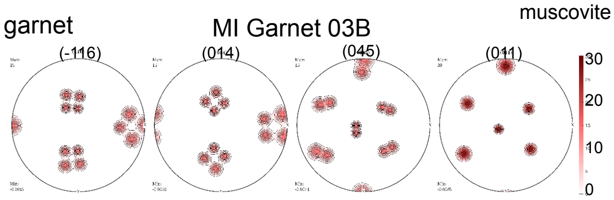

garnet = 68,137
chlorite = 98
muscovite = 87

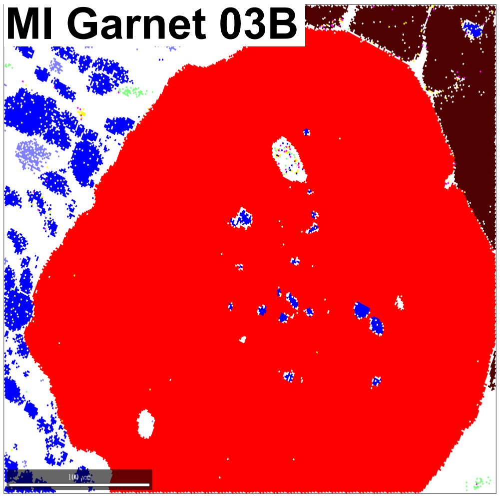

Color Coding:

🟥 Garnet
🟦 Quartz
🟩 Ilmenite
🟫 Staurolite
🟩 Chlorite
🟨 Muscovite
🟪 Biotite
🟦 Plagioclase

Foliation is always oriented horizontal, unless deflected by the subsequent growth of staurolite.

**Figure S5 cont**

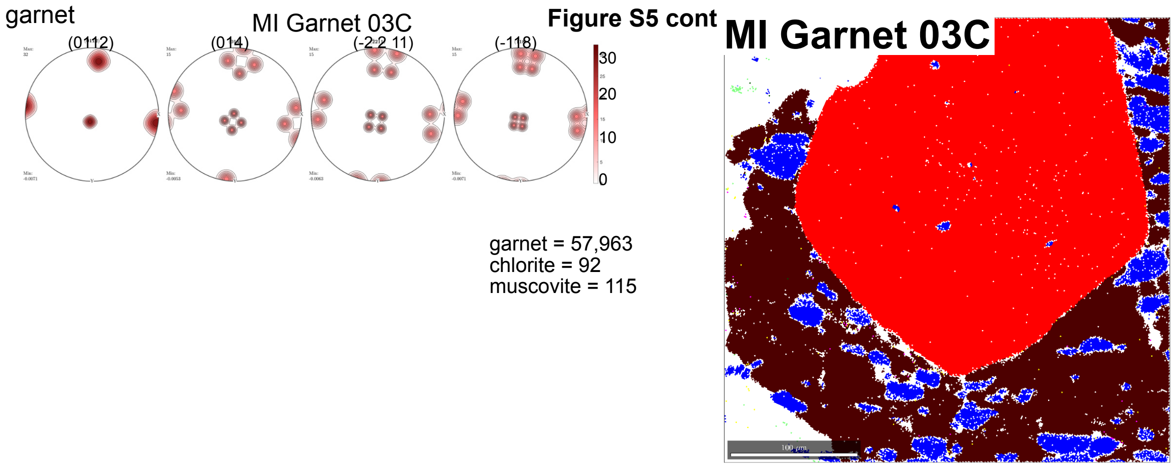

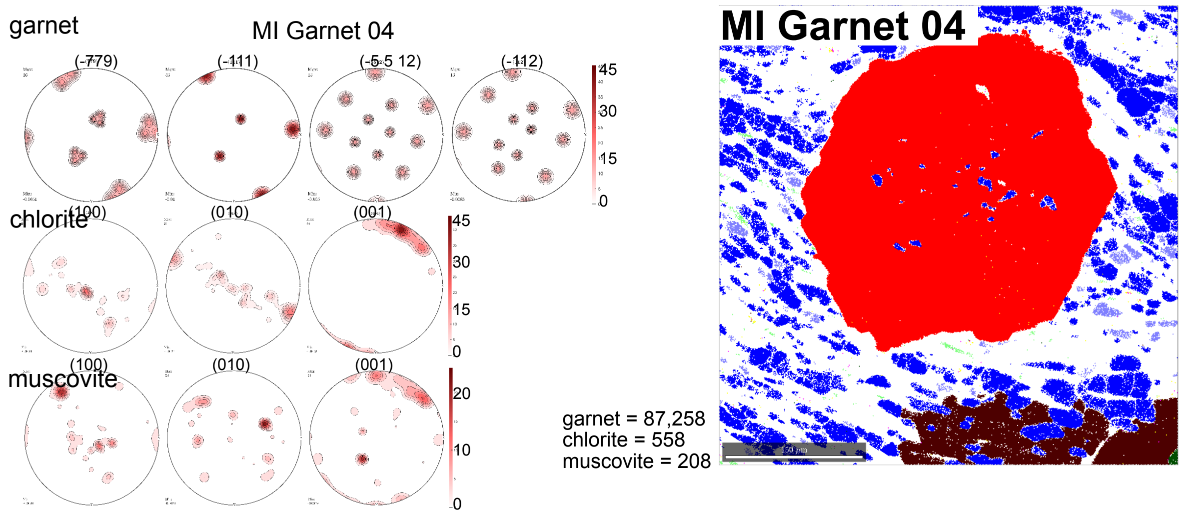

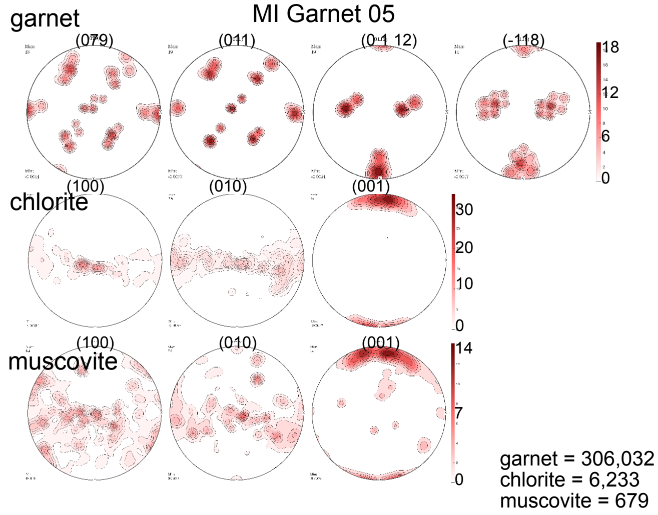

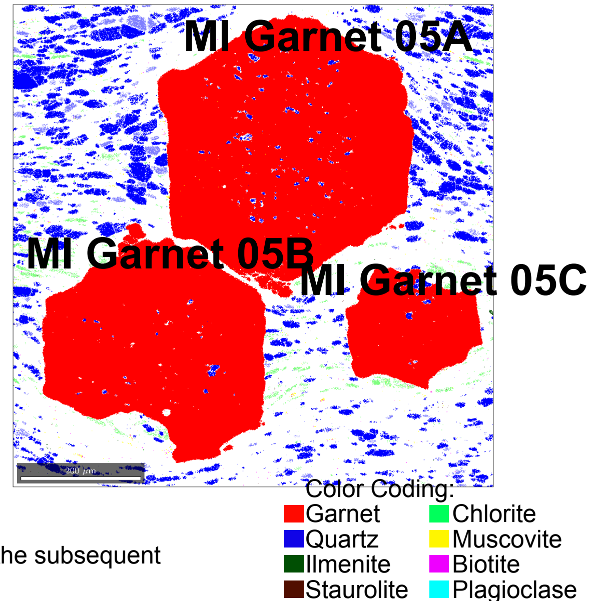

Foliation is always oriented horizontal, unless deflected by the subsequent growth of staurolite.

**Figure S5 cont**

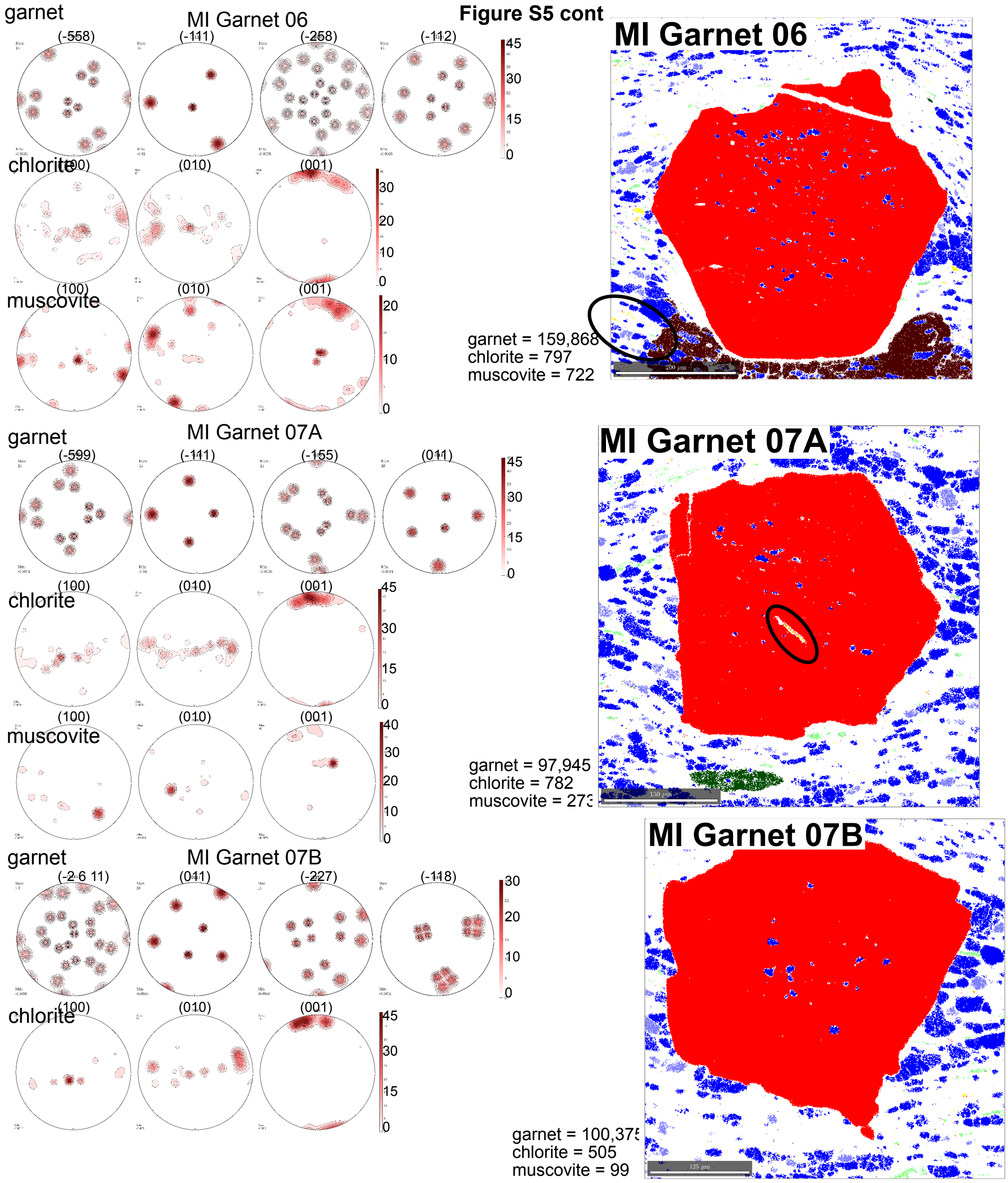

Color Coding:

| | |
|---|---|
| 🟥 Garnet | 🟩 Chlorite |
| 🟦 Quartz | 🟨 Muscovite |
| 🟩 Ilmenite | 🟪 Biotite |
| 🟫 Staurolite | 🟦 Plagioclase |

Foliation is always oriented horizontal, unless deflected by the subsequent growth of staurolite.

**Figure S5 cont**

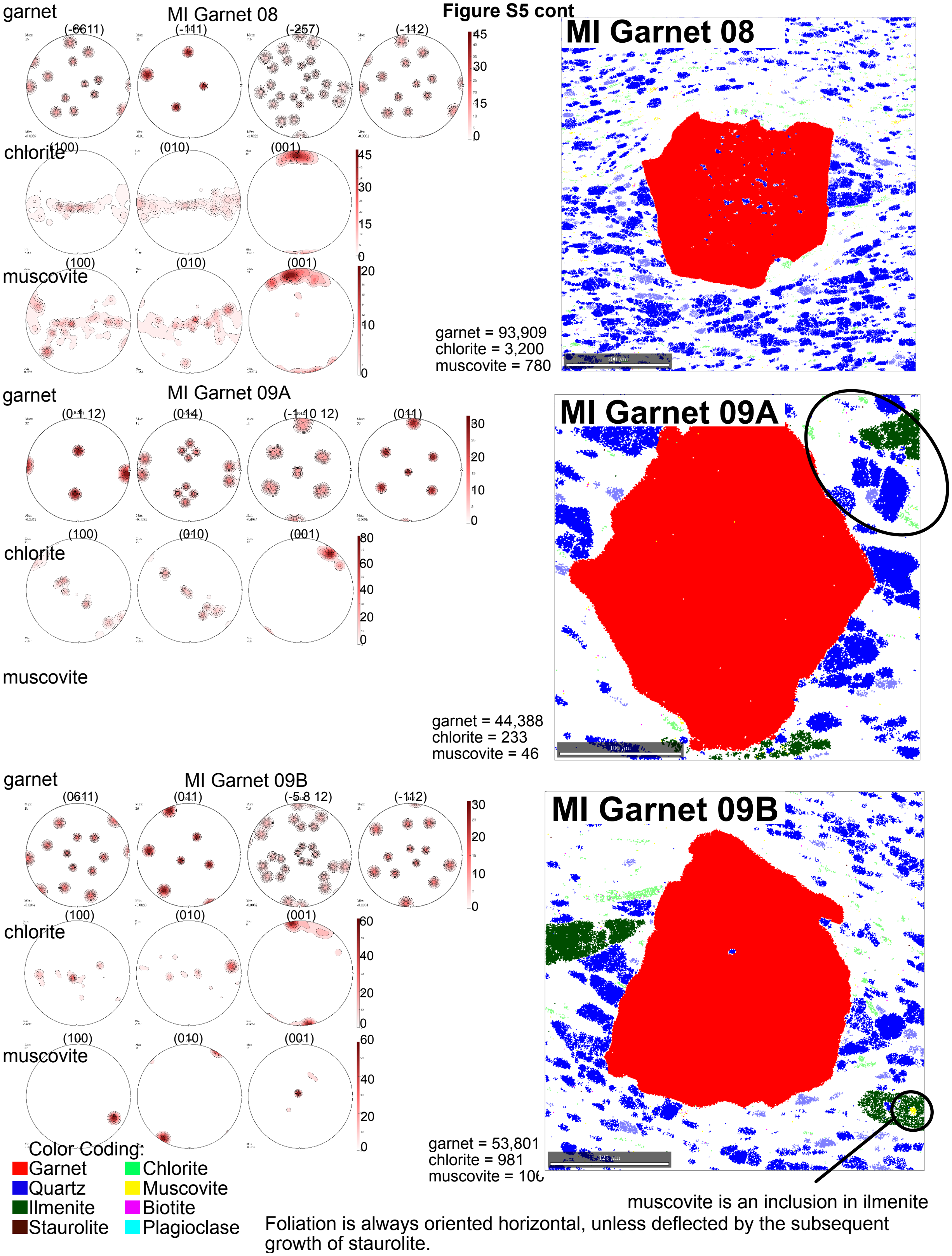

Foliation is always oriented horizontal, unless deflected by the subsequent growth of staurolite.

**Figure S5 cont**

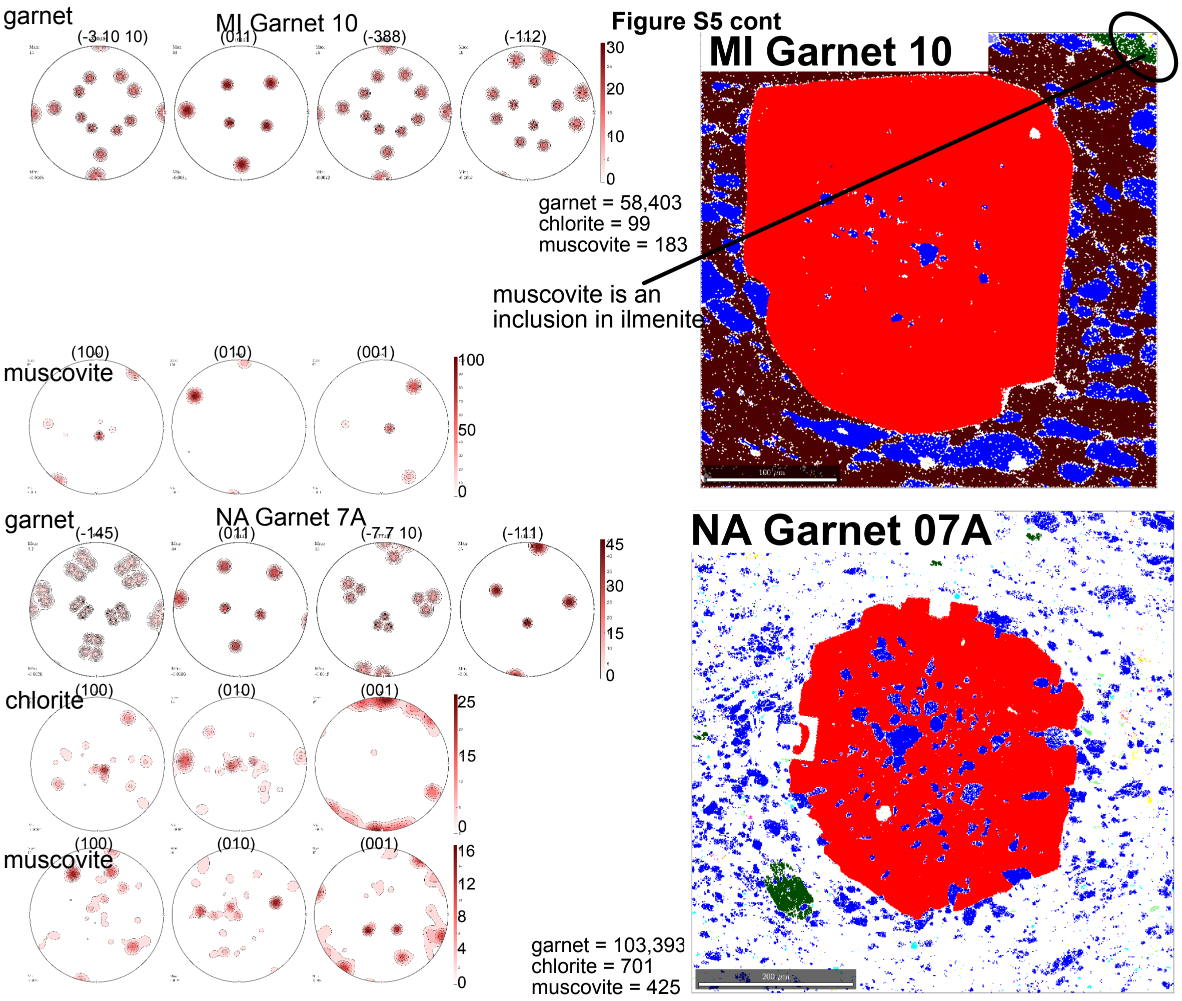

garnet = 58,403
chlorite = 99
muscovite = 183

muscovite is an inclusion in ilmenite

garnet = 103,393
chlorite = 701
muscovite = 425

Color Coding:

🟥Garnet 🟩Chlorite
🟦Quartz 🟨Muscovite
🟩Ilmenite 🟪Biotite
🟫Staurolite 🟦Plagioclase

Foliation is always oriented horizontal, unless deflected by the subsequent growth of staurolite.

**Figure S6-** SEM images of FIB liftout

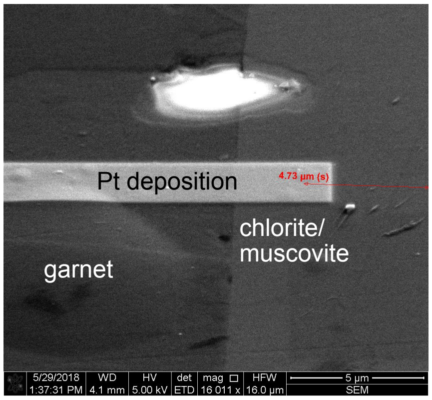

SEM image of the TEM foil location. Sample orientation is the same as above.

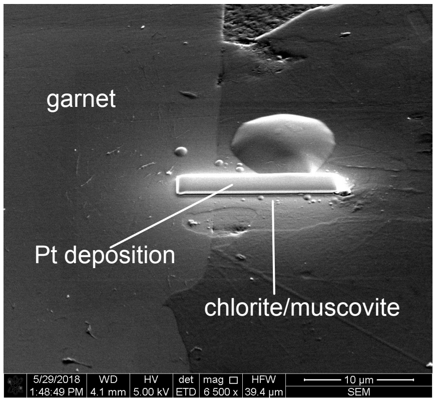

SEM image of the TEM foil location. Sample is tilted at an angle to show the Pt deposition (which is the exact location of the TEM foil).

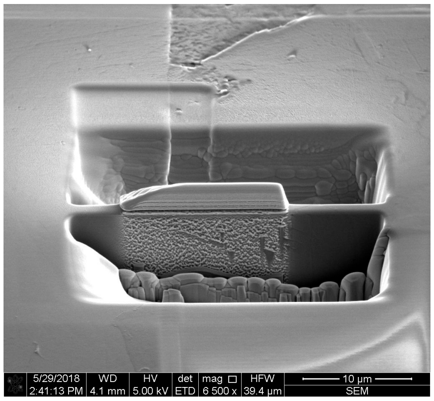

SEM image of the TEM foil location. Sample is tilted at an angle to show the Pt deposition (which is the exact location of the TEM foil).

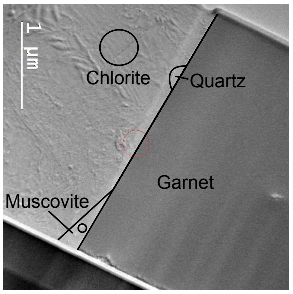

Overview of TEM sample showing locations noted below.

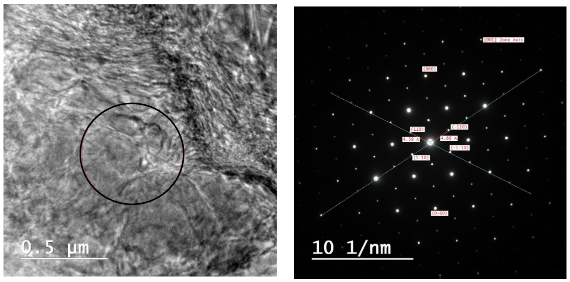

Chlorite diffraction pattern (right)
and location of diffraction pattern (left).

Indexed planes show this is oriented
parallel to the [001] zone axis.

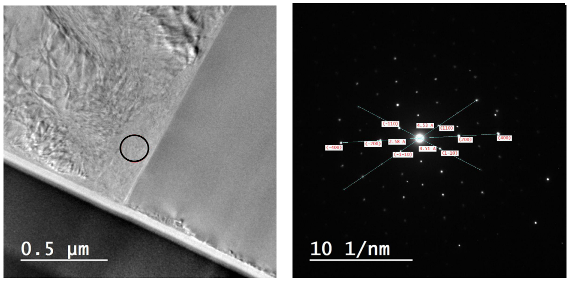

Muscovite diffraction pattern (right)
and location of diffraction pattern (left).

Indexed planes show this is oriented
parallel to the [001] zone axis.

**Figure S7-** Top: overview of TEM sample showing locations of chlorite and muscovite diffraction patterns. The sample was not tilted between collecting the chlorite and muscovite diffraction patterns. They are both in the same orientation, looking down the [001] zone axis.

**Video S1:** 3D orientation of muscovite and garnet for the $(079)_{gt}$ orientation.
**Video S2:** 3D orientation of muscovite and garnet for the $(\bar{7}79)$ orientation.
**Video S3:** 3D orientation of muscovite and garnet for the $(\bar{1}16)$ orientation.

## References

Currie, K.L., Whalen, J.B., Davis, W.J., Longstaffe, F.J., Cousens, B.L., 1998. Geochemical evolution of peraluminous plutons in southern Nova Scotia, Canada-a pegmatite-poor suite. Lithos 44, 117–140. https://doi.org/10.1016/S0024-4937(98)00051-6

Pattison, D.R.M., Tinkham, D.K., 2009. Interplay between equilibrium and kinetics in prograde metamorphism of pelites: an example from the Nelson aureole, British Columbia. Journal of Metamorphic Geology 27, 249–279. https://doi.org/10.1111/j.1525-1314.2009.00816.x

Pattison, D.R.M., Vogl, J.J., 2005. Contrasting sequences of metapelitic mineral-assemblages in the aureole of the tilted Nelson Batholith, British Columbia: Implications for phase equilibria and pressure determination in andalusite-sillimanite-type settings. Canadian Mineralogist 43, 51–88. https://doi.org/10.2113/gscanmin.43.1.51

Taylor, F., Schiller, E., 1966. Metamorphism of the Meguma group of Nova Scotia. Canadian Journal of Earth Sciences 3, 959–974.

White, C.E., Barr, S.M., 2010. Lithochemistry of the Lower Paleozoic Goldenville and Halifax groups, southwestern Nova Scotia, Canada: Implications for stratigraphy, provenance, and tectonic setting of the Meguma terrane. Geological Society of America Memoir 206, 347–366. https://doi.org/10.1130/2010.1206(15).

## Appendix C: Supplemental Material to Chapter 3

Nagurney et al. Crystallographically Controlled Void Space in the Harkness Quartzite

### ***Explanation of Chi Squared Random Distribution***

The image below shows a schematic quartz crystal, which was used to determine the random distribution of void space at grain boundaries. For simplicity, we assumed that every quartz grain had an oval shape. The grain boundary of the gray quartz crystal is color coded based on the orientation of the quartz that is normal to that segment of the grain boundary (red = normal to a/m axis, green = normal to c axis, white = normal to neither). We assumed for our void space orientation measurements that any grain boundary within 20º of the a/m axis was considered normal to the a/m axis and any grain boundary within 10º of the c axis was considered normal to the c axis. These specific values were chosen based on the human error associated with determining the orientation of every void space. In the orientation plots of each grain in the associated figures (Supplemental Data Part I), it is easier to see when the c axis of quartz is normal to the grain boundary than when the a/m axis of quartz is normal to the grain boundary. Thus, we can assume that our determination of the grain boundary segment that is normal to the c axis is accurate within 10º and our determination of the grain boundary segment that is normal to the a/m axis of accurate within 20º.

To compute the random distribution of void spaces, we assumed that for each quartz crystal, the total grain boundary length = 360º, based on our assumption of an oval crystal shape. Based on this assumption and the associated human error discussed above, 40º of the grain boundary length, or 11%, should be normal to the c axis of quartz, 80º of the grain boundary length, or

22%, should be normal to the a/m axis of quartz, and 240º of the grain boundary length, or 66% should be normal to neither of those two axes.

These proportions were then used to determine the expected value for a random distribution of void spaces in Sample PF77_YZ and PF77_XZ. We assumed that a random distribution of grain boundary voids would be distributed around grains so that 11% of them would be normal to the c axis of quartz, 22% of them would be normal to the a/m axis of quartz, and 66% of them would be normal to neither of those axes.

Based on these proportions, for our 494 grain boundary voids (the total number of grain boundary voids measured in PF77_YZ Area 1), if the grain boundary voids were randomly distributed, 55 of the voids (11% of 494) should be normal to the c axis, 110 of the voids (22% of 494) should be normal to the a/m axis, and 329 of the voids (66% of 494) should be normal to neither the a/m axis or the c axis. These values were then used as our expected values in the chi squared statistic.

For Sample PF77_XZ, we measured 441 grain boundary voids, so if they grain boundary voids were randomly distributed, 49 of the voids (11% of 442) should be normal to the c axis, 98 of the voids (22% of 442) should be normal to the a/m axis, and 294 of the voids (66% of 442) should be normal to neither the a/m axis of the c axis, and these values were used for our expected random distribution of void space for the $X^2$ test for Sample PF77_XZ.

We also conducted a sensitivity test to see if changing the assumed human error changed the results of our $X^2$ test (see attached excel spreadsheet). Changing the expected distribution did not change the results of our $X^2$ test: all values for 4 different expected distributions show that there is a statistically significant relationship between the orientation of quartz and the distribution of void space in the Harkness Quartzite.

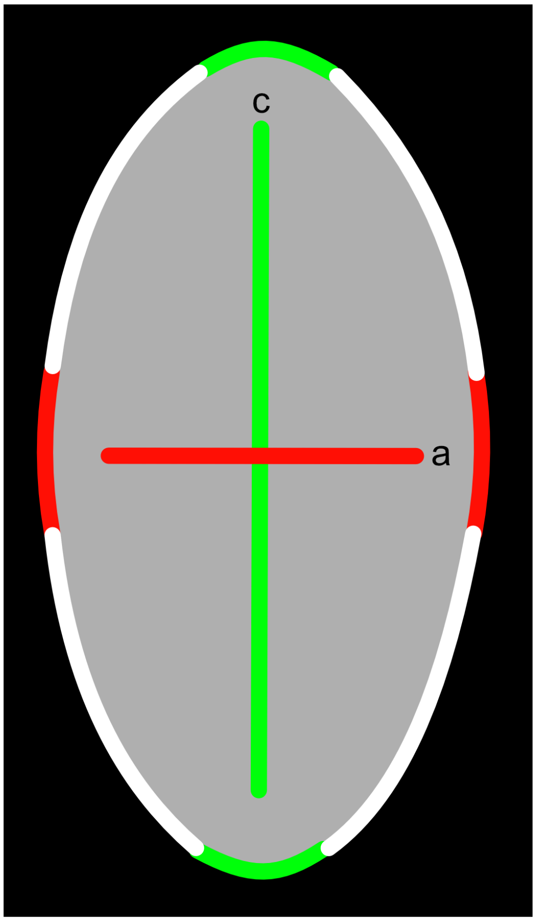

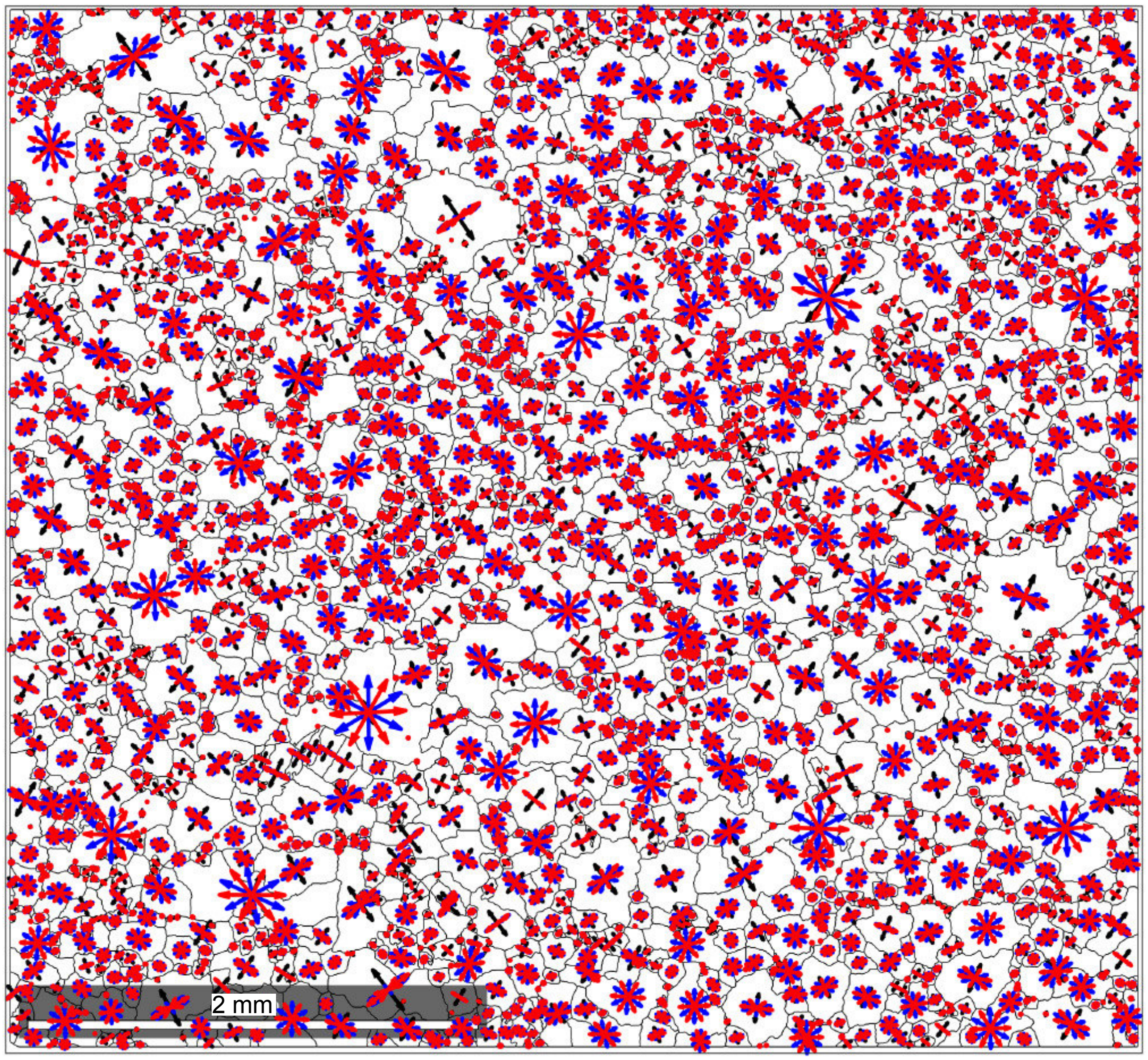

***PF77_02 Area 1 Arrows:*** This figure was used to determine the orientation of the quartz crystals on either side of the grain boundary voids. The arrows are the directions of the c axis (black), a axis (blue), and m axis (red). The arrows were calculated based on the mean orientation of every grain. In this figure, they are plotted on top of a map of the grain boundaries.

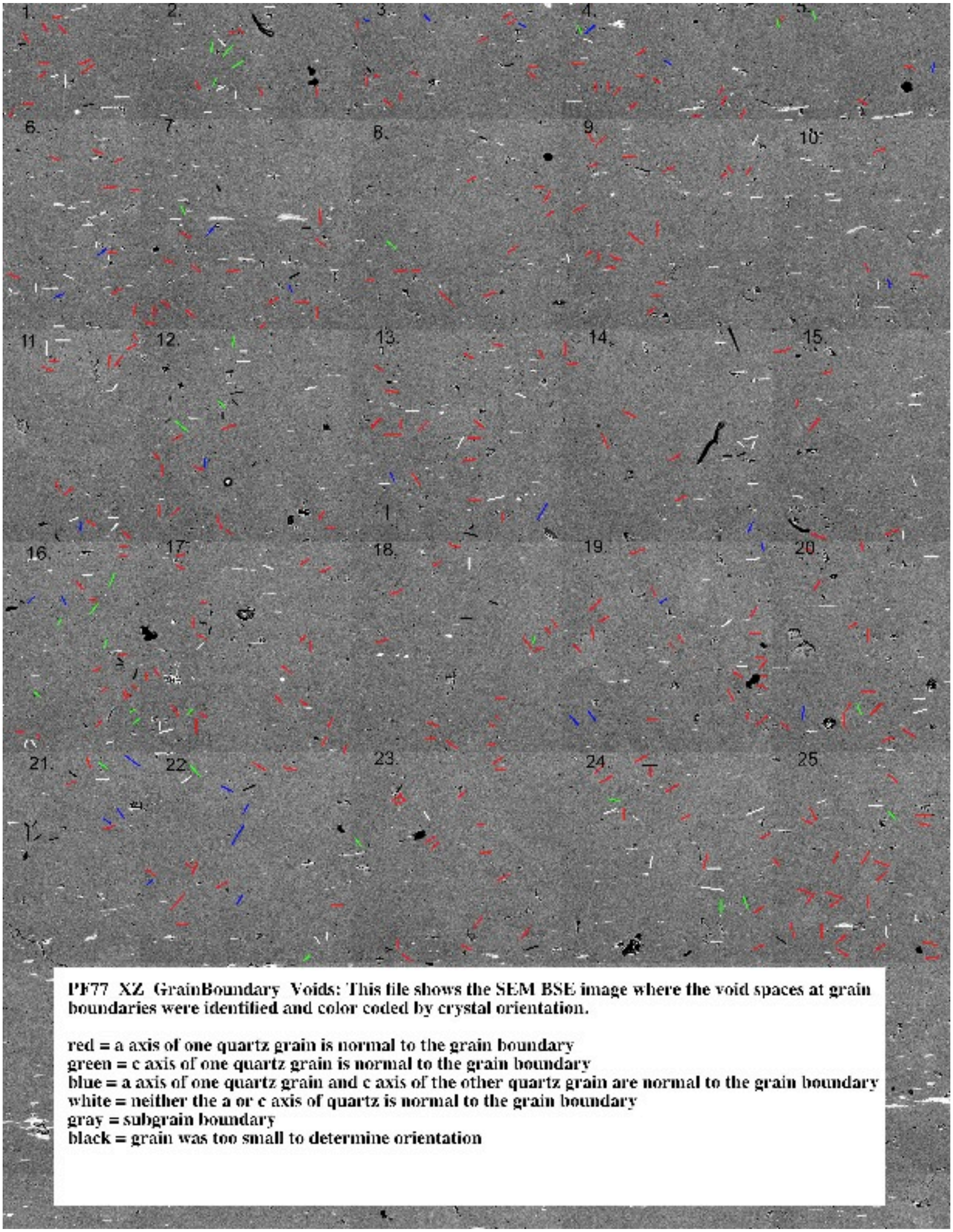

**PF77 XZ GrainBoundary Voids:** This file shows the SEM BSE image where the void spaces at grain boundaries were identified and color coded by crystal orientation.

red = a axis of one quartz grain is normal to the grain boundary
green = c axis of one quartz grain is normal to the grain boundary
blue = a axis of one quartz grain and c axis of the other quartz grain are normal to the grain boundary
white = neither the a or c axis of quartz is normal to the grain boundary
gray = subgrain boundary
black = grain was too small to determine orientation

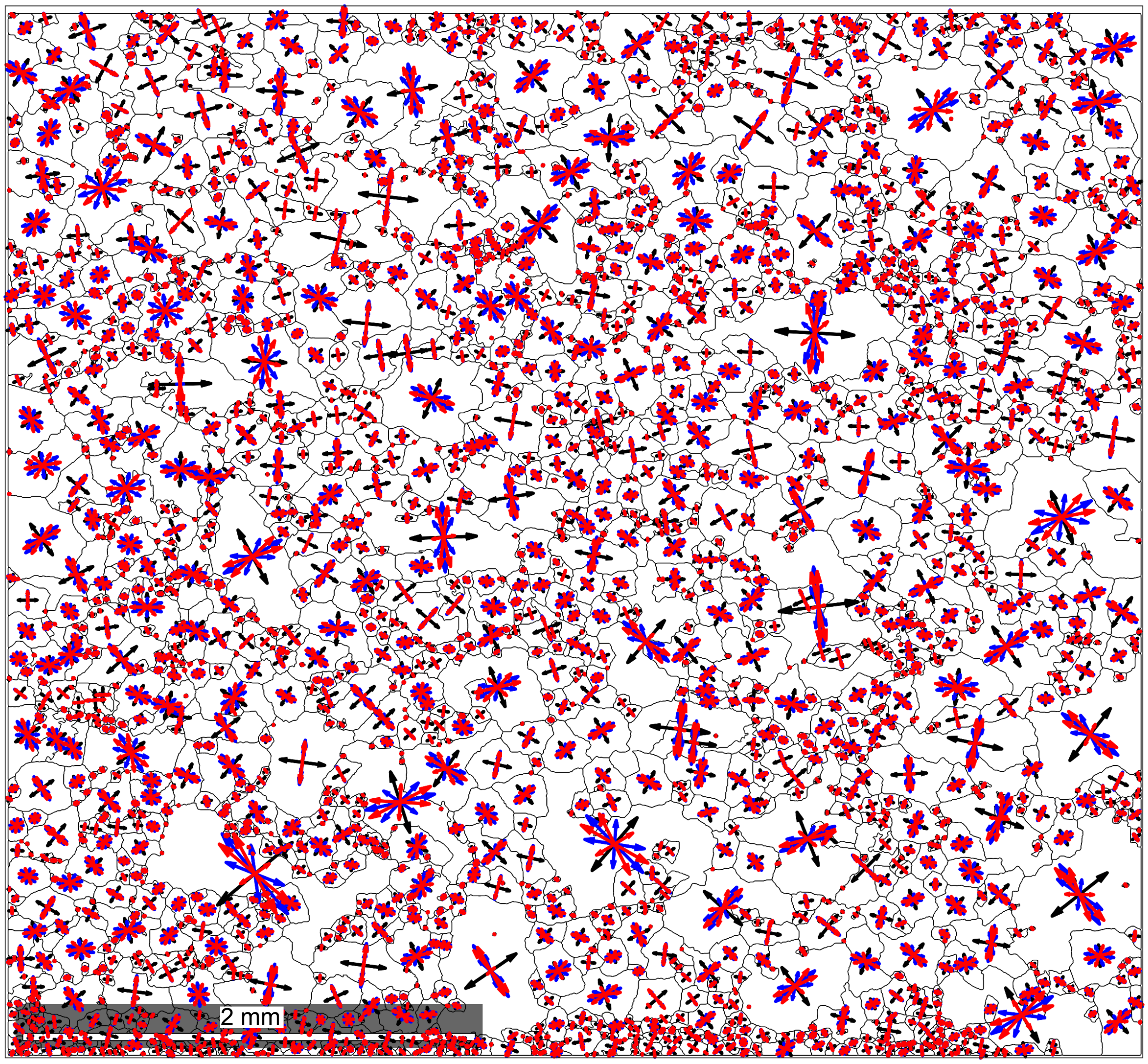

***PF77_01 Area 1 Arrows:*** This figure was used to determine the orientation of the quartz crystals on either side of the grain boundary voids. The arrows are the directions of the c axis (black), a axis (blue), and m axis (red). The arrows were calculated based on the mean orientation of every grain. In this figure, they are plotted on top of a map of the grain boundaries.

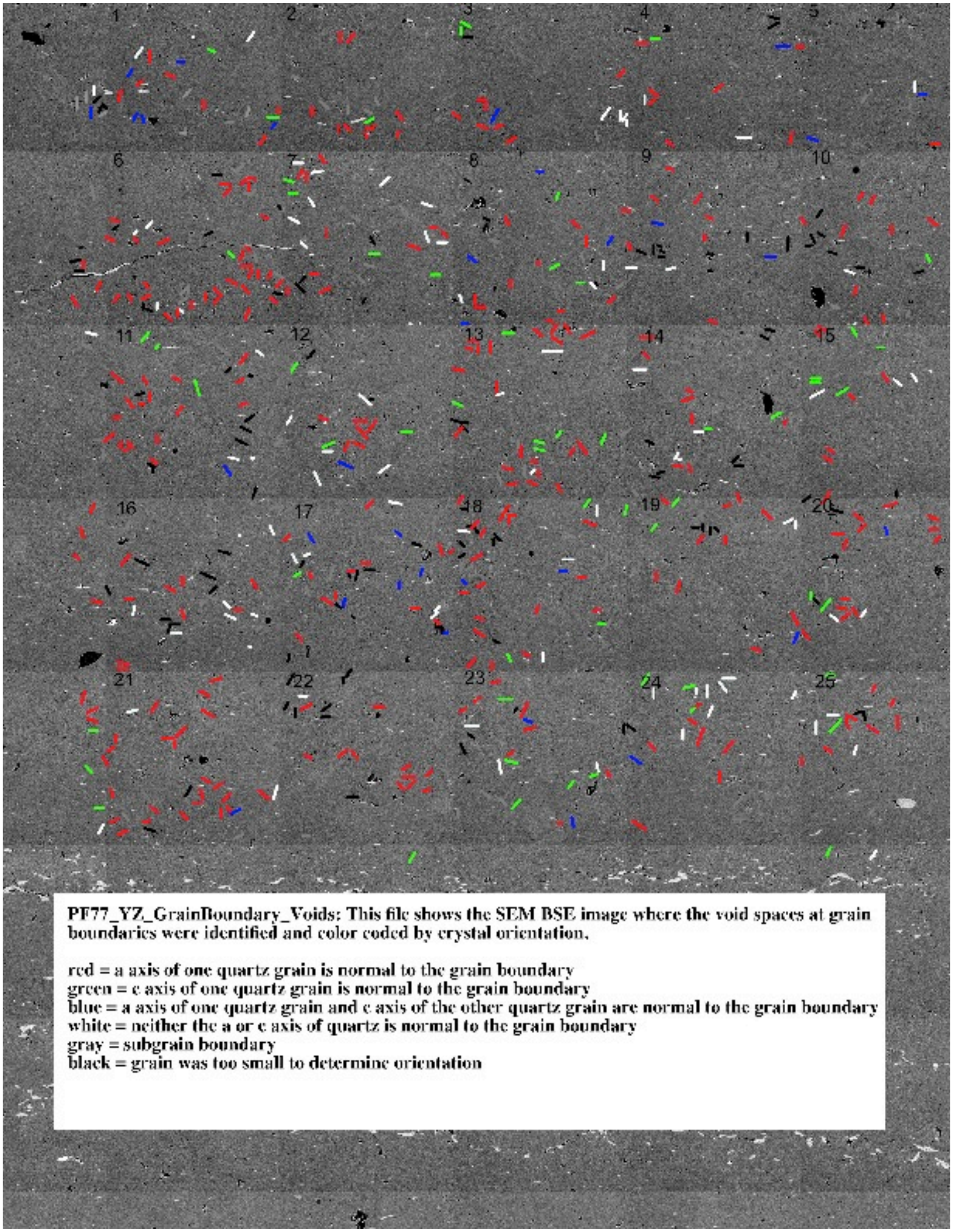

**PF77_YZ_GrainBoundary_Voids:** This file shows the SEM BSE image where the void spaces at grain boundaries were identified and color coded by crystal orientation.

red = a axis of one quartz grain is normal to the grain boundary
green = c axis of one quartz grain is normal to the grain boundary
blue = a axis of one quartz grain and c axis of the other quartz grain are normal to the grain boundary
white = neither the a or c axis of quartz is normal to the grain boundary
gray = subgrain boundary
black = grain was too small to determine orientation

# Appendix D: Supplemental Material to Chapter 4

## Supplemental Material

### Part I: Choice of Samples for Samples Not Described in Main Text

*Examples with Minimal Overstepping*

Sample W122 is from the Danba Structural Culmination in eastern Tibet, where a complete Barrovian sequence is exposed (Weller et al. 2013). Sample W122 was chosen because combined petrographic, geochronologic, and thermobarometric analysis reveal that metamorphism was continuous and the crystallization of garnet occurred simultaneously with the main stage of compression in this area (Weller et al. 2013), which suggests a simple prograde metamorphic *P-T* history.

Sample DM_06_128 is from the Kootenay Arc, British Columbia (Moynihan and Pattison 2013). This sample was chosen for this study as previous work has shown that the garnet core isopleths intersect at 10ºC greater than garnet-in, which suggests minimal overstepping of the garnet-in reaction (Moynihan and Pattison 2013).

*Samples with Apparent Overstepping*

Sample 12TM16 is from the Flinton Group, southeastern Ontario and was chosen for this study as an example in which garnet nucleation was moderately overstepped (32 ºC 1.1 kbar) (McCarron et al. 2014).

Sample ED34 is from the Menderes Massif, southwest Turkey (Etzel et al. 2019). This sample was chosen because garnet is moderately (25ºC and 0.8 kbar) overstepped in this sample (Etzel et al. 2019).

Sample D13-75 is from the Himalayan metamorphic core (Central Himalaya) in western Nepal (Iaccarino et al. 2017). This sample was chosen for this study because garnet appears to be moderately (30ºC and 0.7 kbar) overstepped in this sample (Iaccarino et al. 2017).

Sample TH203B is from the Albion Mountains, Idaho and was chosen for this study because garnet is overstepped by 50ºC and 0.7 kbar in this sample (Kelly et al. 2015) so this is an ideal example to use to see the effects of a large overstep of the garnet-in reaction.

Sample SSFM307-7G is from the Funeral Mountains, eastern California (Craddock Affinati et al. 2019). Pseudosection modelling reveals that garnet nucleation in this sample was overstepped by greater than 50ºC and 2 kbar (Craddock Affinati et al. 2019), so this sample is an ideal example of significant temperature overstepping.

## Part II: Bulk Rock Composition and Garnet Crystal Core Composition

Supplemental Material Part II = Bulk Rock Composition and Garnet Crystal Core Composition

| Component | Sikkim; 24-99 (Gaidies, et al., 2015) | Rappold Complex; 35F03 (Gaidies, et al., 2008) | Eastern Tibet W122 (Weller et al. 2013) | Kootenay Arc DM_06_128 (Moynihan & Pattison 2013) | Eastern Vermont TM549a (Spear et al. 2014) | Pomfret Dome AV26A (Bell et al. 2013) |
|---|---|---|---|---|---|---|
| SiO2 | 73.43 | 58.80 | 63.86 | 70.32 | 65.28 | 74.02 |
| TiO2 | 0.52 | 0.89 | 0.88 | 0.83 | 0.00 | 0.00 |
| Al2O3 | 12.50 | 18.91 | 15.87 | 11.71 | 14.39 | 8.98 |
| MgO | 3.19 | 4.76 | 6.08 | 4.00 | 6.31 | 5.22 |
| FeO | 6.10 | 10.77 | 8.19 | 8.44 | 6.25 | 5.91 |
| MnO | 0.05 | 0.06 | 0.09 | 0.18 | 0.17 | 0.10 |
| CaO | 0.67 | 0.47 | 0.68 | 1.06 | 1.22 | 1.53 |
| Na2O | 0.95 | 0.76 | 1.18 | 1.37 | 2.04 | 2.03 |
| K2O | 2.60 | 4.56 | 3.17 | 2.09 | 4.34 | 2.21 |
| Total | 100 | 100 | 100 | 100 | 100 | 100 |
| | | | | | | |
| $X_{alm}$ | 0.68 | 0.73 | 0.68 | 0.49 | 0.538 | 0.59 |
| $X_{gr}$ | 0.16 | 0.14 | 0.09 | 0.27 | 0.112 | 0.25 |
| $X_{sps}$ | 0.12 | 0.08 | 0.16 | 0.21 | 0.292 | 0.1 |
| $X_{py}$ | 0.05 | 0.05 | 0.07 | 0.02 | 0.0577 | 0.06 |

| Component | Nelson Aureole 93-CW-04 (Gaidies et al. 2011) | SE Ontario 12TM16 (McCarron et al. 2014) | SW Turkey ED34 (Etzel et al. 2019) | Central Himalaya D13-06 (Iaccarino et al. 2017) | Albion Mountains TH203B (Kelly et al. 2015) | Funeral Mountains 7G (Craddock Affinati et al. 2020) |
|---|---|---|---|---|---|---|
| SiO2 | 69.80 | 66.06 | 82.50 | 83.07 | 67.08 | 54.48 |
| TiO2 | 0.83 | 0.96 | 0.89 | 0.32 | 1.10 | 0.80 |
| Al2O3 | 14.03 | 12.34 | 6.66 | 5.87 | 16.48 | 17.58 |
| MgO | 3.50 | 3.46 | 2.39 | 2.97 | 3.20 | 9.02 |
| FeO | 6.30 | 12.11 | 4.71 | 4.95 | 5.82 | 10.47 |
| MnO | 0.14 | 0.16 | 0.07 | 0.11 | 0.19 | 0.25 |
| CaO | 0.55 | 1.38 | 0.58 | 0.98 | 0.52 | 1.66 |
| Na2O | 0.92 | 0.38 | 0.65 | 0.93 | 1.51 | 2.84 |
| K2O | 3.94 | 3.14 | 1.55 | 0.80 | 4.10 | 2.92 |
| Total | 100 | 100 | 100 | 100 | 100 | 100 |
| | | | | | | |
| $X_{alm}$ | 0.56 | 0.76 | 0.71 | 0.74 | 0.71 | 0.64 |
| $X_{gr}$ | 0.07 | 0.12 | 0.16 | 0.13 | 0.11 | 0.16 |
| $X_{sps}$ | 0.31 | 0.07 | 0.06 | 0.07 | 0.1102 | 0.13 |
| $X_{py}$ | 0.06 | 0.05 | 0.07 | 0.06 | 0.0656 | 0.07 |

## Part III: Comparison of Calculated ds5.5 Pseudosections to the Published Literature

**Sikkim, Himalaya Sample 24-99:** The previously published pseudosection for sample 24-99 was calculated with Theriak-Domino and ds5.5 (Gaidies et al. 2015). Using the intersection of garnet core isopleths, Gaidies et al. (2015) determined that garnet in sample 24-99 nucleated at 518 ºC and 4.5 kbar (their Figure 10B). This is in close agreement to the 526 ºC and 5.0 kbar that garnet was calculated to nucleate at in this study (Figure 2). In both our calculation and the published literature, the field in which garnet is first stable also contains chlorite, feldspar, muscovite, ilmenite, garnet, and quartz. This mineral assemblage almost matches the observed mineral assemblage in the rock, however biotite is present in the rock matrix and not stable until greater *P*-*T* conditions than garnet-in in both our pseudosection and that calculated by Gaidies et al. (2015), but biotite is calculated to be stable in the peak field defined by Gaidies et al. (2015) in our calculation, so this distinction is not important. Our pseudosection calculation is very similar to that of Gaidies et al. (2015).

**Rappold Complex: Sample 35F03:** Previously published phase equilibria for 35F03 were calculated using Theriak-Domino and ds5.5 (Gaidies et al. 2008). Garnet core isopleth intersections suggested that garnet nucleation occurred at 533 ºC and 5.2 kbar (Gaidies et al. 2008), in good agreement with an intersection at 531 ºC and 4.4 kbar in our calculation (Figure 3). In both cases, garnet core isopleths intersect at garnet-in, suggesting no appreciable garnet overstepping. The calculated mineral assemblage at this point is similar in both cases, with both calculations containing chlorite, garnet, ilmenite, muscovite, quartz, and plagioclase, though biotite stable instead in our calculation and chloritoid is stable in the calculation of Gaidies et al. (2008). Our calculation matches the mineral assemblage in the rock matrix (Gaidies et al. 2008).

**Eastern Tibet Sample W122:** Weller et al. (2013) used THERMOCALC and ds5.5 to calculate the pseudosection in their study (their Figure 7a). They do not determine the *P*-*T* conditions of garnet nucleation in their study, thus we cannot compare our conditions (547ºC and 4.9 kbar) or stable phases (chlorite, garnet, ilmenite, muscovite, plagioclase, quartz) to theirs (Supplemental Figure 1). However, the topologies of the two pseudosections look very similar. The rock matrix represents peak *P*-*T* conditions and contains biotite, garnet, ilmenite, muscovite, plagioclase, quartz, and staurolite (Weller et al. 2013).

**Kootenay Arc Sample DM_06_128:** Moynihan & Pattison (2013) calculated their pseudosection using ds5.5 and Theriak-Domino (their Figure 7a). The garnet core isopleths in their calculation intersect at 500ºC and 5.2 kbar (Moynihan and Pattison 2013), which is in good agreement with the 491ºC and 5.1 kbar we calculated (Supplemental Figure 2). In both our calculation and that of Moynihan & Pattison (2013) chlorite, garnet, ilmenite, muscovite, quartz, and plagioclase are stable in the field of garnet nucleation. In the rock matrix, chlorite is not present, but staurolite is, which is a result of the peak *P-T* conditions of the rock being greater than the *P-T* stability field of garnet nucleation, and thus chlorite has reacted out of the rock in the sample. (Moynihan and Pattison 2013)

**Eastern Vermont Sample TM549A:** A previously published pseudosection for this sample was calculated using Gibbs (Spear et al. 2014) and the thermodynamic data of (Spear and Pyle 2010). Detailed phase equilibria with labeled mineral assemblage fields were not originally presented for this sample, so it is not possible to directly compare our results. However, the rock matrix contains biotite, chlorite, epidote, garnet, ilmenite, muscovite, plagioclase, and quartz (Menard and Spear 1994). This is similar to our calculated mineral assemblage, with the exception that epidote is not stable in the field of garnet nucleation and we do not consider ilmenite in this calculation. The position of our calculated garnet-in reactions are at lower pressure and temperature than originally presented (Spear et al. 2014; their Figure 8B), consistent with previous comparisons of the SPaC and ds5.5 datasets (Pattison and DeBuhr 2015; Waters 2019). Spear et al. (2014) used multiple methods to calculate the *P-T* conditions of garnet nucleation, noting that the intersection of garnet core isopleths would occur at 520 ºC and 7.1 kbar, at lower *P*-*T* than garnet-in in their calculation. In our calculation, garnet core isopleths intersect 540 ºC and 5.8 kbar, within the garnet stability field (Figure 4).

**Pomfret Dome, Vermont Sample AV26A:** Bell et al. (2013) calculated a pseudosection for AV26A using THERMOCALC. They inferred garnet nucleation based on the intersection of garnet core isopleths at 550 ºC and 8.0 kbar (their Figure 6F). Isopleths intersect at 540ºC and 7.4 kbar in our diagram (Figure 5). In both cases, biotite, chlorite, garnet, muscovite, plagioclase, and quartz are stable in the field of garnet nucleation, but since there is no discussion of the minerals present in the rock sample (Bell et al. 2013), it is not possible to compare our pseudosection calculations to that of the rock sample.

**Nelson Aureole, British Columbia Sample 93-CW-4:** A pseudosection for 93-CW-4 was originally calculated using Theriak-Domino ds5.5 (Gaidies et al. 2011). Gaidies et al. (2011) calculated garnet nucleation based on the maximum driving force for garnet nucleation at 545 ºC and 3.5 kbar. Garnet core isopleths do not tightly intersect in the either our calculation (Figure 6A) or that of Gaidies et al. (2011) (their Figure 6). The topologies of our pseudosection is similar to that of Gaidies et al. (2011), which was originally calculated by Pattison & Tinkham (2009). Our pseudosection calculation matches the mineral assemblage in the rock, with the exception that chlorite is stable in our pseudosection but it reacted out of the rock matrix by the final stage of garnet growth (Pattison and Tinkham 2009). However, chlorite was likely present during the nucleation of garnet so this is not an important difference.

**Southeastern Ontario Sample 12TM16:** McCarron et al. (2014) used ds5.5 and Theriak-Domino in their pseudosection calculation. Based on the intersection of garnet core isopleths, they determined that garnet nucleated at 512ºC and 4.0 kbar (their Figure 6a), which is slightly less than the 530ºC and 4.4 kbar we calculated (Supplemental Figure 3). In both the pseudosection calculated by McCarron et al. (2014) and the one calculated in this study, biotite, chlorite, garnet, ilmenite, muscovite, plagioclase, and quartz are stable in the field of garnet nucleation. This is identical to the minerals preserved in the rock matrix (McCarron et al. 2014).

**Southwest Turkey Sample ED34:** Etzel et al. (2019) used Theriak-Domino and an updated version (through 2010) of ds5.5 in their pseudosection calculation (their Figure 7e). They calculated (based on the intersection of garnet core isopleths) garnet nucleation at 565ºC and 6.0 kbar, which agrees with the 550ºC and 6.3 kbar determined in our recalculation of Sample ED34 (Supplemental Figure 4). In both our recalculation and the original biotite, chlorite, garnet, ilmenite, muscovite, plagioclase and quartz are stable in the field of garnet nucleation. There is not a description of the mineral assemblages in the rock matrix (Etzel et al. 2019), so it is not possible to compare the mineral assemblages calculated in our study to that in the rock matrix.

**Central Himalaya Sample D13-75:** Iaccarino et al. (2017) used Perple_X and the 2002 update of ds55. In their pseudosection, Iaccarino et al. (2017) calculated garnet to nucleate at 520ºC and 5.5 kbar based on the intersection of garnet core isopleths (their Figure 8b), which is in good agreement with the 530ºC and 5.4 kbar calculated in our pseudosection (Supplemental Figure 5). In both calculations, biotite, chlorite, garnet, ilmenite, muscovite, plagioclase, and quartz are stable in the field of garnet nucleation, which matches the mineral assemblage in the rock sample (Iaccarino et al. 2017).

**Albion Mountains Sample TH203B:** Kelly et al. (2015) calculated their pseudosection using an updated (through 2010) version of ds5.5 and Theriak-Domino. Based on the intersection of garnet core isopleths, they determined garnet nucleated at 550ºC and 5.1 kbar, which is at the same *T*, but lower *P* than our recalculation, which found that the garnet core isopleths intersected at 550ºC and 6.3 kbar (Supplemental Figure 6). In both cases, biotite, chlorite, garnet, ilmenite muscovite, plagioclase, and quartz are stable in the field of garnet nucleation, which matches the rock sample with the exception of chlorite, which reacted out of the rock by the final stage of garnet growth, so it is not preserved in the rock sample (Kelly et al. 2015).

**Funeral Mountains Sample SSFM307-7G:** The previously calculated pseudosection used Theriak Domino and ds5.5 with a modified muscovite activity model (Craddock Affinati et al. 2019). In their pseudosection (their Figure 7d), garnet is calculated to nucleate, based on the intersection of garnet core isopleths, at 550ºC and 6.1 kbar, which is at a similar *T*, but lower *P* than our recalculation, where garnet nucleates at 552ºC and 7.1 kbar (Supplemental Figure 7). The pseudosection by Craddock Affinati et al. (2019) has garnet-in at lower *P-T* conditions than 500ºC and 4.0 kbar, which is in contrast to our recalculation (Supplemental Figure 7). In both our study and that of Craddock Affinati et al. (2019) biotite, chlorite, garnet, muscovite, plagioclase, and quartz are stable in the field of garnet nucleation. In our study ilmenite is stable, but ilmenite is not considered in the pseudosection in the source literature. However, this difference is minor.

## Part IV: Results for Examples Not Included in the Main Text

### *Samples with Minimal Overstepping*

**Eastern Tibet Sample W122:** Along the *P-T* path, garnet is stable at 547 ºC and 4.9 kbar, which is coincident with the *P-T* that the garnet core isopleths intersect, and thus garnet is not overstepped in this sample (Supplemental Figure 1A). At garnet-in in the TEC $\mu_{MnO}$, $\mu_{MgO}$, $\mu_{CaO}$, and $\mu_{FeO}$ all immediately diverge from zero, with $\mu_{Al2O3}$ diverging at 2 ºC greater than garnet-in, which is effectively at garnet-in (Supplemental Figure 1C). Thus, there is a trend where all chemical potentials experience a difference between the TEC and MSC at garnet-in.

**Kootenay Arc Sample DM_06_128:** Garnet is stable at 487 ºC and 4.8 kbar and the garnet core isopleths intersect at 491 ªC and 5.0 kbar, which equates to 4 ºC and 0.2 kbar of overstep, but which is nearly coincident with garnet-in (Supplemental Figure 2A). Immediately up temperature of garnet-in $\Delta\mu_{MgO}$ is positive and $\Delta\mu_{MnO,}$ $\Delta\mu_{CaO}$, and $\Delta\mu_{FeO}$ are negative. $\Delta\mu_{Al2O3}$ becomes negative at 492 ºC and 5.1 kbar, which is nearly coincident with garnet-in and the *P-T* conditions where the garnet core isopleths intersect (Supplemental Figure 2C).

*Samples with Apparent Overstepping*

**Southeastern Ontario Sample 12TM16:** Garnet is stable at 496 ºC and 3.4 kbar and the garnet core isopleths intersect at 530 ºC and 4.4 kbar (Supplemental Figure 3A). This equates to 34 ºC and 1.0 kbar of overstep. At 496 ºC and 3.4 kbar, $\Delta\mu_{MnO}$ is negative and $\Delta\mu_{MgO}$ is positive. $\Delta\mu_{FeO}$ becomes negative at 505 ºC and 3.6 kbar and $\Delta\mu_{CaO}$ becomes positive at 511 ºC and 3.8 kbar. $\Delta\mu_{Al2O3}$ is the final component to experience a deviation between the TEC and MSC, at 513 ºC and 3.8 kbar (Supplemental Figure 3C).

**Southwest Turkey Sample ED34:** Along the prograde *P-T* path, garnet is stable at 524 ºC and 5.1 kbar and the garnet core isopleths intersect at 550 ºC and 6.3 kbar, which amounts to 26 ºC and 1.2 kbar of overstepping (Supplemental Figure 4A). At 524 ºC and 5.1 kbar $\Delta\mu_{MnO}$ and $\Delta\mu_{FeO}$ are immediately negative and $\Delta\mu_{MgO}$ is positive. $\Delta\mu_{CaO}$ and $\Delta\mu_{Al2O3}$ are initially zero, becoming negative at 532 ºC and 5.5 kbar (Supplemental Figure 4C).

**Central Himalaya Sample D13-75:** Garnet is stable at 508 ºC and 4.4 kbar along the prograde *P-T* path and the garnet core isopleths intersect at 530 ºC and 5.4 kbar, which results in 22 ºC and 1.0 kbar of overstep (Supplemental Figure 5A). At all *P-T* conditions above where garnet is stable in the TEC, $\Delta\mu_{MnO}$, $\Delta\mu_{FeO}$, and $\Delta\mu_{CaO}$ are negative and $\Delta\mu_{MgO}$ is positive (Supplemental Figure 5C). $\Delta\mu_{Al2O3}$ is initially zero and becomes negative at 532 ºC and 5.5 kbar, which is effectively the *P-T* conditions at which the garnet core isopleths intersect.

**Albion Mountains Sample TH203B:** Along the prograde *P-T* path, garnet is stable at 507 ºC and 4.4 kbar (Supplemental Figure 6A). The garnet core isopleths intersect at 550 ºC and 6.3 kbar, which equates to 43 ºC and 1.9 kbar of overstepping. After garnet is stable in the TEC, but suppressed in the MSC $\Delta\mu_{MnO}$ and $\Delta\mu_{CaO}$ are immediately negative and $\Delta\mu_{MgO}$ is positive. $\Delta\mu_{Al2O3}$ is the final component to experience a different between the TEC and MSC, becoming negative at 532 ºC and 5.5 kbar (Supplemental Figure 6C).

**Funeral Mountains Sample SSFM307-7G:** Along the prograde *P-T* path garnet is stable at 518 ºC and 5.4 kbar and the garnet core isopleths intersect at 552 ºC and 7.1 kbar, so garnet is overstepped by 34 ºC and 1.7 kbar (Supplemental Figure 7A). At the *P-T* where garnet is stable in the TEC $\Delta\mu_{MnO}$ is immediately negative and $\Delta\mu_{MgO}$ is immediately positive, $\Delta\mu_{FeO}$ and $\Delta\mu_{CaO}$ become negative at 520 ºC and 5.5 kbar. $\Delta\mu_{Al2O3}$ is the final component to experience a difference between the TEC and MSC at 551 ºC and 7.0 kbar, which is nearly coincident with the *P-T* conditions where the garnet core isopleths intersect (Supplemental Figure 7C).

## Part V: Comparison of Results with Thermocalc Datasets 5.5 and 6.2

### *Ds6.2 Calculations not Described in Main Text:*

*Rappold Complex Sample 35F03:* In the ds6.2 calculation, garnet core isopleths intersect at 537 ºC and 4.9 kbar, consistent with 12 ºC and 0.5 kbar of overstepping (Supplemental Figure 8A). At *P-T* conditions greater than garnet-in in the TEC, $\Delta\mu_{MnO} < 0$ (Supplemental Material Figure 1C). $\Delta\mu_{MgO}$, $\Delta\mu_{CaO}$, $\Delta\mu_{FeO}$, and $\Delta\mu_{Al2O3}$ are initially zero, with $\Delta\mu_{MgO}$ becoming positive at 530 ºC and 4.6 kbar, $\Delta\mu_{FeO}$ becoming negative at 532 ºC and 4.7 kbar, $\Delta\mu_{CaO}$ becoming positive at 535 ºC and 4.8 kbar, and $\Delta\mu_{Al2O3}$ being the final chemical potential to experience a difference between the TEC and MSC at 541 ºC and 5.0 kbar (Supplemental Figure 8C).

In both ds5.5 and ds6.2 the general topologies of the pseudosections for this sample are very similar, with a few minor differences. Biotite is stable across the entire *P-T* range of interest in the ds6.2 diagram but is unstable at low temperature in ds5.5 (Figure 3A, Supplemental Figure 8A). In calculations with both datasets, biotite, chlorite, garnet, ilmenite, muscovite, plagioclase, and quartz are stable in the field where garnet core isopleths intersect (Figure 3A, Supplemental Figure 8A). The garnet stability field is slightly expanded in ds6.2 versus ds5.5, but the *P-T* where the garnet core isopleths intersect barely changes between the two calculations, so there is more reported overstep in the ds6.2 calculation. This is consistent with other studies (White et al. 2014; Waters 2019) which also showed a greater garnet stability field in ds6.2 versus ds5.5.

The ds5.5 calculation shows a difference in the chemical potential of all oxide components of interest between the TEC and MSC at all *P-T* conditions greater than garnet-in in the TEC (Figure 3A). Deviation in $\Delta\mu_{CaO}$, $\Delta\mu_{FeO}$, and $\Delta\mu_{Al2O3}$ in the ds6.2 calculation are delayed to slightly higher *P-T*, though all chemical potentials experience a deviation at *P-T* conditions nearly coincident with those at which the garnet core isopleths intersect (Supplemental Figure 8C).

*Eastern Vermont Sample TM549a:* The intersection of garnet core isopleths in TM549a calculated with ds6.2 is at 550 ºC and 6.3 kbar (Supplemental Figure 9A), which is consistent with 45 ºC and 2.0 kbar of overstepping. At all *P-T* conditions above garnet-in, $\Delta\mu_{MnO}$ is negative (Supplemental Figure 9C). $\Delta\mu_{MgO}$ becomes positive and $\Delta\mu_{CaO}$ becomes negative ~10 ºC above garnet-in, while $\Delta\mu_{FeO}$ becomes negative ~ 15 ºC above garnet-in (Supplemental Figure 9A) and $\Delta\mu_{Al2O3}$ is zero until 531 ºC and 5.4 kbar (Supplemental Figure 9C).

The general topologies of pseudosections calculated with ds5.5 and ds6.2 are nearly identical (Figure 4A & Supplemental Figure 9C). In both calculations, biotite, chlorite, garnet, muscovite, plagioclase, and quartz are stable in the field where the garnet core isopleths intersect (Figure 4A & Supplemental Figure 9C). A small staurolite stability field that is present in the ds6.2 calculation is absent in the ds5.5 calculation. The ds6.2 calculation implies a larger amount of overstep (45 ºC versus 35 ªC) than the ds5.5 calculation.

In both the ds5.5 and ds6.2 pseudosection calculations, $\Delta\mu_{MgO}$ is positive and $\Delta\mu_{MnO}$, $\Delta\mu_{CaO}$, and $\Delta\mu_{FeO}$ are negative at *P-T* conditions above garnet-in, but in the ds6.2 calculation there is a larger *P-T* interval where $\Delta\mu_{MgO}$, $\Delta\mu_{CaO}$, and $\Delta\mu_{FeO}$ equal zero (Figure

4C & Supplemental Figure 9C). Both calculations produce a *P-T* range in which $\Delta\mu_{Al2O3}$ is effectively zero directly above garnet-in, with a correlation between the *P-T* conditions at which $\mu_{Al2O3}$ differs between the TEC and MSC and the intersection of garnet core isopleths, though that correlation is less explicit in ds6.2.

*General Comparison of Phase Stability in ds5.5 versus ds6.2:*

In general, pseudosections calculated here in ds5.5 and ds6.2 are very similar, but there are a few key differences. The stability ranges of muscovite, chlorite, andalusite, sillimanite, and feldspar for all examples are typically the same in each dataset. The extent of garnet stability is also similar between the ds5.5 and ds6.2 calculations for samples 24-99 (Sikkim), AV26A (Pomfret Dome), and TM549A (Eastern Vermont). However, for sample 35F03 (Rappold Complex) the garnet stability field is slightly expanded in ds6.2 and for sample 93-CW-4 (Nelson Aureole), the stability field of garnet in the ds6.2 calculation is considerably more extensive than in ds5.5. For an average pelitic rock, (White et al. 2014) calculated a slightly expanded stability field of garnet in ds6.2 compared to ds5.5. However, for a pelitic rock that reached mid to upper amphibolite facies from the High Himalaya, (Waters 2019) found an extreme difference in the stability field of garnet, with ds6.2 calculating garnet to be stable over a far wider *P-T* range than ds5.5, consistent with the Nelson Aureole example here.

The stability of biotite tends to be consistent between the two thermodynamic datasets except in the case of sample 24-99 (Sikkim). In the ds5.5 calculation, biotite is stable above ~550 ºC, first appearing at temperatures above garnet-in at most pressures. However, in ds6.2, biotite is calculated to be stable across the entire *P-T* range of the pseudosection. Neither White et al. (2014) nor Waters (2019) show any difference in the stability range of biotite between ds5.5 and ds6.2 in their calculations. It is currently unclear to us the cause of the differences in the stability of biotite in ds5.5 and ds6.2 in the Sikkim example.

For samples 24-99 (Sikkim), 35F03 (Rappold Complex), and 93-CW-4 (Nelson Aureole), the stability fields of staurolite are almost identical between calculations with each dataset. For sample AV26A (Pomfret Dome), the stability field of staurolite is larger in ds5.5. For sample TM549A (Eastern Vermont), staurolite is not calculated to be stable in the ds5.5 pseudosection, but is present in the ds6.2 pseudosection. White et al. (2014) calculate a slightly expanded staurolite stability field in their ds6.2 pseudosection compared to their ds5.5 pseudosection.

There are some differences in the stability field of paragonite between ds5.5 and ds6.2 for sample 24-99 (Sikkim), and paragonite is not stable in either calculation for sample 35F03 (Rappold Complex). For sample AV26A (Pomfret Dome) paragonite is not present our ds5.5 pseudosections, but is stable at high pressures and low temperatures in the ds6.2 calculation. For sample 93-CW-4 (Nelson Aureole) and sample TM549A (Eastern Vermont), the paragonite stability field is expanded in ds6.2 compared to ds5.5. These results are consistent with White et al. (2014) who also showed an expanded field for paragonite at high pressures and low temperatures in their calculations for an average pelite.

*Comparison of Chemical Potential Calculations:*

There are many similarities of the $\Delta\mu_{\text{component}}$ calculations between ds5.5 and ds6.2, with a few key differences. In all calculations with both datasets, $\Delta\mu_{\text{MnO}}$ is negative immediately up temperature of garnet-in. $\Delta\mu_{\text{MgO}}$ is positive at *P-T* conditions above garnet-in, though this is delayed by several degrees in the Nelson Aureole and Pomfret Dome examples with ds5.5 and in the Rappold Complex and Eastern Vermont examples in ds6.2. However, these differences in $\Delta\mu_{MgO}$ are minor. Trends in $\Delta\mu_{CaO}$, are nearly identical for ds5.5 and ds6.2, though the *P-T* condition at which $\Delta\mu_{CaO}$ deviates from zero can be slightly different in calculations with ds5.5 and ds6.2. In both ds5.5 and ds6.2, for the examples where garnet is apparently overstepped (Eastern Vermont, Pomfret Dome, Nelson Aureole), $\Delta\mu_{FeO}$ is zero immediately above garnet-in, becoming negative at higher *P-T*. For each sample the *P-T* at which $\Delta\mu_{FeO} \neq 0$ is slightly different between the ds5.5 and ds6.2 calculations. In 4/5 ds5.5 calculations and 5/5 of the ds6.2 calculations, $\Delta\mu_{Al2O3}$ is the final component to experience a deviation between the TEC and MSC. Since the trends are very similar between the ds5.5 and ds6.2 calculations, this shows that these trends are present in pseudosection calculations regardless of the choice of thermodynamic dataset.

## Supplemental Material References

Bell, T.H., Rieuwers, M.T., Cihan, M., Evans, T.P., Ham, A.P., and Welch, P.W. (2013) Interrelationships between deformation partitioning, metamorphism and tectonism. Tectonophysics, 587, 119–132.

Craddock Affinati, S., Hoisch, T.D., Wells, M.L., and Vervoort, J.D. (2019) Pressure-temperature-time paths from the Funeral Mountains, California, reveal Jurassic retroarc underthrusting during early Sevier orogenesis. GSA Bulletin, 1–19.

Etzel, T.M., Catlos, E.J., Ataktürk, K., Lovera, O.M., Kelly, E.D., Çemen, I., and Diniz, E. (2019) Implications for Thrust-Related Shortening Punctuated by Extension From P-T Paths and Geochronology of Garnet-Bearing Schists, Southern (Çine) Menderes Massif, SW Turkey. Tectonics, 38, 1974–1998.

Gaidies, F., Krenn, E., De Capitani, C., and Abart, R. (2008) Coupling forward modelling of garnet growth with monazite geochronology: An application to the Rappold Complex (Austroalpine crystalline basement). Journal of Metamorphic Geology, 26, 775–793.

Gaidies, F., Pattison, D.R.M., and de Capitani, C. (2011) Toward a quantitative model of metamorphic nucleation and growth. Contributions to Mineralogy and Petrology, 162, 975–993.

Gaidies, F., Petley-Ragan, A., Chakraborty, S., Dasgupta, S., and Jones, P. (2015) Constraining the conditions of Barrovian metamorphism in Sikkim, India: P-T-t paths of garnet crystallization in the Lesser Himalayan Belt. Journal of Metamorphic Geology, 33, 23–44.

Iaccarino, S., Montomoli, C., Carosi, R., Massonne, H.J., and Visonà, D. (2017) Geology and tectono-metamorphic evolution of the Himalayan metamorphic core: insights from the Mugu Karnali transect, Western Nepal (Central Himalaya). Journal of Metamorphic Geology, 35, 301–325.

Kelly, E.D., Hoisch, T.D., Wells, M.L., Vervoort, J.D., and Beyene, M.A. (2015) An Early Cretaceous garnet pressure–temperature path recording synconvergent burial and exhumation from the hinterland of the Sevier orogenic belt, Albion Mountains, Idaho. Contributions to Mineralogy and Petrology, 170, 1–22.

McCarron, T., Gaidies, F., McFarlane, C.R.M., Easton, R.M., and Jones, P. (2014) Coupling thermodynamic modeling and high-resolution in situ LA-ICP-MS monazite geochronology: evidence for Barrovian metamorphism late in the Grenvillian history of southeastern Ontario. Mineralogy and Petrology, 108, 741–758.

Menard, T., and Spear, F.S. (1994) Metamorphic P-T paths from calcic pelitic schists from the Strafford Dome, Vermont, USA. Journal of Metamorphic Geology, 12, 811–826.

Moynihan, D.P., and Pattison, D.R.M. (2013) An automated method for the calculation of P-T paths from garnet zoning, with application to metapelitic schist from the Kootenay Arc, British Columbia, Canada. Journal of Metamorphic Geology, 31, 525–548.

Pattison, D.R.M., and DeBuhr, C.L. (2015) Petrology of metapelites in the Bugaboo aureole, British Columbia, Canada. Journal of Metamorphic Geology, 33, 437–462.

Pattison, D.R.M., and Tinkham, D.K. (2009) Interplay between equilibrium and kinetics in prograde metamorphism of pelites: an example from the Nelson aureole, British Columbia. Journal of Metamorphic Geology, 27, 249–279.

Spear, F.S., and Pyle, J.M. (2010) Theoretical modeling of monazite growth in a low-Ca metapelite. Chemical Geology, 273, 111–119.

Spear, F.S., Thomas, J.B., and Hallett, B.W. (2014) Overstepping the garnet isograd: a comparison of QuiG barometry and thermodynamic modeling. Contributions to Mineralogy and Petrology, 168.

Waters, D.J. (2019) Metamorphic constraints on the tectonic evolution of the High Himalaya in Nepal: the art of the possible. Geological Society, London, Special Publications, 483.

Weller, O.M., St-Onge, M.R., Waters, D.J., Rayner, N., Searle, M.P., Chung, S.L., Palin, R.M., Lee, Y.H., and Xu, X. (2013) Quantifying barrovian metamorphism in the danba structural culmination of eastern tibet. Journal of Metamorphic Geology, 31, 909–935.

White, R.W., Powell, R., Holland, T.J.B., Johnson, T.E., and Green, E.C.R. (2014) New mineral activity-composition relations for thermodynamic calculations in metapelitic systems. Journal of Metamorphic Geology, 32, 261–286.

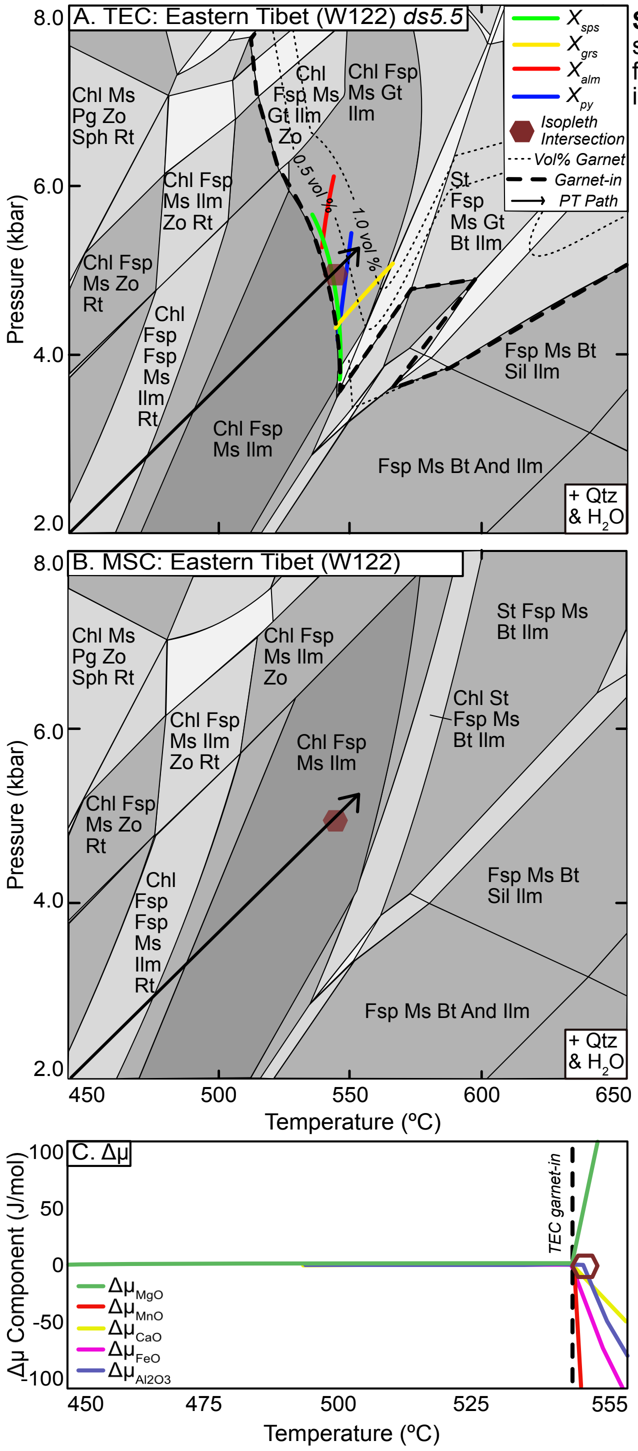

**Supplemental Figure 1:** A. TEC pseudosection for sample W122 (Eastern Tibet). B. MSC pseudosection for sample W122. C. $\Delta\mu_{\text{component}}$ along *P-T* path shown in A & B.

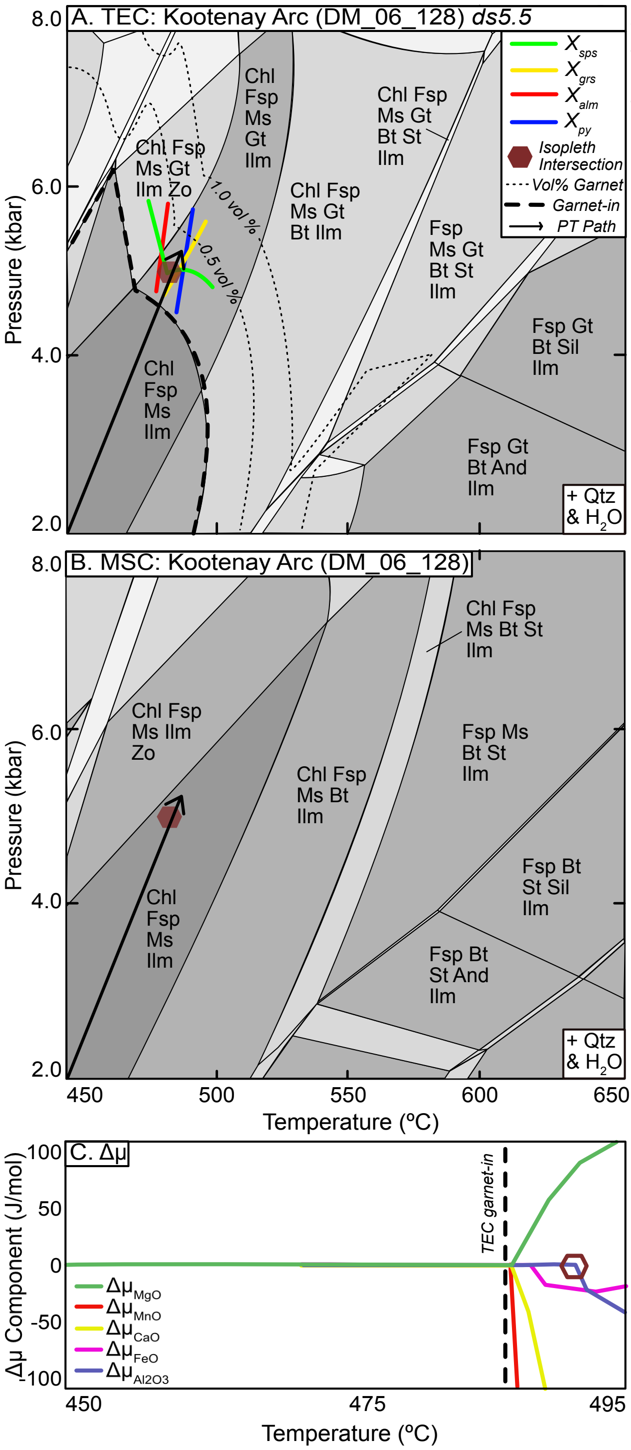

**Supplemental Figure 2:** A. TEC pseudosection for sample DM_06_128 (Kootenay Arc). B. MSC pseudosection for sample DM_06_128. C. $\Delta\mu_{component}$ along *P-T* path shown in A & B.

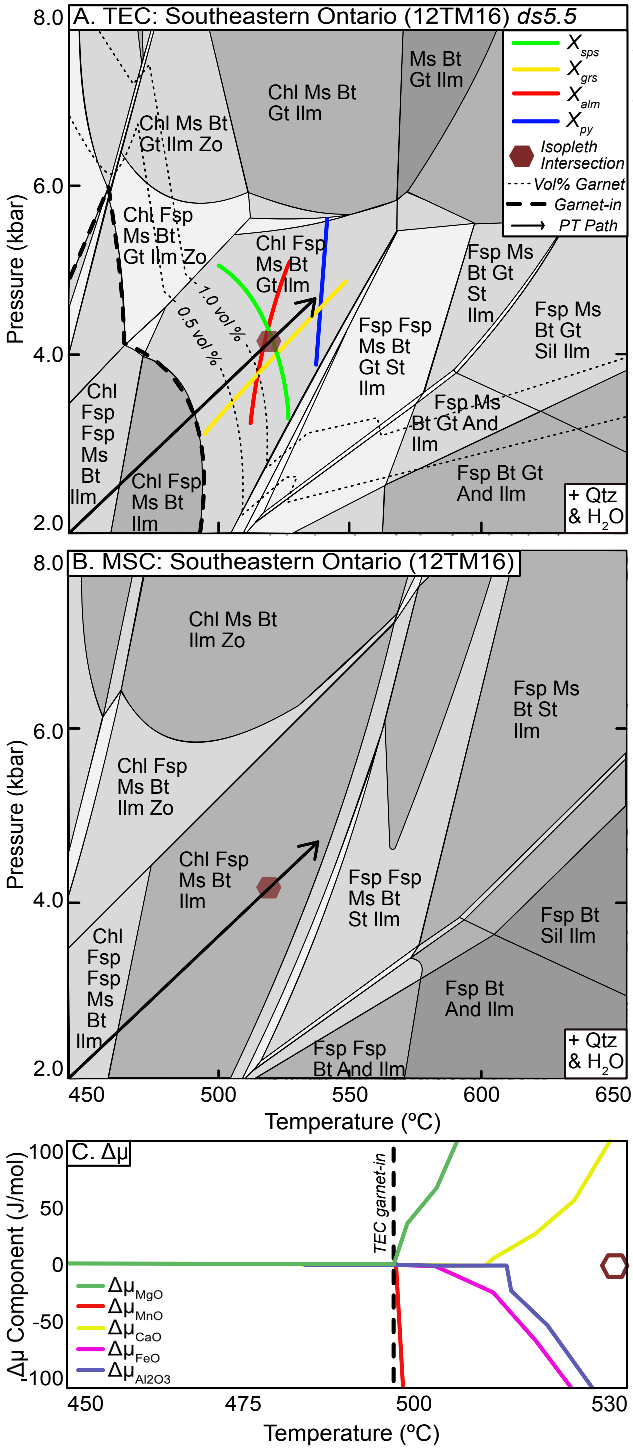

**Supplemental Figure 3:** A. TEC pseudosection for sample 12TM16 (Southeastern Ontario). B. MSC pseudosection for sample 12TM16. C. $\Delta\mu_{component}$ along *P*-*T* path shown in A & B.

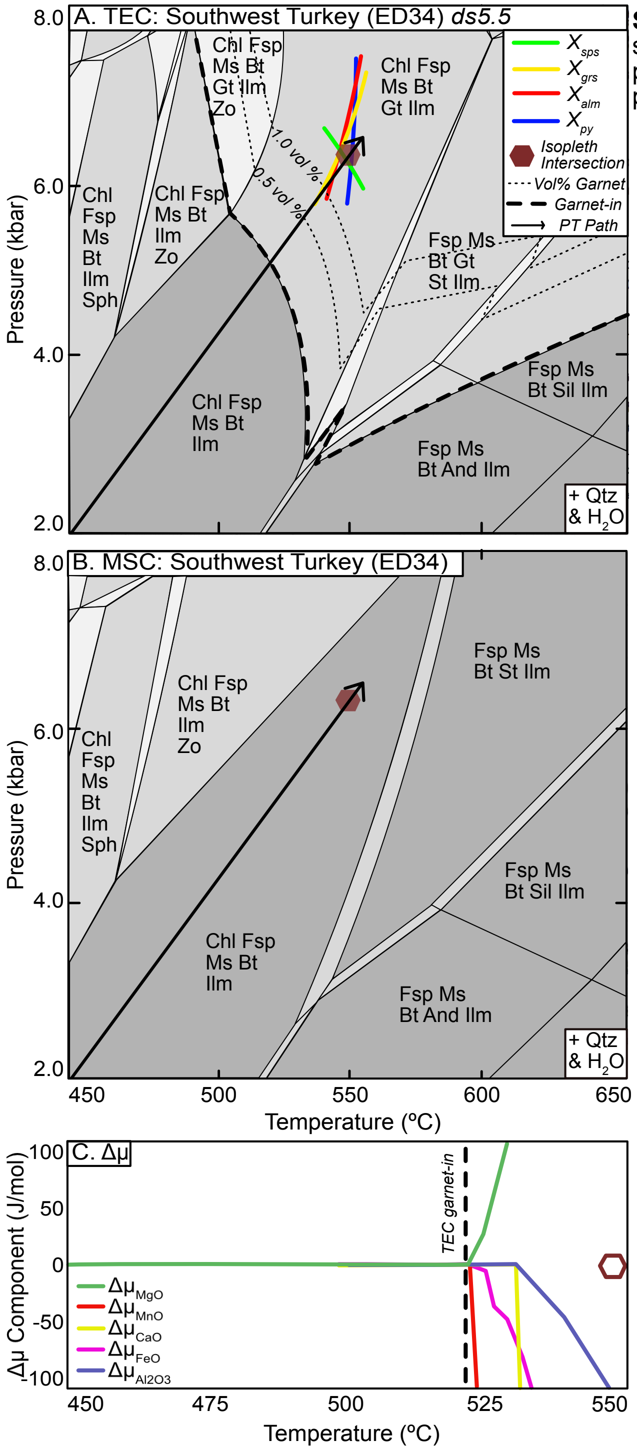

**Supplemental Figure 4:** A. TEC pseudosection for sample ED34 (Southwest Turkey). B. MSC pseudosection for sample ED34. C. $\Delta\mu_{component}$ along *P-T* path shown in A & B.

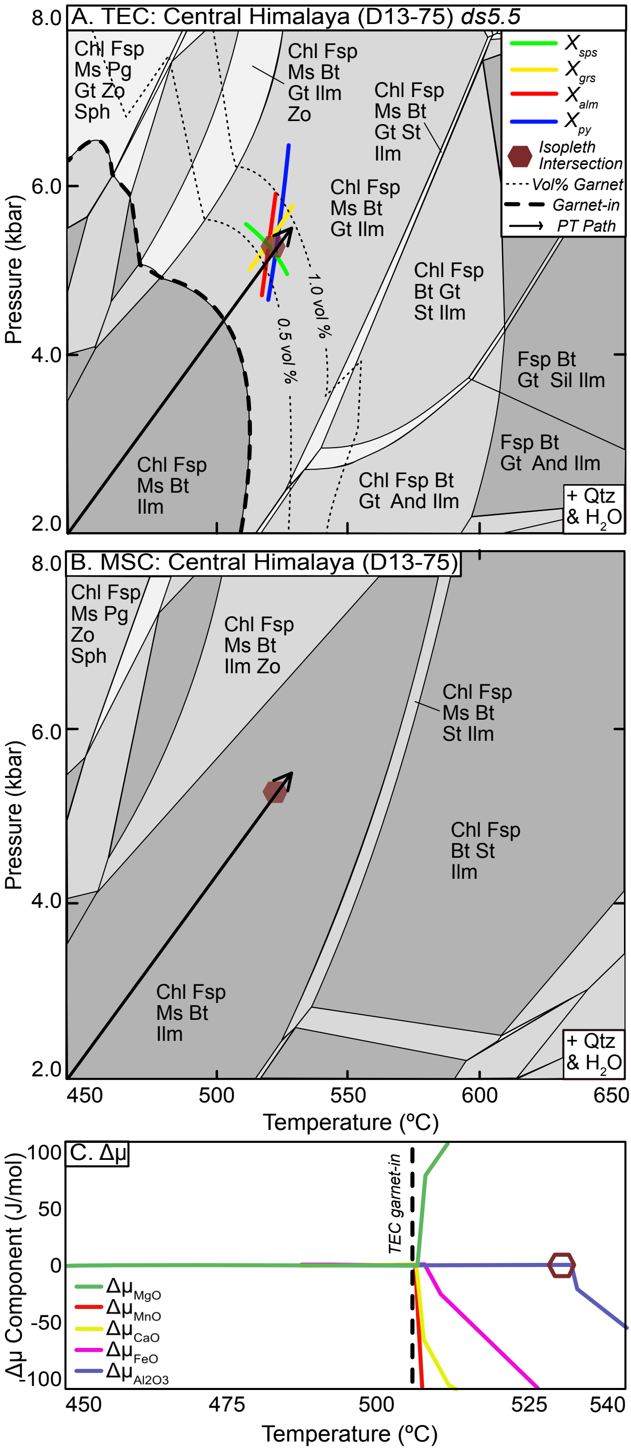

**Supplemental Figure 5:** A. TEC pseudosection for sample D13-75 (Central Himalaya). B. MSC pseudosection for sample D13-75. C. $\Delta\mu_{component}$ along *P-T* path shown in A & B.

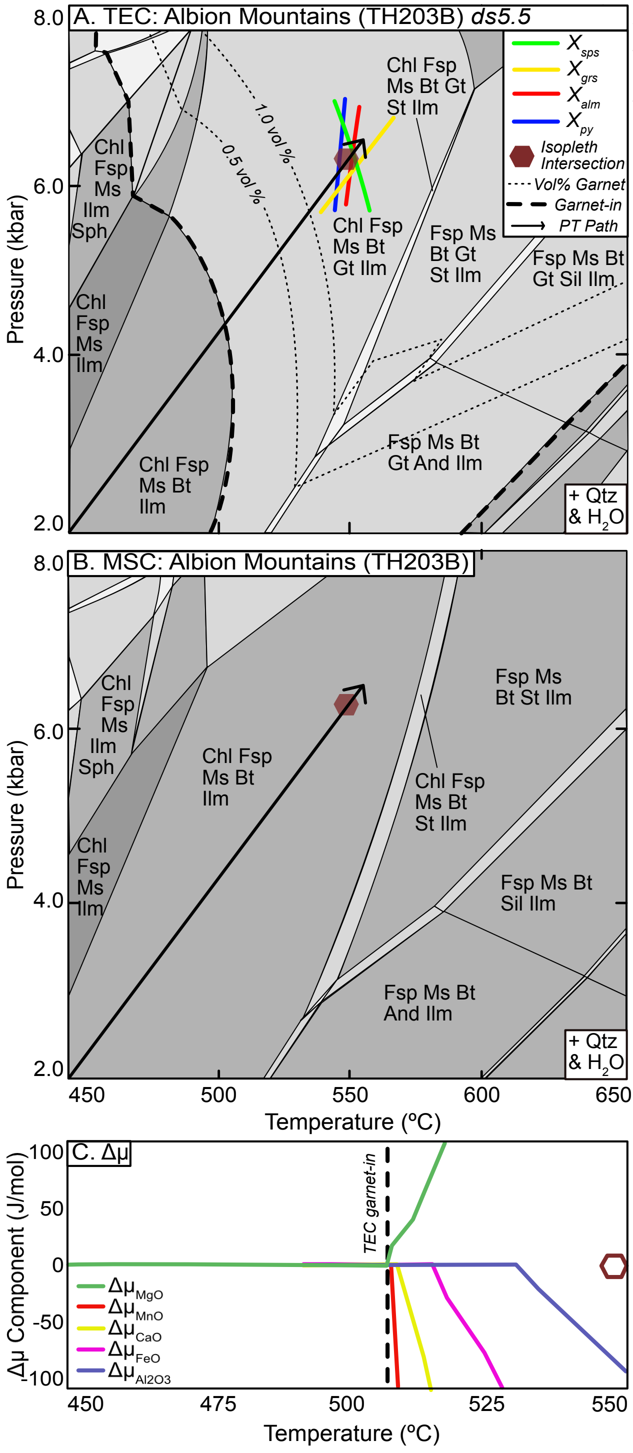

**Supplemental Figure 6:** A. TEC pseudosection for sample TH203B (Albion Mountains). B. MSC pseudosection for sample TH203B. C. $\Delta\mu_{component}$ along *P-T* path shown in A & B.

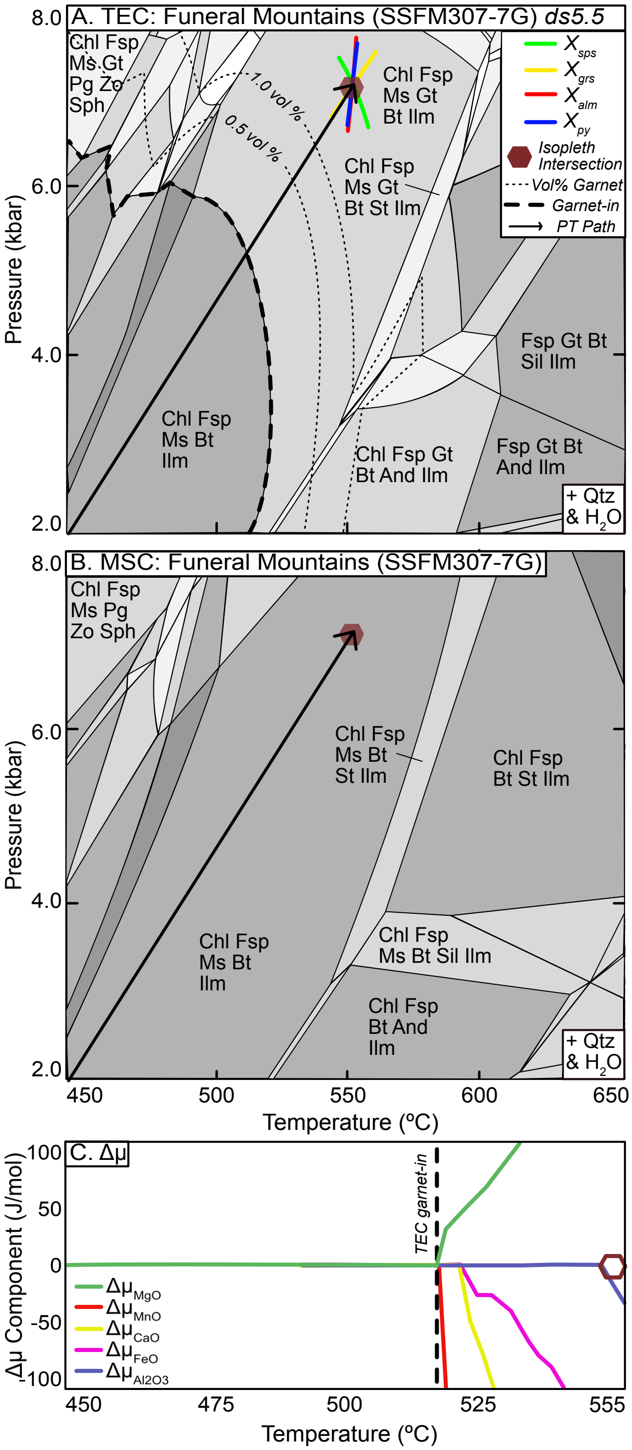

**Supplemental Figure 7:** A. TEC pseudosection for sample SSFM307-7G (Funeral Mountains). B. MSC pseudosection for sample SSFM307-7G. C. Δμ$_{component}$ along *P-T* path shown in A & B.

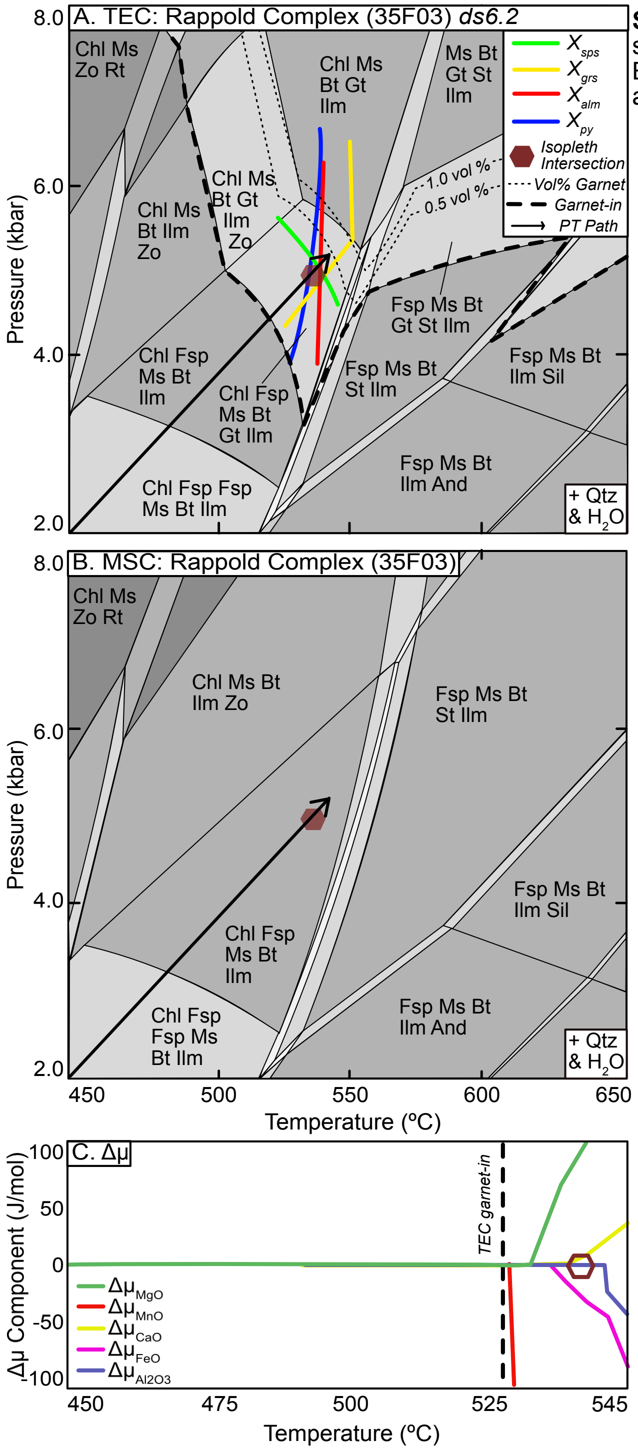

**Supplemental Figure 8:** A. TEC pseudosection for sample 35F03 (Rappold Complex) calculated with ds6.2 B. MSC pseudosection for sample 35F03. C. $\Delta\mu_{component}$ along *P-T* path shown in A & B.

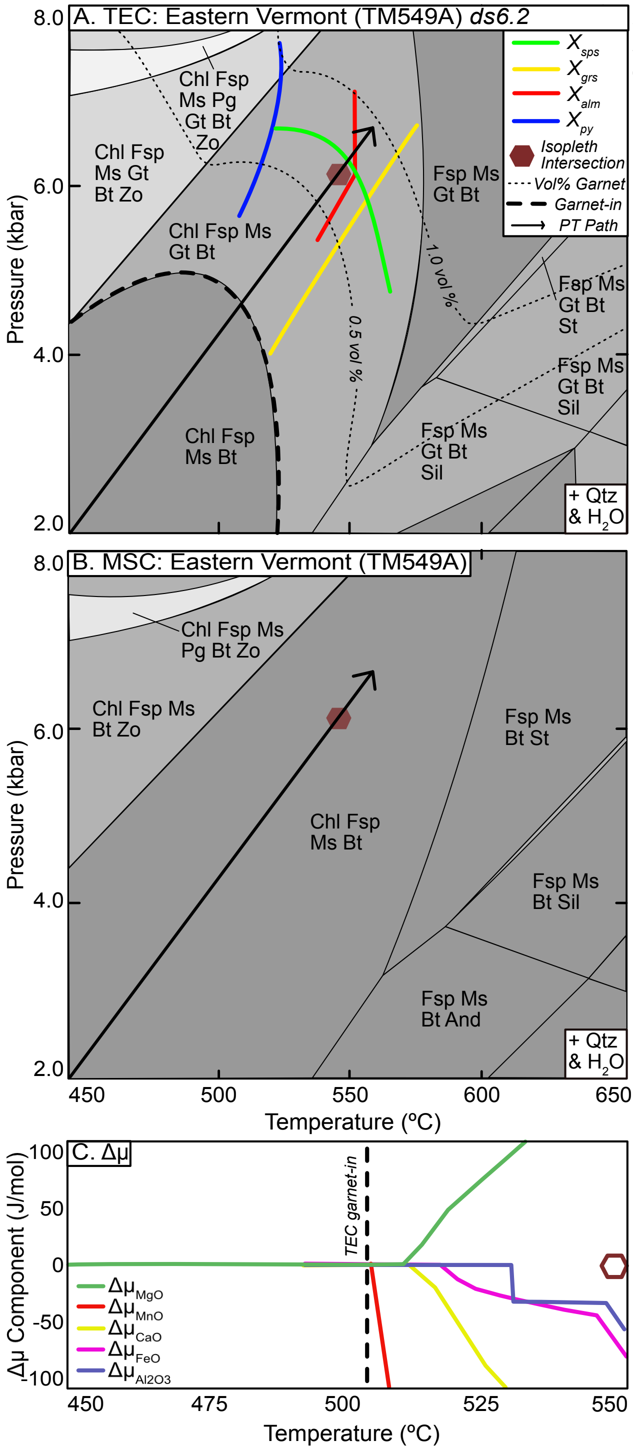

**Supplemental Figure 9:** A. TEC pseudosection for sample TM549A (Eastern Vermont) calculated with ds6.2. B. MSC pseudosection for sample TM549A. C. $\Delta\mu_{component}$ along *P-T* path shown in A & B.